
A Scanning Single-Electron Transistor Array Microscope Probes the Hall Potential Profile in the Fractional Quantum Hall Regime

Von der Fakultät Mathematik und Physik der Universität Stuttgart zur
Erlangung der Würde eines Doktors der Naturwissenschaften (Dr. rer. nat.)
genehmigte Abhandlung

vorgelegt von
Andreas W. Gauß
aus Herrenberg

Hauptberichter : Prof. apl. Dr. Jürgen Weis
Mitberichter : Prof. Dr. Peter Michler
Tag der mündl. Prüfung : 28.03.2019

MAX-PLANCK-INSTITUT FÜR FESTKÖRPERFORSCHUNG
Stuttgart, 2019

Contents

1	Goal and Structure of this Thesis	1
2	Two-Dimensional Electron Systems and the Quantum Hall Effect	5
2.1	Formation of a two-dimensional electron system (2DES) inside an (Al,Ga)As heterostructure	5
2.2	2DES in low magnetic fields - classical magneto transport	8
2.3	2DES in high magnetic fields - Landau level quantization	10
2.4	Combination of high magnetic field and electric field	11
2.5	The Integer Quantum Hall Effect (IQHE)	12
2.6	The Fractional Quantum Hall Effect (FQHE)	13
3	Microscopic Picture of the Integer Quantum Hall Effect	17
3.1	Former experimentally observed Hall potential profiles	17
3.2	Inhomogeneous 2DES in high magnetic fields: an electrical compressible/incompressible landscape is formed	20
3.3	Interpretation of Hall potential profile evolution: biased current flows in incompressible regions	24
3.4	Partial electrostatic depletion leads to incompressible stripes in front of contacts	26
3.5	Hot spots - local areas of dissipation	28
3.6	The microscopic picture of the Integer Quantum Hall Effect	29
3.7	Electrical breakdown of the IQHE: edge-dominated and bulk-dominated QH regime identified in electrical transport measurements	33
3.8	Closed incompressible ring necessary for quantized Hall resistance	35
3.9	Summary	40
4	The Scanning Single-Electron Transistor (SET) Array Microscope and Quantum Hall Sample	41
4.1	Our scanning probe microscope setup in the Precision Laboratory of the Institute	42
4.2	Basics to single-electron transistor	44

4.2.1	Arrangement of a metallic single-electron transistor (SET)	44
4.2.2	Single-electron charging energy	46
4.2.3	Current versus source-drain bias voltage characteristics	48
4.2.4	Current versus gate voltage characteristics: Coulomb-blockade oscillations	50
4.2.5	Charge stability diagram	51
4.3	Free-standing single-electron transistors as local electrometers	54
4.4	SET characterization at low temperature	57
4.5	2DES in (Al,Ga)As heterostructures shaped as Hall bar sample: Special design rules	59
4.6	Hall bar characterization at low temperature	62
4.7	Summary	64
5	Measurement Principle - Hall Potential Profiles and Current Densities	67
5.1	Electrostatic effects affecting the SET island potential	68
5.2	Coulomb-blockade oscillation (CBO) method	72
5.3	Tip position shifted by applied magnetic field	75
5.4	DC feedback loop measurement technique	76
5.5	AC method to determine changes in capacitive coupling	80
5.6	Dealing with charge instabilities of the SET	82
5.7	Get access to Hall potential profiles - two traces (α and β) have to be measured	83
5.8	Extract the current density distribution from Hall potential profiles	86
5.9	Summary	87
6	Hall Potential Profiles Acquired in the Integer Quantum Hall Regime	89
6.1	Hall potential profiles around Landau level filling factor $\nu = 2$	90
6.2	An overall increased Hall voltage drop indicates decreased dissipation along the sample	96
6.3	First Hall potential profiles around $\nu = 3$ and $\nu = 1$	98
6.4	Summary	101
7	Hall Potential Profiles in the Fractional Quantum Hall Regime	103
7.1	Breakdown behavior of the fractional quantum Hall state $\nu = 2/3$	104
7.2	First Hall potential profiles in the $\nu = 2/3$ fractional quantum Hall state	106
7.3	Reversed current direction leads to mirrored Hall potential profiles	109

7.4	Evolution of Hall potential profiles and local current density distribution in the $\nu = 2/3$ fractional quantum Hall state	111
7.5	Drop of the dissipation around $\nu = 2/3$	114
7.6	Hall potential profiles spatially resolved within an Hall bar area	115
7.7	Inhomogeneity of the 2DES is observed	118
7.8	Breakdown of the edge-dominated quantum Hall regime with rising Hall voltage	120
7.9	Fractional quantum Hall state $\nu = 3/5$ is probed	122
7.10	Summary	126
8	Why do we see always the same Hall Potential Profile Evolution passing a Quantum Hall Plateau?	127
9	Imaging the Electrically Compressible/Incompressible 2DES Landscape with an SET	131
9.1	Electrically compressible/incompressible 2DES landscape	131
9.2	Measurement principle using one SET	132
9.3	Proposal for another method - using several SETs	137
9.4	Summary	139
10	Summary	141
11	Deutsche Zusammenfassung	151
12	Appendices	163
A	Improved SET Design and Cleanroom Fabrication Process	165
B	Electrical Characterization of Further SETs	175
C	Hall Potential Profiles around $\nu = 2/3$ close to Potential Probing Contact	177
D	Supplementary Measurement Data Showing the 2DES Inhomogeneity along the Hall Bar	181
E	Accessing Equilibrium Currents with a Free-standing Hall Sensor	183
F	Probing the Temperature Distribution above a Hall Bar under Quantum Hall Conditions	189
G	Eddy Currents with Changing Magnetic Field	191
G.1	Hysteretic potential changes during magnetic flux variations	192

G.2	Hysteretic potential changes spatially resolved	194
G.3	Chemical potential variation	195
G.4	Summary	196
H	Design Proposal to Enhance the Working Temperature of the SET Array to 1.4 Kelvin	199
I	Decoupling of the 2DES-Bulk from the Edge in the Quantum Hall Regime	205
I.1	DC method	207
I.2	AC method	208
I.3	Comparison with results obtained in previous works	212
I.4	Summary	213
J	Hall Potential Profiles in more Complex Situations	215
K	Development Steps necessary to Realize a Hall Sensor Cross on a Free-Standing Tip	221
L	View on the Microscopic Setup	229
	Bibliography	229

List of symbols and abbreviations

Abbreviations

Notation	Description
2DES	two-dimensional electron system
AC	alternating current
AC FBL	AC feedback loop
$\text{Al}_x\text{Ga}_{1-x}\text{As}$	aluminum gallium arsenide
(Al,Ga)As	aluminum gallium arsenide
AQHE	anomalous quantum Hall effect
AuGeNi	gold germanium nickel
CBO	Coulomb-blockade oscillations
CF	composite fermion
CGS	Chklovskii, Shklovskii and Glazman
COM	common
D	drain lead electrode
DC	direct current
DC FBL	DC feedback loop
DOS	density of states
Env	environment
FIB	focused ion-beam
FQH	fractional quantum Hall
FQHE	fractional quantum Hall effect
FWHM	full width at half minimum
GaAs	gallium arsenide
IQH	integer quantum Hall
IQHE	integer quantum Hall effect
IV	current-voltage
MOSFET	metal oxide semiconductor field-effect transistor
S	source lead electrode

SdH	Shubnikov-de-Haas
SEM	scanning electron microscope
SPM	scanning probe microscope
SET	single-electron transistor
LL	Landau level(s)
MBE	molecular-beam epitaxy
PID	proportional-integral-derivative (controller)
QH	quantum Hall
QHE	quantum Hall effect
QUILLS	quasi-inter Landau level scattering
RIE	reactive-ion etching

Physical constants

Notation	Description
h	Planck constant
\hbar	reduced Planck constant
e	elementary charge
$-e$	electron charge
Φ_0	magnetic flux quantum
π	ratio between circle circumference and diameter
μ_B	Bohr magneton
m_e	free electron mass
ϵ_0	vacuum permittivity
k_B	Boltzmann constant

Symbols

Notation	Description
a_B^*	effective Bohr radius
a_ν	spatial width of incompressible stripe with filling factor ν
d_0	electron screening length
e^*	effective fractional charge
g^*	Landé factor
i	integer filling factor
I_x	externally biased current flowing along a Hall bar

j_x	current density along a Hall bar
j_x^*	current density obtained as derivative of Hall potential
k	integer number
k_x, k_y	wave vector components along x, y
l	distance between Hall bar probing contacts
\tilde{l}	length of active Hall sensor area
l_B	magnetic length
m^*	effective electron mass
n	natural number
n_{2D}	sheet electron density inside a 2DES
n_L	Landau level degeneracy
s	Spin quantum number
t	time
v_D, \vec{v}_D	drift velocity (vector)
w	Hall bar cross-section width
\tilde{w}	width of active Hall sensor area
y_ν	center position of incompressible stripe with filling factor ν
x, y, z	spatial Cartesian coordinates
z_i	position (x_i, y_i) of the i -th electron, given as $z_i = x_i + iy_i$
ΔV_{COM}	DC feedback loop signal change
$\delta(x)$	Dirac delta function
ϵ	dielectric constant
ϵ	electron eigenenergy
$\epsilon_F^{(S)}, \epsilon_F^{(D)}$	Fermi levels of lead electrodes source and drain
ϵ_l	Landau level energy
ϵ_Σ	total electron energy
κ	electrical 2DES compressibility
μ	electron mobility
μ_{ch}	chemical potential
μ_{elch}	electrochemical potential
∇	differential operator in space
ϕ	electrostatic potential
Φ_{isl}	electrostatic SET island potential
$\Psi(x, y, z)$	electron wave function
ρ_{xx}, ρ_{xy}	resistivity tensor elements: diagonal and off-diagonal
τ	mean scattering time

ν	Landau level filling factor
ν^*	effective Landau level filling factor
$\nu_{\text{gate}}^{(\text{SD})}$	local filling factor below the gates in front of S/D contact
$\nu_{\text{gate}}^{(\text{side})}$	local filling factor below the gates along a Hall bar edge
ω	AC signal frequency
ω_c	cyclotron frequency
B^*	effective magnetic flux density
B, \vec{B}	magnetic flux density (vector)
B_z	magnetic flux density component along z
$C_{2\text{DES}}$	partial capacitance: SET island to Hall bar 2DES
C_{D}	partial capacitance: SET island to drain lead
C_{Env}	partial capacitance: SET island to environment
C_{G}	partial capacitance: SET island to gate electrode
C_i	partial capacitance: SET island to electrode i
C_{S}	partial capacitance: SET island to source lead
C_{Stray}	partial capacitance: SET island to electrodes except S/D
C_{Σ}	total SET island capacitance
$D(\varepsilon)$	density of states
\vec{E}	electric field vector
E_{C}	SET single-electron charging energy
E_{Δ}	energy difference for subsequent SET island charging
$E_{\text{F}}, \varepsilon_{\text{F}}$	Fermi energy
E_{N}	electrostatic potential energy to add N electrons to SET island
E_y	electric field component along y direction
F	electric field of triangular confinement potential
\vec{F}_{Lorentz}	Lorentz force acting on electrons
G, G_{max}	electrical conductance, maximum electrical conductance
I_{Dia}	diamagnetic current in incompressible stripe
I_{SET}	electrical current through an SET
$I_{\text{SET}}^{(\text{nom})}$	nominal electrical SET current; working point
N	number of electrons
$N_{2\text{D}}$	number of electrons in an area of 2DES
N_{Φ_0}	number of magnetic flux quanta in an area of 2DES
Q	electrical charge
R_i^{T}	resistance of SET tunnel barrier i

R_{sensor}	resistance of active Hall sensor area
R_{series}	resistance in series to Hall sensor
R_{xx}, R_{xy}	longitudinal and transversal (Hall) resistance
T	absolute temperature
$V(z)$	confinement potential in z -direction
$\hat{V}_{\text{COM}}^{(\text{AC,SD})}$	detectable AC voltage amplitude during α -trace
$\hat{V}_{\text{COM}}^{(\text{AC,COM})}$	detectable AC voltage amplitude during β -trace
V_{D}	electrostatic potential of SET lead electrode drain
V_{DS}	voltage applied between lead electrodes source and drain
$V_{\text{DS}}^{(1/2)}$	full-voltage-width-at-half-minimum of conductance dip
V_{Env}	electrostatic potential of environment
V_{G}	electrostatic potential of SET gate electrode
V_{H}	Hall voltage
V_i	electrostatic potential of electrode i
V_{2DES}	electrostatic potential of Hall bar 2DES
\hat{V}_{2DES}	AC voltage amplitude
\tilde{V}_{2DES}	calibrated Hall potential profile across the 2DES width
$\tilde{V}_{\text{2DES}}^{(\text{norm})}$	normalized calibrated Hall potential profile
V_{G}	gate potential
V_{S}	electrostatic potential of SET lead electrode source
V_{sensor}	voltage drop across the active Hall sensor area
V_x, V_y	longitudinal and transversal (Hall) voltage

Chapter 1

Goal and Structure of this Thesis

In 1980 Klaus von Klitzing observed during Hall measurements on MOSFETs, hosting a two-dimensional electron system, at low temperatures fixed values of the Hall resistances R_{xy} while varying the electron concentration or the applied magnetic field. He realized that the specific resistance values of these plateaus are described with $h/(ie^2)$ (i is integer) and they just depend on fundamental physical constants h (Planck constant) and e (electrical charge), and not on sample properties. In 1985 Klaus von Klitzing was rewarded with the Nobel prize for this observation and interpretation. This effect is nowadays denoted as quantum Hall effect (QHE) [1]. Since 1990 the QHE is used as a resistance standard. More recently, it played a key role in the redefinition of the *Système International d'unités* (SI unit system). From May 2019 [2–4] the SI units are defined by fixing the values of fundamental physical constants as h , e , c and k_B .

In 1982 Störmer, Tsui and Laughlin [5, 6] (Nobel prize in 1998) observed and discussed in samples with higher charge carrier mobilities and at lower temperatures the fractional quantum Hall effect. Here, additionally to integer quantum Hall plateaus, further resistance plateaus are observable with $R_{xy} = h/(\nu e^2)$ where ν are special fractional numbers. The current understanding of this fractional quantum Hall effect is that electron-electron interaction leads to quasi-particles with fractional effective charge.

Long time it was not clear why these quantized resistance values appear - is it a bulk-effect or an edge-effect? In the middle of the 1990s, Peter Weitz [7] from our group at the Max Planck Institute built a scanning electrostatic force microscope to measure Hall potential profiles at 1.4 K, in order to settle this question. Since then, many local scanning probe experiments [7–17] on two-dimensional electron systems in (Al,Ga)As heterostructures were performed in our group using this microscope.

Peter Weitz [7–9] and his successor Erik Ahlswede [10–12] made systematic measurements of Hall potential profiles as a function of the applied magnetic flux density B . Over integer quantum Hall plateaus they observed a spatial evolution of the current flow which cannot be described in the edge-state picture that is often found in textbooks. At the lower magnetic field side of the plateau the current is located close to the etched sample edges, while it moves into the sample bulk for the higher magnetic field side of the plateau.

Rolf Gerhardt and coworkers observed in theoretical, self-consistent calculations [18] for a two-dimensional electron system in the quantum Hall regime that a landscape of electrostatically compressible/incompressible regions evolves which changes with magnetic flux density. Together with the experimental data this was a good base to develop a microscopic picture for the integer quantum Hall effect (IQHE), describing the observed Hall potential evolution. The externally biased current flows only inside electrically incompressible regions of the two-dimensional electron system.

Then Frank Dahlem studied the influence of annealed potential probing contacts on the two-dimensional electron system [13–15]. He observed that the contacts lead to a partial electrostatic depletion at their boundary to the electron system - like etched sample edges - and thus, to electrostatic incompressible regions in front of the probing contacts. So, the externally biased current does not flow through the probing contacts, but within incompressible regions in front of them.

Experiments were continued by Konstantinos Panos [16,17] who studied the breakdown of the integer quantum Hall effect, which occurs for high voltage drops across electrostatically incompressible regions. In addition, he exchanged the (Al,Ga)As material system with monolayer graphene and showed that the hitherto developed microscopic picture of the IQHE is also valid there.

At present, the microscopic picture of the integer quantum Hall effect is a good base for understanding the integer quantum Hall regime. The question now is: How does the current distribution look like, when the regime is changed from the integer to the fractional quantum Hall regime.

To access the fractional quantum Hall regime a new cryogenic system which reaches 16 mK base temperature and magnetic flux densities up to 18 T, as well as high-mobility samples, have become necessary. My predecessor Marcel Mausser built

and characterized in 2012 the new scanning probe microscope setup for this purpose [19]. This new microscope is operated within a He^3/He^4 mixture. Hence, the formerly used electrometer - which is a metal tip on a piezoelectric cantilever - cannot be used anymore due to damping and resonance effects caused by the mixture. It is replaced by an array of eight electrically independent single-electron transistors as sensitive local electrometers which were developed by Jochen Weber [20]. Marcel Mausser finished his PhD with first measurements of Hall potential profiles taken with our new scanning single-electron transistor array microscope across an (Al,Ga)As sample in the integer quantum Hall regime [21].

In this thesis we present very first systematic local measurements of the current density distribution in two-dimensional electron systems in (Al,Ga)As at high magnetic fields when fractional quantum Hall conditions are present.

This thesis is structured in the following way:

In **chapter 2** necessary basic introductions are given to the formation of two-dimensional electron systems and the quantum Hall effect. **Chapter 3** then explains the current microscopic picture of the integer quantum Hall effect, before in **chapter 4** the new scanning single-electron transistor array microscope is discussed and in **chapter 5** the measurement technique is demonstrated. **Chapter 6** shows first systematic Hall potential measurements with this microscope in the integer quantum Hall regime to demonstrate its functionality. Then in **chapter 7** first Hall potential profiles in the fractional quantum Hall regime are shown, before in **chapter 8** a microscopic explanation is given, why for integer and fractional quantum Hall states always the same Hall potential profile evolution is expected. **Chapter 9** explains a measurement technique to probe the underlying electrically compressible/incompressible landscape of the 2DES together with first measurement results.

A summary and perspective of this thesis is given in **chapter 10** (English) and **chapter 11** (German). In the **appendix**, supplementary information can be found.

Chapter 2

Two-Dimensional Electron Systems and the Quantum Hall Effect

The aim of this thesis is to locally probe the spatial distribution of an externally biased current within a high-mobility two-dimensional electron system under fractional quantum Hall conditions. The high electron mobility two-dimensional electron system (2DES) used in this thesis is embedded in an (Al,Ga)As heterostructure grown by molecular-beam epitaxy (MBE). This system has to be pre-characterized at low temperatures to ensure that integer and fractional quantum Hall states are observable.

In this chapter the formation of a 2DES is described and the heterostructure that is investigated within this thesis is presented. Influences of low and high magnetic fields on the two-dimensional electron system are discussed and the quantum Hall effect is shortly introduced, before the microscopic picture of the integer quantum Hall effect is presented in the following chapter 3.

2.1 Formation of a two-dimensional electron system (2DES) inside an (Al,Ga)As heterostructure

The confinement of electrons into a TWO-DIMENSIONAL ELECTRON SYSTEM (2DES)¹ can be realized in many ways. Common systems are silicon metal-oxide-semiconductor field-effect transistors Si:MOSFET [22], semiconductor heterostructures [23], graphene [24], oxide heterostructures [25,26] and topological insulators [27,28]. In this thesis we investigate an (Al,Ga)As semiconductor heterostructure hosting a 2DES that

¹It is called two-dimensional, as electron movement is restricted to the x,y plane with no movement in z direction.

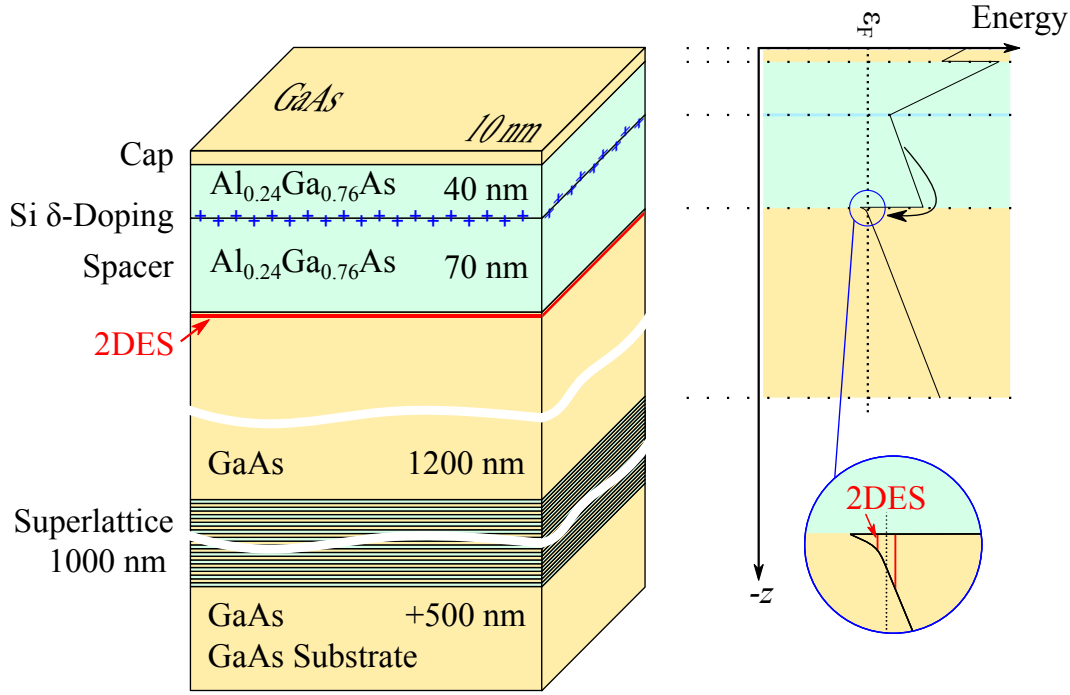


Figure 2.1: GaAs and (Al,Ga)As layer sequence of the heterostructure investigated in this thesis and internally referred as #D110222A. On the left, a schematic of the layer sequence is shown. From bottom to the top we have: A GaAs substrate, a superlattice to smooth the substrate surface, a GaAs buffer including the 2DES, and a delta doped silicon layer embedded between two spacing layers to increase the mobility in the 2DES and to saturate electronic states at the surface. Latter one is protected against oxidation by a thin GaAs cap layer. On the right, the resulting band bending of this heterostructure is simulated, showing the subband energies due to the confinement in z -direction in red.

shows stable many-body correlation effects leading to fractional quantum Hall plateaus. To have many-body correlation effects in a 2DES it is necessary to have clean and homogeneous samples. One parameter that gives information about the homogeneity could be the electron mobility

$$\mu = \left| \frac{-e\tau}{m^*} \right| \quad (2.1)$$

which is a measure for the mean free path; high values of μ are equivalent to long mean scattering times τ and thus, long mean free paths for the electrons. Nowadays mobilities of $35 \times 10^6 \text{ cm}^2/(\text{V s})$ can be achieved [29] in modulation doped (Al,Ga)As quantum well heterostructures grown by molecular beam epitaxy [30]. In GaAs - where the electrons are confined - the effective electron mass is $0.067m_e$ [31, 32], while m_e denotes the free electron mass.

The heterostructure investigated during this thesis was grown in the ETH Zurich in the group of W. Wegscheider and is schematically shown on the left of figure 2.1. The aim of the heterostructure is, to realize a conduction band bending with

2.1. Formation of a two-dimensional electron system (2DES) inside an (Al,Ga)As heterostructure

a spatially very local energy minimum below the Fermi energy ε_F , where later the two-dimensional electron system forms. Hereby, a highly silicon doped (Al,Ga)As layer supplies the 2DES with electrons and also saturates electron trap states at the surface of the (Al,Ga)As heterostructure. For this thesis, the layer composition has to be a compromise: scanning experiments favor a 2DES in close proximity to the surface, but high mobilities are achieved when the 2DES is buried several hundred nanometers deep in the heterostructure.

The growth procedure should be sketched shortly: on top of a commercially available {100} GaAs wafer substrate the following layers are grown: (1) Firstly, 500 nm GaAs act as starting layer covering the substrate. To smooth the layer growth and trap impurities from the substrate, a superlattice with 100 repetitions of 7 nm $\text{Al}_{0.24}\text{Ga}_{0.76}\text{As}$ and 3 nm GaAs is added. Next (2), 1.2 μm GaAs bulk material is grown, followed by (3) a 70 nm $\text{Al}_{0.24}\text{Ga}_{0.76}\text{As}$ spacer layer and a highly silicon doped layer of (Al,Ga)As. At the interface between the GaAs layer and the $\text{Al}_{0.24}\text{Ga}_{0.76}\text{As}$ spacer, the 2DES forms later. The spacer layer separates ionized donor atoms in the silicon doped layer from the 2DES, leading to longer mean scattering times τ . Thus, wide spacer layers lead to high mobilities μ but a lower electron concentration in the 2DES. (4) Another 40 nm $\text{Al}_{0.24}\text{Ga}_{0.76}\text{As}$ are grown to separate the silicon donors from the surface, which is then capped by (5) 10 nm GaAs to suppress oxidation of the aluminum in deeper layers. The cap also pins the electrochemical potential at room temperature into the middle of the bandgap of GaAs. In the past, cap thicknesses of 5 nm have led to non-working 2DES after some years of storage.

The right side of figure 2.1 shows the simulated band bending of the conduction band minimum². In a zoom-in the conduction band minimum with two subband energies of the 2DES is enlarged. One can expect a typical expansion of the wave function of about 10 nm.

The eigenenergies in such a 2DES can be calculated by solving the time-independent Schrödinger equation [32] for a single electron that moves freely in the x, y plane, but within a confinement potential $V(z)$

$$\left(-\frac{\hbar^2}{2m^*} \nabla^2 + V(z) \right) \Psi(x, y, z) = \varepsilon_{\Sigma} \Psi(x, y, z). \quad (2.2)$$

²Simulation was performed using the program 1D Poisson from Gregory Snider [33].

An ansatz for the wave function $\Psi(x, y, z) = \phi(z) \cdot \exp[i(k_x x + k_y y)]$ with the wave vector components k_x and k_y , leads for a triangular confinement potential³ to the eigenenergies [31]

$$\varepsilon_{\Sigma}^{(n)} = \varepsilon_{x,y} + \varepsilon_z = \left(\frac{\hbar^2 k_x^2}{2m^*} + \frac{\hbar^2 k_y^2}{2m^*} \right) + c_n \left(\frac{eF\hbar^2}{2m^*} \right)^{1/3} \quad (2.3)$$

for different integer subbands $n = (1, 2, 3, \dots)$. Here, $c_n = -a_n$ are numerically calculated zeros a_n of the Airy function⁴ $Ai(x)$ which appears in the solution of the Schrödinger equation for this case; for example $c_1 = 2.338$ [31, 34, 35]. At low temperatures a strict 2DES is formed only when the lowest subband energy is occupied; the Fermi energy ε_F lies between the lowest and the next higher subband. The density of states (DOS) $D(\varepsilon)$ - describing the number of available states per energy and volume (or area) - is constant for a 2DES [31, 32] and described by

$$D(\varepsilon) = \frac{m^*}{\pi\hbar^2}. \quad (2.4)$$

The Fermi energy ε_F depends linearly on the charge carrier density n_{2D} of the 2DES [31], as

$$\varepsilon_F = \frac{\pi\hbar^2}{m^*} n_{2D}. \quad (2.5)$$

Typical charge carrier densities n_{2D} of (Al,Ga)As heterostructures used in our group range between $1 \times 10^{14} \text{ m}^{-2}$ to $1 \times 10^{16} \text{ m}^{-2}$.

2.2 2DES in low magnetic fields - classical magneto transport

Electrical characterization of two-dimensional electron systems are often done by shaping the 2DES in a Hall bar geometry, schematically shown in figure 2.2. A small bias voltage V_{DS} is applied between the source (S) and drain (D) contact, resulting in a current I_x along the Hall bar. While the perpendicularly oriented magnetic flux density B is varied, the longitudinal voltage drop V_x and the transversal Hall voltage drop V_y are measured. One obtains the longitudinal resistance $R_{xx} = V_x/I_x$ and the Hall resistance $R_{xy} = V_y/I_x$.

The transport behavior at low magnetic fields can be described within the Drude

³The assumption here is an infinitely high potential at one side and a linearly increasing one on the other side. The linear increase is described by $e \cdot F \cdot z$ with e as electron charge, F as electric field and z the spatial dimension.

⁴An approximation is given by $c_n = [3/2\pi \cdot (n - 1/4)]^{2/3}$, see [31].

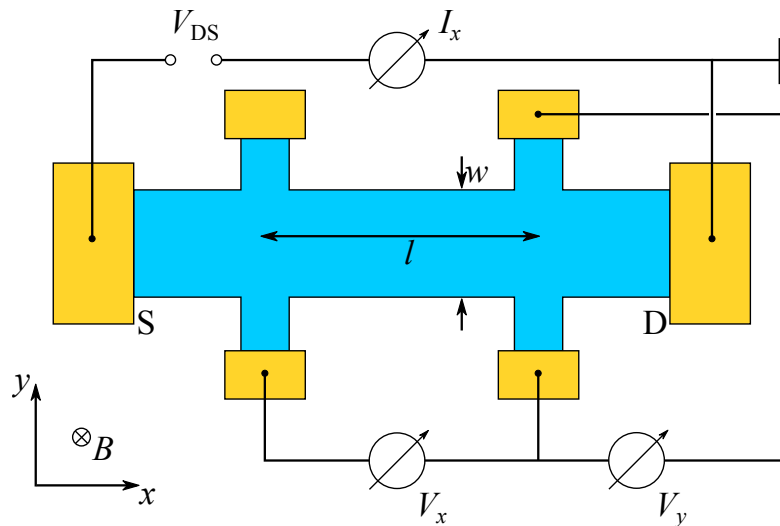


Figure 2.2: Schematic illustration of a 2DES embedded in a six-terminal Hall bar geometry with perpendicularly applied magnetic field B and the electrical connections necessary for magneto transport measurements. The Hall bar dimensions l and w are known from the cleanroom fabrication process. A voltage V_{DS} is applied between the source (S) and drain (D) contact, resulting in a current I_x . The voltages V_x and V_y are measured, and together with I_x the longitudinal resistance R_{xx} and the transversal Hall resistance R_{xy} are determined.

relation for electrical transport [36, 37], which are given [31, 32] by the electrical longitudinal and Hall resistivity components, as

$$\varrho_{xx} = (e \cdot n_{2D} \cdot \mu)^{-1}, \quad (2.6)$$

$$\varrho_{xy} = B \cdot (e \cdot n_{2D})^{-1}. \quad (2.7)$$

Here μ denotes the electron mobility which describes - within the Drude model - the average drift velocity \vec{v}_D of a representative electron when an electric field \vec{E} is applied. For a homogeneous 2DES the equations

$$R_{xx} = \frac{l}{w} \cdot \frac{1}{e \cdot n_{2D} \cdot \mu}, \quad (2.8)$$

$$R_{xy} = \frac{B}{e \cdot n_{2D}}, \quad (2.9)$$

describe the measurable integral quantities. The Hall resistance R_{xy} depends linearly on the magnetic flux density B and can be used to determine the charge carrier type⁵ and the charge carrier density n_{2D} . The longitudinal resistance R_{xx} is independent of B , but depends on the spatial dimensions, more precisely the Hall bar width w and the distance l between probing contacts. With R_{xx} the

⁵Instead of two-dimensional electron systems, also two-dimensional hole systems can be realized.

charge carrier mobility μ can be experimentally determined.

2.3 2DES in high magnetic fields - Landau level quantization

Exposing a two-dimensional electron system to strong perpendicular magnetic fields leads to closed cyclotron orbits of the electron trajectories. This results in a further quantization of the eigenenergies, named LANDAU LEVELS. These discrete eigenenergies are given by a harmonic oscillator like energy spectrum [31, 32, 38]

$$\varepsilon_l(B) = \hbar\omega_c \left(l + \frac{1}{2} \right) \quad l \in \{0, 1, 2, \dots\}, \quad (2.10)$$

where l denotes the Landau level quantum number and $\omega_c = eB/m^*$ the cyclotron frequency. Considering the lowest 2DES subband energy $\varepsilon_{\Sigma}^{(n=1)}$ described in (2.3), and additionally the energetic electron spin splitting by the Zeeman energy $\varepsilon_{\text{Zeeman}} = sg^*\mu_B B$, the total energy of a 2DES electron becomes

$$\varepsilon_{\Sigma}^{(n=1,l,s)}(B) = \varepsilon_{\Sigma}^{(n=1)} + \hbar\omega_c \left(l + \frac{1}{2} \right) + sg^*\mu_B B, \quad (2.11)$$

with two spin directions $s = \pm 1/2$, the Bohr magneton $\mu_B = e\hbar/(2m_e)$ and an effective Landé factor g^* . In GaAs the Zeeman energy is much smaller than the cyclotron energy for a given B .

The electron density in the 2DES is n_{2D} ; these electrons start to fill up the Landau levels starting with the energetically lowest, until this one is completely filled, then continuing to occupy subsequently the next higher Landau levels.

How many electrons can occupy a specific Landau level is described by a magnetic flux density dependent degeneracy [31], given by

$$n_L(B) = \frac{eB}{h}. \quad (2.12)$$

With increasing magnetic flux density B the degeneracy increases and electrons redistribute from energetically higher Landau levels into lower ones. The number of occupied Landau levels can be calculated [31] by dividing the 2DES electron density n_{2D} by the Landau level degeneracy n_L . This is called the Landau level filling factor

$$\nu = \frac{n_{2D}}{n_L}, \quad (2.13)$$

or shortly, just FILLING FACTOR. It is also possible to describe ν by the ratio of

electrons within a homogeneous area of the 2DES to the number of magnetic flux quanta in the same area, as

$$\nu = \frac{N_{2D}}{N_{\Phi_0}} = \frac{N_{2D}}{\Phi/\Phi_0}. \quad (2.14)$$

Thus, for integer filling factors ν each magnetic flux quanta corresponds to ν electrons. In the fractional quantum Hall regime flux quanta and electrons are discussed to form quasi-particles, so called composite fermions. In this case several flux quanta are virtually attached to a single electron.

2.4 Combination of high magnetic field and electric field

What happens when a 2DES is exposed to high perpendicular magnetic flux densities B , while additionally a homogeneous electric field $E = E_y$ in y direction is present? The Schrödinger equation takes the form of a harmonic oscillator [12, 16, 39, 40] and the corresponding electron eigenenergies calculate to

$$\varepsilon_{l,k_x}(B) = \hbar\omega_c \left(l + \frac{1}{2} \right) - \frac{m^* E^2}{2B^2} + eY E \quad l \in \{0, 1, 2, \dots\}, \quad (2.15)$$

with the center coordinate $Y = -\hbar k_x (eB)^{-1}$. Compared to the formerly in (2.10) derived energy of a Landau level, additional terms have to be considered. With a non-zero electric field E the degeneracy within a Landau level is lifted as it gets tilted along Y , sketched in figure 2.3. Electrons with a different k_x , respectively Y , are energetically shifted proportional to E . The group velocity v_g of an electron can be calculated, by its quantum mechanical expectation value, to be $v_g = E/B$ [12, 41]. It is perpendicular to both, the electric field and the magnetic field. It

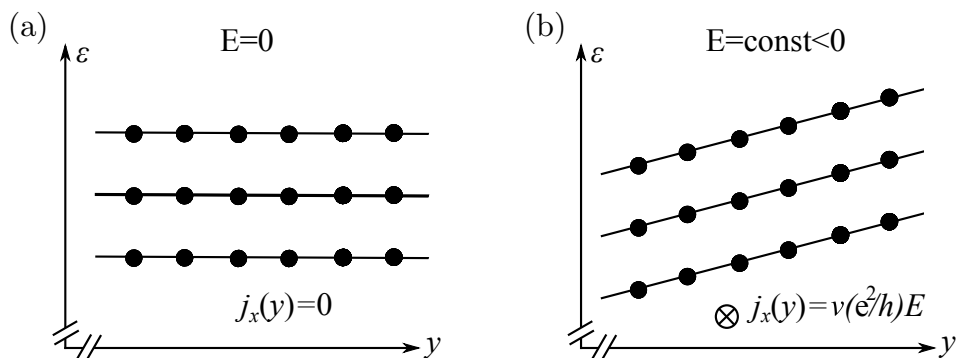


Figure 2.3: Influence of an electric field on Landau levels. (a) No electric field E_y is present. Electronic states within a Landau level are degenerated. (b) With an applied electric field, the degeneracy within a Landau level is lifted as they get tilted along y and all electronic states get the same group velocity v_g .

has to be emphasized that all electrons below the Fermi energy get locally the same group velocity v_g and contribute to the current density j_x in x direction. It is given by [12, 39, 42]

$$j_x = -en_{2D}v_g = \nu \frac{e^2}{h} E_y. \quad (2.16)$$

We conclude: Is a perpendicular magnetic field applied to the 2DES, then an electric field in y direction leads to a current density j_x in x direction. This relation will later become important for the interpretation of Hall potential profiles, taken in a cross-section of a 2DES under quantum Hall conditions.

2.5 The Integer Quantum Hall Effect (IQHE)

In the classical magneto transport regime, formerly presented in section 2.2, equation (2.8) describes a magnetic field independent longitudinal resistance R_{xx} and equation (2.9) a Hall resistance $R_{xy}(B)$ that increases linearly with a perpendicularly applied magnetic field. The measurement in figure 2.4, performed on a 2DES in a six-terminal Hall bar geometry (compare figure 2.2) at 4.2 K and exposed to high perpendicular magnetic fields, shows deviations from this classically expected transport behavior [43].

For magnetic flux densities higher than 1 T the Hall resistance R_{xy} (blue) does

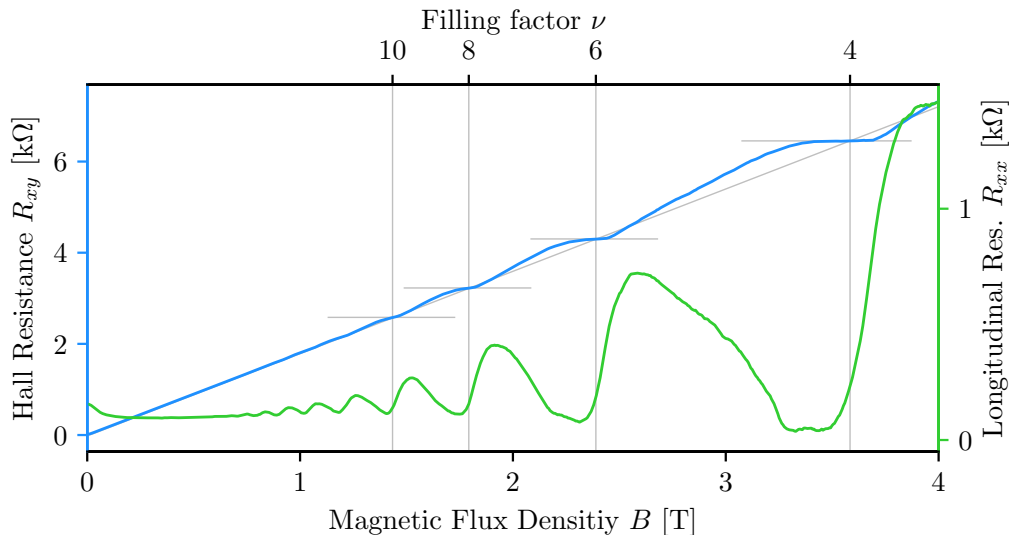


Figure 2.4: Hall resistance R_{xy} (blue) and longitudinal resistance R_{xx} (green) measured on a 2DES with $n_{2D} \approx 3.4(9) \times 10^{15} \text{ m}^{-2}$ exposed to high magnetic flux densities B at a temperature of 4.2 K; the setup is mainly as described in section 2.2, figure 2.2. For magnetic flux densities above 1 T the Hall resistance R_{xy} deviates from the linear regression, classically expected; a plateau structure with quantized values $h/(ie^2)$ emerges. R_{xx} is not constant, but shows Shubnikov-de-Haas oscillations; during plateaus of $R_{xx}(B)$, it approaches small values close to zero.

not always follow the linear regression (gray) and it shows plateau structures in B with well defined resistance values of [1]

$$R_{xy}(\nu) = \frac{h}{i \cdot e^2}, \quad (2.17)$$

with i as integer numbers ($i = 1, 2, 3, \dots$). Some quantized resistance values described by equation (2.17) are indicated by horizontal gray lines within the graph. Moreover, in contrast to a magnetic field independent longitudinal resistance as in equation (2.8), the longitudinal resistance R_{xx} (green) shows Shubnikov-de-Haas oscillations (SdH) [44] reaching small resistance values during plateau regions of R_{xy} . This effect was first observed in 1930 by L. Shubnikov and W. de Haas [45] and is a direct result of Landau level quantization.

The quantized Hall resistance values in (2.17) are independent of sample properties as spatial dimensions or charge carrier concentration; they just depend on fundamental physical constants. Nowadays, this effect from 1980 is well-known as INTEGER QUANTUM HALL EFFECT (IQHE) and in 1985 Klaus von Klitzing was awarded the Nobel prize for his observation and interpretation. Since 1990 this effect is used as resistance standard [46–49]. It also played a key role in the redefinition of the SI unit system, where in the year 2019 fundamental physical constants - as e , h , c and k_B - will be fixed.

In chapter 3 the underlying microscopic picture of the IQHE will be presented.

2.6 The Fractional Quantum Hall Effect (FQHE)

In the previous section the IQHE was measured at 4.2 K. Quantized plateaus of $R_{xy}(B)$ are observed at values of $h/(ie^2)$ while R_{xx} shows resistance oscillations. The same measurement at lower temperatures, higher magnetic flux densities and with samples having higher electron mobilities in the 2DES, leads to a different observation: In addition to the IQHE where i was an integer number, quantized Hall plateaus are also observed for

$$R_{xy}(\nu) = \frac{h}{\nu \cdot e^2}, \quad (2.18)$$

with ν as special fractions. Most Hall plateaus can be observed for odd denominators of ν , when⁶

$$\nu = \frac{1}{k+1} \quad \text{and} \quad \nu = 1 - \frac{1}{k+1} \quad (2.19)$$

⁶The second relation follows naturally from electron-hole symmetry.

with even integer values of k . But also some fractions with even denominators - as $\nu = 5/2$ - have been observed [50]. The first experimentally observed fraction was $\nu = 1/3$, seen by Tsui *et al.* [5] in 1982. In accordance to the IQHE, this effect is known today as FRACTIONAL QUANTUM HALL EFFECT (FQHE).

But in contrast to the IQHE the treatment of the FQHE is more complicated; its origin cannot be a single-particle effect, but electron-electron interaction [6] leads to many-body correlations. A theoretical description of these many-body interactions is challenging.

Firstly, R. B. Laughlin [6] proposed for fractional filling $1/k$ of the lowest Landau level trial wave functions to solve the Hamiltonian that includes now a Coulomb interaction term. These wave functions are given by [6, 51, 52]

$$\Psi_{1/k} = \prod_{i < j} (z_i - z_j)^k \cdot \exp \left(- \sum_i \frac{|z_i|^2}{4l_B^2} \right), \quad (2.20)$$

with z_i and z_j as positions⁷ of the i -th and j -th electron, respectively, and k as odd integer value. This ansatz has the following properties [51, 52]: Firstly, as k is odd due to spin polarization of the lowest Landau level, Ψ is an anti-symmetric function, and secondly, the electron-electron interaction in the product term leads to a vanishing spatial probability for two electrons at the same position - at any time they are separated - and therefore to an energy reduction of the system. For $k = 1$ this represents non-interacting electrons in the IQHE. It can be shown [6], that adding to a homogeneous 2DES area an additional vortex with one magnetic flux quanta passing through it, can be treated equally to adding a quasi-particle with effective but fractional charge $e^* = e/k$.

For both, the experimental and theoretical work to discover a new quantum liquid with fractional charge excitation, R. B. Laughlin, H. L. Störmer and D. C. Tsui were awarded jointly the Nobel price in 1998.

Another approach was developed by Jain [53] in 1989; it is also based on the coupling of electrons and magnetic flux quanta via vortices. But, in this model only even numbers k of flux quanta attach to an electron [51]; this forms a new quasi-particle, the so-called COMPOSITE FERMION (CF). At a magnetic flux density $B_{1/2}$, resulting in a filling factor of $\nu = 1/2$ (two flux quanta per electron) a system of CFs has formed; more precisely, the remaining effective magnetic flux density $B^* = B - B_{1/2}$ becomes zero as all flux quanta are used for the formation of the CF. Increasing the magnetic flux density above $B_{1/2}$, additional flux quanta, not

⁷The position (x, y) is expressed by a complex number $z = x + iy$.

coupled to electrons, are present. Consequently, the CFs feel an effective magnetic flux density of B^* (which is smaller than B). This elegant way of description leads to formation of fractional quantum Hall states when the effective filling factor $\nu^* = N_{2D}/N_{\Phi_0}^*$ equals an integer number. For example, fractional filling factor $\nu = 1/3$ can be thought of as integer filling factor $\nu = 1$ for the CFs.

Chapter 3

Microscopic Picture of the Integer Quantum Hall Effect

In the previous chapter 2 we have seen, if a small current is biased to a 2DES which is itself exposed to a perpendicular magnetic field, a classical approach cannot explain the appearance of extended plateaus in the Hall resistance R_{xy} with B , while at the same time the longitudinal resistance R_{xx} vanishes to zero.

Within this chapter we present experiments and theoretical works that led to the current microscopic picture of the integer quantum Hall effect which is capable to explain both of these effects. Firstly, local non-invasive Hall potential measurements are discussed, showing a characteristic spatial evolution of the Hall potential profile with the magnetic field. This behavior can be understood in terms of the evolution of an electrically compressible/incompressible landscape inside the 2DES. Together with additional scanning experiments close to metallic probing contacts and experiments using the pressure fountain effects in super-fluid helium to track points of heat dissipation, this leads to the microscopic picture of the IQHE. Recent magneto-transport measurements¹ on gated and ungated Hall bar structures further confirm this picture.

3.1 Former experimentally observed Hall potential profiles

About two decades ago, Peter Weitz [7–9] built up a scanning probe microscope operated at 1.4 K. Together with his successor Erik Ahlswede [10–12] he investigated two-dimensional electron systems (2DES) inside an (Al,Ga)As heterostructure exposed to perpendicular magnetic flux densities up to 13 T; integer quantum Hall

¹These measurements were mainly performed by two master students I supervised.

conditions were present. A metal coated tip placed at the end of an oscillating cantilever was used as sensitive electrostatic force sensor in close proximity (normally about 30 nm [12] and 40 nm [7]) to the sample surface where a 2DES was buried about 40 nm below the surface (compare figure 3.1 (b)). Measurements of the resonance frequency shift of the cantilever in connection with a two-step measurement technique yield insight into current induced Hall potential profiles. In this way they got very local and non-invasive access to image where the Hall voltage drops when the 2DES is in integer quantum Hall conditions.

Figure 3.1 (a) shows their measured Hall potential profiles for Landau level filling factors around $\nu = 2$ [54]. This filling factor is representative for discussion here, as all other probed integer filling factors ν showed a similar behavior - this can be seen in a color-coded representation in figure 3.1 (c).

Different types of Hall potential profiles, like linear and non-linear ones, can be identified. For a varying magnetic flux density B , starting from high values in the off-plateau region around filling factor $\nu = 1.67$ and lowering it over the integer quantum Hall plateau with $\nu = 2$ to the off-plateau region with filling factor $\nu \geq 2.4$, the following can be observed:

1. At $\nu = 1.67$ the Hall potential profile is mainly linear over the sample width. As the local current density (2.16) is proportional to the Hall potential gradient [12, 16, 39, 42], this means the current flow is homogeneous over the sample width. This is expected as we are in the classical Hall regime. These types of Hall potential profiles are referred to as TYPE I (blue).
2. With increasing filling factor the linear Hall potential drop becomes non-linear. The drop happens now mainly in the 2DES center (=bulk region) - compare Hall potential profile for $\nu = 1.88$ and $\nu = 1.96$. These are TYPE III profiles (orange).
3. For integer bulk filling factor $\nu = 2$ the Hall voltage drop happens completely in the bulk region of the sample. No drop is observed close to the etched mesa edges. That means, the current flows exclusively in the bulk (center) region of the sample.
4. When ν exceeds integer filling factor 2, the drop in the bulk of the sample separates continuously into two equal drops; one on each side of the sample center, compare $\nu = 2.09$ and $\nu = 2.14$. Now the current flows in two paths which

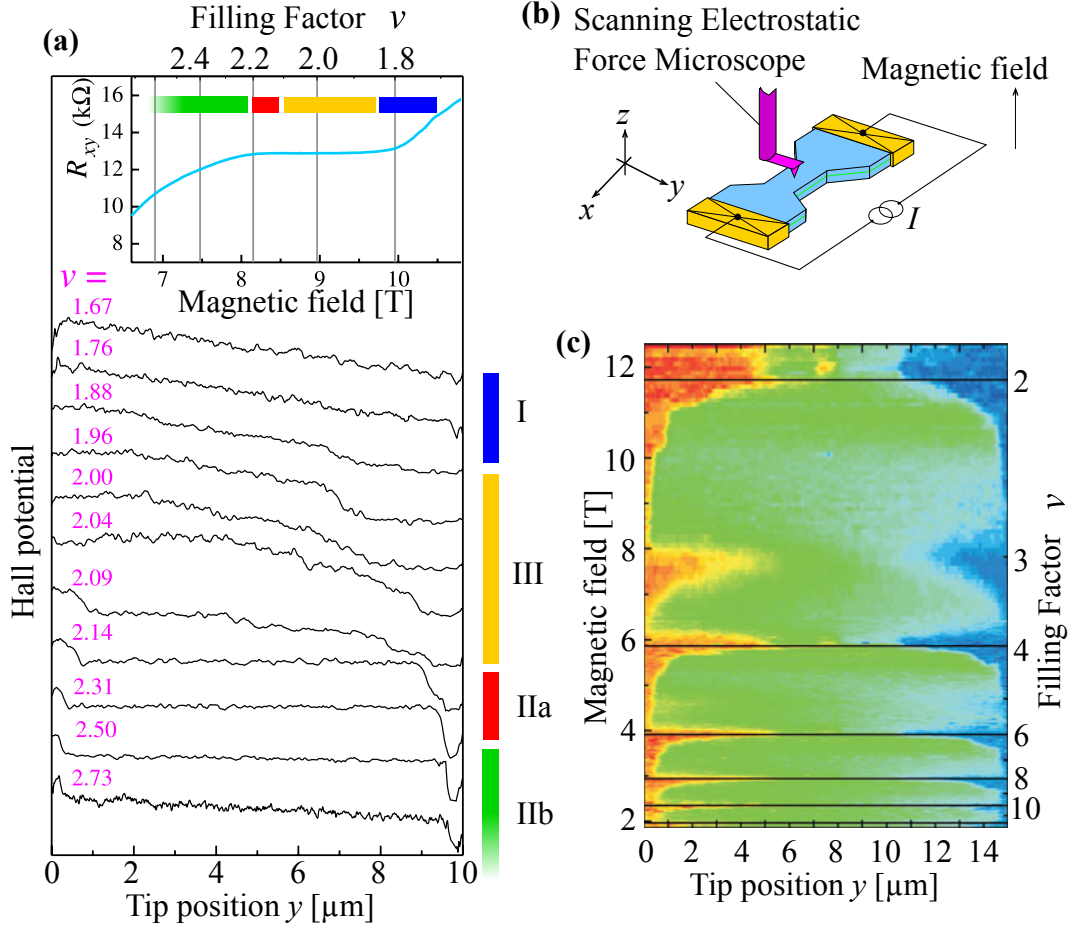


Figure 3.1: Systematic measurements of (calibrated) Hall potential profiles taken in a cross-section of a two-terminal device, shown in (b). It includes a 2DES which is in integer quantum Hall conditions. Hall potentials are probed as a function of the tip position y across the sample width, and magnetic flux density. In (a) the obtained Hall potential profiles for the quantum Hall plateau with filling factor $\nu = 2$ are presented. Four different profile types can be distinguished. The color-coded representation in (c) shows a repeating behavior of the Hall potential profile evolution around each even integer filling factor. Adapted from [17,54] with permission of the Royal Society, copyright 2011.

5. become smaller in width² and move closer to the etched sample edges when the filling factor is further increased (compare $\nu = 2.14$ and $\nu = 2.31$). No Hall potential drop is observed within the bulk region. These profiles are referred to as TYPE IIa (red).
6. When the integer quantum Hall plateau is left at the lower magnetic field side the current redistributes again. At $\nu = 2.73$ a Hall voltage drop in the bulk reappears, while still a distinct drop at the sample edges is observed. These profiles are referred to as TYPE IIb (green).
7. Over a wide range of filling factors ν the linear voltage drop is continuously

²The gradient in the Hall potential drop gets steeper, resulting in a smaller width within which the drop happens.

restored (blue) - we are again in the classical Hall regime (type I Hall profiles will be measured); this can be seen for example in figure 3.1 (c).

Figure 3.1 (c) shows Hall potential profiles over a wide range of filling factors in a false-color representation. The above mentioned evolution of the Hall voltage drop in y repeats for each even integer filling factor with $1 < \nu < 11$.

The observation of a spatial evolution of the Hall voltage drop - and thus an evolution of extended current carrying regions - was new. It was in disagreement with the edge-state picture [55–57] widely used till then. There a current flow is expected in quasi-one-dimensional edge states at the Fermi level, close to the sample edges. A new model was necessary to describe the measured current distribution.

3.2 Inhomogeneous 2DES in high magnetic fields: an electrical compressible/incompressible landscape is formed

Free electrons always tend to rearrange themselves in order to screen and thus minimize electrostatic potential differences resulting in a rearranged electrostatic potential landscape. Among others, a few reasons for potential gradients in real samples can be (1) charged states on the wafer surface, (2) gates in close proximity to the 2DES or (3) chemical imperfections in the heterostructure. In real samples, the electron density n_{2D} towards edge regions of a two-dimensional electron system is naturally depleted to zero. That causes a strong electrostatic potential reconstruction there - often denoted as edge reconstruction.

Chklovskii, Shklovskii and Glazman [58] proposed a quantitative electrostatic theory (sometimes referred to as CGS model) for the evolution of the electrostatic potential landscape in a semi-infinite 2DES, when it is inside a strong perpendicular magnetic field where Landau level quantization takes place. In their calculations, donor concentration fluctuations and charge discreteness are neglected. Far from boundaries the electron concentration was assumed homogeneous and equal to the positive background. The edge depletion was induced via an in-plane metal gate next to the 2DES (compare figure 3.2 (a)). Then the electron density distribution $n_{2D}(y)$ from the edge towards the 2DES bulk, which is an electrostatic problem taking also the DOS into account, was solved analytically.

From the edge towards the bulk they found alternating electrostatically compressible and incompressible stripes, sketched in figure 3.2 (c,d). Here, compressibility

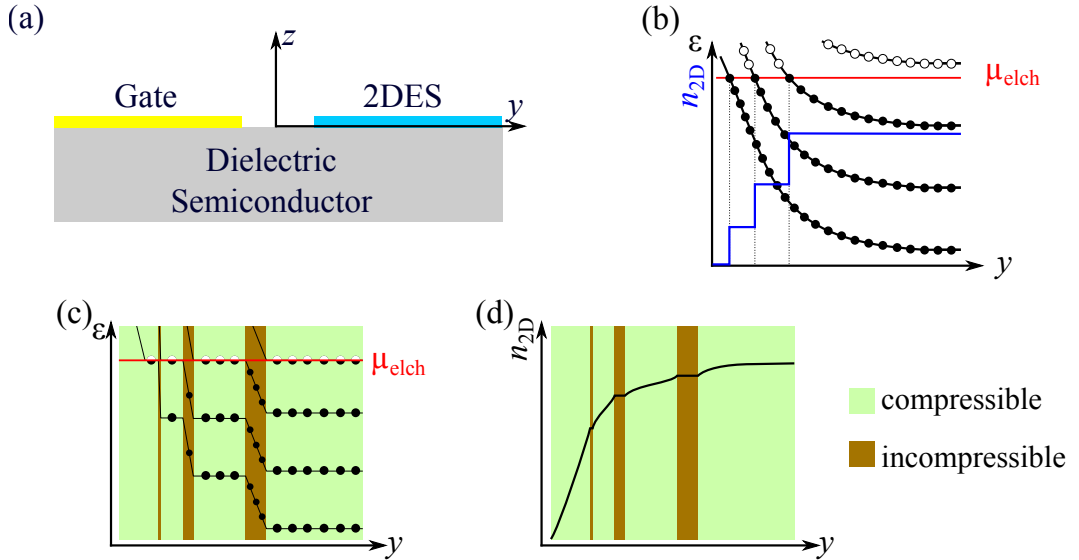


Figure 3.2: Sketch to illustrate formation of electrically compressible and incompressible regions in a semi-infinite 2DES, confined on one side by an in-plane metallic gate. (a) Geometry used for calculations: in close proximity to a 2DES a metal gate with a negative potential leads to a spatial dependent 2DES depletion. (b) The assumption before calculations of Chklovskii *et al.* [58] is a continuous energetic up-bending of Landau levels towards the 2DES edge, resulting in sudden changes of the carrier density $n_{2D}(y)$. (c,d) The calculations of Chklovskii *et al.* showed, alternating electrically compressible (green) and incompressible (brown) stripes along the edge are energetically more favorable. Increasing the electron concentration from the edge towards the bulk, the first Landau level gets filled. When it is locally completely filled, a large amount of chemical energy μ_{ch} is necessary to occupy the second Landau level; hence, it is more favorable to keep $n_{2D}(y)$ constant within a finite width a_ν , see (d), which costs a small amount of electrostatic energy. Consequently, the Landau levels are bent downwards within these regions of constant $n_{2D}(y)$, see (c). When the necessary electrostatic energy to keep n_{2D} constant overcomes the necessary chemical potential, the second Landau level gets filled and n_{2D} increases again.

κ is defined via the derivative of the chemical potential μ_{ch} with respect to the electron concentration n_{2D} as

$$\kappa^{-1} = n_{2D}^2 \cdot \frac{\partial}{\partial n_{2D}} \mu_{ch}. \quad (3.1)$$

In incompressible regions the Fermi energy ε_F lies between two Landau levels, while Landau levels beneath ε_F are occupied and Landau levels above ε_F are empty. Hence, the local filling factor ν in these regions can be described by an integer value. As no free states are available to electrons in incompressible regions, they cannot rearrange themselves and electrostatic potential gradients cannot be screened - these regions have an insulator-like behavior.

Chklovskii *et al.* calculated [58] under neglect of spin splitting the center position y_ν and the spatial width a_ν of incompressible stripes with filling factor ν

as

$$y_\nu = \frac{d_0}{1 - \left(\frac{\text{int}(\nu)}{\nu}\right)}, \quad (3.2)$$

$$a_\nu = 4 \frac{y_\nu}{\nu} \sqrt{\frac{\text{int}(\nu) a_B^*}{\pi d_0}}. \quad (3.3)$$

Here, $y_\nu = 0$ describes the 2DES edge and in this description

$$a_B^* = \frac{4\pi\epsilon_0\epsilon\hbar^2}{e^2m^*} \quad (3.4)$$

denotes the effective Bohr radius of the material with a dielectric constant ϵ , while

$$d_0 = \frac{4\epsilon_0\epsilon}{\pi e^2} \cdot \frac{|eV_g|}{n_{2D}} \quad (3.5)$$

is the screening length that depends on the electron concentration n_{2D} and the negative gate voltage V_g .

Later, Gerhardt and Lier [18] used a more intuitive self-consistent approach to calculate the distribution of electrostatically compressible and incompressible regions inside an electrostatically confined 2DES that is exposed to a strong perpendicular magnetic field. They considered an equilibrium of the electrochemical potential, which is the sum of the chemical potential $\mu_{\text{ch}}(n_{2D}(y))$ and the electrostatic potential energy $-e\phi(y)$,

$$\mu_{\text{elch}}(y) = \mu_{\text{ch}}(n_{2D}(y)) - e\phi(y). \quad (3.6)$$

In an iterative loop, $\phi(y)$ and $\mu_{\text{ch}}(y)$ were used to calculate the electron density $n_{2D}(y)$ in the Thomas-Fermi approximation

$$n_{2D}(y) = \int_{-\infty}^{\infty} D(\varepsilon) \cdot f(\varepsilon + e\phi(y) - \mu_{\text{ch}}(y)) d\varepsilon. \quad (3.7)$$

Here, the Fermi function $f(\varepsilon) = (1 + \exp(\varepsilon/k_B T))^{-1}$ includes the temperature dependence T , and the density of states

$$D(E) = \frac{g_s}{2\pi l_B^2} \sum_{j=0}^{\infty} \delta\left(E - \hbar\omega_c \left(j + \frac{1}{2}\right)\right) \quad (3.8)$$

includes the magnetic field dependence given by $\omega_c = eB/m^*$. In a next step, from this $n_{2D}(y)$ the electrostatic potential and the chemical potential were calculated.

3.2. Inhomogeneous 2DES in high magnetic fields: an electrical compressible/incompressible landscape is formed

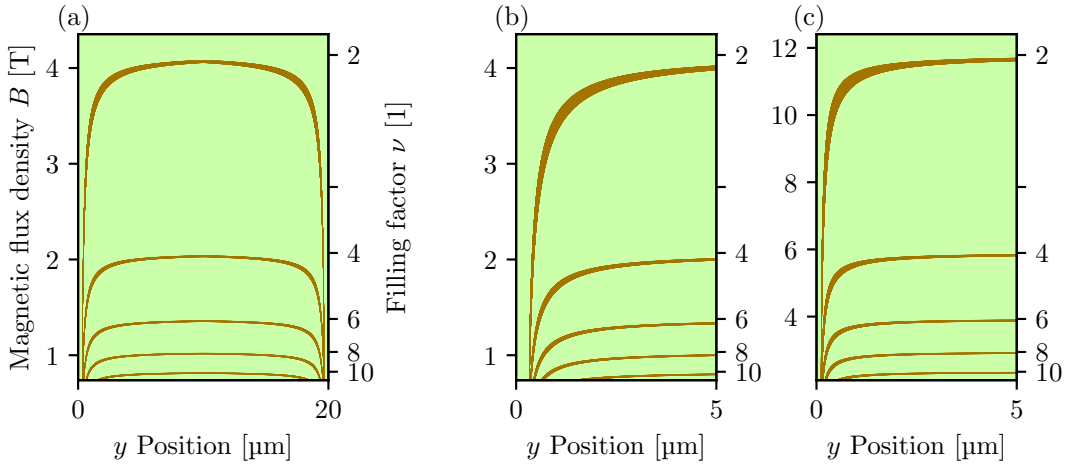


Figure 3.3: Spatial position and width of incompressible regions (brown) in an otherwise compressible 2DES (green) for local filling factors $\nu \in \{2, 4, 6, 8, 10\}$ as a function of the applied magnetic flux density B , which is connected via the experimentally determined electron concentration n_{2D} to a bulk filling factor ν . The complete sample width of $20 \mu\text{m}$ is calculated in (a) for a electron density of $2 \times 10^{15} \text{ m}^{-2}$ using equations (3.2) and (3.3). A symmetrical behavior from the center of the sample towards the edges can be observed. A zoom to the vicinity of one 2DES edge at $y = 0 \mu\text{m}$ is shown in (b). A comparison of (b) to a calculation with a higher electron density of $5.7 \times 10^{15} \text{ m}^{-2}$ in (c) can be made: Higher electron densities lead to the formation of incompressible stripes closer to the 2DES edge.

After numerical conversion the electron density profile $n_{2D}(y)$, the chemical potential $\mu_{\text{ch}}(y)$ and the electrostatic potential $\phi(y)$ are obtained.

By adding additional enclosing simulation loops, also non-equilibrium conditions as current-biasing are easy to include in this model. For zero temperature, strong magnetic fields and distances from the edge which are larger than the effective Bohr-radius, their results are in astonishing agreement with the analytical results of Chklovskii *et al.*, see therefore [18].

To illustrate how the compressible/incompressible landscape changes with a perpendicularly applied magnetic flux density B , we use equations (3.2) and (3.3) from the CGS model and assume an electron density of $2 \times 10^{15} \text{ m}^{-2}$, typical for the (Al,Ga)As heterostructure we investigate within this thesis. In contrast to the theory of Chklovskii *et al.*, the 2DES edge in our samples is defined by an etched mesa structure and not by a metal electrode. At this etched mesa, dangling bonds are present that lead to charged surface states. In our calculations we take this into account by assuming the Fermi energy to be pinned in the middle of the band gap of our semiconductor (mid-gap pinning) [59, 60]. Since GaAs has a band-gap of 1.4 eV [61, 62] the confining gate voltage is set to $V_g = -0.7 \text{ V}$. We neglected the fact, that incompressible regions do not form (they are electrically transparent

for electrons) when they are smaller than the magnetic length $l_B = \sqrt{\hbar(eB)^{-1}}$. Normally³, only the innermost incompressible region is wide enough to be present.

Figure 3.3 (a) illustrates the position and width dependence of even integer incompressible stripes (brown) within an otherwise compressible 2DES (green), numerically calculated for a 20 μm wide 2DES sample. In figure 3.3 (b) the data of (a) is shown in a smaller region around the left 2DES edge, starting at $y = 0 \mu\text{m}$. For comparison, figure 3.3 (c) shows a calculation for the same zoomed area but for a sample used in the experiments of Erik Ahlswede, which had a higher electron density of $5.7 \times 10^{15} \text{ m}^{-2}$ [12].

For each integer filling factor ν_i the same evolution can be observed: Between two integer filling factors ν_i and ν_{i-1} , with $\nu_i > \nu > \nu_{i-1}$, an incompressible stripe start to evolve close to both 2DES edges at $y = 0 \mu\text{m}$ and $y = 20 \mu\text{m}$. When the filling factor ν is decreased, the center positions of these stripes move closer into the middle (named "bulk") of the 2DES while they become wider at the same time. Close to integer filling factor ν_{i-1} , these incompressible stripes are wide enough that they merge in the 2DES bulk. The bulk region of the 2DES is now completely incompressible, surrounded by a compressible region along the sample edges. At integer filling factor the incompressible bulk disappears⁴.

A comparison between (b) and (c), and thus, samples with electron densities of $2 \times 10^{15} \text{ m}^{-2}$ and $5.7 \times 10^{15} \text{ m}^{-2}$, respectively, indicates the following: The higher the electron density, the closer to the 2DES edge the incompressible stripes form. This is reasonable, since a higher electron density leads to a smaller screening length d_0 and thus, a steeper electron density profile towards the edges.

3.3 Interpretation of Hall potential profile evolution: biased current flows in incompressible regions

Measurements of Ahlswede *et al.* [54] (compare fig. 3.1) showed an evolution of the Hall voltage drop with varying magnetic field. Theoretical calculations of an inhomogeneous 2DES in strong perpendicular magnetic fields by Chklovskii *et al.* [58] and Gerhardts *et al.* [18] demonstrated the existence of alternating electri-

³When metallic gates are used in addition to the etched mesa structure a really smooth charge carrier density profile from the edge to the bulk can be realized. Then it is possible to have more than one incompressible stripe parallel to the edge, but with different ν .

⁴In a real sample long-range electron density fluctuations lead to a stabilization of the incompressible bulk even to lower filling factors where $\nu < \nu_{i-1}$.

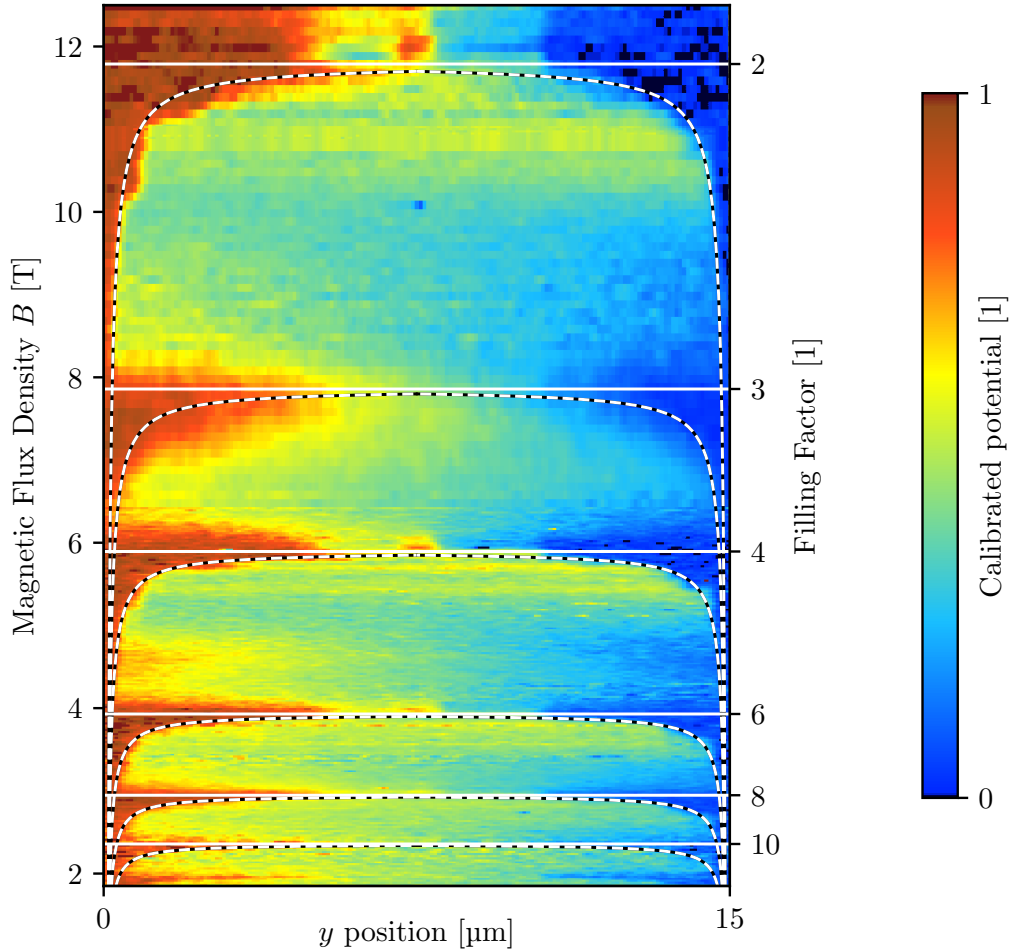


Figure 3.4: False-color representation of calibrated Hall potential profiles obtained in the IQH regime by Ahlswede *et al.* [12], formerly shown in figure 3.1; plotted versus the tip position y along the sample width and the magnetic flux density B (corresponding filling factor ν). Horizontal lines are added to indicate integer filling factors (solid). The center position of incompressible stripes, calculated with eq. (3.2), are also included (dashed). No fit parameter is available or necessary; only the measured [12] electron concentration n_{2D} is used. Calculated positions of incompressible stripes and measured Hall potential drops coincide. We are thankful that Erik Ahlswede made his data accessible to create this plot. A comparable plot is also shown in [16].

cally compressible and incompressible regions and their evolution with the applied magnetic field. In this section both facts are discussed together. Figure 3.4 shows a false-color replot of the calibrated Hall potential profiles from figure 3.1, versus the tip position y along the sample width and the magnetic flux density B that corresponds to a filling factor ν . The center position of incompressible stripes, calculated with equation (3.2), are superimposed with dashed lines. For calculation, absolutely no free parameter is available to fit the data and stripe position, only the experimentally measured n_{2D} from [12] enters.

Obviously, there is a striking agreement between measured Hall voltage drops and calculated incompressible stripe positions. Recapping section 2.4 we know:

Electrostatic potential gradients tilt Landau levels and lead locally to a current density j_x perpendicularly to the magnetic flux density B and the electric field E_y . Hence, the current flows at positions where a Hall voltage drop happens [12,16]. In figure 3.4 Hall voltage drop and incompressible stripe positions coincide, leading to the conclusion of Ahlswede *et al.* [12]:

For an integer quantum Hall plateau, the externally biased current flows inside spatially extended incompressible regions of the same local filling factor through the sample. As the Fermi level lies there between fully occupied and empty Landau levels, this current flow has to be dissipationless. In contrast, within the off-plateau region - the classical Hall regime - the current is dissipative and homogeneously distributed across the compressible 2DES width.

3.4 Partial electrostatic depletion leads to incompressible stripes in front of contacts

In order to characterize a 2DES electrically - e.g. by a measurement of the longitudinal and Hall resistance - potential probing contacts that measure the electrochemical potential μ_{elch} locally at the edges are unavoidable. That is surely reason enough to have a closer look into their vicinity, more precisely at their interface to the 2DES. Figure 3.5 shows the Hall potential landscapes that were measured by Ahlswede *et al.* [12] on a four-terminal Hall bar geometry, in an area close to an annealed metallic contact. The presented filling factors again are lying close around integer $\nu = 2$.

As already seen in section 3.1, in figure 3.5 a transition of the Hall voltage drop from the 2DES bulk (a) to a Hall voltage drop at the sample edges (c-d) can be identified. The homogeneity of the Hall potential profiles in x direction for given filling factors ν imply a pretty homogeneous electron density of the 2DES in this area. Remarkably, flat Hall potential regions appear directly in front of the interface of the metallic contact, a Hall potential drop appears more to the bulk. This can be seen all along the etched contact arm and for all illustrated filling factors.

A flat potential at the contact interface implies that no current flows into the contact. Instead, there must be an electron depletion in front of the contact. Thus, the Landau levels are bent there locally and an incompressible stripe along the contact interface appears, which isolates the outermost compressible region from

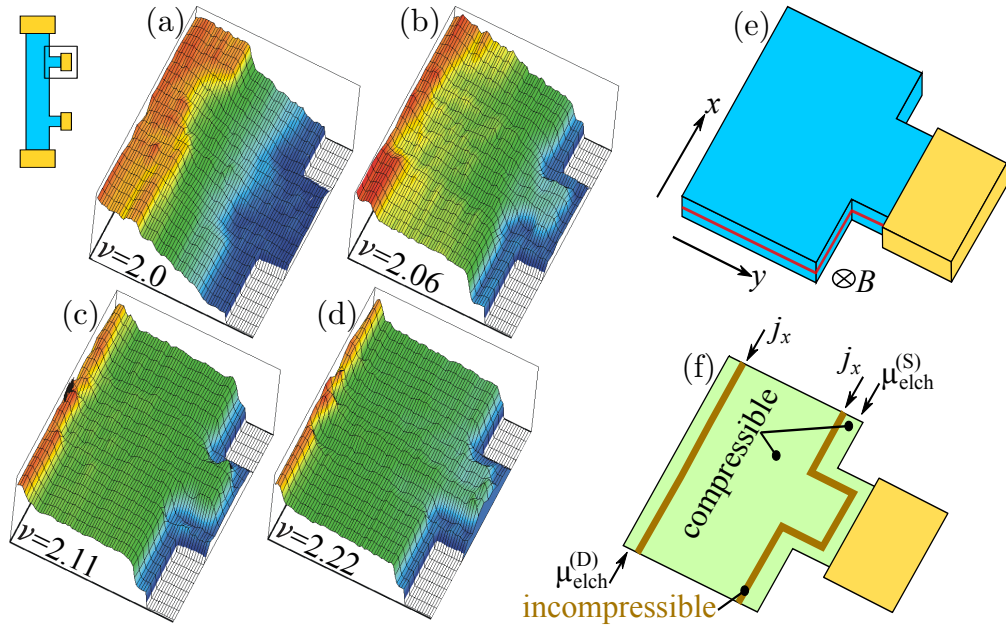


Figure 3.5: False-color representation of the spatially resolved Hall potential landscape in vicinity of a metallic probing contact. Different filling factors around integer $\nu = 2$ (a-d) were measured by Ahlswede *et al.* [12] on a four-terminal Hall bar, compare small inset and a zoom-in (e). A potential drop towards the contact with flat regions directly at the contact interface indicates the presence of an incompressible stripe in front of it, which is isolating bulk and edge. No current flows through the metallic contact. Adapted from [12].

the bulk. The outer compressible stripe becomes an equipotential line of μ_{elch} , while the incompressible stripe carries the current density j_x : No current enters the contact, μ_{elch} and j_x are spatially separated. This contact depletion is comparable to one which is present at etched mesa structures, but in front of contacts the electron density stays finite and does not drop completely to zero.

This depletion in front of contacts, which leads to a current flow in an incompressible stripe that does not enter the contact, explains also that finite contact resistances do not affect quantized Hall resistance values. We can summarize these experiments in the following way:

Due to the naturally occurring depletion in front of potential probing contacts, an incompressible stripe evolves in front of them and isolates the bulk from the edge. It carries with the Hall voltage drop the current density j_x . The biased current never enters the contact and is spatially separated from a compressible region along the contact interface conducting $\mu_{\text{elch}}^{(S)}$ or $\mu_{\text{elch}}^{(D)}$, respectively. Only the lower magnetic field side of a QH plateau is affected from the depletion in front of the contacts, as the incompressible stripe could become too thin there and thus, lose its isolating properties. The higher magnetic field side of

the plateau - where the whole 2DES center region is incompressible - is not affected.

3.5 Hot spots - local areas of dissipation

Until now, the discussion focused on regions far away from source/drain contacts. In this section, experiments which show heat dissipation exactly there are discussed.

Klaß *et al.* [63, 65] used the pressure fountain effect in super-fluid helium to spatially resolve heat dissipation in Hall bar samples, compare figure 3.6. Under integer quantum Hall conditions and with small bias currents, virtually all dissipation happens symmetrically in two spots, the so-called HOT SPOTS; one at each opposite corner of both contacts in the current path. Both hot spots grow linearly in size with an increasing current, upon a certain threshold is reached; then an asymmetry in their size is observed. While the hot spot on the positive (+) biased side shrinks and then remains constant in size, the one at the negative (-) biased side still grows continuously⁵. For narrower contact arms the hot spot of the drain side (+) moves away from the contact into the region where the 2DES widens up, while the source contact (-) stays unaffected. A reversed current direction does not change hot spot positions⁶; this happens only when the applied magnetic field direction is reversed. For non-integer filling factors dissipation is also observed in the sample bulk.

⁵This behavior was observed in all ten samples that were investigated.

⁶Except in the mentioned case of narrow 2DES arms.

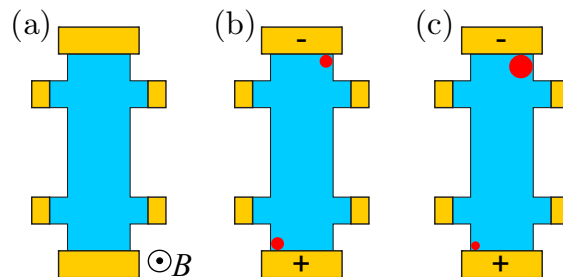


Figure 3.6: Schematical result of measurements of Klaß *et al.* [63]. The pressure fountain effect in super-fluid helium is used to identify regions of heat dissipation (red). (a) No current is applied to the sample; no heat dissipation can be observed. (b) A small bias current let two spatially separated spots of dissipation appear. They are in opposite corners of the source and drain contact and called hot spots. (c) For high bias currents, their size changes asymmetrically: At drain (+) the hot spot shrinks and then stays constant, while the one at source (-) grows with applied current. Hall bar schematic is an adaption from [64].

We conclude from these measurements:

Under integer quantum Hall conditions, virtually all heat dissipation occurs at two hot spots in opposite corners of source and drain contact. They are symmetrical in size for small currents and become asymmetric at higher current biases.

3.6 The microscopic picture of the Integer Quantum Hall Effect

Experimentally observed Hall potential profiles of Weitz *et al.* [7–9] and Ahlswede *et al.* [10–12], theoretical calculations to compressible and incompressible regions by Chklovskii *et al.* [58] and Gerhardtts *et al.* [18], together with observed hot spots by Klaß *et al.* [63] made it possible to understand the current flow in a 2DES under integer quantum Hall conditions.

This MICROSCOPIC PICTURE of the integer quantum Hall effect is described in the following. The sketch in figure 3.7 is used for discussion and always the externally biased current (simply named "current") is discussed, while equilibrium currents - not carrying a net current through the sample - are neglected.

1. Starting in the off-plateau region (a) where the CLASSICAL HALL REGIME is present, Hall potential profiles of type I (figure 3.1) are observed: a linear voltage drop across the sample width and thus a homogeneous current distribution is observed. In this situation the whole 2DES is electrically compressible and R_{xy} increases monotonously with the magnetic flux density B , while the longitudinal resistance R_{xx} is finite.
2. With increasing magnetic flux density B , the Hall potential profile becomes non-linear. The Hall voltage drop in the bulk becomes smaller, while an increasing Hall voltage drop close to the sample edges is observed; one on each sample side at position where an incompressible stripe with integer filling factor forms. Type IIb Hall potential profiles are observed.
3. When the integer quantum Hall plateau is entered at the lower magnetic field side (b), the Hall voltage drops entirely over the innermost incompressible stripes; in figure 3.1 type IIa profiles are observed. With higher magnetic fields the center position of these stripes moves towards the center of the 2DES (the bulk) while their width increases (c). Due to the current flow in close proximity to the sample edges this regime is denoted as

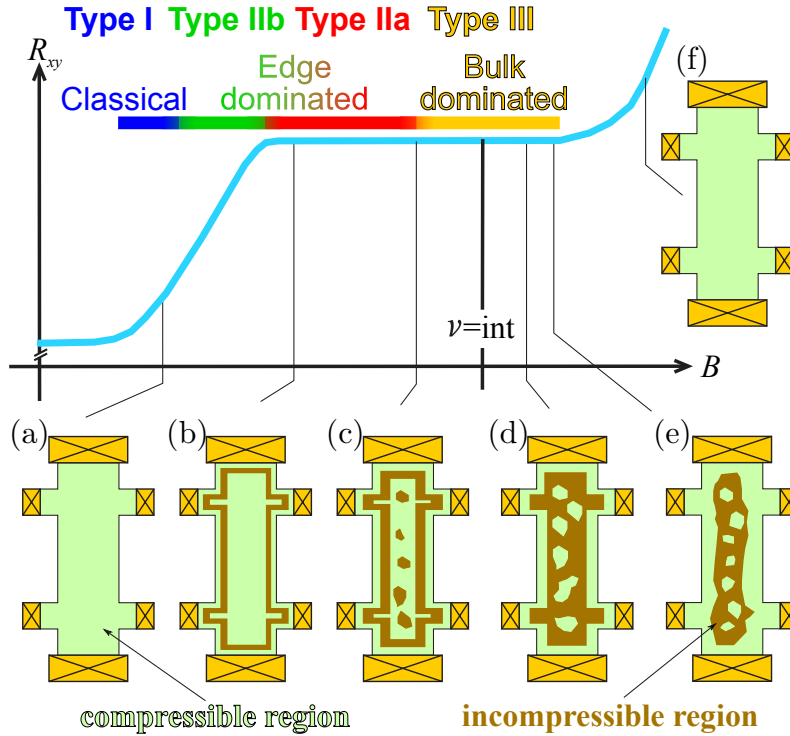


Figure 3.7: Schematic representation of the electrically compressible/incompressible landscape evolution in a two-dimensional electron system when the magnetic flux density B is ramped over a quantum Hall plateau in R_{xy} . In the off-plateau region (a) and (f) the *classical* Hall regime is present and the 2DES is completely compressible. Linear Hall potential profiles of type I are measured and the current is distributed homogeneously across the sample width. Incompressible stripes with integer local filling factor $\nu = i$ start to form in close proximity to the 2DES edge when the magnetic field is increased towards the quantum Hall plateau. The current flow is continuously with B redistributed into these incompressible stripes, while a decreasing Hall voltage drop in the bulk is observed; type IIb Hall potential profiles are measured in this *edge-dominated* regime. When the incompressible stripes are wide enough to carry all externally biased current (b), the Hall plateau is entered at the lower magnetic field side and Hall potential profiles of type IIa are probed. They show pronounced Hall voltage drops in the regions of incompressible stripes where the current is carried dissipationless through the sample, while the bulk region shows no drop anymore. With increasing magnetic flux density these incompressible stripes get wider and their center position moves in direction of the 2DES bulk (c). In vicinity of integer filling factor the stripes merge and the 2DES bulk is mainly incompressible interrupted by compressible droplets due to long-range potential fluctuations (d). In this *bulk-dominated* regime the current flows in the incompressible bulk and Hall potential profiles of type III are measured. For a finite magnetic field range compressible droplets become incompressible and stabilize the quantum Hall plateau to the higher magnetic field range (e) before the 2DES becomes again entirely compressible (f) and the quantum Hall plateau is left at the higher magnetic field side. Adapted from [54, 64] with permission of the Royal Society, copyright 2011.

EDGE-DOMINATED QUANTUM HALL REGIME. The longitudinal resistance approaches zero within the plateau region, as the electrochemical potential μ_{elch} is equipotential along one sample edge.

4. In close vicinity to integer filling factor $\nu = i$, both incompressible stripes widened enough that they merge in the center of the 2DES; a mainly incompressible bulk is present (between (c) and (d)). Due to inhomogeneties and long-range potential fluctuations, compressible droplets appear within the otherwise incompressible bulk. These droplets become incompressible at slightly higher magnetic flux densities, stabilizing the quantum Hall effect for a finite magnetic field range around integer filling factor (d). The Hall voltage drop is measured in the incompressible bulk, while no drop is observed at the compressible edges (figure 3.1 - type III profiles). According to the current flow in the bulk, this region is called BULK-DOMINATED QUANTUM HALL REGIME⁷. The incompressible bulk region spatially shrinks towards higher magnetic fields (e), and
5. when the incompressibility in the bulk is lost, also quantization of R_{xy} is lost; the Hall plateau has ended at the higher magnetic field side (f). The 2DES is again completely compressible, and type I Hall potential profiles are measured again.

As already mentioned in section 3.2, this evolution of the compressible/incompressible landscape repeats for each integer filling factor.

For a further discussion of the microscopic picture of the integer quantum Hall effect, we discuss a Hall bar cross-section with incompressible stripes along the sample edges; only the innermost incompressible region is wide enough to be completely isolating, compare figure 3.8. In equilibrium with no externally biasing - in figure 3.8 (a) - the electrochemical potential μ_{elch} is constant across the sample. Within incompressible regions Landau levels (LL) are locally bent, what leads to a common group velocity v_g for all LL below the Fermi energy there. The potential gradients in the left incompressible stripes are opposite in sign compared to incompressible regions on the right side; thus v_g and accordingly the current density j_x is directed in opposite directions. These PERSISTENT CURRENTS surround the sample already in equilibrium without carrying any net current through the sample.

In case of an externally driven current, compare figure 3.8 (b), the sample is in non-equilibrium. The Hall voltage drops across the sample width and leads to an

⁷Sometimes also denoted as DISORDER-DOMINATED QUANTUM HALL REGIME.

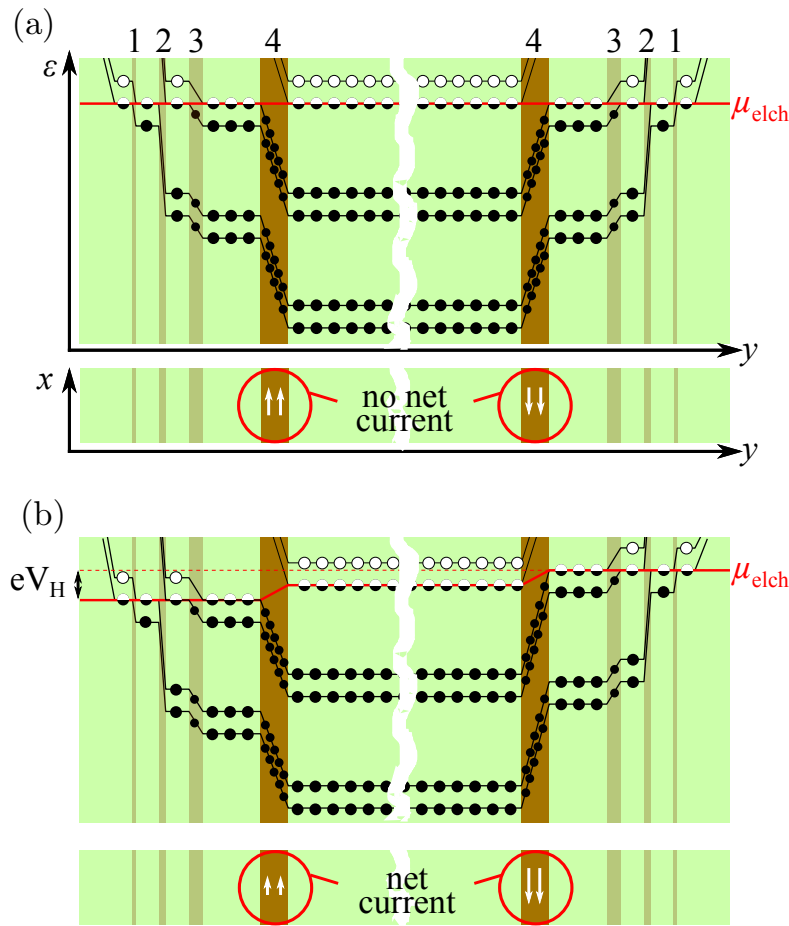


Figure 3.8: Landau level bending in a cross-section of a Hall bar schematically shown for equilibrium (a) and non-equilibrium (b), for a bulk filling factor $5 > \nu_{\text{bulk}} > 4$ and quantized Hall resistance R_{xy} . Dot fillings represent Landau level fillings. In equilibrium (a) the electrochemical potential is constant across the sample; potential drops are screened in compressible regions, unscreened in incompressible regions. In incompressible regions these drops lead to a common group velocity v_g with opposite direction on both sample sides. Hence, persistent currents surround the sample in equilibrium without carrying any net current through the sample. For non-equilibrium (b) an additional Hall voltage decreases/increases the potential drop in incompressible stripes leading to different current densities and compared to equilibrium a net current through the sample. Idea to this picture from [12, 21, 54, 66].

additional electric field E_y in y direction. Within electrically incompressible regions - with integer filling factor ν - the current flows dissipationless. Consequently, the Hall voltage drop is located there, what leads to a superimposed electric field only in these incompressible regions. One-sided the potential gradient is enhanced, while it is decreased on the opposite side. Accordingly, the local current density⁸ is enhanced or decreased, respectively, resulting in a net current through the sample. Integration of the resulting current density⁹ $j_x(y)$ along the cross-section w of the

⁸In figure 3.8 this is indicated by varying arrow lengths.

⁹The net current density is the difference between the current density in non-equilibrium (b) and the current density in equilibrium (a).

sample

$$I_x = \int_0^w j_x(y) dy = \nu \frac{e^2}{h} V_H \quad , \quad (3.9)$$

yields a quantized value for $R_{xy} = V_H/I_x$ as long as all current flows within incompressible regions of the same local filling factor ν . Here, V_H denotes the Hall voltage.

3.7 Electrical breakdown of the IQHE: edge-dominated and bulk-dominated QH regime identified in electrical transport measurements

A stable integer quantum Hall plateau is characterized by a vanishing longitudinal resistance R_{xx} and a quantized Hall resistance R_{xy} . The breakdown of the quantum Hall effect occurs for high voltage biases V_{DS} , respectively high currents I_x through the sample: a deviation from the quantized Hall resistance R_{xy} and an increase of R_{xx} are observed [16, 17, 67].

The measurement of R_{xx} is non-local and depends on the compressible/incompressible landscape between two probing contacts¹⁰ in a distance l (figure 2.2). R_{xy} in contrast is more local, it depends mainly on the landscape between two opposite lying contacts with a short distance w . As l is normally larger than w the longitudinal resistance R_{xx} is a more sensitive observable to investigate a breakdown of the QHE. Figure 3.9 shows exemplarily a breakdown measurement performed by the master student P. Haremski [66]¹¹ on a six-terminal Hall bar structure around bulk filling factor $\nu = 2$. A comparable behavior was also observed for other integer filling factors. The longitudinal resistance R_{xx} is multiplied by the sample width w and presented in a false-color representation as a function of (1) the filling factor ν and corresponding magnetic flux density B and (2) the applied bias voltage V_{DS} . An intentionally small chosen dark color range presents regions of vanishing R_{xx} and indicates a stable QHE along the sample between the probing contacts.

The graph is obviously asymmetric around integer filling factor $\nu = 2$. At the lower magnetic field side the breakdown threshold voltage V_{th} increases strongly (from some millivolt up to hundredths of millivolt) towards integer bulk filling factor.

¹⁰Meant are probing contacts on the same side of the Hall bar structure.

¹¹Comparable measurements to figure 3.9 were already done earlier in our group by the PhD student K. Panos [16]. P. Haremski's project covered the investigation of width dependence and gate influence on the breakdown behavior, which was not done before.

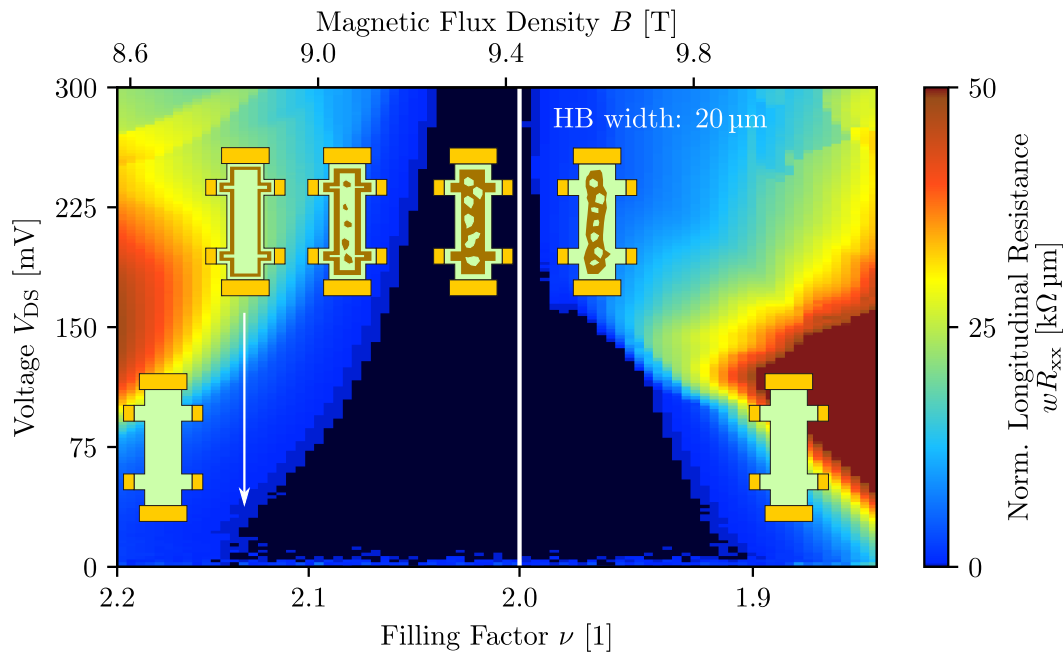


Figure 3.9: Shown is the longitudinal resistance R_{xx} (normalized by multiplying it with the sample width w , here $w = 20 \mu\text{m}$) around integer filling factor $\nu = 2$. It is measured at 1.4 K as a function of the magnetic flux density B and corresponding bulk filling factor ν , and the applied bias voltage V_{DS} . In dark regions a vanishing R_{xx} is measured indicating that the QHE is stable in the whole region between the probing contacts (along length l). The edge-dominated and bulk-dominated QH regime can be identified as asymmetry between the low and high magnetic field side of the plateau. In the low magnetic field range (edge-dominated regime) the breakdown threshold voltage increases strongly towards integer bulk filling factor, where abruptly a lower threshold voltage is measured. The dome-like structure for $\nu < 2$ is the bulk-dominated (or disorder-dominated) QH regime. The dome is symmetrical around $\nu = 2$ but non-dominant in the edge-dominated regime for $\nu > 2$. Small Hall bar insets point up the expected compressible/incompressible landscape present at some magnetic flux densities. The graph is generated using data from Patricia Haremski [66].

When ν becomes smaller than 2, an abrupt drop in the breakdown threshold is observed and a dome-like region where $R_{xx} \approx 0$ remains.

The asymmetry between the low and high magnetic field side of the quantum Hall plateau is in agreement with the edge- and bulk-dominated regime, respectively, described in the microscopic picture of the integer QHE. Let us remind: Whenever the Hall voltage drop across the incompressible stripe leads to a critical electric field E_C there, the electrical breakdown of the QHE occurs. In the lower magnetic field side, the edge-dominated regime, an incompressible stripe with local filling factor $\nu = 2$ forms at both sample edges. The Hall voltage drop V_H across the sample cross-section is now equal to the applied bias voltage V_{DS} . As this drop happens only within the incompressible stripes, their width determines the local electric field E_y there. As these stripes become wider with increasing B , they can

withstand a higher Hall voltage drop before E_C is reached. Hence, we observe a continuous increase of the breakdown threshold voltage with B . At bulk filling factor $\nu = 2$ the bulk is mainly incompressible and high V_{th} can be observed. For filling factors slightly smaller than $\nu = 2$ (higher B) a perfectly homogeneous 2DES would become entirely compressible, and zero longitudinal resistance would vanish. But, long-range disorder in real sample stabilizes the QHE towards $\nu < 2$, as regions with slightly higher $n_{2\text{D}}$ become incompressible with a filling factor $\nu = 2$ for slightly higher values of B . The incompressible/compressible landscape changes strongly with B in this regime and only a drastically reduced uninterrupted area of the 2DES width remains incompressible. Consequently, a smaller Hall voltage drop is enough to reach E_C , V_{th} drops abruptly. Hence, the dome-like region with $R_{xx} \approx 0$ has its origin in disorder. Due to symmetry reasons we assume to have this disorder symmetrical around integer filling factor. That means, below integer filling factor, there is a regime where an incompressible stripe at the sample edge coexists with disorder in the bulk¹².

We can conclude: the results of these transport measurements are consistent with the microscopic picture of the integer quantum Hall effect and can be interpreted with the evolution of the compressible/incompressible landscape. Both, edge- and bulk-dominated regimes can be identified by their different breakdown behavior.

3.8 Closed incompressible ring necessary for quantized Hall resistance

In previous sections we have seen that a well quantized Hall resistance R_{xy} and zero longitudinal resistance R_{xx} are measured only, when the externally biased current flows exclusively in incompressible regions of the same local filling factor ν . In other words: a topology with a closed incompressible ring going along the edges of the 2DES is necessary to observe the IQHE. It is insignificant if the incompressible ring is realized by a thin stripe in the edge-dominated QH regime or by a wide incompressible center region in the bulk-dominated QH regime, as long as all externally biased current flows within these incompressible regions with same ν , and not within compressible regions of other ν .

Former argument is experimentally analyzed by the master student Rostyslav Savytsky [68] using electrically separated gates¹³ along the Hall bar edges and

¹²This stabilizes the quantum Hall effect as the current can distribute in spatially wider regions.

¹³An anisotropy, depending on the crystal axes, in the pinch-off voltage for total electron depletion under the gates makes separated gates and a calibration of all gates necessary.

in front of source and drain contacts, compare the Hall bar sketch in figure 3.11 (a). Hence, by applying a voltage to these gates the local electron density profile $n_{2D}(y)$ and, correspondingly, the local filling factor can be changed under the gates.

In first experiments, the edge region is continuously depleted via a negative voltage V_G applied to side gates A and B for different magnetic fields, while the S gate and D gate have a fixed potential (e.g. ground potential), compare figure 3.10 (a,b). The following could be observed, see also figures figures 3.11 (b.i) and (b.ii):

1. An extension of zero longitudinal resistance regions to lower magnetic fields [66,68].
2. At the same time, contrary, the Hall resistance deviates from integer quantized values.
3. The higher magnetic field side of quantum Hall plateaus is mainly unaffected by the side gates.

Depleting the 2DES at the sample edges leads to a smoother gradient in the electron density profile $n_{2D}(y)$ towards the bulk, making incompressible stripes under the side gates A and B wider and more stable. They isolate the compressible edge from the inner bulk region and the electrochemical potential along each edge becomes an equipotential line; R_{xx} remains zero in a wide magnetic field range for negative side gate voltages. On the other hand, the constant potential applied to the S and D gate leaves incompressible stripes beneath them unchanged during a measurement; their width depends only on B . When these stripes in front of S and D become too weak, a dissipative current flows inside the mainly compressible bulk and R_{xy} loses quantization. Hence, when R_{xx} is zero it does not necessarily mean that R_{xy} is quantized, compare for example the region $5\text{ T} < B < 7\text{ T}$ in figures 3.11 (b.i) and (b.ii). R_{xx} is zero, while a quantization of $R_{xy} = h/(2e^2)$ for $\nu = 2$ is not observed.

In opposite configuration, the side gates A and B are on fixed negative potentials $V_G^{(\text{Side})}$, and S and D gates are used to continuously deplete the 2DES, compare figure 3.10 (c,d). Here, R_{xx} shows no significant change in a large range of B and V_G , while quantized R_{xy} is now achieved in a wider B field range (the specific range depends on the initially chosen $V_G^{(\text{Side})}$):

Why? The negative voltage $V_G^{(\text{Side})}$ applied to the side gates ensures strong incompressible stripes beneath them, while the width of the incompressible stripe under the S and D gates are tuned via V_G . When depletion of electrons under the S and D gates leads to incompressible stripes of same local filling factor $\nu_{\text{gate}}^{(\text{SD})}$,

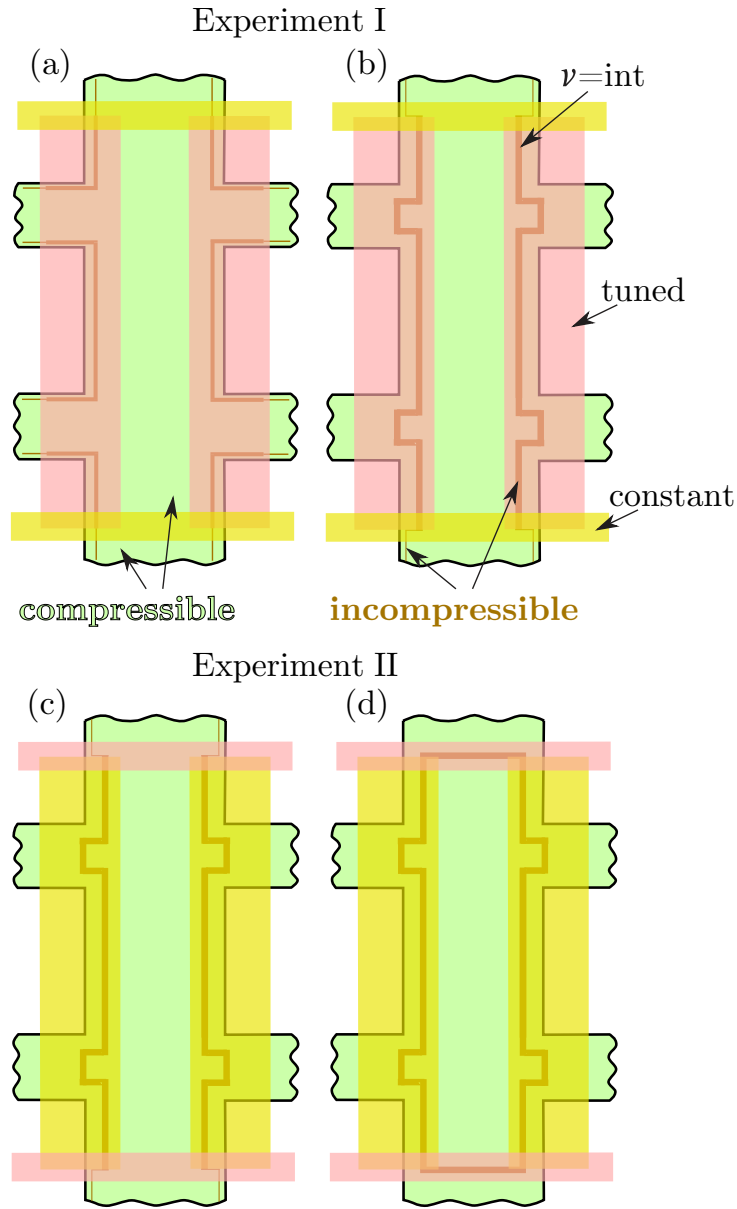


Figure 3.10: Schematic Hall bar structure and electrically compressible/incompressible 2DES landscape. Described are first experiments of Rostyslav Savytskyy investigating the influence of gate electrodes on the edge-dominated quantum Hall regime. Gates indicated in yellow remain at fixed potential, while gates in red are varied during a measurement. (a,b) Only the side gate potentials are changed commonly. (a) A quantum Hall plateau is left to the lower magnetic field side. Incompressible regions are too thin to decouple the compressible edge from the compressible bulk. No incompressible ring is present; R_{xx} is non-zero and R_{xy} is not quantized. (b) A negative potential applied to the side gates leads to a smoother slope in the electron density profile below them. Incompressible stripes become wider and decoupling of the compressible edge from the bulk happens; R_{xx} becomes zero, while R_{xy} is still not quantized as a dissipative current remains in the bulk. (c,d) A constant negative potential applied to the side gates ensures wide incompressible stripes along the sample. Varying gate potentials in front of the bias contacts S and D are applied. (c) is a comparable situation as in (b): R_{xx} is zero, while R_{xy} is not quantized. Applying a negative potential to S and D gates reduces there the slope in the electron concentration, what leads to wider incompressible regions. An incompressible ring closes. All externally biased current flows dissipationless within incompressible regions of same integer filling factor. Thus, in addition to $R_{xx} = 0$ now R_{xy} is quantized. Adapted from [68].

as present under the side gates with $\nu_{\text{gate}}^{(\text{Side})}$, then the incompressible ring with same filling factor is closed and in addition to zero R_{xx} the Hall resistance R_{xy} is quantized.

Now we discuss a subsequent experiment which experimental results are shown in figure 3.11 (c.i) and (c.ii); again the magnetic flux density B and gate voltages V_G are varied. This time V_G is applied commonly to side gates A and B and the gates in front of the bias contacts S and D, creating a ring with the same local filling factor ν_{gate} beneath the gates. Shown in the plots are the longitudinal resistance R_{xx} (c.i) and the derivative of the Hall resistance R_{xy} with respect to the magnetic flux density B (c.ii). This representation of R_{xy} makes Hall plateaus (R_{xy} has a plateau with $\partial R_{xy}/\partial B = 0$) easier identifiable as yellow regions. Dark regions of R_{xx} correspond to a vanishing longitudinal resistance. White and black lines added to the graphs indicate the local filling factor dependence (simplified¹⁴: $\nu_{\text{gate}} \propto V_G/B$) for integer incompressible regions under the gates.

Let us remind: at parameters where these lines are in the plots, an integer incompressible region with local filling factor ν_{gate} is present under all four gates. This leads to a closed incompressible ring of same integer filling factor around the sample edges, more precisely under the gates. The incompressible stripes at the sample sides are wide enough to decouple the bulk region from the compressible edge, making the edge an equipotential line of μ_{elch} , leading to $R_{xx} = 0$. The gates in front of source and drain contacts close the incompressible ring; no dissipative current flow happens through compressible regions and thus, R_{xy} is well quantized.

For fixed gate voltages (e.g. $V_G = 0$ mV, indicated by a green dashed line) and changing B , zero resistance regions of R_{xx} are measured that correspond to quantized Hall resistances R_{xy} ; we have stable quantum Hall conditions. These regions are interrupted by highly resistive regions in R_{xx} and changing R_{xy} values; in these regions the classical Hall regime between two QH plateaus is present. Obviously, regions of zero R_{xx} and quantized R_{xy} seem to follow the added white/black lines where an incompressible ring of same local integer filling factor ν_{gate} is present.

To summarize these experiments: zero longitudinal resistance does not necessarily mean that the Hall resistance is quantized. An incompressible stripe strong enough to decouple the compressible edge region from the bulk region ensures an equipotential line of μ_{elch} at the probing contacts and thus $R_{xx} = 0$. For a closed incompressible ring of same local filling factor ν , the externally biased current flow

¹⁴The actual dependence with all prefactors can be found in [68].

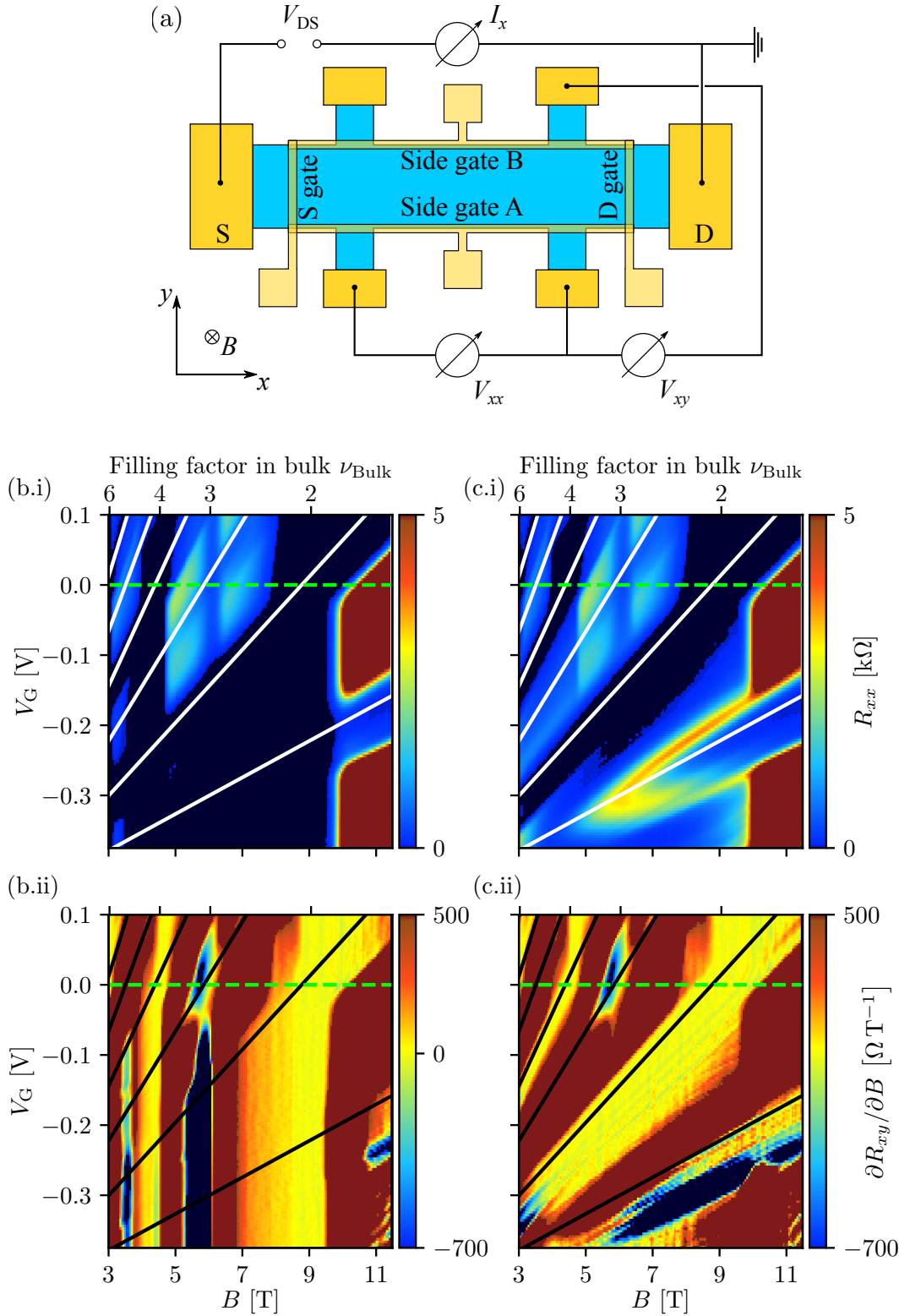


Figure 3.11: Measurement of a six-terminal Hall bar structure with additional gates along the Hall bar edges and in front of the source and drain contacts (a) to investigate the topology of the edge-dominated quantum Hall regime. Results of two experiments are shown: in (b,x) only the side gates are tuned, and in (c,x) all four gates are tuned commonly. Shown is a false-color representation of the longitudinal resistance R_{xx} (b.i and c.i) and derivative of the Hall resistance R_{xy} with respect to B (b.ii and c.ii), both measured as a function of the magnetic flux density B and applied gate voltage V_G . Added lines (white and black) correspond to integer filling factors ν_{gate} below the gates. The plots are generated using data from Rostyslav Savvitsky [68].

happens exclusively within these incompressible regions of same filling factor what leads then to quantized values of R_{xy} .

3.9 Summary

In this chapter, Hall potential profiles that were obtained in previous works were shown. They have been measured with a scanning probe microscope at 1.4 K, which had a metal coated tip at the end of an oscillating cantilever as probe.

It turned out that the observed Hall potential profiles show an evolution with the perpendicularly applied magnetic flux density, which is similar for all probed integer quantum Hall plateaus. This observation is correlated with the evolution of an electrically compressible/incompressible landscape within the 2DES. Hereby the externally biased current is distributed in the 2DES and flows then in the QH regime dissipationless inside incompressible regions, driven by the Hall voltage drop over these incompressible regions. It is perpendicular to both, the applied magnetic flux density and the Hall field. When all externally biased current flows exclusively inside incompressible regions of the same filling factor ν , the Hall resistance is quantized with $R_{xy} = h / (\nu e^2)$.

Within this microscopic picture it was possible to understand and explain all subsequent experiments. To name some: Hall samples which were systematically changed in their properties (as e.g. width), potential changes applied to gates along the Hall bar, and the influence of potential probing contacts.

Chapter 4

The Scanning Single-Electron Transistor (SET) Array Microscope and Quantum Hall Sample

Former scanning probe experiments of our group that have measured the electrostatic potential landscape on a 2DES in Hall bar geometry were carried out at working temperatures of about 1.4 K [12], and thus they are limited to the integer quantum Hall regime. Consequently, the question is: What will change if the fractional quantum Hall regime is investigated where electron-electron correlation are present?

A new type of scanning probe microscope built by M. Mausser [19], now operated in the milli-Kelvin temperature regime, together with higher possible magnetic flux densities makes the fractional quantum Hall regime accessible for non-invasive local measurements with an one-dimensional array of single-electron transistors acting as local electrometers.

In this chapter this microscope setup with its main specifications is introduced. The metallic single-electron transistor tip array which is used to probe locally Hall potential profiles is explained, and its characteristics, obtained at low temperature, are shown. The usage of single-electron transistors as local electrometers require to follow some design rules for the samples we want to investigate. These rules are presented afterwards. An electrical characterization of the Hall bar structure at low temperatures ensures that well pronounced fractional QH states are observable.

4.1 Our scanning probe microscope setup in the Precision Laboratory of the Institute

In order to get access to fractional quantum Hall states it is unavoidable to (1) lower the working temperature of the scanning probe microscope, and (2) to ensure at the same time higher possible magnetic flux densities. For this purpose my predecessor M. Mausser [19,21] built a scanning probe microscope (SPM), now operated inside a top-loading $^3\text{He}/^4\text{He}$ dilution refrigerator, reaching milli-Kelvin temperatures. Hence, our measurements will be performed within a $^3\text{He}/^4\text{He}$ mixture. An electrostatic force microscope with an oscillating cantilever cannot be used in this new setup, as cantilever oscillations stimulate resonant oscillations of the $^3\text{He}/^4\text{He}$ mixture. Therefore, single-electron transistor (SET) tips without moving parts are foreseen as local electrometers.

The microscope head is shown schematically in figure 4.1 (a): Both, probing tips and the sample of interest are glued to specially prepared chip-holders before they are mounted within the green marked region into the SPM. A continuous scan movement of the tip array with respect to the underlying sample is realized with a 7.5 cm long piezo scan tube, shown in orange; it gives a lateral scan range of about $27\ \mu\text{m}$ by $27\ \mu\text{m}$ in the x - y plane parallel to the sample surface, and about 300 nm in vertical z direction.

As voltage differences as high as 428 V are necessary to achieve maximum deflection of the scan tube, while simultaneously small SET currents in the pA range and Hall bar voltages in the μV range have to be measured, the microscope has to be separated into a low-voltage (cyan) and two high-voltage parts (pink) which are separated to each other by an electric shielding. Consequently, the scan tube is surrounded by a grounded brass tube (upper yellow).

As mentioned, the piezo tube is used later for a continuous scanning, but its limited scan range is not sufficient to position the SET tip array from its initial position over the Hall bar structure on a millimeter wide sample. Hence, a long-range positioning system becomes necessary. Four inertial piezo modules in cube shape (light blue) from the company Attocube [69] are installed: Two linear stepper modules with a lateral position range of 3.2 mm by 3.2 mm in the x - y plane, one linear stepper module with vertical position range of 2.5 mm in z -direction, and a goniometer module to compensate possible angle mismatches between the sample normal and the tip array. All these SPM parts are installed within a round, non-magnetic stainless steel frame with a diameter of about 24 mm [19, 21].

Mechanical movement of probing tips and sample hamper their electrical connec-

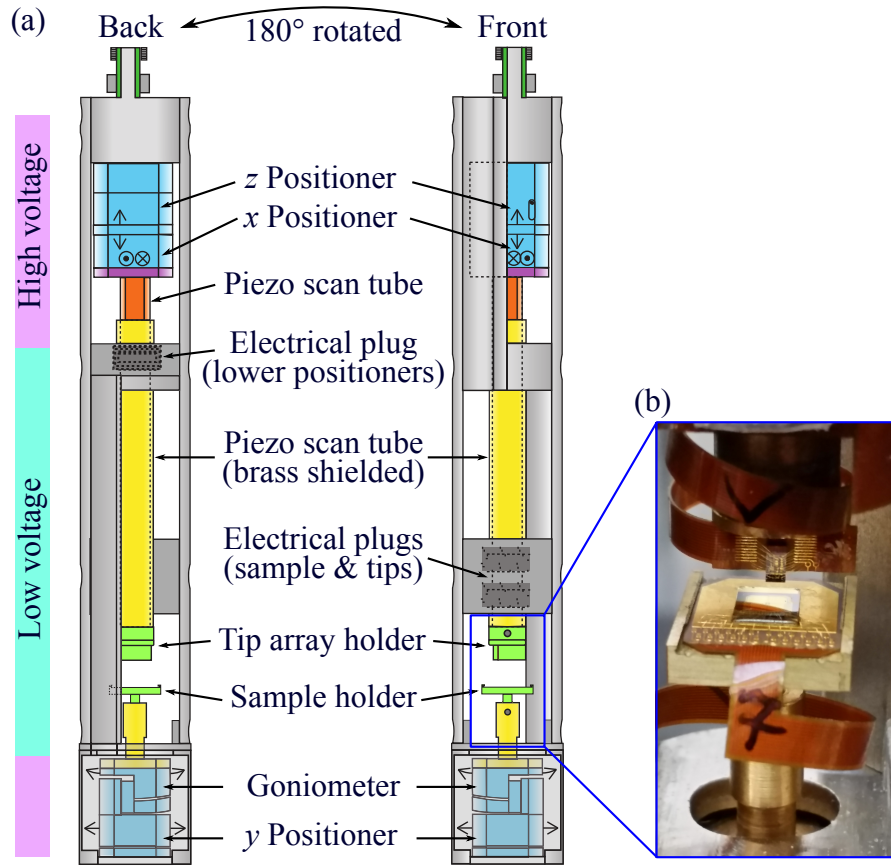


Figure 4.1: Schematic overview of the approximately 0.2 m long scanning probe microscope head, realized at the end of a 2.5 m long [19] sample rod that is operated inside a $^3\text{He}/^4\text{He}$ dilution refrigerator. (a) Sketch of main microscope parts seen from the back (left) and front (right). High voltage parts, necessary for positioning and scanning, are shielded from low voltage parts as sample and SET array. (b) Picture showing the area around the sample holder and tip holder in the microscope. Flexible capton circuit boards (which are not included in (a)), necessary to electrically connect sample and SETs, can be seen. Subfigure (a) is adapted from [21].

tion. To overcome this issue, a flexible capton circuit board - compare figure 4.1 (b) - is used as interface between the sample and a 50-pin plug¹ from the company Molex [70] that is statically mounted at the sample rod. The plug itself is connected to an interface circuit board where 48 constantan loom wires, coming from two 24-pin Fischer plugs in the sample rod head, are soldered. In this manner, sample and SETs can be electrically connected to external measurement devices. A similar approach is used to address the positioning and scan units, but here, copper and superconductive looms are used in series to achieve small wire resistances² at low temperatures. Further information and a detailed wiring can be found in [19].

¹The Molex part numbers are: 54722-0507 (receptacle) and 55560-0507 (plug).

²The positioning system applies high frequency saw-tooth signals which require small RC components between the amplification controller and each piezo positioner. Otherwise, high frequency components from the falling signal slope are filtered.

The sample rod with the SPM is mounted in a top-loading Kelvinox-400 $^3\text{He}/^4\text{He}$ dilution refrigerator from the company Oxford Instruments with a cooling power of $400\ \mu\text{W}$ at $100\ \text{mK}$, reaching a base temperature of $16\ \text{mK}$, while the electron system of the SET has a reported temperature [21] of about $40\ \text{mK}$. This effective temperature is reached, although 96 wires are going down from the sample rod top into the mixing chamber, where all parts of the microscope are located in the liquid helium mixture to ensure best thermal coupling and thus cooling. Included into the dilution refrigerator is a superconducting magnet that can reach magnetic flux densities of $18\ \text{T}$ in the sample/tip area.

The dilution refrigerator with the SPM is hung into a hole of a concrete block with a weight of about 190 tons [71,72] that is damped by ten active/passive two-chamber dampers; in this way unwanted vibrations coupling into the scanning experiment are reduced. This construction together with the laboratory is encapsulated within a concrete box that achieves an acoustic damping of $60\ \text{dB}$ [72] towards other laboratories. In addition, a metal shielding around this concrete box with $60\ \text{dB}$ attenuation [72] reduces high-frequency electromagnetic influences. This scanning-friendly environment is part of the newly built Precision Laboratory of the Max Planck Institute for Solid State Research, Stuttgart.

4.2 Basics to single-electron transistor

This section gives an overview of the basic working principle of a single-electron transistor (SET). Firstly, an arrangement of an SET is described and the single-electron charging energy is introduced. Afterwards the characteristics of the current through the SET is discussed for both, a changing bias voltage and a voltage applied to a close-by electrode. In the end, a complete charge stability diagram of the SET is shown.

4.2.1 Arrangement of a metallic single-electron transistor (SET)

Controlling a current flow between two leads - namely source and drain - with a gate electrode can be realized either by a field effect transistor (FET) or a single-electron transistor (SET). In both cases the gate electrode controls an energy barrier and thus, the electrical conductance through the device. But, there is a difference between both: In case of an FET, the electrical conductance is affected by continuously changing the charge carrier concentration within a conductive channel. For an SET the quantized nature of electrical charge is important;

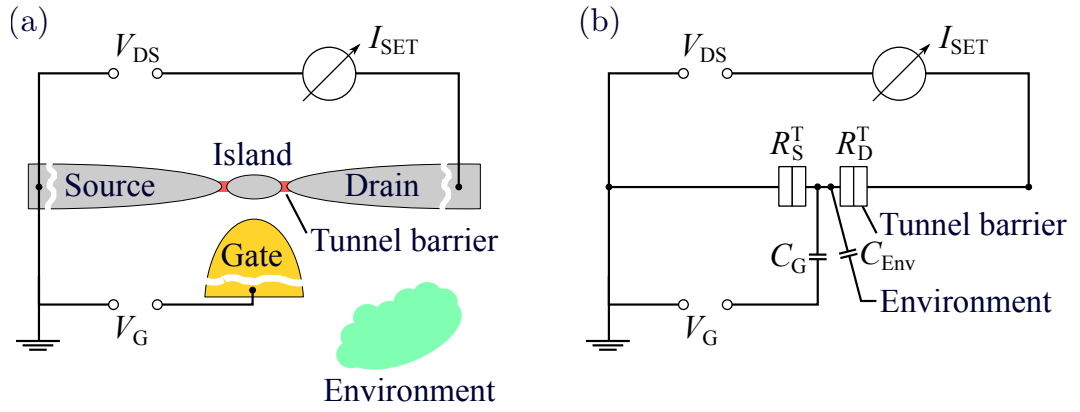


Figure 4.2: (a) Schematic arrangement of a metallic single-electron transistor (SET). Via tunnel barriers a small metallic quasi-isolated island is connected to metal lead electrodes, denoted as source and drain lead. A weak coupling between island and leads is necessary to get localized electron wave functions on the island. With applied bias voltage V_{DS} an energy barrier dependent current I_{SET} through the SET is measured. Both, a voltage V_G applied to a metal gate close-by, or electrostatic changes in the capacitively coupled environment can change the electrostatic potential of the SET island and thus the current flow. (b) Equivalent circuit diagram of the biased SET while current I_{SET} is recorded. Tunnel barriers are characterized as resistance R_i^T with a capacitance C_i in parallel; they are shown with a simplified symbol here.

Coulomb interaction of electrons located on a small quasi-isolated metallic island between two metallic leads results in an energy barrier, either blocking or allowing electrical current. Theoretical works from D. V. Averin and K. K. Likharev [73] in 1986 proposed such a single-electron transistor (SET) and, since they are used as probes in our new scanning probe microscope they are discussed in the following.

Figure 4.2 shows schematically the arrangement of a planar metallic SET (a) and the equivalent circuit diagram (b). A quasi-isolated metallic island is coupled via two tunneling barriers towards two metal lead electrodes, namely source and drain. Weak tunneling between island and leads is necessary to have spatially localized electrons on the island resulting in a strong Coulomb interaction between them. The tunnel barriers are replaced in the equivalent circuit diagram by a capacitance C_i parallel to a tunnel resistance R_i^T . The SET island couples mainly to (1) the lead electrodes, (2) a metallic gate electrode³ in close proximity to the SET island where a potential V_G can be applied, and (3) additional electrodes in the close environment to the SET which normally cannot be intentionally affected by the measurement setup. The total capacitance C_Σ of the SET island is the sum over all partial capacitances. In the shown case this means

$$C_\Sigma = \sum_i C_i = C_S + C_D + C_G + C_{Env}, \quad (4.1)$$

³This is a basic schematic representation. It is also possible to have several gate electrodes.

with couplings to source and drain leads C_S and C_D , the gate electrode C_G and the environment C_{Env} .

4.2.2 Single-electron charging energy

In the following, the minimum necessary charging energy to bring an extra electron onto, or to remove an electron from the electrically neutral island, is introduced [21, 73–76].

The SET island potential Φ_{isl} is determined by two contributions: (1) The charge difference Q from the electrically neutral island, and (2) electrostatic contributions from close-by electrode potentials V_i . This can be written as [21]

$$\Phi_{\text{isl}}(Q) = \frac{Q}{C_\Sigma} + \sum_i \frac{C_i}{C_\Sigma} V_i = -\frac{Ne}{C_\Sigma} + \sum_i \frac{C_i}{C_\Sigma} V_i. \quad (4.2)$$

To charge an electrostatically neutral island by an additional charge of $Q = -Ne$ from N electrons, the necessary electrostatic potential energy E_N is calculated by integration of a small element dQ in presence of the island potential Φ_{isl} over the total charge

$$E_N = \int_0^{-Ne} \Phi_{\text{isl}}(Q) dQ = N^2 \frac{e^2}{2C_\Sigma} - Ne \sum_i \frac{C_i}{C_\Sigma} V_i. \quad (4.3)$$

The first part describes the energy that is necessary to bring N electrons in this arrangement from close-by electrodes at ground potential onto the island. The second term takes the electrostatic influence into account, when the potential of these electrodes is changed from the initial ground potential. Adding to these N additional electrons one more single electron, the energy difference $\Delta E_{N \rightarrow N+1}$ to charge the island from N to $N+1$ electrons is

$$\Delta E_{N \rightarrow N+1} = E_{N+1} - E_N = \left(N + \frac{1}{2}\right) \frac{e^2}{C_\Sigma} - e \sum_i \frac{C_i}{C_\Sigma} V_i. \quad (4.4)$$

Consequently, the energy difference E_Δ for subsequent charging with two electrons becomes

$$E_\Delta = \Delta E_{N+1 \rightarrow N+2} - \Delta E_{N \rightarrow N+1} = \frac{e^2}{C_\Sigma}. \quad (4.5)$$

As N can be chosen freely in the equation, E_Δ is valid for all subsequent charging.

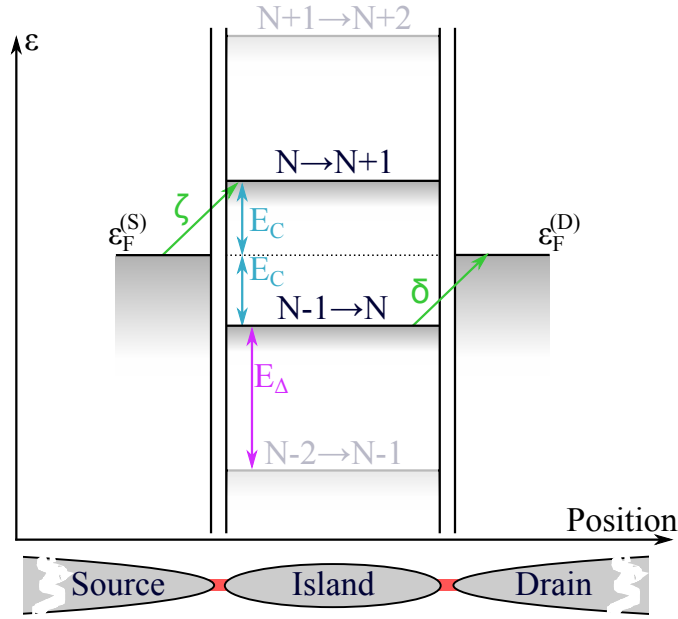


Figure 4.3: Energy level scheme of a metal island quasi-isolated via tunnel barriers from lead electrodes, namely source and drain. Some quasi-Fermi niveaus of the island are indicated (e.g. $N-1 \rightarrow N$) and assumed to be symmetrical around the source level $\varepsilon_F^{(S)}$. Here, N describes the island with N electrons on it. In this case, to add a single electron to the island (see arrow ζ), or remove an electron (see arrow δ) a charging energy $E_C = e^2/2C_\Sigma$ has to be overcome.

Figure 4.3 is a sketch of the energy level scheme of a metallic SET. As a result, quasi-Fermi levels where the SET can be charged with N electrons and $N + 1$ electrons are energetically below and above the Fermi levels of source $\varepsilon_F^{(S)}$ and drain $\varepsilon_F^{(D)}$. In this configuration the SET island is charged by N electrons. The energy level to add an additional electron to the island is above the electron energy $\varepsilon_F^{(D)}$ of lead electrodes; no further electron can be added to the island. In the shown scheme, the necessary energies to add an electron to (see arrow ζ) or to remove an electron from (see arrow δ) the island are identical; it will be named SINGLE-ELECTRON CHARGING ENERGY E_C , given by

$$E_C = \frac{E_\Delta}{2} = \frac{e^2}{2C_\Sigma} . \quad (4.6)$$

Furthermore, these symmetrical energy barriers make a current flow through the SET in the sketched situation impossible (COULOMB-BLOCKADE), as the electron number on the island is fixed when two conditions are fulfilled: (1) The bias $|V_{DS}| < |\varepsilon_F^{(S)} - \varepsilon_F^{(D)}|/e$ does not exceed E_C , and (2) the thermal energy $k_B T$ of SET electrons is much smaller than the charging energy E_C . We can conclude:

E_C depends on the total capacitance C_Σ , and thus, on the SET island size and its capacitive coupling to lead electrodes; small islands with small capacitive coupling to source and drain leads are favorable to

achieve higher working temperatures.

In case of external biasing with $V_{\text{DS}} > e/2C_{\Sigma}$, the SET quasi-Fermi levels are energetically lowered and subsequent single-electron transport over the SET island becomes possible; the electron number fluctuates between N and $N + 1$ electrons. Here, the intermediate situation with $N + 1$ electrons on the island is limited by a lifetime τ ; due to Heisenberg uncertainty relation $\Delta E \approx h/\tau$ the island quasi-Fermi levels are broadened in energy. To observe a well pronounced Coulomb-blockade effect, the inequality $\Delta E \ll E_C$ must be fulfilled. Assuming symmetrical tunnel barriers, each tunnel barrier must have a minimum resistance [74, 75, 77] of

$$R_i^T \gg \frac{h}{e^2} \approx 25.8 \text{ k}\Omega. \quad (4.7)$$

4.2.3 Current versus source-drain bias voltage characteristics

In terms of the formerly shown energy level scheme in figure 4.3, we discuss the current-voltage characteristic $I_{\text{SET}}(V_{\text{DS}})$, sketched in figure 4.4. The SET is assumed with (1) symmetric capacitive couplings ($C_S = C_D$) to the lead electrodes, (2) an asymmetric bias keeping $V_S = 0$, and (3) an influence of a positive gate electrode potential, shifting the island quasi-Fermi levels by a constant value of $-eV_G \cdot C_G/C_{\Sigma}$. In addition we set $k_B T = 0$ to neglect thermal excitation in the following. In general, a current flow becomes possible only, when at least one quasi-Fermi level for a certain charge state lies energetically between the Fermi levels of the source and drain leads; either the energy barrier between source and island ($\Delta E_{S \rightarrow \text{isl}}$) and/or between drain and island ($\Delta E_{D \rightarrow \text{isl}}$) has to vanish [75].

The formerly discussed charging energy E_C , necessary to excite single electrons onto or from the island, leads to a non-linear $I_{\text{SET}}(V_{\text{DS}})$ characteristics (see figure 4.4, pink curve). Without any voltage biasing (a), the quasi-Fermi level to charge the island with N electrons lies below, and the quasi-Fermi level to charge it with $N + 1$ electrons lies above the Fermi level $\varepsilon_F^{(S)}$; N electrons are statically on the SET island. The SET shows Coulomb-blockade with small bias voltages V_{DS} ; no current I_{SET} is expected.

This changes with an applied bias voltage $V_{\text{DS}} > 0$ starting in subfigure (b). The Fermi level of the drain contact $\varepsilon_F^{(D)}$ shifts by $-eV_{\text{DS}}$ and in accordance to equation (4.4) the island quasi-Fermi levels shift by $-eV_{\text{DS}} \cdot C_D/C_{\Sigma}$. The first shift reduces the energy barrier for an electron from the island to the drain lead ($\Delta E_{\text{isl} \rightarrow D}$), the second one from the source lead to the island ($\Delta E_{S \rightarrow \text{isl}}$). At a certain threshold

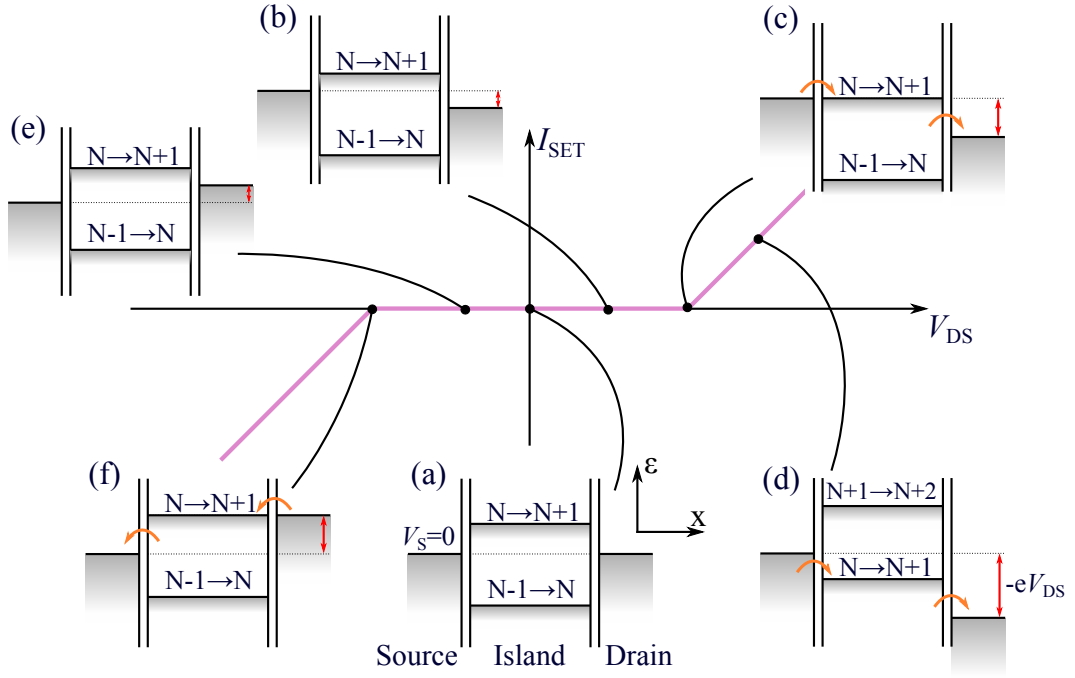


Figure 4.4: Non-linear current-voltage characteristic $I_{\text{SET}}(V_{\text{DS}})$ of an SET with corresponding energy level schemes. Here, ε and x denote the energy and position, respectively. The temperature should be 0 K and due to close-by gate electrodes a small shift of the islands quasi-Fermi levels is assumed (see later figure 4.6). (a) The presence of an energy barrier to charge the island, either positively or negatively, prohibits a current flow at small bias voltage, $I_{\text{SET}} = 0$. (b) A bias voltage shifts the Fermi levels of both, the drain lead and the island; still a barrier to get an electron onto or from the island is present. (c) The energy barrier to get an additional electron from the source lead onto the island and vice versa has vanished; electron transport from source to drain via the island ($N \rightarrow N + 1$) becomes possible. (d) Quasi-Fermi level ($N \rightarrow N + 1$) lies between $\varepsilon_{\text{F}}^{(\text{D})}$ and $\varepsilon_{\text{F}}^{(\text{S})}$; the island charge changes between N and $N + 1$ electrons, thus a current I_{SET} can be measured. (e+f) The same situation as described above, but for negative biasing. Here, the energy barrier between drain and island vanishes.

bias voltage⁴ $V_{\text{DS}}^{(\text{th})}(V_{\text{G}})$, as shown in (c), the energy barrier $\Delta E_{\text{S} \rightarrow \text{isl}}$ has vanished; single-electron transport from the Fermi level $\varepsilon_{\text{F}}^{(\text{S})}$ to the island and back becomes possible. Charge on the SET island is not static anymore; the electron number fluctuates between N and $N + 1$. Hence, a current I_{SET} arises as electrons also subsequently tunnel from the source lead to the island to the drain lead. With a further increase of V_{DS} (d) the quasi-Fermi levels are shifted energetically downwards; one more quasi-Fermi level lies below $\varepsilon_{\text{F}}^{(\text{S})}$ and it becomes possible to charge the island with $N + 1$ electrons. Tunneling events occur more often and mainly from the source lead to the island instead of vice versa; the current I_{DS} increases.

The discussion for negative bias voltages $V_{\text{DS}} < 0$ can be done in a similar way; the island quasi-Fermi levels are shifted by $eV_{\text{DS}} \cdot C_{\text{D}}/C_{\Sigma}$, while $\varepsilon_{\text{F}}^{(\text{D})}$ is shifted by

⁴In this example when $0 = E_{\text{C}} - eV_{\text{G}} \cdot C_{\text{G}}/C_{\Sigma} - eV_{\text{DS}} \cdot C_{\text{D}}/C_{\Sigma}$.

eV_{DS} . The energy barriers from drain to island ($\Delta E_{\text{D} \rightarrow \text{isl}}$) and from island to source get smaller ($\Delta E_{\text{isl} \rightarrow \text{S}}$) as shown in figure 4.4 (e). For sufficiently negative V_{DS} as indicated in figure 4.4 (f), the energy barrier ($\Delta E_{\text{D} \rightarrow \text{isl}}$) vanishes and electron flow from drain to source via the island becomes possible.

4.2.4 Current versus gate voltage characteristics: Coulomb-blockade oscillations

In a next step the dependence of the SET current to an electrostatic potential change V_{G} on a close-by gate electrode is discussed with means of figure 4.5. As before, the SET is assumed with (1) symmetric capacitive couplings ($C_{\text{S}} = C_{\text{D}}$) to the lead electrodes, (2) at zero temperature $T = 0$ with (3) an asymmetric bias keeping $V_{\text{S}} = 0$. Now, a constant $|V_{\text{DS}}| < e/2C_{\Sigma}$ is applied, while the gate voltage V_{G} is changed.

A variation of V_{G} will shift the electrostatic potential of the SET island and consequently, the SET island quasi-Fermi levels, see equations (4.2) and (4.4). Hence, changing energy differences between lead electrodes and island quasi-Fermi levels result in alternating regions of zero SET current I_{SET} - the so-called Coulomb-blockade (CB) - and regions of non-zero I_{SET} . COULOMB-BLOCKADE OSCILLATIONS (CBOs) are observed as a function of V_{G} .

In detail it looks like the following: In absence of a gate voltage $V_{\text{G}} = 0$ (a), the highest quasi-Fermi level below both, $\varepsilon_{\text{F}}^{(\text{S})}$ and $\varepsilon_{\text{F}}^{(\text{D})}$, is shifted by $\Delta E_{N-1 \rightarrow N}$; the island charge is fixed with N electrons, no fluctuations in electron number occur and I_{SET} is zero. Applying $V_{\text{G}} > 0$ shifts the island energy levels downwards; the energy barrier $\Delta E_{\text{S} \rightarrow \text{isl}}$ shrinks. For a sufficiently high⁵ gate voltage $V_{\text{G}} \geq V_{\text{G}}^{(\text{th})}$, where $V_{\text{G}}^{(\text{th})}$ denotes a threshold voltage given by $e/2C_{\text{G}} - V_{\text{DS}}C_{\text{D}}/C_{\text{G}}$, the higher energetically quasi-Fermi level is lowered enough in energy, that the quasi-Fermi level to charge the island with $N + 1$ electrons equals $\varepsilon_{\text{F}}^{(\text{S})}$ (b); single-electrons can freely tunnel from the source lead onto the island and back. Moreover, one electron can tunnel from source to the island and subsequently, one electron with an energy above $\varepsilon_{\text{F}}^{(\text{D})}$ can leave the island towards drain; the charge on the island fluctuates by a single electron and a current onset in I_{SET} is observed. Gate voltages $V_{\text{G}}^{(\text{th})} < V_{\text{G}} < \left(V_{\text{G}}^{(\text{th})} + V_{\text{DS}} \cdot C_{\Sigma}/C_{\text{G}} \right)$ allow for single-electron tunneling from source to drain via the island, leading to a peak in the $I_{\text{SET}}(V_{\text{G}})$ characteristic (c+d). A further increase of V_{G} shifts the quasi-Fermi level $N \rightarrow N + 1$ below $\varepsilon_{\text{F}}^{(\text{D})}$;

⁵In accordance to equation (4.4), when $E_{N \rightarrow N+1} = 0$; thus, $V_{\text{G}} = V_{\text{G}}^{(\text{th})} = e/2C_{\text{G}} - V_{\text{DS}}C_{\text{D}}/C_{\text{G}}$ is necessary.

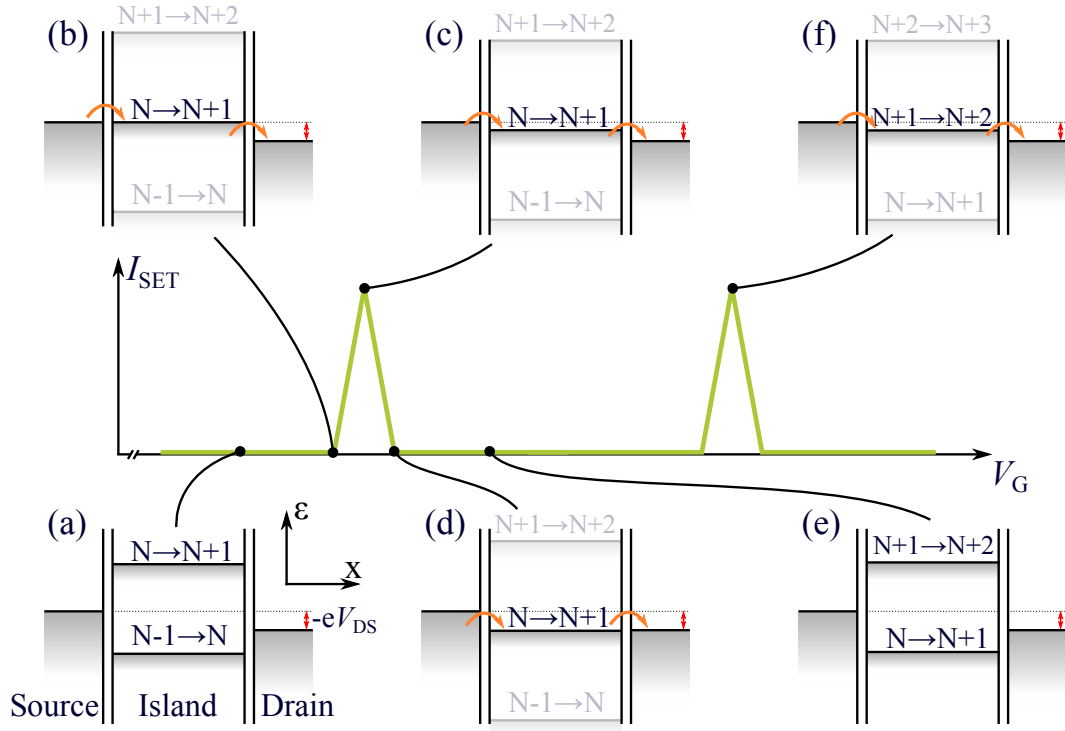


Figure 4.5: Dependency of the SET current to a gate potential change to illustrate $I_{\text{SET}}(V_G)$. The SET is biased with a small, but constant voltage V_{DS} . Capacitive coupling between gate electrode and island leads to a shift of quasi-Fermi levels on the island as the gate potential changes. Coulomb-blockade oscillations are measured: Alternating regions of Coulomb-blockade ($I_{\text{SET}} = 0$) and finite current. (a+e) Coulomb-blockade; the island charge is fixed either at N electrons (a) or $N + 1$ electrons (e), no electron flow happens. (b) Energy barrier for single-electron transport between source lead and island vanishes; electron transport becomes possible. (c) Quasi-Fermi level $N \rightarrow N + 1$ lies between $\varepsilon_{\text{F}}^{(\text{D})}$ and $\varepsilon_{\text{F}}^{(\text{S})}$; the island charge can change between N and $N + 1$ electrons, thus electron transport happens from source to drain. (d) Charge on the island becomes static with $N + 1$ electrons; no current flow happens anymore. (f) Current flow as described in (c); this time the island charge changes between $N + 1$ and $N + 2$ electrons.

the charge on the island becomes static with $N + 1$ electrons and again, Coulomb-blockade is observed in $I_{\text{SET}}(V_G)$ (d+e).

The described behavior repeats periodically with the gate voltage as seen in (f); depending on an applied gate voltage V_G , the island is subsequently charged/discharged by an electron with a periodicity of e/C_G ; this leads to Coulomb-blockade oscillation peaks in $I_{\text{SET}}(V_G)$.

4.2.5 Charge stability diagram

We discussed that electrical transport in an SET shows Coulomb-blockade regions present in both characteristics, $I_{\text{SET}}(V_{\text{DS}})$ and $I_{\text{SET}}(V_G)$. An increase of either the bias voltage V_{DS} or the gate potential V_G results in vanishing energy barriers be-

tween SET island and lead electrodes source and drain, enabling single-electron tunneling. Hence, an electrical current I_{SET} through the SET is measured. Now the complete parameter space $I_{\text{SET}}(V_{\text{DS}}, V_{\text{G}})$ is discussed in this section, which gives a CHARGE STABILITY DIAGRAM of an SET, schematically shown in figure 4.6. Assumed are (1) zero temperature $T = 0$, and (2) an asymmetric bias with $V_{\text{S}} = 0$.

Figure 4.6 (a) shows color-coded the number of electrons fluctuating on the SET island for a variation of both voltages, V_{DS} and V_{G} . Overlaid labels indicate possible electron numbers on the SET island statically or temporarily occupied; multiple labels in one region correspond to an electron number fluctuation on the island and a current through the SET. The following regions can be identified:

Coulomb blockade is presented by dark gray regions: The island is charged with fixed number of electrons (e.g. N), no quasi-Fermi level lies between source and drain energy levels $\varepsilon_{\text{F}}^{(\text{S})}$ and $\varepsilon_{\text{F}}^{(\text{D})}$. Hence, no charge fluctuations are present and the current I_{SET} is zero in these regions.

Single-electron tunneling bordering on the Coulomb-blockade region, colored in light gray: One quasi-Fermi level of the SET island lies between $\varepsilon_{\text{F}}^{(\text{S})}$ and $\varepsilon_{\text{F}}^{(\text{D})}$; the island charge fluctuates by one electron charge $-e$. As result, a current I_{SET} is measured.

Multi-Electron tunneling in our case more precisely two-electron tunneling, colored in bright gray: The energy difference from drain $\varepsilon_{\text{F}}^{(\text{D})}$ to source $\varepsilon_{\text{F}}^{(\text{S})}$ is greater than e^2/C_{Σ} and quasi-Fermi levels of at least two charge states are energetically between $\varepsilon_{\text{F}}^{(\text{D})}$ and $\varepsilon_{\text{F}}^{(\text{S})}$. The island charge can change energetically by more than two electrons at the same time, resulting in higher current changes I_{SET} with V_{DS} . For higher bias voltages V_{DS} more quasi-Fermi levels fit between $\varepsilon_{\text{F}}^{(\text{D})}$ and $\varepsilon_{\text{F}}^{(\text{S})}$ and multi-electron tunneling at the same time becomes possible for more electrons.

Slopes between different tunneling regions can be calculated via equation (4.4); the descending slope (orange) describes the case when $\Delta E_{\text{S} \rightarrow \text{isl}}$ has vanished⁶ and is given by

$$\frac{V_{\text{g}}}{V_{\text{DS}}} = -\frac{C_{\text{D}}}{C_{\text{G}}}, \quad (4.8)$$

while the ascending slope (red) is correlated with a vanishing energy barrier $\Delta E_{\text{isl} \rightarrow \text{D}}$

⁶The SET quasi-Fermi level $N - 1 \rightarrow N$ is aligned with $\varepsilon_{\text{F}}^{(\text{S})} = 0$, yielding to $0 = (N + \frac{1}{2}) \frac{e^2}{C_{\Sigma}} - eV_{\text{DS}}C_{\text{D}}/C_{\Sigma} - eV_{\text{G}}C_{\text{G}}/C_{\Sigma}$, solved by the given slope.

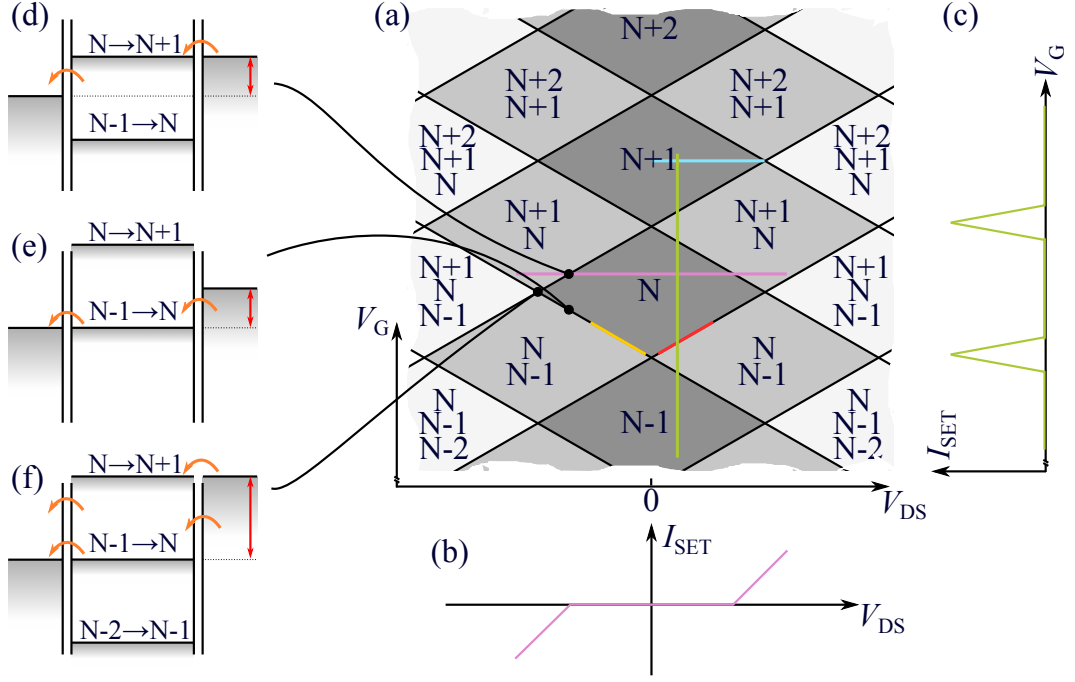


Figure 4.6: Charge stability diagram of an SET as a function of bias voltage V_{DS} and gate voltage V_G . (a) Charge states of the SET are presented in false-color representation; two line-cuts along V_{DS} and V_G , formerly presented in figures 4.4 and 4.5, are indicated and shown in (b) and (c). Dark gray color corresponds to regions of Coulomb-blockade; the electron number on the SET is static, no current I_{SET} is observed. Adjoining light gray are regions of single-electron tunneling; the island charge fluctuates by one electron, e.g. between N and $N + 1$ electrons; a current flow is observed. Bright regions represent multi-electron tunneling, more specifically, two-electron tunneling; charge on the island fluctuates by two electrons, e.g. $N - 1, N$ and $N + 1$. (d,e,f) Energy schemes of transition regions: (d) Single electron tunneling becomes possible; island charge fluctuates between N and $N + 1$ electrons (see linecut). (e) Same situation as (d), but a gate potential induced shift of the island energy levels is present; now, the island charge fluctuates between $N - 1$ and N electrons. (f) Boundary into two-electron tunneling regime; energy levels $N - 1 \rightarrow N$ and $N \rightarrow N + 1$ are between $\varepsilon_F^{(D)}$ and $\varepsilon_F^{(S)}$. The island charge can fluctuate by two electrons.

between SET island and drain lead, while the slope calculates⁷ to

$$\frac{V_g}{V_{DS}} = \frac{C_\Sigma - C_D}{C_G}. \quad (4.9)$$

The maximum threshold voltage $V_{DS}^{(th)}$ (cyan) where Coulomb-blockade can be observed, corresponds with a simultaneous vanishing of both tunneling barriers $\Delta E_{S \rightarrow isl}$ and $\Delta E_{isl \rightarrow D}$. It is independent of the ratio between C_S and C_D and is

⁷Now the quasi-Fermi level $N - 1 \rightarrow N$ is aligned with $\varepsilon_F^{(D)} = -eV_{DS}$, leading to $-eV_{DS} = (N + \frac{1}{2}) \frac{e^2}{C_\Sigma} - eV_{DS}C_D/C_\Sigma - eV_G C_G/C_\Sigma$.

derived⁸ to

$$V_{\text{DS}}^{(\text{th})} = \frac{e}{C_{\Sigma}}. \quad (4.10)$$

With the discussion in this section, the following can be summarized:

For a fixed bias voltage V_{DS} the electrostatic potential of the island depends on close-by gate electrodes; $I_{\text{SET}}(V_{\text{G}})$ shows e/C_{G} periodic Coulomb-blockade oscillations. This dependence makes an SET suitable as sensitive electrometer, as even the change of a fraction of the elementary charge e in close proximity to the SET can be detected. As it is possible to replace the gate by any kind of electrode - like a sample we want to investigate - a scanning SET microscope that is sensitive to local electrostatics is realizable with the following steps: (1) the sample will replace the gate and (2) the SET has to be fabricated on a tip to be able to approach the sample surface.

4.3 Free-standing single-electron transistors as local electrometers

The realization of a scanning single-electron transistor microscope depends strongly on whether it is possible to fabricate the SET in a way that the island can be approached into close proximity to the sample surface. Consequently, the formerly described SET with a metallic island, two tunneling barriers and both lead electrodes must be placed on a free-standing tip structure.

In the scanning SET microscope used for this thesis, an one-dimensional array of eight (Al,Ga)As tip structures with one single-electron transistor on each tip is used. This array with several SETs was first realized by Jochen Weber [20, 76] during his PhD thesis and is unique for scanning SET microscopy; other groups are normally limited to only one SET⁹ [21, 80, 81]. Since then, the SET array design and its fabrication process has improved constantly.

During this thesis we also spent eight months to make the process working reliably with a new (Al,Ga)As heterostructure¹⁰. The heterostructure is shown in subfigures (α) and (β) inside figure 4.7 and it is internally named #D150728A. It

⁸The equations $(N + 1 + 1/2) e^2/C_{\Sigma} - eV_{\text{DS}}C_{\text{D}}/C_{\Sigma} - eV_{\text{G}}C_{\text{G}}/C_{\Sigma} = 0$ (for quasi-Fermi level $N \rightarrow N + 1$) and $(N + 1/2) e^2/C_{\Sigma} - eV_{\text{DS}}C_{\text{D}}/C_{\Sigma} - eV_{\text{G}}C_{\text{G}}/C_{\Sigma} = -eV_{\text{DS}}$ (for quasi-Fermi level $N - 1 \rightarrow N$) have to be fulfilled simultaneously.

⁹or one SQUID [78, 79].

¹⁰Now it is possible to use a big variety of heterostructures, even without 2DES inside; this now enables one to reduce the tip thickness and further increase E_{C} leading to higher SET working temperatures.

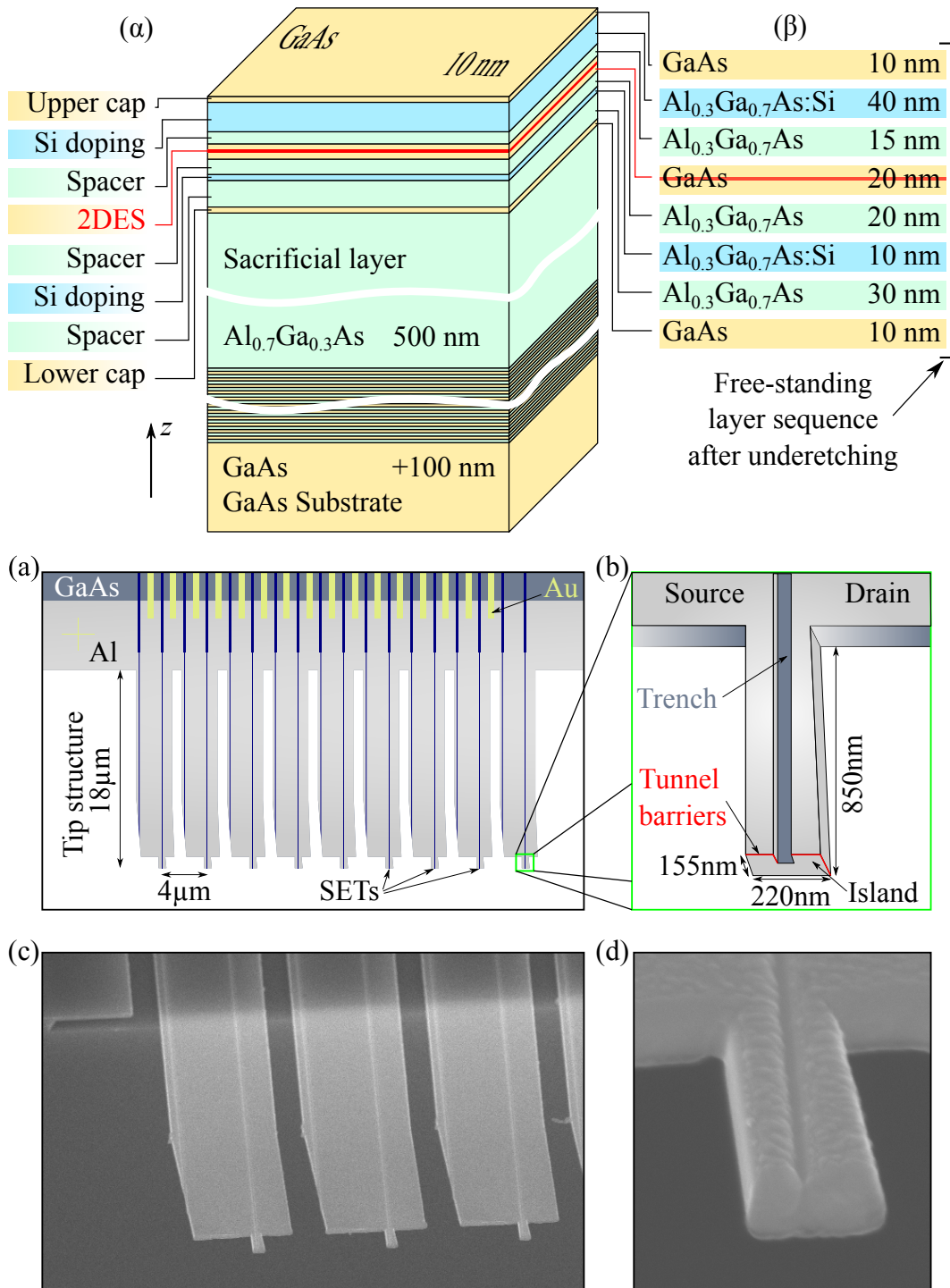


Figure 4.7: Single-electron transistor array as fabricated and used in this thesis. It is shown as sketch (a+b) and SEM picture (c+d). ($\alpha+\beta$) Scheme of new heterostructure #D150728B which is slightly changed to the original ones #81689 and #81732 [43,76], before (α) and after underetching (β). (a) On base of this heterostructure a one-dimensional array of nine, 18 μm long free-standing tips is fabricated. Aluminum evaporation and controlled oxidation yield eight functional single-electron transistors, one at each tip (one tip is a dummy for calibration). Gold lines ensure reliable electrical contact. (b) Enlarged sketch of an SET. An evaporated island is quasi-isolated from source and drain electrodes by two tunnel barriers, one on each side. An etched trench guarantees electrical isolation between the leads. (c) SEM picture showing partly the single-electron transistor array. (d) SEM picture of a single-electron transistor on a tip. Figure arrangement partly inspired by [21].

includes a 2DES in order¹¹ to have the possibility to (1) integrate low-temperature amplifiers like HEMTs in close proximity to the SETs and (2) replace some SETs by Hall sensors that use this 2DES. The fabrication of the newest tip design (see figure 4.7) is sketched in the following. A detailed description together with an overview of the complete wafer die design and necessary cleanroom steps can be found in appendix A.

Fabrication of an SET array is very time-consuming, it needs about 2.5 weeks in the cleanroom facility. Hereby, the fabrication consists mainly of two tasks: (1) a free-standing tip array structure with electrical connections is realized and (2) on this tip array working single-electron transistors are processed. The tip structure fabrication has mainly five steps of electron-beam lithography and subsequent reactive-ion etching or high-vacuum evaporation. After these steps, the (Al,Ga)As die hosts (1) 18 μm long free-standing tips structured as membrane¹², and (2) 80 nm to 160 nm wide trenches which electrically separate later the lead electrodes of and between SETs, (3) ohmic contacts that electrically connect the 2DES, and (4) gold electrodes to electrically contact the SETs with bonding wires and a chip carrier. Next, a focused ion-beam (FIB) using gallium ions together with a scanning electron microscope (SEM) is used to decrease the width at the very end of the tip structure where the SET is later formed (in the following called "SET structure"). SET-island sizes of about 180 nm to 250 nm can be technically realized, while sizes of 220 nm are easily achieved in this thesis. This size reduction increases the single-electron charging energy E_C and the spatial resolution of the SET. After this tip-shaping, SETs are fabricated by a two-step aluminum evaporation in ultra-high vacuum while the sample is cooled down to about -50° Celsius; lower temperatures reduce aluminum grain sizes and give a more homogeneous aluminum layer. During the first evaporation under a 60° angle to the sample surface normal the lead electrodes for the SETs, namely source and drain, are evaporated. After a controlled oxidation at partial pressure of 1.95×10^{-1} mbar for 20 min, which creates both aluminum-oxide tunneling barriers, the island is evaporated from the bottom. As last step, the wafer chip is scratched perpendicularly to the tip membrane in height of the underetched region. The FIB together with the SEM is used again to separate the tips from the membrane structure and to evaporate platinum rectangles at the interface between gold electrodes and aluminum. Then the SET tip structure is broken free.

¹¹In the very beginning it was also intended to short-cut the SETs via the 2DES. At low temperatures, metal gates should deplete the 2DES and open these short-cuts.

¹²The membrane structure stabilizes the tip structure and prevents that SEM induced electrostatic charging of the tip bends it downwards to the substrate.

By design and fabrication changes during this thesis, about 75% of the single-electron transistors are working now¹³. All SETs with electric room temperature resistances in the range of 30 k Ω to 1 M Ω showed functional SET characteristics at low temperatures [76].

4.4 SET characterization at low temperature

At about 40 mK the SETs are electrically characterized, compare figure 4.8; the SET island couples electrostatically to the lead electrodes, the environment and the sample, while a varying DC bias V_{DS} is applied. Discussed here is SET#2 which is used for most measurements in the fractional quantum Hall regime. Further characteristics can be found in appendix B. A large initial distance between island and sample leads to a small capacitive coupling C_G ; to measure a charge stability diagram in this situation the following is done: Instead of the gate potential V_G the potential of both lead electrodes (source and drain) is commonly changed as V_{COM} ¹⁴.

Figure 4.9 (a) shows the SET current I_{SET} in a color-coded pseudo-3d representation as function of the bias voltage V_{DS} and the common voltage V_{COM} . Well defined Coulomb-blockade regions (green) with $I_{SET} = 0$ are observed. In order that an SET is able to detect potential variations all the time, the SET characteristics should not cross regions where Coulomb-blockade is present; I_{SET} has to be non-zero all time. With higher modulation amplitudes of I_{SET} , potential changes

¹³In the beginning roughly 18% were working.

¹⁴The main idea is the following: Instead of shifting the quasi-Fermi levels of the island by V_G , the potential of both lead electrodes is shifted commonly with V_{COM} , probing the ladder structure of the island quasi-Fermi levels.

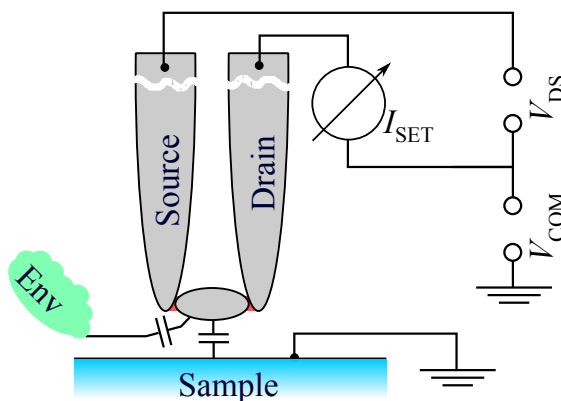


Figure 4.8: Schematic circuit diagram to characterize SETs at low temperature. The SET couples capacitively to the 2DES inside the sample and the environment. Measured is a charge stability diagram by varying the voltage V_{COM} commonly applied to source and drain, and the bias voltage V_{DS} .

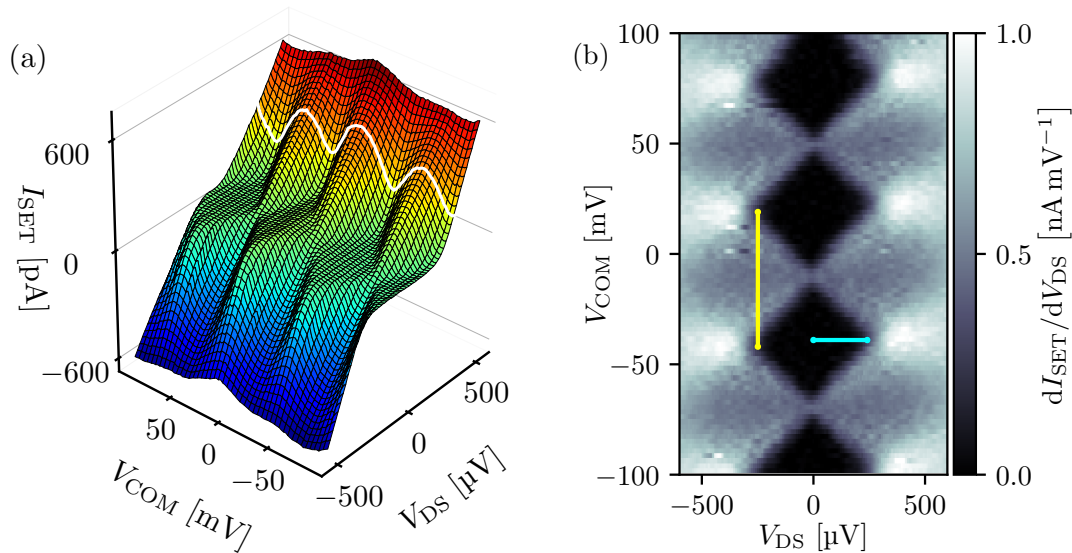


Figure 4.9: Electrical characterization of the SET we used for most measurements in the fractional quantum Hall regime. The electrical setup is sketched in the schematic shown in figure 4.2, but with fixed $V_G = 0$ and a common potential offset V_{COM} to source and drain. (a) Pseudo-3d representation of the SET current I_D as function of the bias voltage V_{DS} , and potential V_{COM} commonly applied to both lead electrodes. The highest Coulomb-blockade oscillation amplitude is measured for $V_{DS} = 348 \mu\text{V}$; this will be the fixed working point for this SET. (b) False-color representation of the differential conductance dI_D/dV_{DS} calculated from the data in (a). Shown in black are zero current regions, while brighter gray shadings correspond to higher differential conductances. Comparison with figure 4.6 gives regions of: Coulomb-blockade (black), single-electron tunneling (gray) and multi-electron-tunneling (bright).

can be detected more sensitively. A voltage bias of $V_{DS} = 348 \mu\text{V}$ was identified to give both: (1) Coulomb-blockade oscillations with I_{SET} always non-zero and (2) the highest modulation amplitude¹⁵. The corresponding CBO is indicated in figure 4.9 in white; this SET bias is defined to be the working point of this SET for further scanning measurements. In figure 4.9 (b) the differential conductance dI_{SET}/dV_{DS} , calculated from data in (a), is presented in false-color representation; compare the theoretical charge stability diagram shown in figure 4.6. Dark colored are Coulomb-blockade regions with $I_{SET} = 0$. Adjacent light gray regions belong to single-electron tunneling regimes and in bright we have multi-electron tunneling regions.

The maximum bias voltage before Coulomb-blockade regions vanish (indicated in cyan), given by $V_{DS}^{(th)} = 0.24 \text{ mV} \pm 0.02 \text{ mV}$, is correlated with (4.6) and (4.10) to

¹⁵A self-written algorithm analyses line-cuts along V_{COM} of the charge stability diagram to find possible working points.

the single-electron charging energy as $E_C = V_{\text{DS}}^{(\text{th})} \cdot e/2$; for this SET we get

$$E_C = 120 \mu\text{eV} \pm 10 \mu\text{eV}. \quad (4.11)$$

This SET's charging energy of $120 \mu\text{eV}$ lies within the usual range, compared to previous works where E_C varied between $25 \mu\text{eV}$ and $265 \mu\text{eV}$ [19–21]. Sharply separated tunneling regions in the charge stability diagram are observed for $E_C \gg k_{\text{B}}T$; a rough guess of the SET working temperature can be made via $E_C = 10 \cdot k_{\text{B}}T$ which gives

$$T \approx 140 \text{mK} \pm 10 \text{mK}. \quad (4.12)$$

The total SET capacitance C_{Σ} can be determined via $E_C = e^2/2C_{\Sigma}$ given in (4.6) to

$$C_{\Sigma} = 6.7 \times 10^{-16} \text{F} \pm 0.6 \times 10^{-16} \text{F} \quad . \quad (4.13)$$

The periodicity of the CBOs in V_{COM} direction (yellow) with 61mV is via $C_{\text{COM}} = e/V_{\text{COM}}$ connected with the common capacitance C_{COM} ; from point of the island, C_{COM} is a parallel circuit of capacitances to the environment and the sample. We calculate

$$C_{\text{COM}} = 2.6 \times 10^{-18} \text{F} \pm 0.2 \times 10^{-18} \text{F}. \quad (4.14)$$

During this characterization the distance to the sample was in the order of 1mm . Hence, C_{COM} is dominated by neighboring SETs in a distance of $4 \mu\text{m}$, which gives $C_{\text{Env}} \approx 2.6 \times 10^{-18} \text{F} \pm 0.2 \times 10^{-18} \text{F}$.

4.5 2DES in (Al,Ga)As heterostructures shaped as Hall bar sample: Special design rules

As mentioned in previous sections, we will use single-electron transistors as very sensitive local electrometers in our scanning probe microscope; this requires some special design rules for the sample. Referring to section 4.2.5, SETs biased with a constant voltage V_{DS} are very sensitive to electrostatic changes of the underlying sample, while on the other hand no topography of the sample can be measured; above areas with no potential change the microscope is literally blind. This becomes problematic, as the 2DES - shaped as six-terminal Hall bar - that we want to investigate with the SET, is not necessarily below the probing tips after the microscope is inserted into the dilution refrigerator.

To overcome this issue, different metallic gate electrodes (also called positioning areas) with the possibility to individually change their potential are placed around

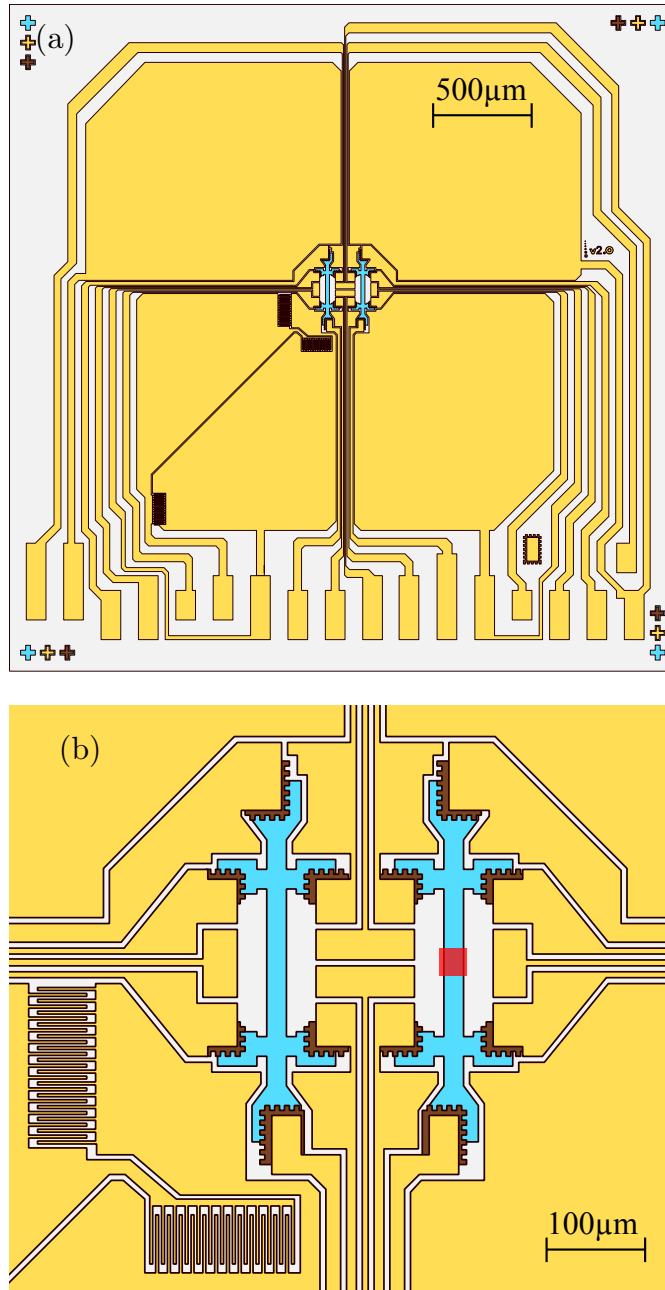


Figure 4.10: Sketch of the sample structure investigated in this thesis. (a) Complete structure with a size of 3.5 mm by 3.5 mm structured on an (Al,Ga)As heterostructure chip (gray) including a 2DES 120 nm below the surface. Wet etching removes the 2DES, except in two six-terminal Hall bar mesa structures with a width of 20 μm centered in the sample. An annealed AuGeNi alloy contacts the 2DES at six positions each, four potential probes and two bias contacts. To navigate with an SET, positioning electrodes made from gold surround the Hall bar structures. (b) Zoom into the region of both Hall bars. A calibration structure (lower left) can be used to calibrate the microscope scan range [21]. To ensure homogeneous 2DES conditions far from any close-by electrode, and to minimize the risk of a tip-sample collision, Hall potential measurements are preferably performed in the red highlighted region.

the Hall bar structure, compare figure 4.10. For redundancy, two Hall bars are fabricated on the same chip, in case one would not work. Close to the Hall bars (light blue) - compare figure 4.10 (b) - fine positioning areas (yellow) are placed. Between the probing contacts they keep a minimum distance of $30\ \mu\text{m}$ to the etched Hall bar edges. This distance reduces the influence of the gate electrodes on the local electrostatics of the Hall bar, while they are used as guidelines to position the SETs between the probing contacts (red marked area) above the Hall bar. The 2DES is contacted via an annealed AuGeNi alloy that forms low resistive ohmic contacts [82] (brown). Gold electrodes going to ohmic contacts are intentionally wide to fill most of the wafer surface. Two gate structures form finger-like calibration structures (lower left) which can be used to calibrate the microscope scan and positioning system initially [21]. Around the centered Hall bars and the fine positioning areas, five large gate electrodes are located, see figure 4.10 (a). A subsequent variation of the electrostatic potential of these big electrodes is used initially to find the probing tips above the sample surface and navigate towards the inner Hall bar structure. The idea is the following: the capacitive coupling between the SET island and each positioning area depends on their distance; if the potential of each area varied one-by-one, we know the SETs are located above that electrode which gives the lowest CBO period. All electrical connections from both Hall bars and all gate electrodes end in bond pads at the lower end of the $3.5\ \text{mm}$ by $3.5\ \text{mm}$ wide wafer die; this reduces the risk of touching them during positioning. In case of touching, the SETs are usually electrically damaged or mechanically broken.

The fabrication process of the sample in the cleanroom facility can be done within four days and following steps are necessary: The (Al,Ga)As heterostructure with internal reference #D110222A¹⁶, shown in figure 2.1, is structured by optical lithography and wet-chemical etching. The 2DES is removed in the whole heterostructure surface, except in two regions shaped as six-terminal Hall bars with a width of $20\ \mu\text{m}$ and length of $150\ \mu\text{m}$ between probing contacts; this structure is investigated later. Further optical lithography steps in combination with high-vacuum evaporation and contact alloying are used to realize AuGeNi contacts to the 2DES, and to gold electrodes.

¹⁶This wafer is grown by C. Reichl in the W. Wegscheider group of ETH Zürich. An initial characterization by them yielded a charge carrier density $n_{2D} = 1.4 \times 10^{15}\ \text{m}^{-2}$ and mobility $\mu_{2D} = 8.9 \times 10^6\ \text{cm}^2/\text{Vs}$.

4.6 Hall bar characterization at low temperature

Before the Hall potential distribution in the fractional quantum Hall regime is measured, the 2DES of the sample is electrically characterized at about 40 mK; we have to ensure that well-pronounced fractional QH states are observed. The tips are positioned over the Hall bar in the center region between both longitudinal probing contacts, while a Hall measurement is performed.

The inset in figure 4.11 shows schematically the measurement setup; a constant bias voltage $V_{DS} = 500 \mu\text{V}$ is applied to the Hall bar which is exposed to a varying perpendicular magnetic flux density B between 0 T and 18 T. Currents I_S into and I_D from the sample are both measured and compared; in this way leakage currents can be excluded. Two high impedance differential amplifiers at probing contacts measure the Hall voltage V_y across the sample width and the longitudinal voltage drop V_x along the sample.

The obtained Hall resistance curve $R_{xy}(B) = V_y/I_D$ (blue, left axis) and longitudinal resistance curve $R_{xx}(B) = V_x/I_D$ (green, right axis) are depicted in figure 4.11. In the low-magnetic field range R_{xy} shows the classical Hall effect; a monotonous linear increase with B . For higher magnetic fields the quantum Hall plateau structure with quantized resistance values h/fe^2 is observed; f can be integer or certain fractions. Some quantized plateau values are added as gray horizontal lines to the plot. In the classical Hall regime at low magnetic fields, a linear fit (gray regression) is calculated to determine the electron density as¹⁷ $n_{2D} = 2.05 \times 10^{15} \text{ m}^{-2} \pm 1.6 \times 10^{13} \text{ m}^{-2}$. This is used to indicate the bulk filling factors ν of some quantum Hall states with vertical gray lines. The longitudinal resistance R_{xx} shows Shubnikov-de-Haas oscillations that approach zero for most of the observed quantum Hall plateaus.

Referring to section 3.9, a quantized Hall resistance in combination with a vanishing longitudinal resistance means the following: the externally biased current flows in the complete area between all probing contacts exclusively within incompressible regions of same filling factor ν . For these QH states - independently on the position between the probing contacts we chose to probe Hall potential profiles - the QHE is well pronounced there. Consequently, QH states with quantized R_{xy} but partly non-zero R_{xx} are locally well pronounced along the sample, but not in the entire area between all probing contacts.

¹⁷The error of n_{2D} is below 1% due to the fit.

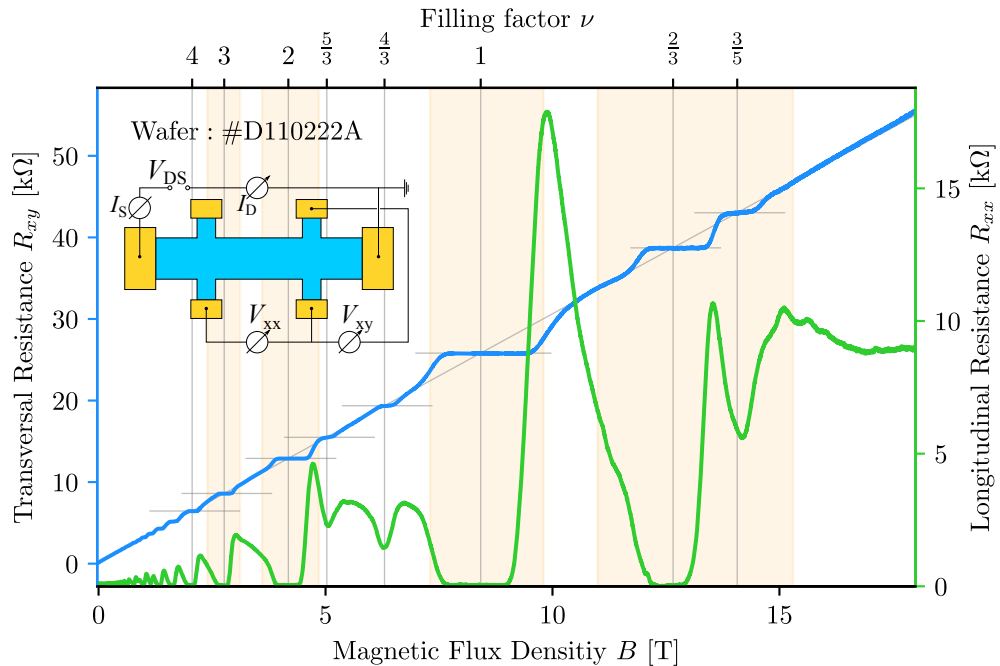


Figure 4.11: Electrical characterization of a 2DES shaped as six-terminal Hall bar geometry, biased with constant voltage V_{DS} in varying perpendicular magnetic flux densities. (INSET) While voltage-biased with $V_{DS} = 500 \mu\text{V}$ the currents I_S into and I_D coming from the Hall bar are measured to exclude leakage currents. Hall voltage V_y and longitudinal voltage V_x are recorded with high impedance differential amplifiers during continuous magnetic field sweeps to calculate the Hall resistance $R_{xy} = V_y/I_D$ and longitudinal resistance $R_{xx} = V_x/I_D$. (DATA) The Hall resistance (blue, left axis) shows a monotonous linear increase in the classical Hall regime at low magnetic flux densities, while quantum Hall plateaus are visible at higher magnetic fields. During well pronounced Hall plateaus the longitudinal resistance (green, right axis) drops to zero. Magnetic field regions highlighted in orange are investigated during this thesis. The internal heterostructure notation is #D110222A.

In previous works, only well pronounced even filling factors ν have been systematically investigated [7, 12, 21]. In this thesis we concentrate on quantum Hall states not yet probed; more precisely filling factors¹⁸ $\nu_m \in \{3, 2, 1, 2/3, 3/5\}$. We want to emphasize that the fractional QH state $2/3$ is well pronounced in this sample which gives the possibility to probe the first fractional quantum Hall state with this sample. The corresponding magnetic field ranges we investigate in the following of this thesis are highlighted in orange. Table 4.1 summarizes for investigated QH states the calculated magnetic fields where bulk filling factors ν_m are expected.

¹⁸Filling factor 2 was already measured by Erik Ahlswede and Peter Weitz [7, 12].

Bulk Filling Factor ν_m [1]	3	2	1	$2/3$	$3/5$
Magnetic Flux Density B [T]	2.83	4.24	8.48	12.71	14.13

Table 4.1: Calculated magnetic flux densities B that correspond to bulk filling factors ν_m of investigated QH states. Except of $\nu_m = 3/5$, all investigated QH states are well pronounced in the Hall bar area enclosed by probing contacts, with R_{xy} quantized and R_{xx} approaching zero.

4.7 Summary

At the beginning of this chapter, the new scanning probe microscope used for this thesis was sketched: a continuous scan range of $27\ \mu\text{m}$ by $27\ \mu\text{m}$ in the x - y plane, and of about $300\ \text{nm}$ in z direction are achieved. Coarse positioning is realized by inertial piezo modules in cube shape from the company Attocube with a positioning range of $3.2\ \text{mm}$ by $3.2\ \text{mm}$ in x - y direction, and of $2.5\ \text{mm}$ in z direction. The SPM is operated in a top-loading Kelvinox-400 $^3\text{He}/^4\text{He}$ dilution refrigerator from the company Oxford Instruments reaching a working temperature of $40\ \text{mK}$, while a superconducting magnet inside the dilution refrigerator can reach magnetic flux densities up to $18\ \text{T}$. This experimental setup is located in the vibrational damped Precision Laboratory of the Max Planck Institute for Solid State Research in Stuttgart.

Afterwards the low-temperature current characteristics of a single-electron transistor (SET), together with the fabrication process to bring them into a free-standing array structure with eight SETs - as local electrometers in the new scanning probe microscope (SPM) - was discussed. Within the first eight months of this thesis, this process together with the SET array design was partly changed to make it reliable and to increase the output of working SETs to about $75\ \%$. Such fabricated SETs had usually a room-temperature resistance between $30\ \text{k}\Omega$ and $1\ \text{M}\Omega$. Characteristics of one SET were presented which showed well pronounced current transport regimes at temperatures of about $40\ \text{mK}$ and the charging energy was determined to be $120\ \mu\text{eV} \pm 10\ \mu\text{eV}$; from this, the maximum working temperature calculates to $140\ \text{mK} \pm 10\ \text{mK}$.

Then, essential design rules for samples that will be investigated with SETs - which are sensitive only to electrostatic changes - were discussed: in addition to the structure of interest, several independent and large gate electrodes are necessary for positioning the SET tips; the sample surface uncovered with gate electrodes should be as small as possible.

Then, the cleanroom fabrication process for our Hall bar sample we investigate in the following was shortly sketched. The 2DES of the Hall bar has an electron density of $n_{2D} = 2.05 \times 10^{15} \text{ m}^{-2} \pm 1.6 \times 10^{13} \text{ m}^{-2}$. Well pronounced integer and fractional QH states are observed at 40 mK.

After the characterization presented in this chapter we can start with Hall potential measurements in the following. The next chapter explains measurement principles.

Chapter 5

Measurement Principle - Hall Potential Profiles and Current Densities

In the further process of this thesis, a single-electron transistor array will be used as sensitive local electrometer to determine Hall potential profiles in a cross-section of a six-terminal Hall bar within the IQH and FQH regime. From the experimental point of view, the measurement itself is more complex; dielectric particles like resist remains, height changes during a scan, and charges on the sample surface, respectively the sample donor layer, affect the measurement. These influences have to be understood in order to extract Hall potential profiles.

Therefore, in this chapter we discuss electrostatic influences on an SET island that come from different sample scenarios which are possibly present during a scan. Then, we show a measurement method that was introduced in [21], to get access to probe with an SET the Hall potential profiles. Firstly, monitoring the CBOs during a scan above the sample surface reflects the variation of the electrostatic potential of the sample. However, it contains many contributions which make the extraction of the 2DES potential difficult. Moreover, it is not unique whether the sample potential rises or decreases. This lack can be overcome by a feedback loop method keeping the SET current constant by controlling the source and the drain electrode potential in common. A modulation of the sample with a small low-frequency AC signal leads to a two-step measurement method to determine Hall potential profiles and further, the current density as a function of the tip position over the 2DES.

5.1 Electrostatic effects affecting the SET island potential

In order to use an SET as local electrometer in a scanning probe experiment, features that electrostatically influence the SET island have to be discussed. Figure 5.1 (a) illustrates an SET on a tip, which is moved above a sample surface. During such a scan, different situations may influence the SET island potential - like a height change between SET and underlying sample. To understand the influence of such changes we recap equation (4.2) from section 4.2.2, describing the electrostatic potential Φ_{isl} of the SET island as

$$\Phi_{\text{isl}}(V_i, C_i, Q_{\text{eff}}) = \frac{Q}{C_{\Sigma}} + \sum_i \frac{C_i}{C_{\Sigma}} V_i + \frac{Q_{\text{eff}}}{C_{\Sigma}} \quad (5.1)$$

$$= -\frac{Ne}{C_{\Sigma}} + \frac{C_S}{C_{\Sigma}} V_S + \frac{C_D}{C_{\Sigma}} V_D + \frac{C_G}{C_{\Sigma}} V_G + \frac{C_{\text{Env}}}{C_{\Sigma}} V_{\text{Env}} + \frac{Q_{\text{eff}}}{C_{\Sigma}}. \quad (5.2)$$

Φ_{isl} depends on electrostatic contributions from close-by electrode potentials V_i that are capacitively coupled via C_i to the island, and local charge accumulations Q_{eff} . To understand a change $\Delta\Phi_{\text{isl}}$ resulting from changes ΔV_i , ΔC_i and ΔQ_{eff} we calculate the total derivative of equation (5.1) as

$$\Delta\Phi_{\text{isl}} \approx \sum_{k \in \{V_i, C_i, Q_{\text{eff}}\}} \frac{\partial}{\partial k} \Phi_{\text{isl}}(V_i, C_i, Q_{\text{eff}}) \Delta k. \quad (5.3)$$

In this discussion only the lead electrodes (source and drain), one gate electrode and the environment are taken into account; for more electrodes that couple to the SET island, equation (5.3) remains still valid, just becomes more complicated. Hence, $\Delta\Phi_{\text{isl}}$ is derived to be¹

$$\Delta\Phi_{\text{isl}} = \textcircled{1} \quad (Q_{\text{eff}} \text{ changes}) \quad (5.4)$$

$$+ \textcircled{2} \quad (V_i \text{ changes}) \quad (5.5)$$

$$+ \textcircled{3} \quad (C_i \text{ changes}) \quad (5.6)$$

$$+ \textcircled{4} \quad (\text{mixed terms due to } C_i \text{ changes}) \quad (5.7)$$

with the terms

$$\textcircled{1} = \frac{1}{C_{\Sigma}} \Delta Q_{\text{eff}} \quad (5.8)$$

$$\textcircled{2} = \frac{C_S}{C_{\Sigma}} \Delta V_S + \frac{C_D}{C_{\Sigma}} \Delta V_D + \frac{C_G}{C_{\Sigma}} \Delta V_G + \frac{C_{\text{Env}}}{C_{\Sigma}} \Delta V_{\text{Env}} \quad (5.9)$$

¹Take into account that the total capacitance is $C_{\Sigma} = \sum_i C_i = C_S + C_D + C_G + C_{\text{Env}}$, which leads to the third line of equation (5.3), expressed in (5.6).

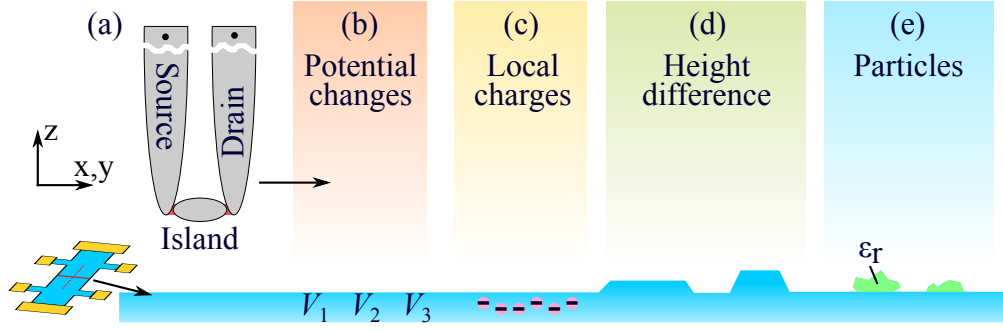


Figure 5.1: Sketch illustrating a scan with an SET tip over a sample surface. Possible influences on the SET island potential are shown subsequently. (a) Schematically drawn SET on a tip as local electrometer, scanning a line (either x or y direction) over a 2DES Hall bar sample. Different scenarios have to be taken into account: (b) Locally different electrostatic potentials in the 2DES; they are not necessarily caused by the external biased current. (c) Surface states or ionized donor atoms. (d) Height changes due to the limited mesa structure, or a slight angle mismatch between the scan plane and the sample surface. (e) Dielectric particles on the sample surface, e.g. undissolved resist clusters.

$$\textcircled{3} = \frac{V_S}{C_\Sigma} \Delta C_S + \frac{V_D}{C_\Sigma} \Delta C_D + \frac{V_G}{C_\Sigma} \Delta C_G + \frac{V_{\text{Env}}}{C_\Sigma} \Delta C_{\text{Env}} \quad (5.10)$$

$$\textcircled{4} = -\frac{\textcircled{5}}{C_\Sigma^2} \cdot (\Delta C_S + \Delta C_D + \Delta C_G + \Delta C_{\text{Env}}) \quad (5.11)$$

$$\textcircled{5} = C_S V_S + C_D V_D + C_G V_G + C_{\text{Env}} V_{\text{Env}} - Ne + Q_{\text{eff}} \quad (5.12)$$

Here, the product $C_{\text{Env}} V_{\text{Env}}$ describes a charge Q_{Env} and thus, the contribution Q_{eff} will be treated in the following as an offset to the environment contribution. With this general description we start to discuss the four possible situations sketched in figure 5.1 (b) to (e), in ascending order:

1. A local change of an electrostatic gate potential from V_1 to V_2 to V_3 , see (b), is probable to occur during a scan. This situation can be treated similar to a constant SET position and a potential change ΔV_G of the gate. All other C_i and V_i with $i \in \{S, D, \text{Env}\}$ are kept unchanged. In this case, equation (5.3) simplifies to

$$\Delta \Phi_{\text{isl}} = \frac{C_G}{C_\Sigma} \Delta V_G, \quad (5.13)$$

It becomes obvious that a potential change during a scan shifts the electrostatic potential of the SET island, and consequently the quasi-Fermi levels on the island. This situation of spatially changing potentials is the one we are interested in later.

2. Local charge accumulations, e.g. by electronic surface states, or ionized donors in the heterostructure below the surface, can be present as indicated in (c). In both cases the charge distribution leads to local electrostatic potential

variations. When the SET moves over this position the island potential changes by

$$\Delta\Phi_{\text{isl}} = \frac{\Delta Q_{\text{eff}}}{C_{\Sigma}}. \quad (5.14)$$

3. Local height differences Δh between SET island and sample surface (d) are assumed. Such changes may occur at etched mesa edges or, when an angle between sample surface and SET scan plane is present. For small distances between gate and SET island a plate capacitor arrangement² can be assumed; the capacitive coupling to the gate calculates to $C_G = \epsilon_0 \epsilon_r A/h$ and depends on the distance change Δh . Thus, a height change h can be treated as a change in the capacitive coupling C_G . The change of the island potential $\Delta\Phi_{\text{isl}}$ calculates with equation (5.4) to

$$\Delta\Phi_{\text{isl}} = \Delta C_G \left(\frac{V_G}{C_{\Sigma}} - \frac{C_G V_G - Ne}{C_{\Sigma}^2} \right). \quad (5.15)$$

Equation (5.15) is in accordance with [21] and illustrates that a height difference on the sample also leads to a shift of the SET island potential.

4. Dielectric particles on the sample surface may be present, see (e). Such particles could be resist residuals from formerly performed lithography steps during the sample fabrication process in a cleanroom. The dielectric constant ϵ_r of these particles usually does not match the one of liquid Helium ($\epsilon_r \approx 1$). In accordance to the plate capacitor model already used, such a particle leads to an effective change of the capacitive coupling. Hence, this situation can be treated in the same manner as a height difference in (d) and leads to equation (5.15).

Here we want to remind: in accordance to equation (5.1) and SET characteristics introduced in chapter 4, changes of the sample potential ($V_{2\text{DES}}$) influence the electrostatic SET island potential Φ_{isl} and shift the energetic position of SET island quasi-Fermi levels, as indicated in figure 5.2 (a)³. When an SET is moved over the sample surface, local electrostatic potential changes lead to a change of the charge Q on the SET island which increases or decreases step-wise, compare figure 5.2 (c). This happens as quasi-Fermi levels of the SET island are shifted below/above the energy levels of both lead electrodes. Consequently, the SET island has a (new)

²This assumption becomes valid for small distances between SET island and sample surface. But, without loss of generality this assumption can be made here for simplicity; all height changes lead to a changed capacitive coupling. The only difference is how these changes scale with distance, which depends on the actual geometry.

³It is assumed that lead electrodes are kept constant at $V_S = V_D = 0$, and initially other gate potentials are also zero.

fixed electron number on it.

In a real measurement, the SET will be exposed to a superposition of all formerly mentioned influences, see figure 5.2 (b). Consequently, it becomes quite difficult to distinguish single contributions on the SET island potential. Hence, it seems difficult to extract those parts, coming exclusively from local electrostatic potential changes of the 2DES, and thus, further measurement and calibration techniques are necessary to determine Hall potential profiles.

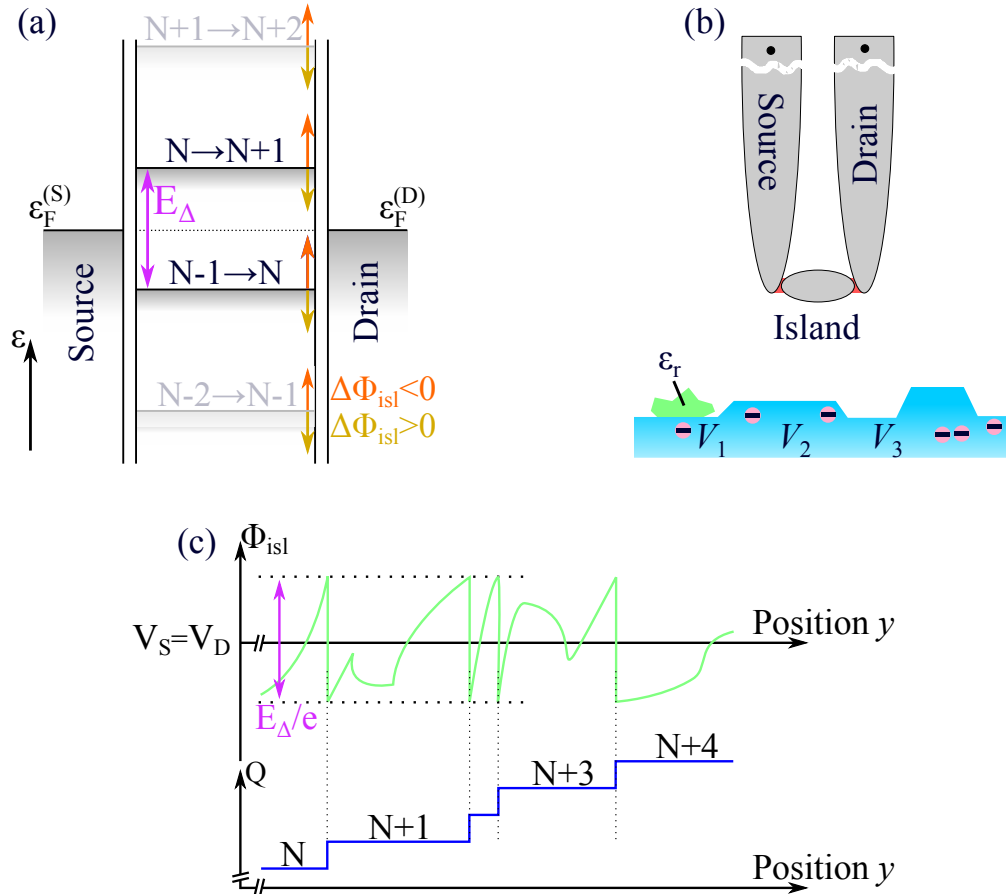


Figure 5.2: (a) Energy level scheme of the metal SET. A change of the sample potential shifts quasi-Fermi levels on the SET island. (b) Assumption of a real situation present during scanning experiments. A superposition of electrostatic potential changes, located charges, height changes and dielectric particles are present. (c) Possible measurement result during a scan: electrostatic changes lead to changes in the SET island charge in a quantized manner, the potential Φ_{isl} of the island jumps accordingly.

5.2 Coulomb-blockade oscillation (CBO) method: Possibility to image the Hall bar with all its electrostatic influences on the SET

The single-electron transistor is now operated as sensitive local electrometer in the scanning probe microscope. The source-drain voltage V_{DS} is fixed to its specific working point (compare section 4.4): Outside of the Coulomb-blockade regime where the SET current I_{SET} is non-zero for all gate voltages and furthermore, showing the highest amplitude modulation of I_{SET} - the highest changes in $\partial I_{SET}/\partial V_i$ for potential changes V_i are measured.

Now, a scan over the sample surface is performed, see figure 5.3 (a). Electrostatic influences as described in the previous section may change Φ_{isl} during this scan. These changes shift the quasi-Fermi levels of the SET island what results in a modulation of the SET current $I_{SET}(x, y)$, compare figure 4.5. In the following we measure I_{SET} as a function of varying parameters, like the tip position, sample-tip distance or sample potential. Occurring oscillations in I_{SET} indicate electrostatic changes in the SET vicinity. We refer to this measurement technique in the following as COULOMB-BLOCKADE OSCILLATION METHOD, or shortly CBO method.

Figure 5.3 (b) shows a false-color representation of currents $I_{SETi}(x, y)$ from three SETs on the array - named by their number i - recorded during an area scan. The scan area is chosen between the longitudinal probing contacts of the 20 μm wide Hall bar, see small inset. Color changes in the plot indicate that the SET current changes as a function of the tip position. On a first view, it becomes obvious that all three achieved scan images seem to show the same features, just shifted in tip position y . Firstly, round dots in a wide and mainly homogeneous area, and secondly, regions with strong changes $\partial I_{SETi}/\partial y$ along the y direction, while thirdly, only small changes in x direction are observed.

During this measurement, SET2 is adjusted to be roughly in middle of the Hall bar cross-section for position $y = 0$. This explains a mainly y -symmetric image achieved with SET2. On the other hand, on our SET array, SET1 and SET3 are SETs directly left and right of SET2 (compare figure 4.7) with a distance of 4 μm defined by electron-beam lithography; this explains that these SETs see a Hall bar region that is shifted by 4 μm in y direction. The occurrence of the wide and homogeneous region - between regions with fast changes in $I_{SETi}(y)$ - can be understood when the effective distance between SET island and 2DES is

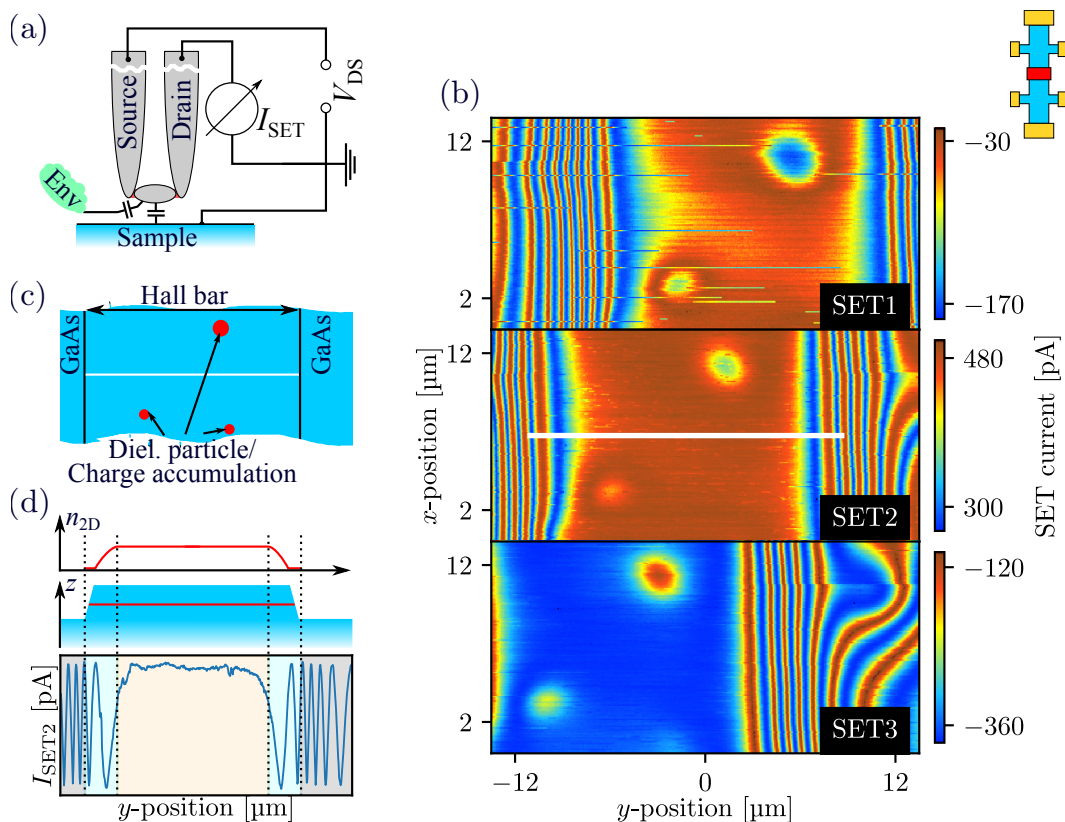


Figure 5.3: Area scan in the region of the Hall bar using the CBO method to image electrostatic influences on the SET island. (a) The SET is DC biased with V_{DS} to its working point, while the current I_{SET} through the SET is monitored. In this configuration the x and y position of the tip array is changed. (b) Measured CBOs of three SETs in a false-color representation as a function of spatial coordinates x and y . All seem to show the same features, only shifted by an offset in y direction. Further details in the text. (c) Round features that appear in the area scans are most likely dielectric particles or charge accumulations on the sample surface. (d) The homogeneous region in the scans results from a homogeneous 2DES and no capacitive changes. Towards the Hall bar mesa edges the electron density n_{2D} vanishes. At the same time the SET moves closer to surrounding gold electrodes (compare figure 4.10). Between SET island and these gold electrodes the work function difference is not compensated, what leads to fast CBOs.

considered, see figure 4.7(d). In the lower part of (d), a line cut $I_{SET2}(y)$ at a constant x -position of $x = 6.75 \mu\text{m}$ is shown. Above, the height profile of the Hall bar structure on the GaAs substrate is sketched together with the expected electron density profile $n_{2D}(y)$ of the 2DES. In this line-cut in (d), three regions - lying symmetrically around $y \approx 0$ - are discussed in the following. We start in the middle and go to the right, while different regions are indicated by their background color:

1. Initially in a wide scan range Δy (background color orange) the current $I_{SET2}(y)$ changes only slightly. This indicates that the electrostatic potential of the SET island Φ_{isl2} is almost constant; no relative height changes to the 2DES/sample or electrostatic potential changes occur. This behavior is

expected in the homogeneous bulk region of the 2DES, where the electron density is constant - only long-range electron density variations may appear.

2. Adjacent, a smaller region (background color cyan) is present, where $I_{\text{SET}2}$ starts to show CBOs in y direction. In this region, the SET tip leaves the wet-chemically⁴ etched mesa structure and thus, the 2DES. Different things happen now: (1) The relative distance between 2DES and SET island starts to increase ($C_{2\text{DES}}$ decreases). (2) Towards the mesa edge the 2DES electron density decreases from its bulk value to zero. (3) More negative charge is accumulated at the mesa edge⁵.
3. In a region with background color gray, a small CBO period of $I_{\text{SET}2}$ in y is observed. Away from the Hall bar, the SET capacitively couples to close-by metal electrodes - normally used for positioning. The work function difference between SET island and these electrodes is not compensated, leading to a potential change in y .

The mesa structure is symmetrical in y direction. When it is left on the left side a similar behavior is observed. Furthermore, the scanned Hall bar area is translation invariant in x direction, leading to only minor changes in this scan direction. Afore mentioned round features where $I_{\text{SET}i}$ changes are either: (1) Dielectric particles with a permeability ϵ_r effectively changing the capacitive coupling between 2DES and SET island, or (2) these regions are charged by itself⁶, compare figure 5.1.

The CBO method is mainly used to make fast area images during tip array positioning and approaching. Figure 5.3 illustrates nicely, that this method cannot be used to state if charge, a potential change, or a change in the capacitive coupling is present - just a change $C_i \cdot V_i + Q_{\text{eff}}$ can be detected. Furthermore, it cannot be distinguished if a change is positive or negative; approaching the Hall bar in y direction and leaving it again, looks mainly the same.

⁴This specification is made as wet-chemical etching leads to a finite slope of the mesa at the Hall bar edge, compared to reactive-ion etching where the mesa etching happens almost with a perpendicular step.

⁵We remind: Dangling bonds lead to charged surface states and a mid-gap pinning of the Fermi-energy, compare section 3.2. On a flat sample surface without any height differences this charge is expected to be homogeneously distributed. But, the mesa stands out of this flat plane and the etched mesa sidewalls effectively lead to a larger negatively charged surface area visible to the SET.

⁶One reason could be that the donor layer is not completely homogeneous. Another reason may be charged particles on the sample surface.

5.3 Tip position shifted by applied magnetic field

In order to identify an evolution of Hall potential profiles with varying filling factors ν it is unavoidable to change the magnetic flux density B while the tip is in close proximity to the sample surface. During such magnetic field changes our microscope shows a little inconvenient behavior: The relative SET tip position shifts slightly against the sample position. This may become even risky when the tip approaches to the sample. In the worst case an SET touches the surface and becomes unusable.

To calibrate the lateral shifts induced by the magnetic field, we use the formerly introduced CBO method to image a small region of the Hall bar showing two small round features, see figure 5.4 (a) and (b). Both features can also be identified in the bottom region⁷ of figure 5.3 (c), SET3. Tracking the x and y position of these features for different magnetic flux densities and for all three SETs yields the corrections $\Delta x(B)$ and $\Delta y(B)$, shown in figure 5.4 (c).

The vertical shift in z direction is determined via the distance dependent CBO period. In section 4.2.5 we derived that the CBO is e/C_{2DES} periodic in V_{2DES} . Assuming a plate condensator arrangement, an increased distance between SET island and sample lowers C_{2DES} and leads to a larger CBO period in V_{2DES} . A measurement of e/C_{2DES} at different B gives insight whether the tip-sample distance increases or decreases. Then, at each magnetic field value, the piezo scan tube is used to compensate z -shifts and recover the initial CBO period before a scan is performed. Hereby, we ensured that a possible shift of $x(z)$ and $y(z)$ resulting from tube elongations can be neglected; it was at least ten times smaller than a shift in B . The elongation in z - which is equal for all SETs - is also shown in figure 5.4 (c).

When B is changed in a small range of less than 3 T at once, the dependencies show a linear behavior⁸. A linear regression that describes the lateral x -shift as $\Delta x(B) = a \cdot B + x_0$, is fitted to the data in figure 5.4 (c). Here, x_0 denotes the initial x position, B the magnetic flux density, and a the magnetic field correction we are interested in. The corrections $\Delta y(B)$ and $\Delta z(B)$ are determined analogously. Values which are obtained for x , y and z components can be found in graph 5.4 (c). Compared with corrections found by Marcel Mausser [21] the deviation⁹ lies within

⁷The tip array was slightly moved to the left, in y direction, between both measurements. This explains the offset in y .

⁸Only for higher magnetic field changes during a single tip approach, a small quadratic correction has to be superposed [21].

⁹The correction in x direction is higher than mentioned in the reference. The deviation is $\approx 180\%$.

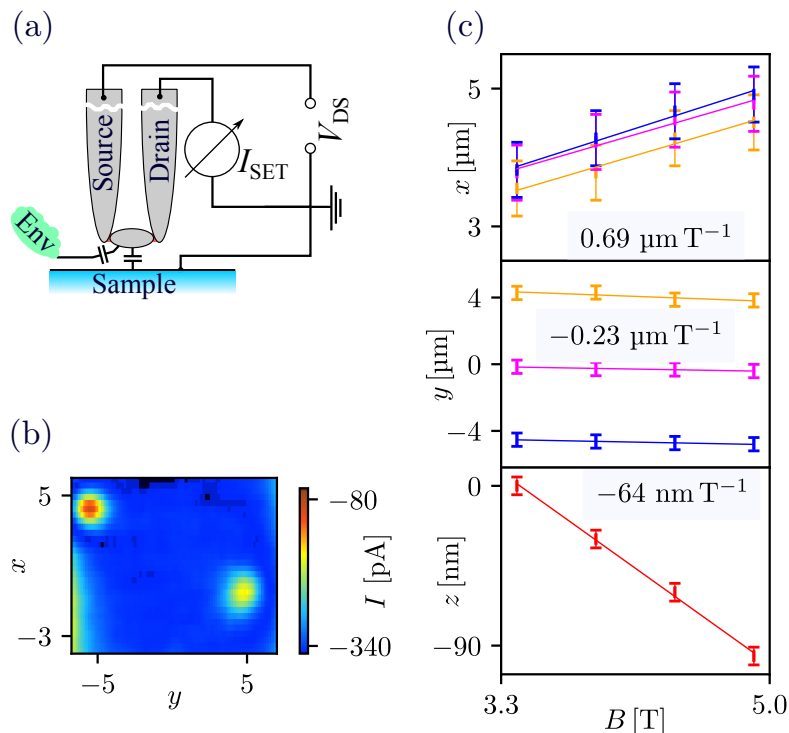


Figure 5.4: Determination of the position shift induced by B : The CBO method (a) is used to image a small area of the Hall bar. A false-color representation of $I_{SET3}(x, y)$, obtained during such a scan, is shown in (b) and shows two features which are tracked in position by three SETs for varying magnetic flux densities B . In (c) necessary corrections that are determined with three SETs (orange, magenta, blue) are given. Points with error-bars indicate the necessary correction - in all three spatial directions - for four values of B . The reason for the observed offset in the centered graph is, that SETs are shifted in y direction by $4 \mu\text{m}$ to each other, compare figure 4.7. In z direction only a common shift is necessary. Given values for a correction along one axis are obtained as mean of the corrections of all three SETs.

10 %. We conclude: with each cool-down of the microscope the spatial corrections with B have to be determined. Within following chapters of this thesis, these corrections will be done without explicitly mentioning them anymore.

5.4 DC feedback loop measurement technique

Until now, with the CBO method the SET was moved over a sample area while the oscillating SET current $I_{SET}(x, y)$ was measured, compare figure 5.3. During a scan, local changes of electrostatic conditions on the sample shift the electrostatic potential of the SET island (compare equation (5.3)) and consequently, the SET quasi-Fermi levels relative to the lead electrodes source and drain; I_{SET} is affected. Thus, the CBO method is especially sensitive to both: electrostatic potential variations ΔV_i and capacitive coupling changes ΔC_i , without distinguishing between

them. Furthermore, from the symmetrically oscillating I_{SET} it is not possible to extract information, whether a change is positive or negative.

Here, we present with means of figure 5.5 a DC FEEDBACK LOOP METHOD, short DC FBL method which was used already with SETs by Y. Wei [83], J. Hüls [84] and J. Weber [76] and applied in scanning probe experiments by M. Mausser [21]. The electrostatic potential of the SET island relatively to the source and drain leads determines the current I_{SET} through the SET. An electrostatic change $\Delta\Phi_{\text{isl}}$ leads to a current change ΔI_{SET} . In order to keep I_{SET} constant, a feedback loop is used to compare I_{SET} with a nominal value and in case of a deviation it applies a voltage commonly to the lead electrode potentials V_{D} and V_{S} . Thus, the relative position of V_{D} and V_{S} to the SET island potential Φ_{isl} is kept constant; they can change with respect to the reference ground potential, but not against each other.

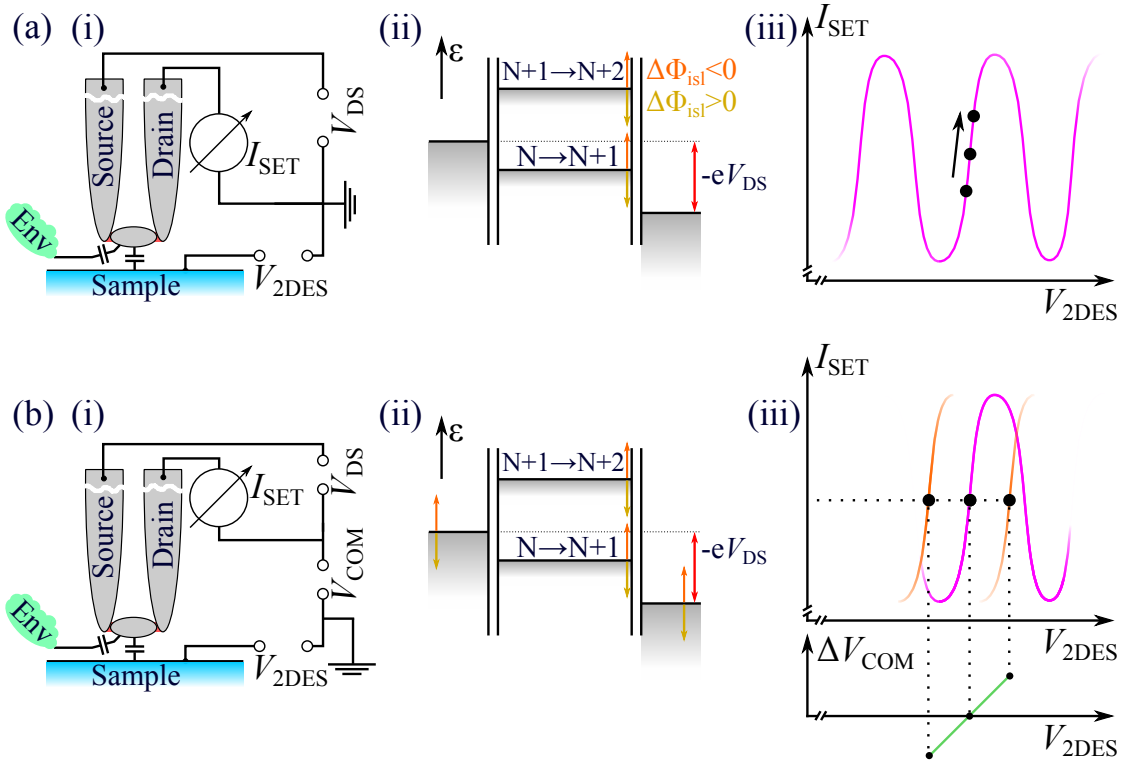


Figure 5.5: Illustration of the working principle of the DC feedback loop method: (a) The SET is operated in the CBO method (i), i.e. a change $\Delta V_{2\text{DES}}$ of the 2DES potential results in energetically up- or down-shifts of quasi-Fermi levels of the SET island (ii). As a result the current I_{SET} changes (iii); CBOs are observed. A statement whether the local $V_{2\text{DES}}$ changed positively or negatively is not possible without further assumptions. (b) A DC feedback loop is used (i), i.e. the measured I_{SET} is continuously compared with a target value $I_{\text{SET}}^{(\text{nom})}$ and in case of deviations, V_{COM} is tuned via a PID controller. Hence, the potential differences between SET island and lead electrodes stay constant (ii). With a change of $V_{2\text{DES}}$ the whole CBO characteristic is shifted, the current I_{SET} stays constant and ΔV_{COM} is directly proportional to $\Delta V_{2\text{DES}}$ (iii).

This is described as

$$\Delta\Phi_{\text{isl}} - \Delta V_{\text{S}} = 0 \quad \text{and} \quad \Delta\Phi_{\text{isl}} - \Delta V_{\text{D}} = 0, \quad (5.16)$$

$$\Delta\Phi_{\text{isl}} = \Delta V_{\text{S}} = \Delta V_{\text{D}} \equiv V_{\text{COM}}. \quad (5.17)$$

Hence, the electrostatic potential change of the island can be measured. In the following we assume only potential changes ΔV_i with constant capacitive couplings C_i and the source and drain potentials are changed commonly by V_{COM} . With results derived in equation (5.3) this leads to the general relation

$$\Delta V_{\text{COM}} = \left(\sum_{i \neq \{\text{S,D}\}} C_i \right)^{-1} \cdot \sum_{k \neq \{\text{S,D}\}} C_k \Delta V_k. \quad (5.18)$$

The summation is done over all electrodes, excluding the lead electrodes source and drain. In case only a local potential change ΔV_{2DES} of the underlying 2DES is considered, equation (5.18) can be simplified to

$$\Delta V_{\text{COM}} = \frac{C_{\text{2DES}}}{C_{\text{2DES}} + C_{\text{Stray}}} \Delta V_{\text{2DES}}. \quad (5.19)$$

Here C_{Stray} denotes remaining capacitive couplings to other electrodes than the 2DES, excluding source and drain. In case the SET island is in close proximity to the sample surface - and thus the 2DES - the capacitive coupling to the 2DES is dominant; C_{Stray} is neglectable. A change of the 2DES potential is directly mapped in a change of V_{COM} . The voltage V_{COM} is in the following also denoted as DC¹⁰ feedback signal.

Figure 5.6 illustrates the data of SET2 collected during an area scan over the Hall bar; the region is the same as already presented in figure 5.3. For the upper graph of figure 5.6 (a) the CBO method is used; variations of $I_{\text{SET2}}(x, y)$ indicate electrostatic changes as discussed in section 5.2. For the lower graph, the DC FBL method is used and the current I_{SET2} through the SET is fixed at a working point $I_{\text{SET2}}^{(\text{nom})}$. The value of this working point is determined by the highest slope in $\partial I_{\text{SET2}} / \partial V_{\text{2DES}}$, indicated in figure 5.5 (b,ii) and (b,iii). The necessary V_{COM} to keep this working point - and therefore, the shift of the electrostatic SET island potential - is shown in false-color representation in this lower graph of figure 5.6 (a).

In the center, a homogeneous DC feedback signal is observed, which results from a

¹⁰This supplement describes that V_{COM} is a dc voltage.

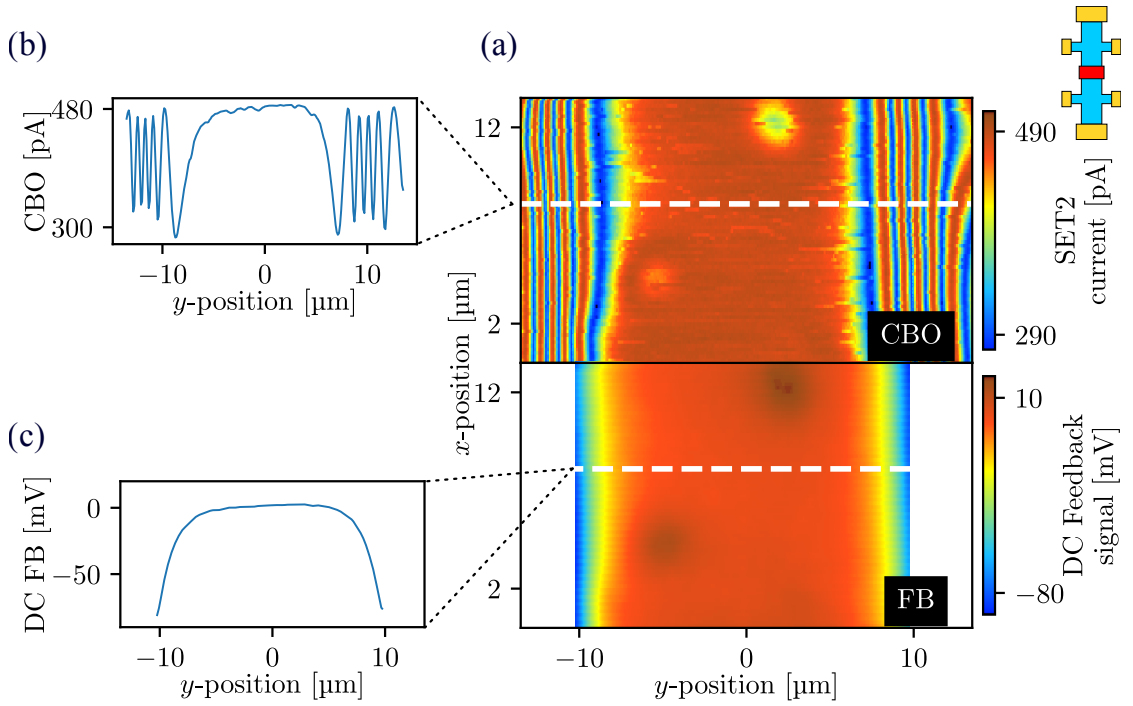


Figure 5.6: Area scan using SET2, once with the CBO method and once with the DC FBL method. (a) False-color representation of the CBOs (upper) and the DC feedback loop signal (lower), both as a function of the tip position in y direction and x direction, respectively. As ΔV_{COM} is technically limited, a smaller scan range in y direction had to be chosen for the FBL method to prevent jumps to the next CBO. (b) Line-cut through the CBO data along a line that shows no dielectric particles. Hall potentials will be probed in this region later on. An absence of SET current changes above the Hall bar indicates a homogeneous 2DES there. (c) Line-cut at the same x position as before, this time in the DC FBL signal. Now it can be stated that the potential decreases, when the Hall bar is left on the right or left side, respectively.

homogeneous 2DES there. This region is only interrupted by three round features where the SET island potential increases. The origin for those features are most probably dielectric photo-resist residuals on the sample surface that lead to a capacitive coupling change $\Delta C_{2\text{DES}}$ between the 2DES and the SET island, and thus, a change of Φ_{isl} . Leaving the Hall bar mesa (small/large y) a steep potential drop is observed. This drop can be seen more clearly in a line-cut along y , shown in figure 5.6 (c). Now, in contrast to the CBO method, the DC FBL method is able to distinguish between rising and dropping electrostatic sample potentials.

5.5 AC method to determine changes in capacitive coupling

The DC FBL method can be extended even further; by now the DC FBL signal gives information about both contributions, (1) electrostatic potential changes ΔV_i and (2) capacitive coupling changes ΔC_i , together. To determine Hall potential profiles, a separation of both contributions becomes unavoidable. In the following we present a method to track only changes of the capacitive coupling between SET and 2DES.

From equations (5.13) and (5.19) and discussions in section 4.2.5 it can be stated that higher capacitive couplings C_{2DES} to the 2DES lead to shorter CBO periods¹¹. That means: When the SET approaches the Hall bar surface, respectively the 2DES, more CBOs can be measured for a given voltage change ΔV_{2DES} . Consequently, the positive and negative slope $\Delta I_{SET}/\Delta V_{2DES}$ of a CBO becomes steeper. Thus, simply by determining the slope $\partial I_{SET}/\partial V_{2DES}$ at a fixed working point $I_{SET}^{(nom)}$, statements about the capacitive coupling to the 2DES can be made.

Necessary for this measurement method is an activated DC feedback loop - which was described in the previous section - to fix the current I_{SET} to its working point. Then, a change ΔV_{2DES} leads to a change ΔV_{COM} in the common voltage, compare equation (5.19). The slope is probed by modulating V_{2DES} with a small AC signal, given by

$$\Delta V_{2DES}(t) = \hat{V}_{2DES} \cdot \sin(\omega t). \quad (5.20)$$

With equation (5.19) the change ΔV_{COM} becomes time-dependent and can be expressed as

$$\Delta V_{COM}(\vec{r}, t) = \frac{C_{2DES}(\vec{r})}{C_{2DES}(\vec{r}) + C_{Stray}(\vec{r})} \Delta V_{2DES}(t). \quad (5.21)$$

Here, for generality it is assumed that the capacitive couplings have a position dependency. It is also assumed that ΔV_{2DES} is spatial invariant; this assumption is valid as the electrostatic potential of the Hall bar can be modulated commonly. Demodulating $\Delta V_{COM}(\vec{r}, t)$ at frequency ω using Lock-in technique yields an AC amplitude $\hat{V}_{COM}^{(AC)}(\vec{r})$ that depends on the spacial-dependent capacitive coupling to the 2DES, described by

$$\hat{V}_{COM}^{(AC)}(\vec{r}) \propto \frac{C_{2DES}(\vec{r})}{C_{2DES}(\vec{r}) + C_{Stray}(\vec{r})}. \quad (5.22)$$

¹¹It was shown that the CBO periodicity with a gate voltage V_i is e/C_i periodic.

The modulation of the 2DES with a small AC signal is denoted as AC FEEDBACK LOOP METHOD, short AC FBL method. Its working principle is illustrated in figure 5.7. It is a useful tool to track the capacitive coupling between the SET island and the 2DES. Together with the CBO method it can be used to position the SET array and approach to the 2DES.

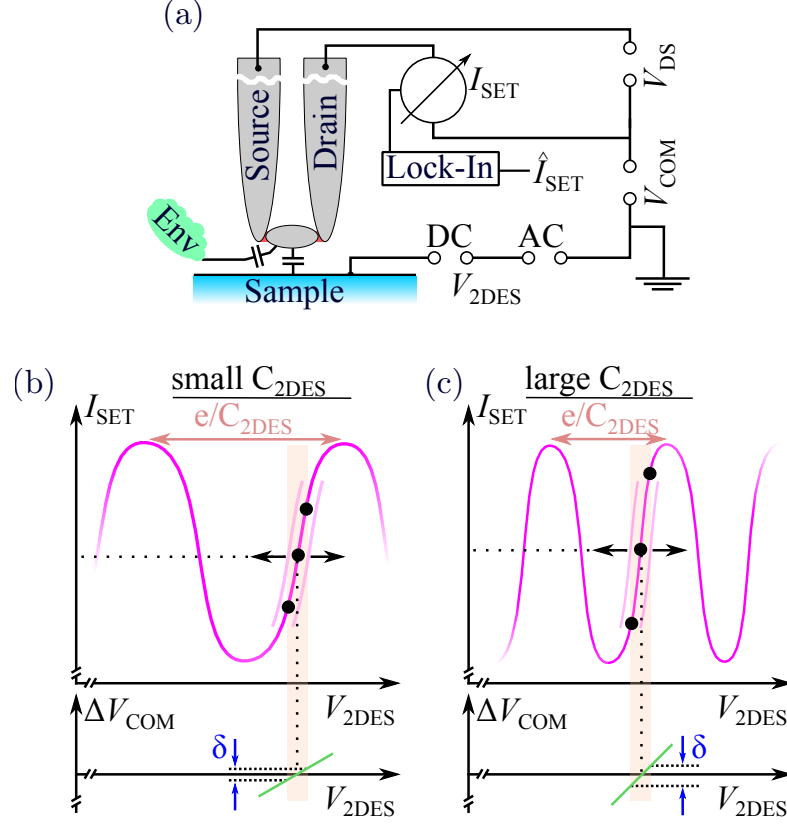


Figure 5.7: Working principle of the AC feedback loop method, with additional activated DC feedback loop. It makes use of the $e/C_{2\text{DES}}$ periodicity of the CBO with $V_{2\text{DES}}$, to determine $C_{2\text{DES}}$. (a) Schematic circuit diagram of this method: In addition to an active DC feedback loop, an AC signal is superposed on the 2DES potential $V_{2\text{DES}}$. (b) Case of a weak capacitive coupling from the 2DES on the SET island. A given change $\Delta V_{2\text{DES}}$ leads to a small current change ΔI_{SET} . Consequently, the DC feedback loop reacts with a potential change ΔV_{COM} to both lead electrodes, to keep I_{SET} constant. This reaction is proportional to the capacitive coupling $C_{2\text{DES}}$, see equation (5.19); hence, only a small change δ is measured with a Lock-in amplifier. (c) Same setup, but this time with a strong coupling $C_{2\text{DES}}$. The experimentally determined change δ is larger.

5.6 Dealing with charge instabilities of the SET

Later we use the SET array with both, activated DC feedback loop and additional AC feedback loop, to perform a scan above the Hall bar. Hereby, a scan over a sample cross-section needs several minutes. In this time it is very common that some non-periodic charge fluctuations in close proximity to the SET island may happen. Consequently, such fluctuations lead to time-limited but sudden changes of Φ_{isl} and thus, jumps in the DC feedback signal and the AC feedback signal¹². Moreover, all our AC measurements are performed at frequencies below 6 Hz to stay close to the DC regime. But, with such low frequencies the Lock-in has to demodulate signals which fall in the $1/f^\alpha$ noise regime. It is obvious, that low frequencies come hand-in-hand with higher noise levels, which leads to additional noise on the AC feedback signal.

Figure 5.8 shows in the upper panel the DC feedback signal, and in the lower panel the AC feedback signal (blue) obtained by demodulating the DC feedback signal; both are recorded over a defined time period. The DC feedback signal shows rectangular-shaped jumps coming from close-by rechargings, which are mostly correlated with high jumps in the AC feedback signal. A high background noise in the AC feedback signal - as discussed - is the result of low measurement frequencies.

For following Hall potential profile measurements, the noise level has to be reduced. One way to reduce it, is to measure the same cross-section of a Hall bar repeatedly N times and calculate the mean signal value. In this way, the amplitude of uncorrelated singular jumps from charge fluctuations are reduced to $1/N$, while the statistical background noise with zero mean is reduced [85, 86] to $1/\sqrt{N}$. The same AC feedback signal measured 24 times¹³ is superposed in the lower panel of figure 5.8 (magenta). The background noise appears reduced and high peaks are suppressed. Unfortunately, the measurement time to probe a single cross-section increases by a factor of N , making Hall potential measurements time consuming.

¹²The Fourier spectrum $\mathcal{F}(\omega)$ of a box function is proportional to $\sin(a\omega)/\omega$. Low frequencies are affected by sudden changes of the signal.

¹³This includes the data shown in blue as data-set #1, with 23 additional measurements.

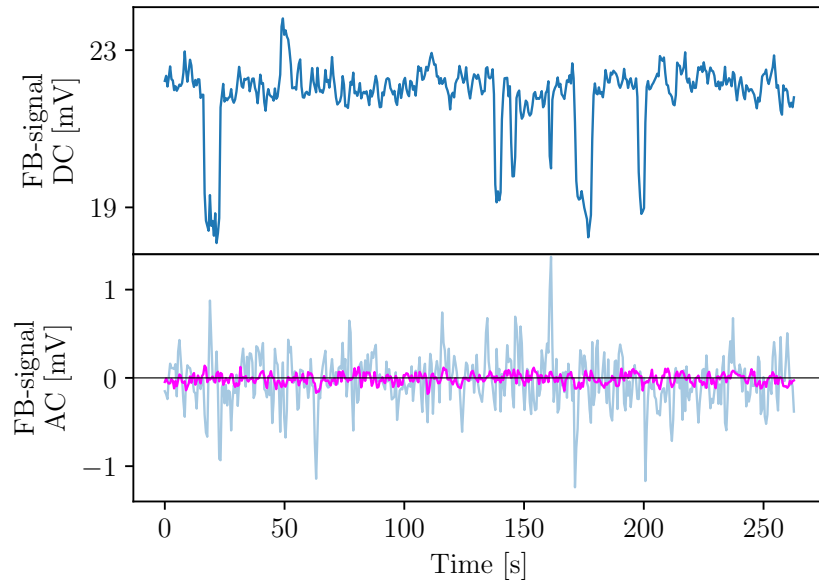


Figure 5.8: A repeated measurement of the same data set and a subsequent averaging is used to reduce (1) background noise and (2) singular peaks in the FBL signals. The data shown here is exemplary to illustrate this method and thus, measured against time instead of a spatial position. (upper) Shown is the DC feedback loop signal which is assumed to be constant under these measurement conditions. Charge fluctuations close to the SET island result in signal jumps. (lower) Signal jumps in the DC FBL signal result in peaks within the AC FBL signal, shown in blue. Repeated measurement of the same data set for 24 times and subsequent averaging leads to the data set shown in pink. The background noise is reduced by a factor of $\sqrt{24}$ and singular occurring peaks are suppressed by a factor of 24.

5.7 Get access to Hall potential profiles - two traces (α and β) have to be measured

To extract Hall potential profiles with the previously mentioned measurement methods is more complicated, see also [21]. An externally biased current through the Hall bar leads to potential changes $\Delta V_{2DES}(\vec{r})$ which are now position-dependent. The former derived equation (5.21) describing the AC feedback loop signal $\Delta V_{COM}(\vec{r}, t)$ has to be adapted to

$$\Delta V_{COM}(\vec{r}, t) = \frac{C_{2DES}(\vec{r})}{C_{2DES}(\vec{r}) + C_{Stray}(\vec{r})} \Delta V_{2DES}(\vec{r}, t). \quad (5.23)$$

Hence, the demodulated AC amplitude signal depends on both contributions, the position-dependent capacitive coupling and now also the position-dependent potential distribution, described as

$$\hat{V}_{COM}^{(AC)}(\vec{r}) \propto \frac{C_{2DES}(\vec{r})}{C_{2DES}(\vec{r}) + C_{Stray}(\vec{r})} \cdot V_{2DES}(\vec{r}). \quad (5.24)$$

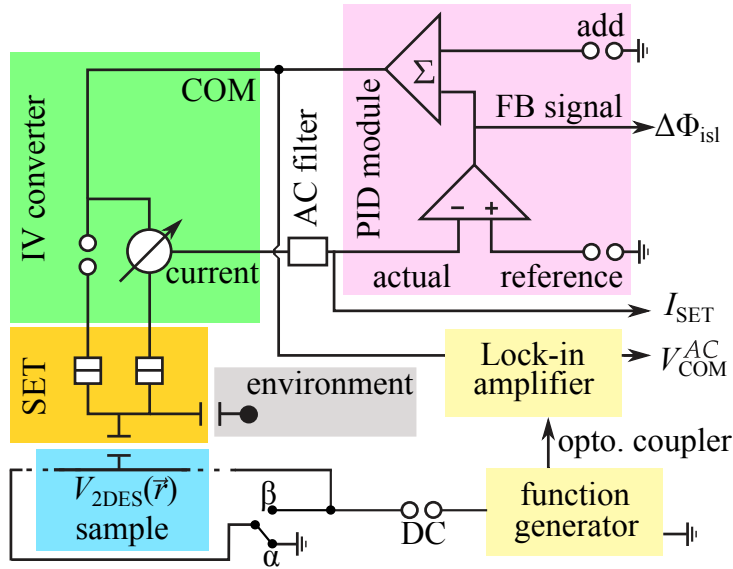


Figure 5.9: Circuit diagram showing the measurement principle to obtain both traces, α -trace and β -trace, to determine the Hall potential profile. During the α -trace an AC voltage is applied to the Hall bar resulting in a current flow. During the β -trace an AC voltage is applied commonly to the Hall bar which leads to a potential change but not to a current flow. Adapted from [21].

Therefore, a single measurement of $\hat{V}_{\text{COM}}^{(\text{AC})}(\vec{r})$ is not sufficient to extract the local Hall potential distribution $V_{2\text{DES}}(\vec{r})$. It is still weighted by a prefactor including the position-dependent capacitive couplings. To get rid of this prefactor two measurements will be performed¹⁴, schematically sketched in figure 5.9. In addition to an activated DC feedback loop for the SET, a small AC signal is applied either commonly to the Hall bar or only to one contact of the Hall bar. The demodulated DC feedback loop signal gives:

1. An α -trace denoted measurement, where an externally voltage bias on the Hall bar leads to a position-dependent Hall potential distribution $V_{2\text{DES}}(\vec{r})$. The AC amplitude is given by

$$\hat{V}_{\text{COM}}^{(\text{AC},\text{SD})}(\vec{r}) = \frac{C_{2\text{DES}}(\vec{r})}{C_{2\text{DES}}(\vec{r}) + C_{\text{Stray}}(\vec{r})} V_{2\text{DES}}(\vec{r}). \quad (\alpha\text{-trace}) \quad (5.25)$$

2. A so-called β -trace without external current. Here, both Hall bar contacts source and drain are commonly modulated to achieve a position-independent potential variation with a demodulated amplitude of

$$\hat{V}_{\text{COM}}^{(\text{AC},\text{COM})}(\vec{r}) = \frac{C_{2\text{DES}}(\vec{r})}{C_{2\text{DES}}(\vec{r}) + C_{\text{Stray}}(\vec{r})} V_{2\text{DES}}. \quad (\beta\text{-trace}) \quad (5.26)$$

Through a division of the data obtained from the α -trace by the data from the β -trace, the capacitive prefactor vanishes. The result is a position-dependent and

¹⁴A comparable method is also mentioned in [7, 12, 16].

5.7. Get access to Hall potential profiles - two traces (α and β) have to be measured

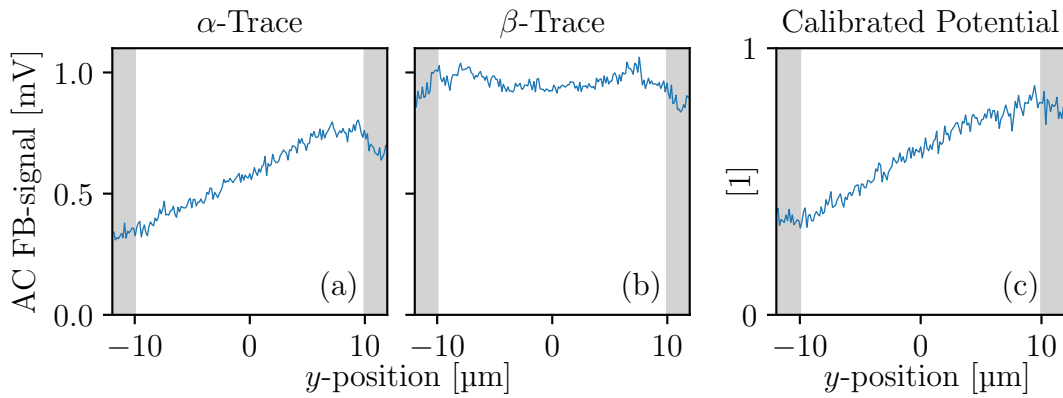


Figure 5.10: Two-step measurement method to determine a Hall potential profile: Firstly, during an α -trace (a), the voltage V_{DS} applied to the source contact of the Hall bar is periodically switched on and off, while the drain contact has constant ground potential. In this way the externally biased current through the Hall bar is modulated. Secondly, during a β -trace (b) both, source and drain contact, are commonly modulated with V_{DS} . No external current flow is induced into the Hall bar, but the 2DES potential changes periodically. (c) A division of the α -trace by the β -trace results in the calibrated Hall potential profile $\tilde{V}_{2DES}(\vec{r})$. Its spans ranges always between 0 and 1. In case of a dissipative resistance in series to the scanned 2DES position, the full span of 1 is not obtained.

CALIBRATED HALL POTENTIAL PROFILE¹⁵ $\tilde{V}_{2DES}(\vec{r})$ that is normalized by the oscillation amplitude V_{2DES} ,

$$\frac{\Delta V_{COM}^{(AC,SD)}(\vec{r})}{\Delta V_{COM}^{(AC,COM)}(\vec{r})} = \frac{V_{2DES}(\vec{r})}{V_{2DES}} \equiv \tilde{V}_{2DES}(\vec{r}). \quad \text{(Calibrated potential)} \quad (5.27)$$

Figure 5.10 shows - for a Hall bar cross-section - an exemplary measurement¹⁶ of the AC feedback signal, that is obtained by demodulating the DC feedback loop signal. The 2DES filling factor is $\nu = 0.89$, when B already left the quantum Hall plateau $\nu = 1$ on the higher magnetic field side and is between $\nu = 1$ and $\nu = 2/3$. In figure 5.10 (a) the α -trace is shown; the Hall bar is biased with a source-drain voltage, resulting in an externally biased current flow. The AC FBL signal increases from left to the right. Regions colored in gray indicate that the Hall bar is left; a signal drop can be observed. In figure 5.10 (b), the externally bias of the Hall bar is removed, but the Hall bar potential is commonly varied to measure the β -trace. In this case, the AC FBL signal is almost constant, while it drops when the Hall bar is left. In accordance to equation (5.27) a division of both traces yields the calibrated Hall potential distribution, compare figure 5.10 (c). In this measurement it shows a linear increase over the Hall bar width.

¹⁵In the following the term "Hall potential profile" refers always to the "calibrated Hall potential profile" if not stated differently.

¹⁶The modulation frequency for this and all subsequent measurements of Hall potential profiles in this thesis is chosen to be 1.283 Hz when not mentioned differently.

5.8 Extract the current density distribution from Hall potential profiles

The question that should be answered at the end of this thesis is: Where does the externally biased current flow in a 2DES under fractional quantum Hall conditions? Equation (2.16) which was introduced in section 2.4 connects the local current density j_x with a local Hall voltage drop $E_y = \partial V_{\text{Hall}}(y) / \partial y$ via

$$j_x = \nu \frac{e^2}{h} E_y \propto \frac{\partial}{\partial y} V_{\text{Hall}}(y). \quad (5.28)$$

Hence, in figures 3.1 and 3.4, a local current density can be found at positions where the color changes (e.g. from blue to green). As the false-color representation of measurement data may be misleading sometimes, depending on the chosen color-set, we introduce here a new method to present positions of externally biased current densities $j_x(y)$. The calibrated Hall potential profile $\tilde{V}_{2\text{DES}}(y)$ determined in the former section and shown in figure 5.10 is further processed. The following steps are performed, compare also figure 5.11: (1) As it is possible to have series resistances to the measured 2DES area, calibrated potentials $\tilde{V}_{2\text{DES}}(y)$ may differ from the whole span $0 \leq \tilde{V}_{2\text{DES}}(y) \leq 1$, as already observed in the calibrated Hall potential of figure 5.10. To ensure comparable results¹⁷, that are independent of such prefactors, all calibrated Hall potential profiles are first normalized by

$$\tilde{V}_{2\text{DES}}^{(\text{norm})}(y) = \gamma \cdot (\tilde{V}_{2\text{DES}}(y) - \xi), \quad (5.29)$$

while $\gamma = \left(\max(\tilde{V}_{2\text{DES}}(y)) - \min(\tilde{V}_{2\text{DES}}(y)) \right)^{-1}$ is a scaling factor describing the amount of series dissipation and $\xi = \min(\tilde{V}_{2\text{DES}}(y))$ is an offset shift. Then, (2) the first derivative

$$j_x^*(y) = \frac{\partial}{\partial y} \tilde{V}_{2\text{DES}}^{(\text{norm})}(y) \propto j_x(y), \quad (5.30)$$

of the normalized Hall potential profile with respect to the y direction is determined via a Savitzky-Golay filter¹⁸. The result is directly proportional to the current density $j_x(y)$. Afterwards, (3) the derivative $j_x^*(y)$ is plotted in a false-color representation with a monotonous color set to indicate local current densities; brighter regions correspond to higher current densities.

¹⁷Without normalization, the current density in equation (5.28) is weighted by a scaling factor γ . Thus, a comparison of derivatives, especially in false-color representation would be misleading, as the absolute maximum values would differ.

¹⁸A second order Savitzky-Golay filter with a window size of 31 points is chosen.

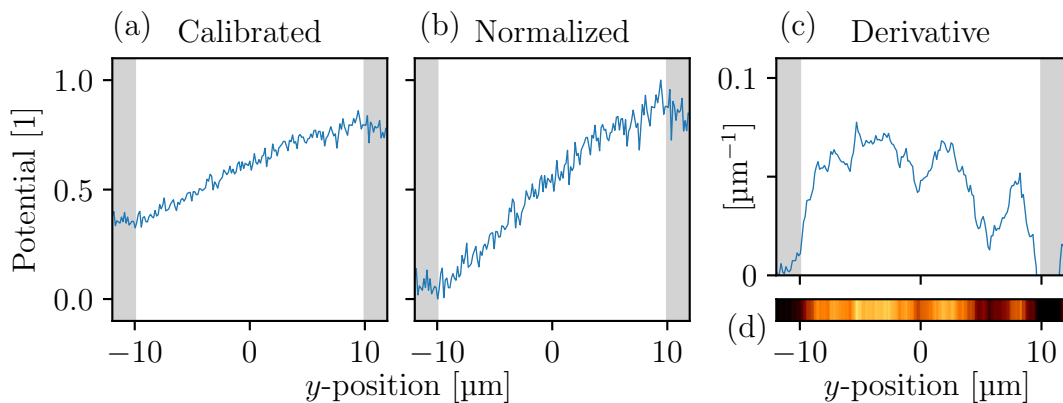


Figure 5.11: Necessary steps to derive a signal that is proportional to the local current density j_x . (a) The calibrated Hall potential profile $\tilde{V}_{2DES}(y)$ determined at filling factor $\nu = 0.89$, see section 5.7 and figure 5.10. This is the starting point in this analysis. (b) Equation (5.29) is used to calculate the normalized Hall potential profile $\tilde{V}_{2DES}^{(norm)}(y)$, spanning the whole range between one and zero. (c) With use of a Savitzsky-Golay filter the derivative $\partial\tilde{V}_{2DES}^{(norm)}(y)/\partial y$ is calculated; it is proportional to the local current density j_x . (d) False-color representation of the derivative that is shown in (c). Bright regions indicate high local current densities j_x .

5.9 Summary

In this chapter the measurement technique to probe Hall potential profiles of a 2DES and to extract information about the local current density were introduced step-by-step.

In the beginning, possible electrostatic influences on the SET island potential Φ_{isl} were discussed; namely a local potential change, charge accumulation, height differences and dielectric particles.

Afterwards, different SET operation methods were shown, while each new method is based on already introduced ones, with some new additions. Firstly, the Coulomb-blockade oscillation (CBO) method was introduced. The SET is operated with a constant bias voltage V_{DS} on its working point that gives always a non-zero SET current I_{SET} with highest CBO amplitude. Secondly, a DC feedback loop was discussed, which keeps the difference between the Fermi levels of the SET island and of the lead electrodes constant by using a PID controller that compares continuously the current I_{SET} through the SET with a nominal value. In case of deviations a voltage V_{COM} is commonly applied to the lead electrodes. Hence, I_{SET} is fixed and ΔV_{COM} gives information whether the change in $\Delta\Phi_{isl}$ was positive or negative. With a commonly applied voltage to both Hall bar lead electrodes, the demodulation of the DC feedback loop signal gives an AC feedback signal which can be used to probe the CBO steepness $\partial I_{SET}/\partial V_{2DES}$ and thus the capacitive

coupling between the SET island and the 2DES.

Further, we saw that a data set obtained during a scan has to be measured N times in order to reduce the noise in the AC FBL signal; background noise is reduced by a factor of \sqrt{N} , while singular events are smaller by a factor of N .

In a next step, the demodulated DC FBL signal was used in a two-step measurement technique to achieve position-dependent Hall potential profiles: (1) An externally biased current flows through the 2DES; this measurement is referred to as α -trace. In a second measurement, (2) no external voltage difference is applied, but the 2DES potential is modulated commonly; this is the β -trace. A division of both yields a purely position-dependent, calibrated Hall potential profile without any influences of capacitive couplings or fixed charges - as ions between 2DES and SET island or on the sample surface.

In a last step, these calibrated potentials were normalized and the derivative with respect to the scan direction was calculated. In this way the information about local current densities j_x can be extracted. This ensures a comparable pseudo-3d false-color representation of the data.

In the following chapter, Hall potential profiles in the integer quantum Hall regime are systematically measured and compared to former measurements of Peter Weitz and Erik Ahlswede.

Chapter 6

Hall Potential Profiles Acquired in the Integer Quantum Hall Regime

The introduced scanning single-electron transistor array microscope is a quite new development in our group. It was built-up by Marcel Mausser [19] during his diploma thesis in 2012. Afterwards he moved the cryostat with the microscope into the Precision Laboratory and demonstrated its functionality. Finally he probed Hall potential profiles in a magnetic field range covering the integer filling factor $\nu = 4$ [21].

The main focus of this chapter is to investigate the Hall potential profiles at further integer filling factors. Hereby, the magnetic field changes between subsequent measurements are chosen small to get an insight into the evolution of these Hall potential profiles with B . Firstly, obtained Hall potential profiles at filling factor $\nu = 2$ are compared to older data of Ahlswede *et al.*, which were already presented in chapter 3; they were obtained at 1.4 K. At the end of this chapter, Hall potential profiles of IQH plateaus $\nu = 3$ and $\nu = 1$ are presented and compared to quantum Hall profiles of even integer filling factors. With the older scanning probe microscope these filling factors were not accessible, due to the smaller possible magnetic field range, and due to higher operation temperature. Consequently, this will be the first time the Hall potential profile evolution will be probed for these ν .

For all following Hall potential profiles in this thesis, the distance between SET island and sample surface is in the range of 50 nm to 200 nm. Hereby the intrinsic work function difference between SET island and 2DES is compensated as good as possible using a method described in [21]. An exemplary potential mismatch of 50 mV in this distance would lead to a change of the electron density n_{2D} in the range of about 2% to 0.6%, when a plate capacitor arrangement - valid as distances are comparable to or smaller than SET island dimensions - is assumed.

6.1 Hall potential profiles around Landau level filling factor $\nu = 2$

Before we try to probe Hall potential profiles in the fractional quantum Hall regime, a crucial point is to demonstrate that the new single-electron transistor array setup yields comparable results to the old scanning electrostatic force microscope. Only in this case, statements about further Hall potential measurements are reliable.

The measurements here are performed in a mostly homogeneous area close to the probing contacts, compare inset in figure 6.1. One SET is used to probe the Hall potential profiles in a cross-section of the Hall bar which does not show any dielectric particles or inhomogeneities.

The AC signal that is applied to the Hall bar during the α -trace and β -trace is rectangular shaped with a peak-to-peak amplitude of $V_{\text{DS}}^{(\text{pp})} = 2 \text{ mV}$, a DC offset of $V_{\text{DS}}^{(\text{dc})} = 1 \text{ mV}$ and a frequency of 1.283 Hz. This AC configuration is chosen in order to (1) ensure only changes between the bias voltage off-state and on-state during the α -trace, (2) that there is no external current flow I_x during the off-state, and (3) to avoid a changing current direction and intermediate current values¹.

Figure 6.1 shows the Hall resistance R_{xy} and the longitudinal resistance R_{xx} for a magnetic field sweep over filling factor $\nu = 2$. Obviously, R_{xy} shows a well pronounced quantum Hall plateau with constant resistance value $h/2e^2$ which is indicated by a horizontal gray line. The fact that R_{xx} deviates in the higher magnetic field side of the plateau in R_{xy} from zero can be understood by an inhomogeneous 2DES along the Hall bar length. A measurement of R_{xx} is more sensitive to dissipation along the Hall bar, compare also section 3.7. The observed deviation means: In some regions quantum Hall conditions are not fulfilled anymore, and thus plateau $\nu = 2$ is locally already left there; dissipation occurs in these regions.

Hall potential profiles are probed every 50 mT in a magnetic flux range between 3.6 T and 4.85 T that is larger than the plateau regime, highlighted in orange within figure 6.1.

In figure 6.2, the Hall potential profiles obtained for different magnetic flux densities B , respectively filling factors ν , in the vicinity of the integer filling factor $\nu = 2$ are presented. Here, figure 6.2 (a) shows selected Hall potential profiles taken at a

¹All Hall potential profiles presented in this thesis are probed in this configuration if not stated differently.

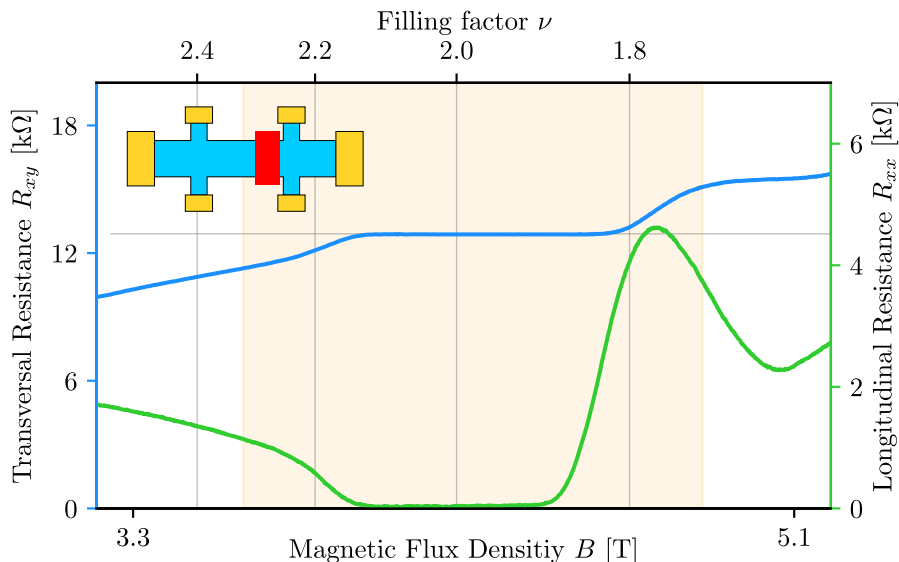


Figure 6.1: Hall resistance R_{xy} (blue) and longitudinal resistance R_{xx} (green) during a magnetic field sweep over filling factor $\nu = 2$. A well pronounced plateau of R_{xy} in B is observed, while R_{xx} drops to zero. Hall potential profiles are probed in a Hall bar region, close to probing contacts, as indicated by a red rectangle in the inset.

variety of filling factors ν as function of the SET tip position. An offset is added to each profile, shifting them relatively to each other to make them comparable within a single graph. Each profile is labeled by the corresponding filling factor. A color-coded representation of all probed Hall potential profiles is shown in figure 6.2 (b). This representation is chosen to get comparable graphs as introduced by Erik Ahlswede, shown in figure 3.1. Also shown in figure 6.2 (b) is our new representation of the data - the current density $j_x^*(y)$. Hall potential profiles shown in figure 6.3 are results of Ahlswede *et al.* [54] (already shown in figure 3.1) and used for comparison reasons here. In figure 6.2 (a) the following can be observed:

1. At high magnetic flux densities (compare $\nu = 1.77$ and $\nu = 1.82$) which are outside of the QH plateau, a linear Hall voltage drop across the Hall bar width is observed.
2. Towards higher ν we enter the QH plateau at the higher magnetic field side. The voltage drop becomes non-linear. It starts to occur only in the bulk region, compare $\nu = 1.84$ and $\nu = 1.86$, and the overall Hall voltage drop rises.
3. At $\nu = 2$ the voltage drop happens in the bulk of the sample and not at the sample edges.
4. Exceeding $\nu = 2$ leads to a smooth transition of the Hall potential profile from an almost linear drop over the bulk (e.g. $\nu = 2.09$) to pronounced drops

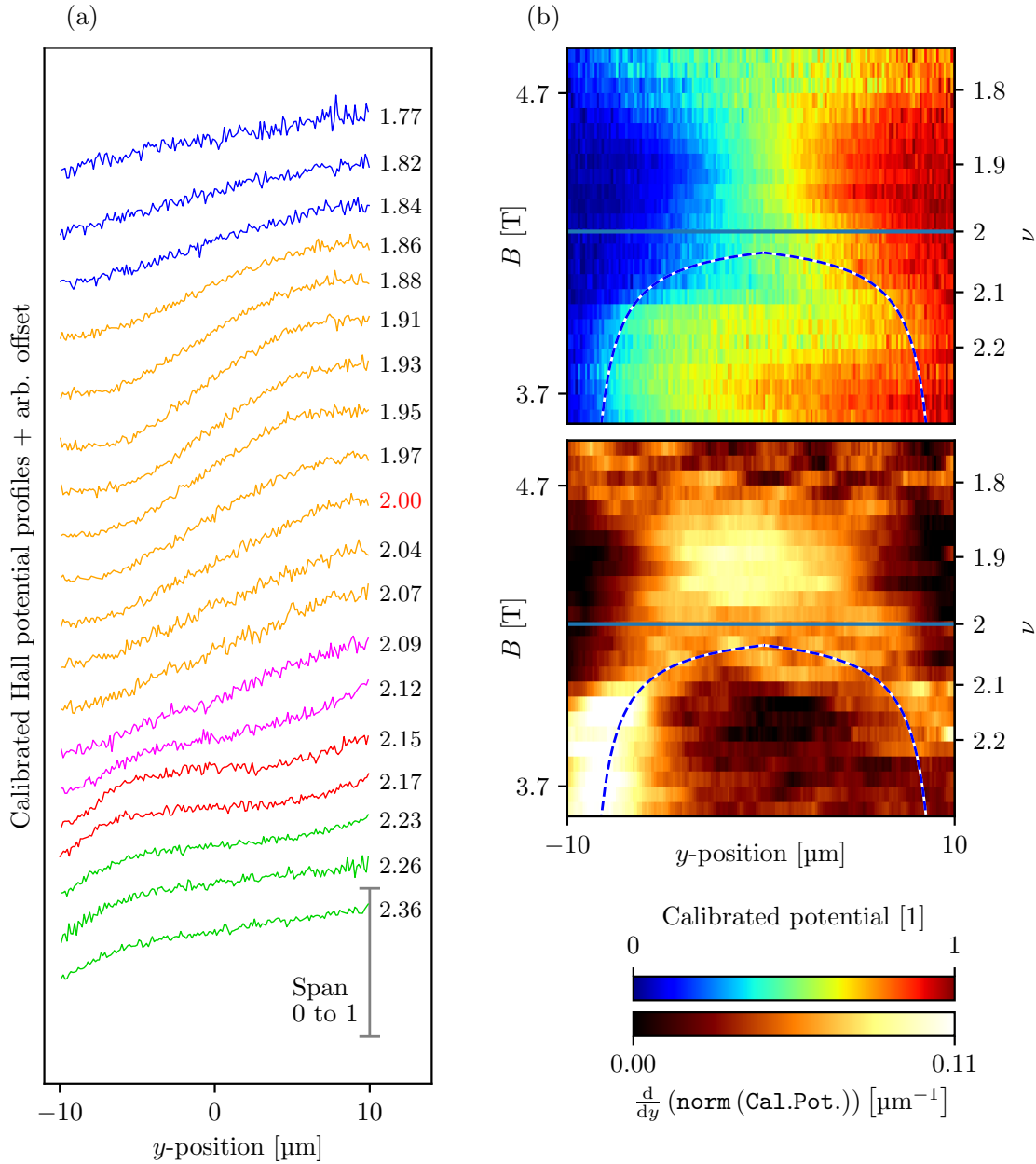


Figure 6.2: Hall potential profiles $\tilde{V}_{2DES}(y)$ obtained with the scanning-single electron transistor array microscope in the vicinity of integer filling factor $\nu = 2$. (a) Selected potential profiles of the magnetic flux range that includes the quantum Hall plateau. The profiles are plotted as a function of tip position y and separated by an offset to enhance the readability. Linear and non-linear drops can be identified. Different Hall regimes are indicated by the line color. In the classical Hall regime (blue) the Hall voltage drops linearly. The edge-dominated QH regime (red) is characterized by pronounced Hall voltage drops close to the sample edges and a flat bulk region, whereas the bulk-dominated QH regime (orange) shows no voltage drop at the edges, but only in the bulk region. (b) (upper) False-color representation of all measured Hall potential profiles $\tilde{V}_{2DES}^{(\text{norm})}(y)$ versus the tip position y and the magnetic flux density B . A similar evolution as in [12, 54] is observed. The calculated center position of $\nu = 2$ incompressible stripe is overlaid as dashed line. The position of the Hall voltage drop follows this line. (lower) The local current density $j_x^*(y)$ is calculated from data shown above. Here, positions of high current densities move with the center position of the incompressible stripe.

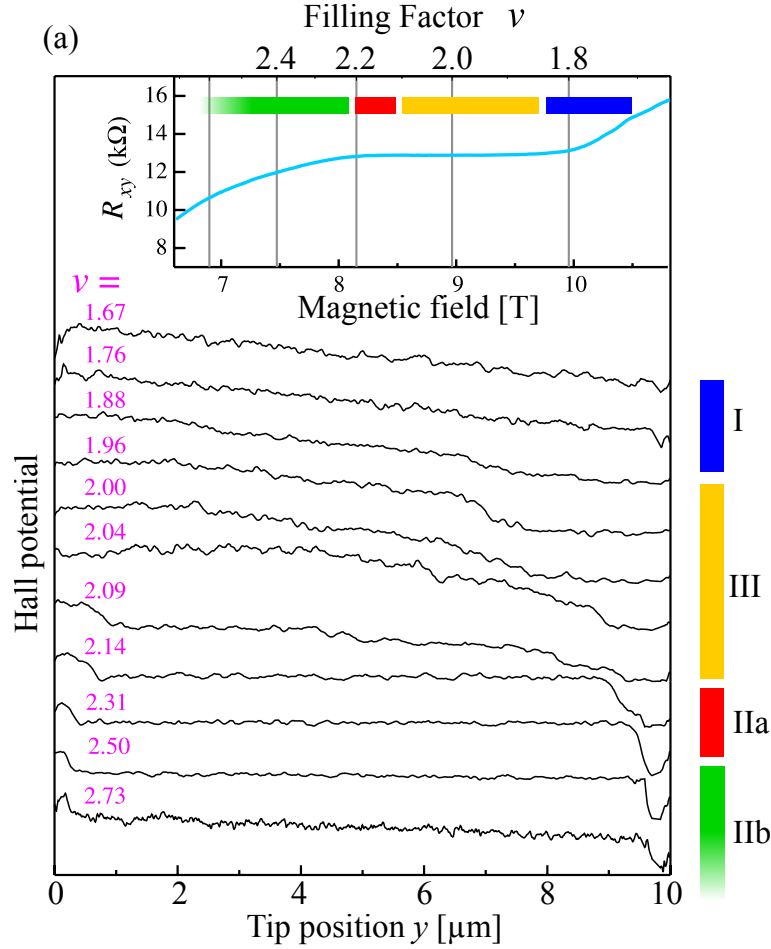


Figure 6.3: Hall potential profiles obtained by Peter Weitz and Erik Ahlswede around integer filling factor $\nu = 2$ with a scanning probe microscope operated at 1.4 K. Four different types of profiles can be observed - linear and non-linear ones. The Hall voltage drop happens at different spatial positions. Adapted from [54].

at both Hall bar edges ($\nu = 2.17$). The overall Hall voltage drop becomes already smaller, indicating dissipation along the sample.

5. Leaving the QH plateau for higher ν results in a smooth transition of the Hall potential back to a linear drop.

Compared with figure 6.3 similar Hall potential profiles can be identified. Obtained profiles with our microscope are colored accordingly to their type in figure 6.3. The evolution in the false-color representation has similarities with figure 3.4. The dashed line indicates the center position of the incompressible stripe with $\nu = 2$ calculated² with (3.2). High current densities seem to appear at expected positions of incompressible regions, compare section 3.2. Two things can be identified: (1) For small values of B in the plateau, a current flow close to the Hall bar edges is observed, and (2) in the high magnetic field range of the plateau a current flow only in the bulk is present.

²For this sample the calculated stripe positions are slightly shifted by 500 nm into the bulk.

But there are also differences between the old measurements and our new data. Most obvious, the Hall voltage drop close to the sample edges in figure 6.2 (e.g. at $\nu = 2.17$) are not that steep as observed in figure 6.3 (e.g. at $\nu = 2.14$). This may have three reasons: (1) The electron density in both samples differs by more than a factor of 2, and (2) the depth of the 2DES in both samples differs by a factor of 3, and (3) the tip sample distance is more than twice times larger in our case. In the following subsections these influences are explained more in detail.

Smaller electron density leads to a dome like profile of $n_{2D}(y)$

The charge carrier density in the sample which is investigated within this thesis has a charge carrier density of $n_{2D} = 2.05 \times 10^{15} \text{ m}^{-2}$ (compare section 4.6), while samples investigated by Erik Ahlswede typically had $n_{2D} = 5.7 \times 10^{15} \text{ m}^{-2}$ [12].

A reduced value of n_{2D} leads to an increased screening length d_0 of electrons towards electric fields, compare section 3.2. Such fields are present towards the sample edges, as the concentration of electronic surface states which are charged is spatially increased there. The etched surface is responsible for this increase. This leads to an electron density profile which increases smoother from the edge towards the bulk, see figure 6.4. A more "dome-like" profile is expected for the sample investigated here.

In section 3.2 it is discussed that the width a_ν of an incompressible stripe depends on this screening length d_0 ; smaller values of n_{2D} lead to an increased d_0 and thus, to wider incompressible stripes.

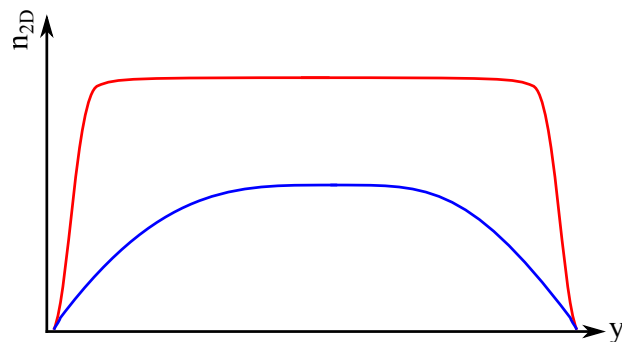


Figure 6.4: Expected electron density profile $n_{2D}(y)$ for two different samples: (red) Erik Ahlswede's sample with an electron density $n_{2D} = 5.7 \times 10^{15} \text{ m}^{-2}$ and (blue) our sample with $n_{2D} = 2.05 \times 10^{15} \text{ m}^{-2}$. A smaller n_{2D} leads to an increased screening length of surface states which have a higher spatial concentration close to the sample edges. Hence, for our sample we expect a dome-like electron density profile. The smaller n_{2D} , the smoother the increase of n_{2D} from the edges towards the bulk and the wider the incompressible stripes.

Increased tip-2DES distance leads to spatially widening of features

In figure 6.2, positions with a high current density match with the center position of the calculated incompressible stripes. But, the extension in y direction of these regions still seems larger than expected from calculations in section 3.2. To understand this spatial extensions, an ideal potential change between V_1 and V_2 is assumed, see sketch in figure 6.5. Assuming an absence of other electrodes, the electric field lines form semicircles centered at the position of the potential change (green). Some equipotential lines are indicated in colors - from blue to red.

Now, an SET is moved in a height of z along the y direction over the potential change. Dependent on z , the SET crosses equipotential lines with large or small changes Δy . In the limit of $z = 0$, all equipotential lines are crossed in a singular point, more precisely, the transition point between V_1 and V_2 . For higher scan distances z , the region to cross the same equipotential lines becomes wider. Consequently, the potential change between V_1 and V_2 appears spatially wider.

Weber *et al.* [76] calculated how a defined potential change ΔV would appear in a distance z during a scan. The change $\Delta y_{10\%,90\%}$ from 10 % to 90 % of ΔV as function of z is described by

$$\Delta y_{10\%,90\%}(z) = \left(\tan(0.1 \cdot 180^\circ)^{-1} - \tan(0.9 \cdot 180^\circ)^{-1} \right) \cdot z \approx 6.2z. \quad (6.1)$$

Hence, for different scan distances z , even steep potential changes ΔV within small Δy appear 6.2 times wider. For scan distances of 50 nm, the measured potential

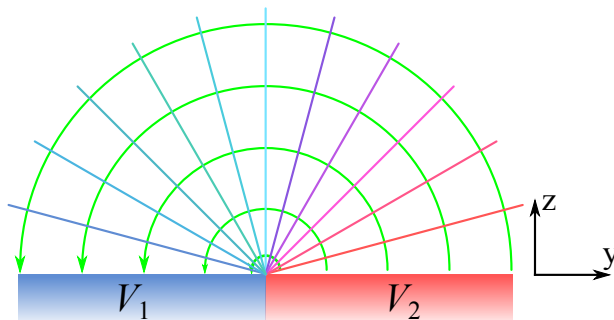


Figure 6.5: Schematic illustration to explain a spatial extension of sudden potential changes with the unavoidable scan distances between SET island and 2DES, picture idea from [76]. Electric field lines (green) have semicircular trajectories with origin at the potential jump, while equipotential lines (blue to red) are fan-shaped, with the same origin. It can be calculated [76] that in a given distance z a potential jump between 10 % to 90 % is seen within a width Δy of $6.2z$. This fact is even more important, as in real samples, the 2DES is buried under the surface.

change has a width of already 310 nm. Thus, small distances to the sample surface are favorable. Referring to the heterostructure we investigate during this thesis, the 2DES is buried 120 nm below the sample surface. Thus, even for zero scan distance between SET island and sample surface, a potential change appears already spatially widened to about 740 nm. In addition, the larger scan distance between SET island and sample surface further enhances this effect.

With regard to experimentally determined Hall potential profiles and local current densities this means: The buried 2DES in combination with a finite scan distance leads to spatially widened potential drops. Thus, statements about the absolute width of incompressible stripes are not easily possible. On the other hand, the y position of the measured potential change is not affected by an increased distance z . Hence, independent of this spatial widening, the center position of experimentally determined Hall voltage drops is valid. Consequently, the argumentation that the Hall voltage drop, respectively regions of high local current densities, follows the center position of incompressible stripes is valid.

6.2 An overall increased Hall voltage drop indicates decreased dissipation along the sample

In the previous section we saw that the height of the overall Hall voltage drop changes within the probed magnetic field range. In this section this observation is discussed more quantitatively. In accordance to section 5.8, the calculation of the current density involves the rescaling of all Hall potential profiles to span the full range between zero and one. This is done via equation (5.29) and includes a scaling factor γ .

We recap: The calibrated Hall potential profile is calculated via a division of the α -trace by the β -trace, what results in the fraction $V_{2DES}(\vec{r})/V_{2DES}$, compare equation (5.27). During the β -trace no externally biased current flows through the sample. Hence, no voltage drop along the sample and wires is expected. This changes in case of the α -trace: An external current is biased which leads to a voltage drop over each series resistance - these resistances can be wires, contacts or electrically compressible 2DES regions. The full bias voltage cannot be detected anymore.

If the Hall voltage drop at the position that we probe with the SET is equal to the entire applied bias voltage, then there is no dissipation along the Hall bar as there are no series resistances present to the probed 2DES cross-section. The

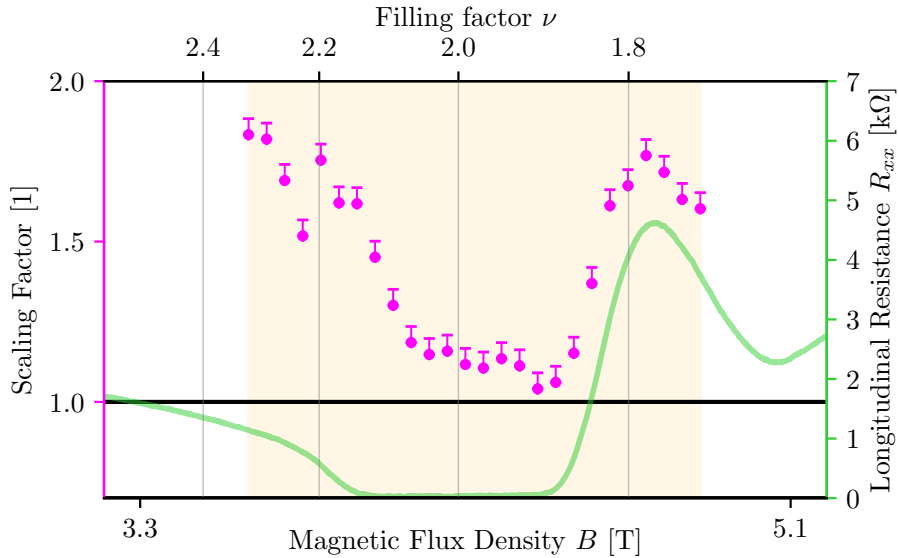


Figure 6.6: Scaling factor γ necessary to renormalize the Hall potential profiles to span the full range between 0 and 1 is shown in magenta. Noise and peaks on the Hall potential profiles may lead to smaller values γ ; hence, the shown values are lower limits. The corresponding longitudinal resistance R_{xx} is also included. The orange region gives the magnetic flux range where Hall potential profiles are probed. Values $\gamma > 1$ indicate dissipation in series to the position where the SET performed line-scans. The following things can be observed: (1) Outside of the quantum Hall plateau (compare also figure 6.1) dissipation happens. (2) As R_{xx} goes to zero, also γ approaches a value around 1. (3) A difference in B is observed, where $\gamma \approx 1.1$ and $R_{xx} = 0$ is observed. This can be caused by 2DES regions between Hall bar lead electrodes and probing contacts. This region is not probed by R_{xx} . (4) It stays always above $\gamma = 1$ what indicates a constant series resistance, e.g. coming from the wiring or contact resistances. (5) The end of R_{xx} determines also the position where γ rises again.

calibrated Hall potential profile would span the complete range between zero and one. In case there are series resistances the scaling factor γ becomes larger than 1. Values below 1 are not expected for γ .

Figure 6.6 shows determined values for γ (pink dots) together with the longitudinal resistance R_{xx} (green). Again, the orange highlighted region indicates the magnetic field range that is probed. The following can be observed: (1) Outside of the quantum Hall plateau (compare also figure 6.1) γ is always larger than 1. The sample is entirely compressible and dissipation happens along its length. (2) When R_{xx} decreases - from the lower magnetic field range towards the plateau - also γ drops. Values of about 1.1 are observed within the region where R_{xx} is zero. In this regime an increasing amount of current is carried dissipationless within incompressible regions with $\nu = 2$, leading to the drop of γ . (3) The magnetic flux density B , where $\gamma \approx 1.1$ and $R_{xx} = 0$ is observed, does not coincide in the lower magnetic field range. This may happen as the 2DES regions between Hall bar lead electrodes and probing contacts is not probed by R_{xx} . An increased electron

density within these regions and consequently, the appearance of incompressibility at higher B in these regions could explain this difference. (4) γ stays always above 1 what indicates series resistances which do not vanish. It can be assumed that these may be the wiring and ohmic contact resistances. (5) When R_{xx} increases towards the higher magnetic field side of the plateau, also γ rises. This is expected; R_{xx} is an integral observable which probes the 2DES between the probing contacts arranged along the Hall bar. When incompressibility is continuously lost, the current flow rearranges into compressible regions where dissipation takes place.

6.3 First Hall potential profiles around $\nu = 3$ and $\nu = 1$

Now we probe Hall potential profiles around integer filling factors which were not accessible in earlier works - either due to higher temperatures or limited magnetic field ranges. Measurements presented here are performed in the same spatial region as before, indicated in the inset of figure 6.1.

Figures 6.7 and 6.8 depict Hall potential profiles for $\nu = 1$ and $\nu = 3$, respectively. In both cases, subfigure (a) shows selected Hall potential profiles as a function of the tip position y , probed at different values B . In (b) all Hall potential profiles are shown in a false-color representation versus both, B and y , together with the resulting current density $j_x^*(y, B)$. The center positions of the corresponding incompressible stripes are overlaid as dashed line. An increased noise level for $\nu = 3$ is the direct result of a decreased number of averaging repetitions N , compare section 5.8. For $\nu = 3$ the current direction is reversed what explains mirrored Hall potentials.

First of all, it seems obvious that the evolution of both Hall potential profiles is comparable to $\nu = 2$ which was presented in section 6.1. The following is valid for both filling factors: (1) Hall potential profiles probed far from the integer value i - with ($\nu < i$) - show a linear Hall voltage drop. They can be identified as type I profiles. (2) Lowering the magnetic flux density, respectively increasing ν , the Hall voltage drop becomes non-linear; a distinct drop in the bulk region with no drop at the sample edges is observed (type III profiles). This behavior changes when $\nu > i$, as the Hall voltage drop smoothly separates from the bulk into two pronounced drops, one towards each sample edge (type IIa profiles). Mainly no potential change happens in the sample bulk. Leaving the QH plateau at the lower magnetic field side ($\nu \gg i$) leads to a recovering of the linear Hall potential profile

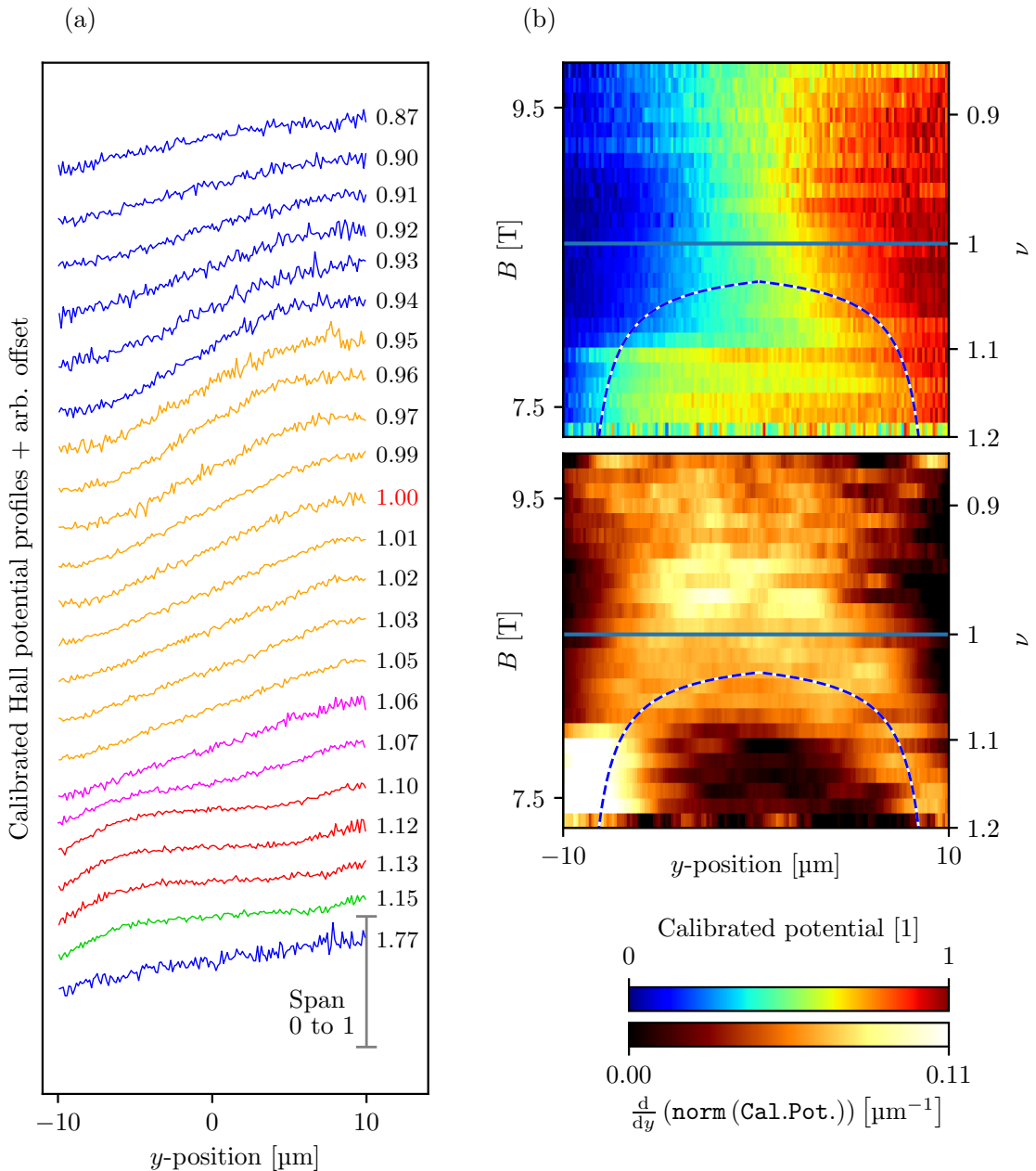


Figure 6.7: Hall potential profiles $\tilde{V}_{2\text{DES}}(y)$ probed around integer quantum Hall state $\nu = 1$. (a) Selected Hall potential profiles, colored by their type in accordance to section 3.6. (b, upper) False-color representation of all (normalized) Hall potential profiles $\tilde{V}_{2\text{DES}}^{(\text{norm})}$ probed in this magnetic field range. (b, lower) Obtained current density $j_x^*(y, B)$. Bright signals indicate a high local current density. Overlaid in both plots are the integer filling factor $\nu = 1$ (solid line) and the center position of the $\nu = 1$ incompressible stripe (dashed line).

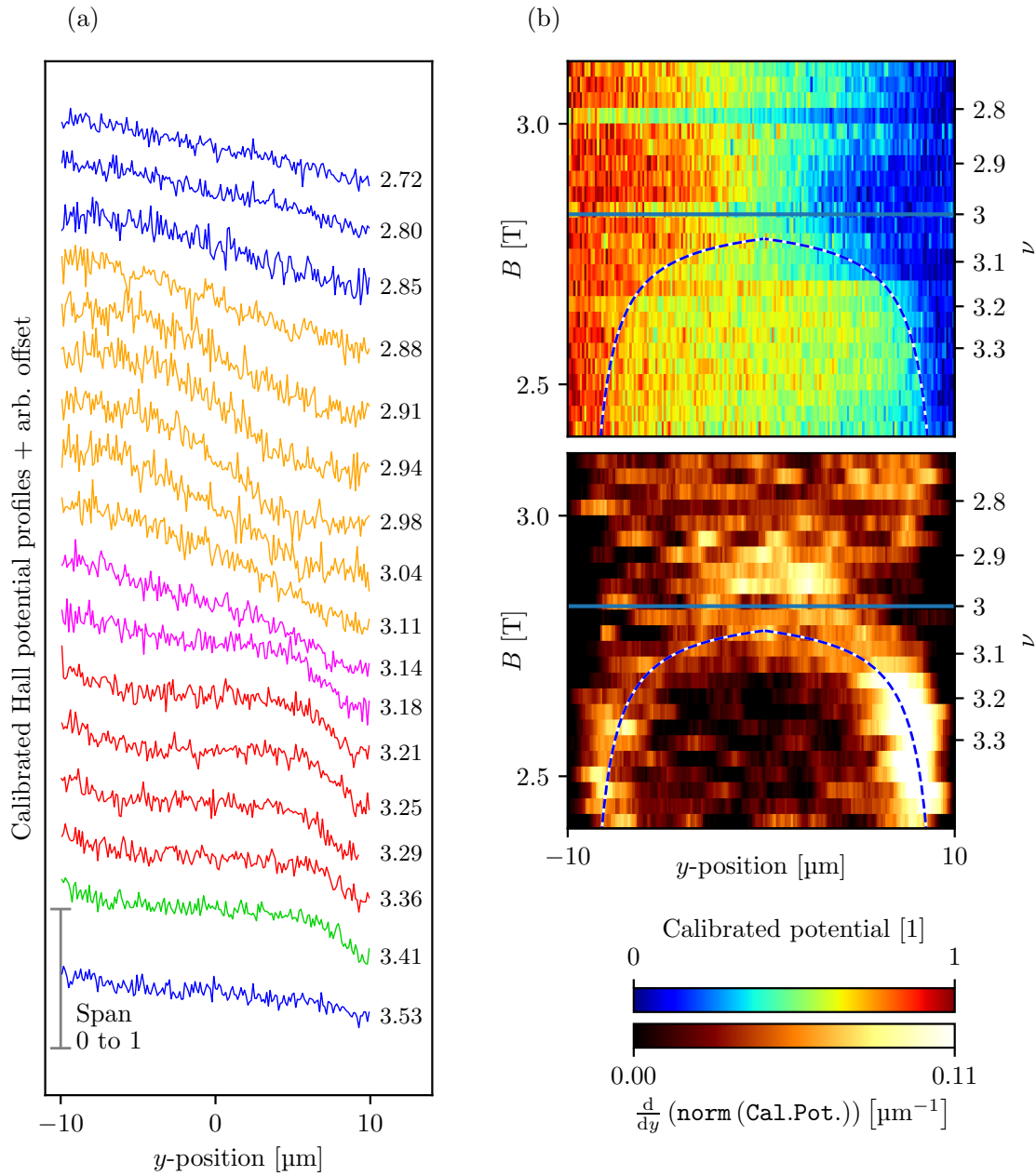


Figure 6.8: Hall potential profiles $\tilde{V}_{\text{2DES}}(y)$ probed around integer quantum Hall state $\nu = 3$. (a) Selected Hall potential profiles plotted versus position y . (b) False-color representation of all (normalized) Hall potential profiles $\tilde{V}_{\text{2DES}}^{(\text{norm})}$, and the current density as a function of y and B .

within a long magnetic field range (type I profiles).

Further, the false-color plots in (b) show in both cases: The position of the Hall voltage drop³ follows the calculated center position of the $\nu = i$ incompressible stripe. Consequently, positions with high current densities are equal to incompressible stripe positions.

6.4 Summary

At the beginning of this chapter, the single-electron transistor array microscope was used to perform systematic measurements of Hall potential profiles. Their evolution with respect to magnetic flux changes were investigated for the integer filling factor $\nu = 2$. This QH plateau has already been investigated in the past by Ahlswede *et al.* [12, 54] using a scanning electrostatic force microscope. All potential profiles and the evolution of the Hall voltage drop, which they observed, could also be identified within our measurements. First measurements of odd filling factors $\nu = 3$ and $\nu = 1$, which were not accessible till now, showed a similar evolution. Figure 6.9 summarizes the obtained results.

Deviations, especially in the slope of the Hall voltage drop close to the sample edges were explained by two influences: (1) A smaller electron density leads to an increased screening length against electric fields, which are present towards etched sample edges. This leads to a broadening of incompressible stripes as introduced in section 3.2. (2) It was demonstrated that a finite distance z between SET island and buried 2DES leads to a spatial widening of experimentally observable Hall voltage drops. A defined change from 10% to 90% of the potential change has a minimum width in y of about $6.2z$ [76]. Nevertheless, the center position of measured potential changes is not affected by z .

In the end, it was demonstrated that local measurements of Hall potentials also yield information about dissipation. Within the QH plateau $\nu = 2$ the detected dissipation evolution follows mainly the evolution of R_{xx} , as expected.

³At these positions a color change happens, either from red to green or green to blue.

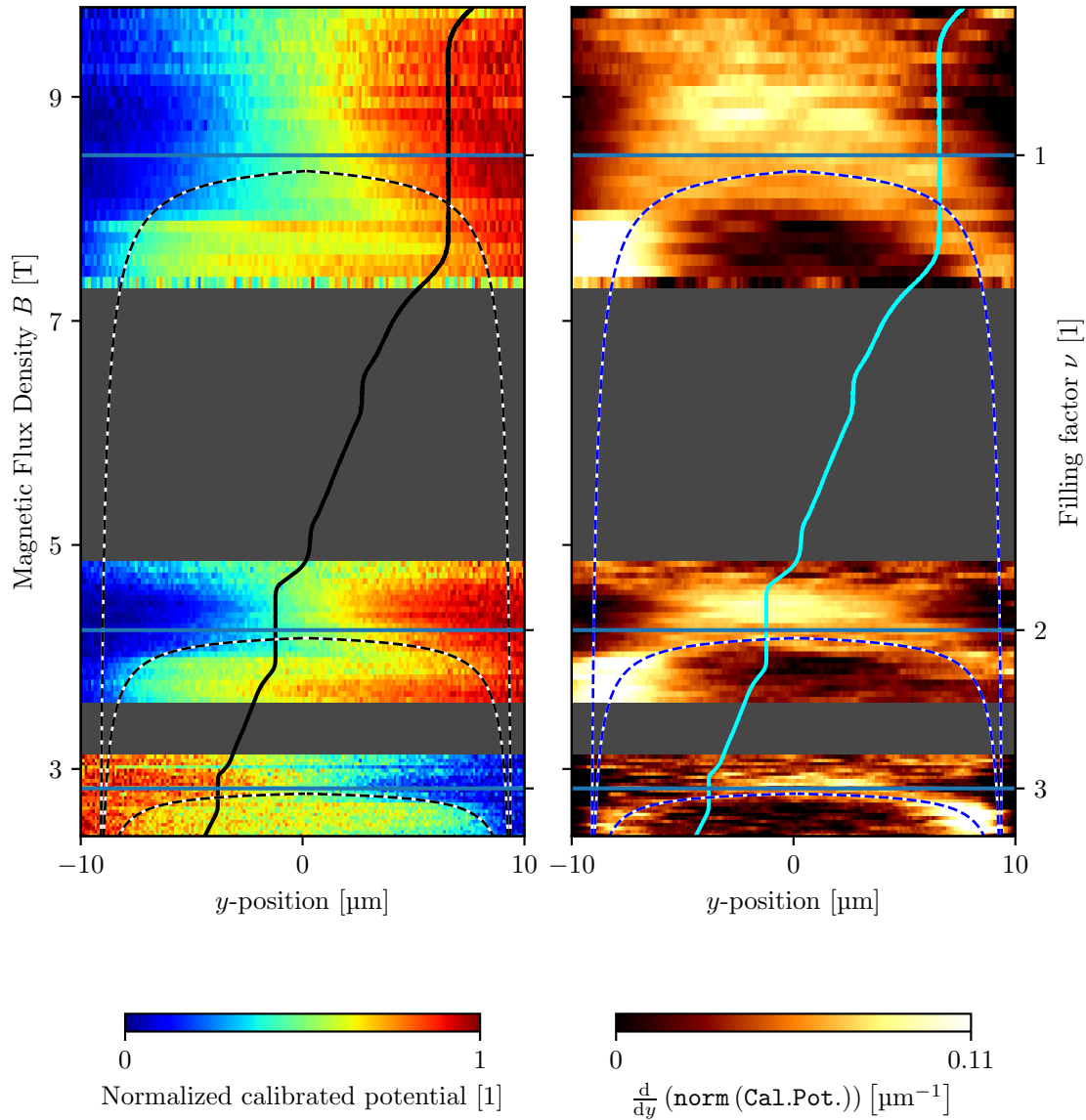


Figure 6.9: False-color representation of Hall potential profiles $\tilde{V}_{2DES}^{(norm)}(y, B)$ (left) and local current densities $j_x^*(y, B)$ (right) with changing magnetic field in the vicinity of integer filling factors $\nu = 1$, $\nu = 2$ and $\nu = 3$. In dashed, the calculated center position of corresponding incompressible stripes with integer filling factor is overlaid. The solid line going into direction of B shows the measured Hall curve from figure 4.11. The evolution from the classical Hall regime into the edge-dominated and bulk-dominated QH regime is similar to measurements of Ahlswede *et al.* and in agreement with the microscopic picture of the IQHE. For quantum Hall plateaus with integer filling factor ν , current densities are located at regions of the ν incompressible stripe.

Chapter 7

Hall Potential Profiles in the Fractional Quantum Hall Regime

Former chapters have prepared us for measurements which are presented in this chapter: Very first measurements of current-induced Hall potential profiles in the fractional quantum Hall regime.

Firstly, transport measurements, more precisely an investigation of the breakdown behavior of the FQHE is performed to get first hints about the microscopic distribution of the external current flow. Results from this measurement also define the bias voltage applied to the Hall bar in following scanning experiments.

Secondly, Hall potential profiles are probed and compared with ones obtained in the integer quantum Hall regime, before the effect of a reversed current direction is experimentally determined. Then an evolution of these Hall potential profiles with changing magnetic flux densities is probed by our scanning single-electron transistor array microscope. Here, the main focus lies on the fractional QH state $\nu = 2/3$. Area scans reveal the current density distribution resolved in both spatial directions. This gives an insight into the homogeneity of this evolution along the sample.

Afterwards, possible influences of an increased bias voltage on Hall potential profiles are probed. Information obtained here enable us to probe a second fractional quantum Hall state, the $\nu = 3/5$ state.

This chapter shows first the experimental results which are then discussed in the end together to get an insight into the underlying physical mechanisms causing these observations.

7.1 Breakdown behavior of the fractional quantum Hall state $\nu = 2/3$

In a first step, we probe the fractional quantum Hall state $\nu = 2/3$, using conventional electrical characterization measurements. The longitudinal resistance $R_{xx}(B)$ and the Hall resistance $R_{xy}(B)$ are determined as described in section 2.2, while the magnetic flux density B is swept. This measurement is repeated for different bias voltages V_{DS} applied to the Hall bar.

For equidistantly recorded bias voltages $0.5 \text{ mV} \leq V_{\text{DS}} \leq 5 \text{ mV}$, $wR_{xx}(B)$ and $R_{xy}(B)$ are shown in figure 7.1. The longitudinal resistance is normalized by the constant Hall bar width w . For small bias voltages, a wide range of magnetic flux densities B shows a vanishing R_{xx} . This indicates stable quantum Hall conditions for $\nu = 2/3$ between the longitudinal probing contacts. For higher V_{DS} , a deviation from $R_{xx} = 0$ is observed; especially in the lower magnetic field range.

The simultaneously recorded Hall resistance R_{xy} , plotted in the middle graph, shows in B a well pronounced fractional quantum Hall plateau with filling factor $\nu = 2/3$ and a weakly pronounced $\nu = 3/5$ quantum Hall plateau. The lower graph illustrates the derivative $\partial R_{xy}(B)/\partial B$. Regions with a value of zero correspond to a vanishing slope in $R_{xy}(B)$, and thus a Hall resistance plateau. It is obvious, that the $R_{xy}(B)$ plateau extension in B depends on the applied bias voltage; smaller V_{DS} lead to wider plateaus in B . For higher bias voltages, the shrinking of the plateau region is more pronounced in the lower magnetic field range compared to the higher magnetic field side.

A two-dimensional measurement is performed to determine the evolution of the quantum Hall breakdown with V_{DS} more in detail. $R_{xx}(B, V_{\text{DS}})$ is measured for more bias voltages V_{DS} and magnetic flux densities B . The results are depicted in figure 7.2. The normalized longitudinal resistance $wR_{xx}(B, V_{\text{DS}})$ is shown color-coded. An intentionally small chosen dark color range presents regions of vanishing R_{xx} , respectively stable quantum Hall conditions. The following is observed:

1. Around the fractional state $\nu = 2/3$ dark regions are observed. Hence it is well pronounced along the Hall bar¹. In contrast, zero resistance states in the fractional state $\nu = 3/5$ are only rudimentary developed; it may be observable in distinct regions between the probing contacts, but not over the whole Hall bar length.
2. For $\nu = 2/3$ an asymmetry in the electrically induced breakdown behav-

¹This statement is valid between the probing contacts.

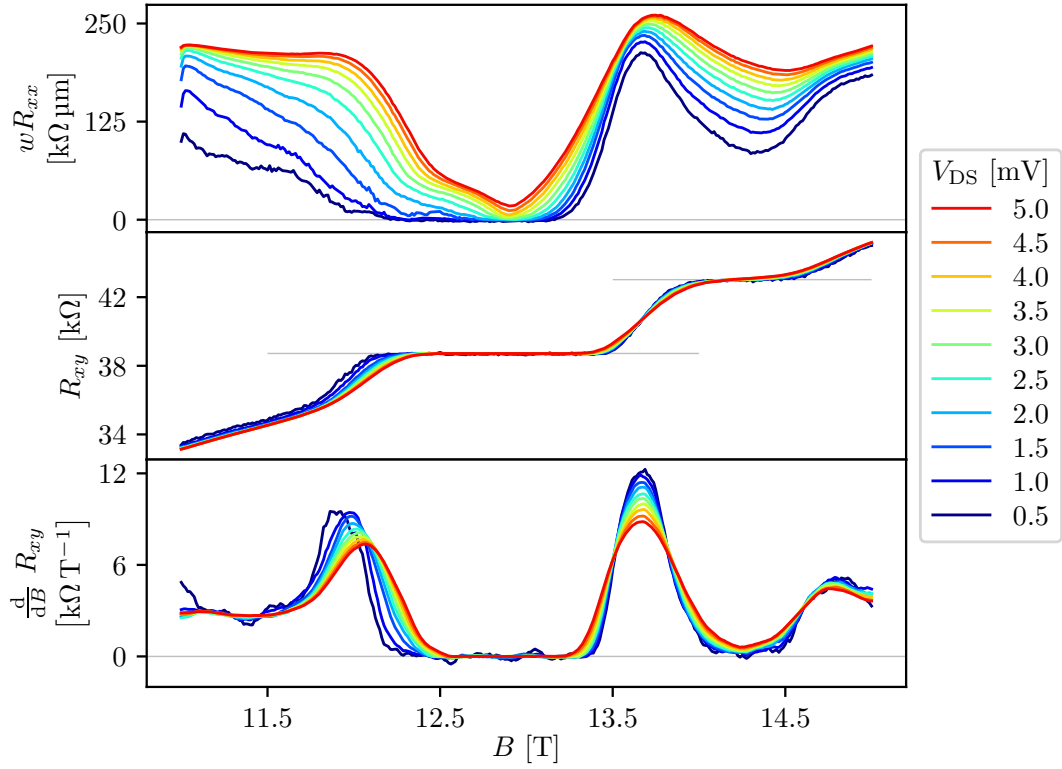


Figure 7.1: Hall measurements in a magnetic field range, including the fractional quantum Hall states $\nu = 2/3$ and $\nu = 3/5$ for different bias voltages V_{DS} . (upper) Normalized longitudinal resistance $w \cdot R_{xx}$. (middle) Hall resistance R_{xy} . (lower) Calculation of the derivative $\partial R_{xy}/\partial y$. A Hall plateau is characterized by a zero slope.

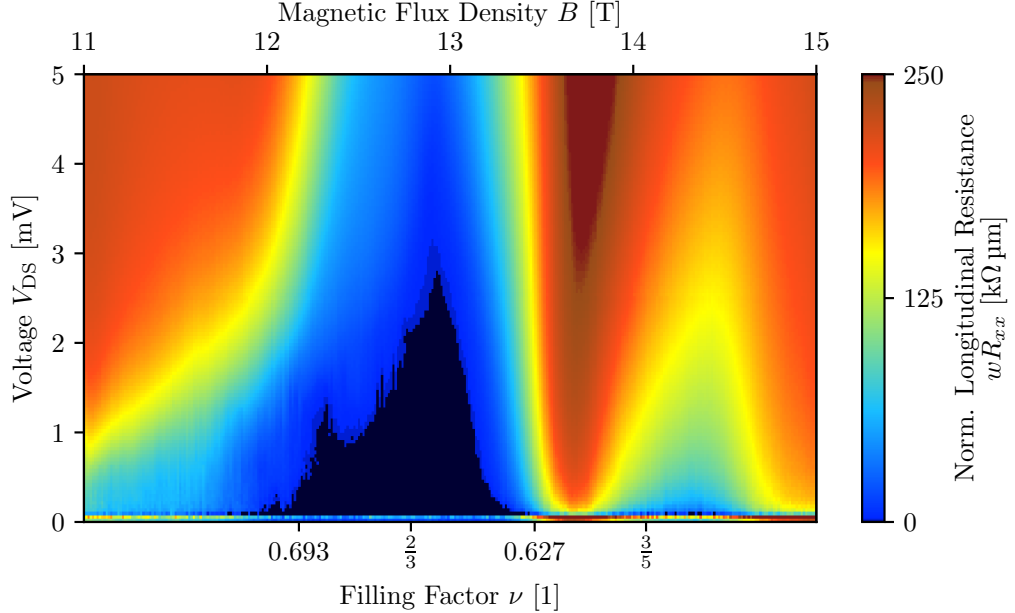


Figure 7.2: Longitudinal resistance R_{xx} normalized with the sample width w , as a function of both, the magnetic flux density B in vicinity of fractional filling factor $\nu = 2/3$, and the applied bias voltage V_{DS} . Dark blue regions represent vanishing values R_{xx} and thus, a stable QHE in the whole region between probing contacts. An asymmetry between low- and high magnetic fields around $\nu = 2/3$ can be observed. A similar behavior was formerly observed and discussed with means of figure 3.9 in the integer quantum Hall effect.

ior between the low-magnetic field side and the high-magnetic field side is present. For small magnetic fields, the breakdown threshold increases with increasing magnetic flux densities. For ν slightly below filling factor $\nu = 2/3$ it is most stable, before a sudden drop of the threshold voltage is observed. After the drop, only a small zero resistance region remains before the dark region completely vanishes towards higher magnetic fields.

3. When the breakdown threshold has its peak value, the fractional QH state is expected to be stable in most regions of the sample. As this happens at a slightly higher magnetic flux density B , respectively smaller filling factor ν than $\nu = 2/3$, this could indicate regions in the sample with a slightly higher n_{2D} .
4. The observed breakdown behavior of the $\nu = 2/3$ state seems to be similar to breakdown measurements in the integer quantum Hall regime, which were shown for $\nu = 2$ in figure 3.9 [66]. On the other hand, a comparison yields, that the maximum threshold voltage is at least 50 times smaller for $\nu = 2/3$ compared with $\nu = 2$. A different energy gap that protects each state may explain this observation; in case of $\nu = 2$ a cyclotron gap is present, while for $\nu = 2/3$ an energy gap is opened by the electron-electron interaction.

These transport measurements indicate the following: The lower magnetic field side of the $\nu = 2/3$ fractional quantum Hall state is more fragile against high bias voltages V_{DS} , than the center region of the quantum Hall plateau and the high magnetic field side of the plateau. In the following the applied bias voltage should not exceed $V_{DS} = 2 \text{ mV}$ to have QH conditions with $R_{xx} \approx 0$.

7.2 First Hall potential profiles in the $\nu = 2/3$ fractional quantum Hall state

One of the main goals of this thesis is to probe Hall potential profiles in the fractional quantum Hall regime in order to state, where the externally biased current flow is located. Transport measurements in the former section already indicated an asymmetry between low magnetic field side and high magnetic field side of the QH plateau. In this and the following sections, the scanning single-electron transistor array microscope is used to probe locally the Hall voltage drop.

In figure 7.3 the Hall resistance R_{xy} and the longitudinal resistance R_{xx} is shown for a magnetic field sweep over two fractional filling factors, $\nu = 2/3$ and $\nu = 3/5$. R_{xy} shows with a value of $h/(2/3 e^2)$ a well pronounced quantum Hall plateau; it

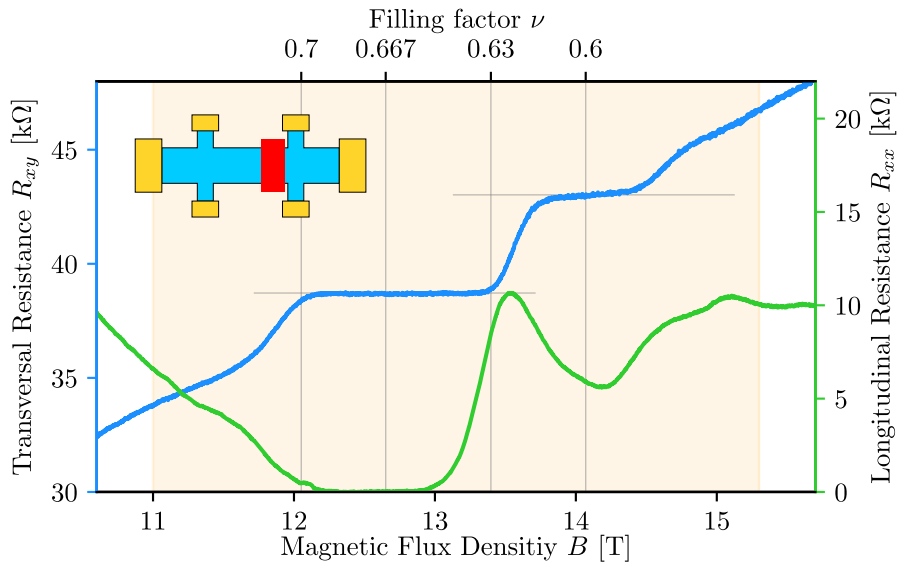


Figure 7.3: Hall resistance R_{xy} (blue) and longitudinal resistance R_{xx} (green) during a magnetic field sweep over fractional filling factors $\nu = 2/3$ and $\nu = 3/5$. A well pronounced plateau of R_{xy} in B is observed for $\nu = 2/3$, where also R_{xx} drops to zero. The small Hall bar inset indicates the location, where Hall potential profiles are probed.

is indicated by a horizontal gray line. First Hall potential profiles in the fractional QH regime are probed in a magnetic flux range between 11.3 T and 13.6 T. This regime is chosen larger than the plateau to ensure that the investigated magnetic field range includes all parts of the quantum Hall plateau with $\nu = 2/3$.

To obtain Hall potential profiles, the same procedure as for the integer QH regime is necessary: The SET tip is moved across a homogeneous Hall bar cross-section, while the calibrated Hall potential profile is determined by the method described in chapter 5. A rectangular 2 mV peak-to-peak oscillation amplitude is chosen in both traces.

Figure 7.4 (a) depicts the Hall potential profiles probed around $\nu = 2/3$. They are compared in figure 7.4 (b) to Hall potential profiles around integer $\nu = 1$; these are taken from figure 6.7. Comparable types of profiles are colored in accordance to section 3.6. It becomes obvious that there is an astonishing similarity between both quantum Hall states. All Hall potential profiles formerly measured around $\nu = 1$ can be also identified around $\nu = 2/3$.

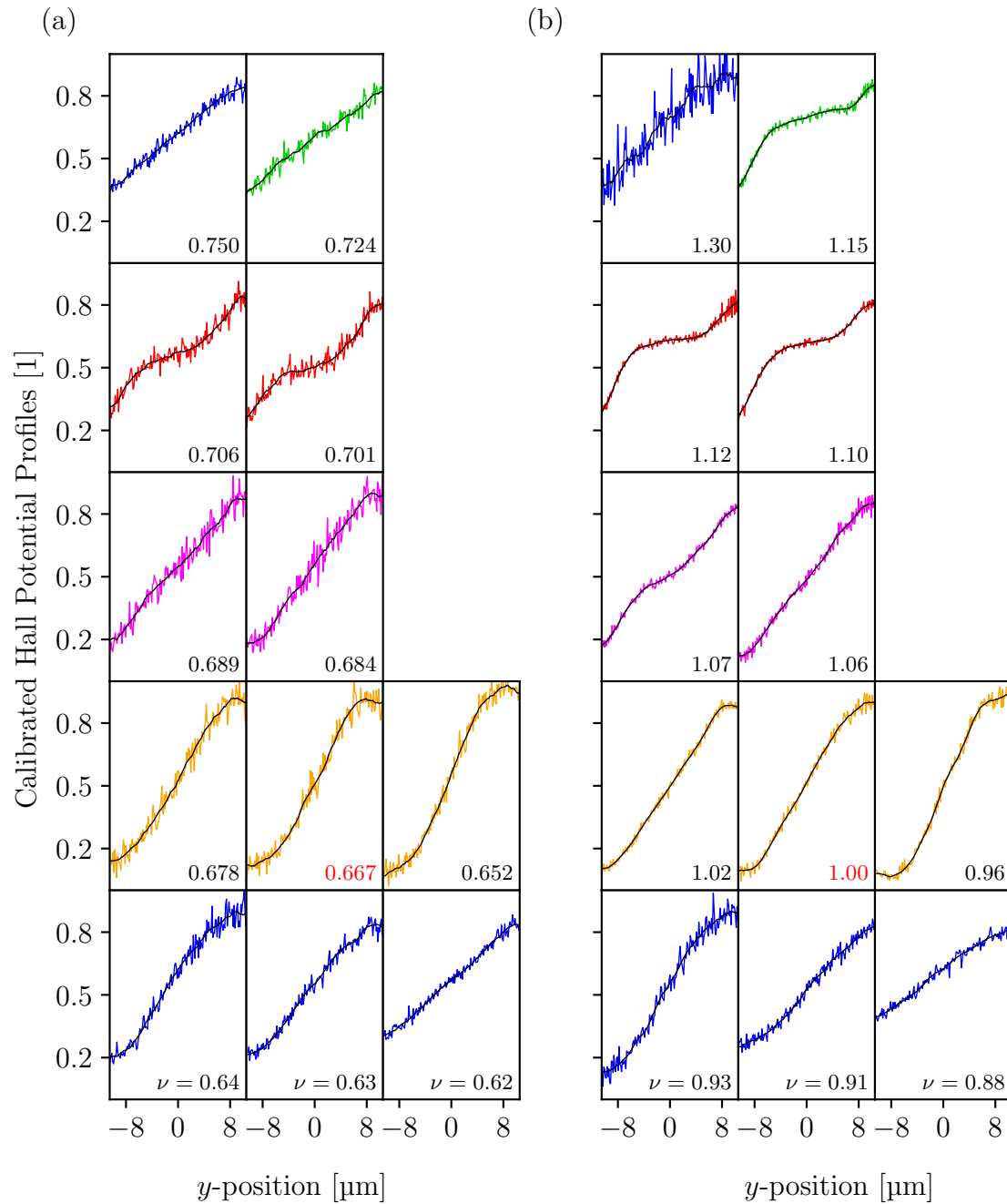


Figure 7.4: Comparison of Hall potential profiles that are probed around fractional quantum Hall state $\nu = 2/3$ (a) and integer quantum Hall state $\nu = 1$ (b). The profiles show an astonishing similarity for both cases: Outside of the quantum Hall plateau, a linear profile type is identified. Within the plateau regime they become non-linear, while the spatial position of the Hall voltage changes.

7.3 Reversed current direction leads to mirrored Hall potential profiles

In a next step the effect of a reversed bias current on the Hall potential profiles around filling factor $\nu = 2/3$ is probed. Figure 7.5 has two panels and shows measured Hall potential profiles for one current direction in (a), and profiles for the reversed current direction in (b). The magnetic flux density is increased from top to the bottom, indicated by the respective filling factor ν in the corner of each subplot. Similar types of Hall potential profiles are colored in accordance to sections 3.6 and 6.1. The difference in the observed noise level is a result of a different number of averaged traces and is not caused by a different current direction.

In both cases mainly similar Hall potential profiles can be observed - the only difference is: They seem to be mirrored around $y = 0$. This observation is in agreement with measurements in the IQHE, compare figure 6.9, where the current direction for $\nu = 3$ was reversed compared to other integer states.

We can conclude, that neither the observed Hall potential profiles, nor their evolution depends on the externally biased current direction.

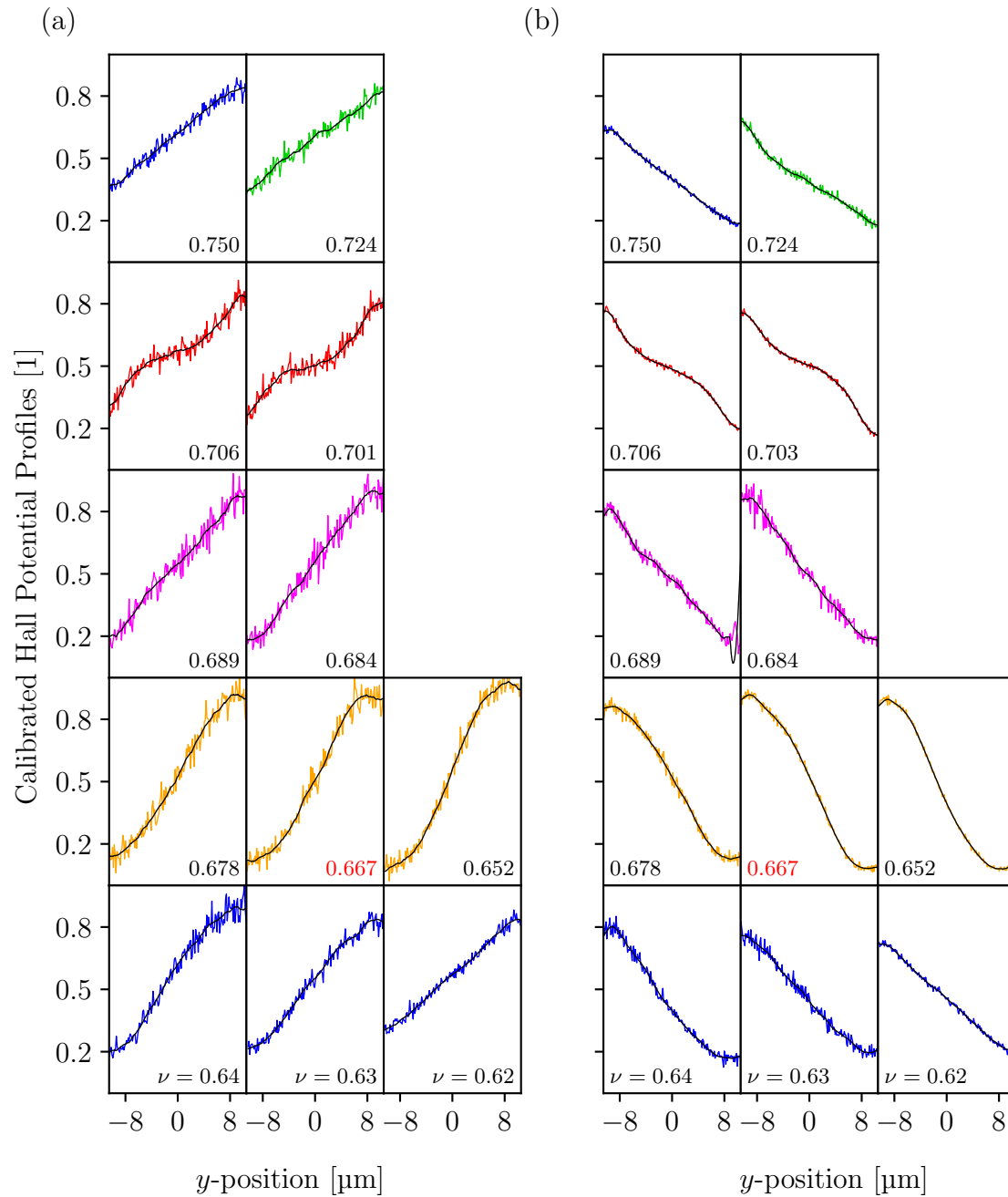


Figure 7.5: Hall potential profiles probed around fractional quantum Hall state $\nu = 2/3$ for reversed current directions. The profiles show the same behavior in all regimes, just mirrored around $y = 0$. This is expected, as reversing the current direction leads to an exchange of the low and high potential side along the sample and thus, a mirrored Hall voltage drop.

7.4 Evolution of Hall potential profiles and local current density distribution in the $\nu = 2/3$ fractional quantum Hall state

Now, the evolution of the Hall potential profiles with B is investigated more in detail. 85 Hall potential profiles are probed in a magnetic flux range between $11 \text{ T} \leq B \leq 14.75 \text{ T}$. The spacial position above the Hall bar is changed in comparison to the previous sections; the new position is indicated in figure 7.6.

Some selected Hall potential profiles - probed at different ν - are depicted in figure 7.7 (a). A constant shift is added to each profile in order to compare them within a single graph. Added labels on the right side of each profile indicate the corresponding filling factor. Comparable Hall potential types are indicated by the same line-color. The following evolution is observed:

1. Approaching the Hall plateau $\nu = 2/3$ from high filling factors (small B), the Hall voltage drop happens mainly linearly across the sample width, compare $\nu = 0.816$ and $\nu = 0.812$.
2. For smaller ν , the Hall voltage drop starts to continuously concentrate in small regions close to the sample edges, while the drop in the bulk diminish, as seen from $\nu = 0.764$ to $\nu = 0.718$.
3. For a further decreasing ν , the drops that are located close to the sample edges move into the center region of the bulk, while at the same time, their spatial extension increases, see for example $\nu = 0.707$ until $\nu = 0.690$.
4. At $\nu = 0.686$ the Hall potential drop seems to be almost linear again, but with a vanishing voltage drop at the sample edges.

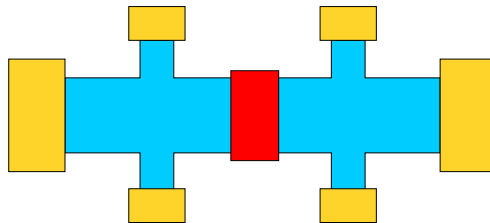


Figure 7.6: Sketch indicating the position (red) above the Hall bar, where the evolution of Hall potential profiles in the fractional quantum Hall regime are measured with smaller steps in the magnetic flux density B .

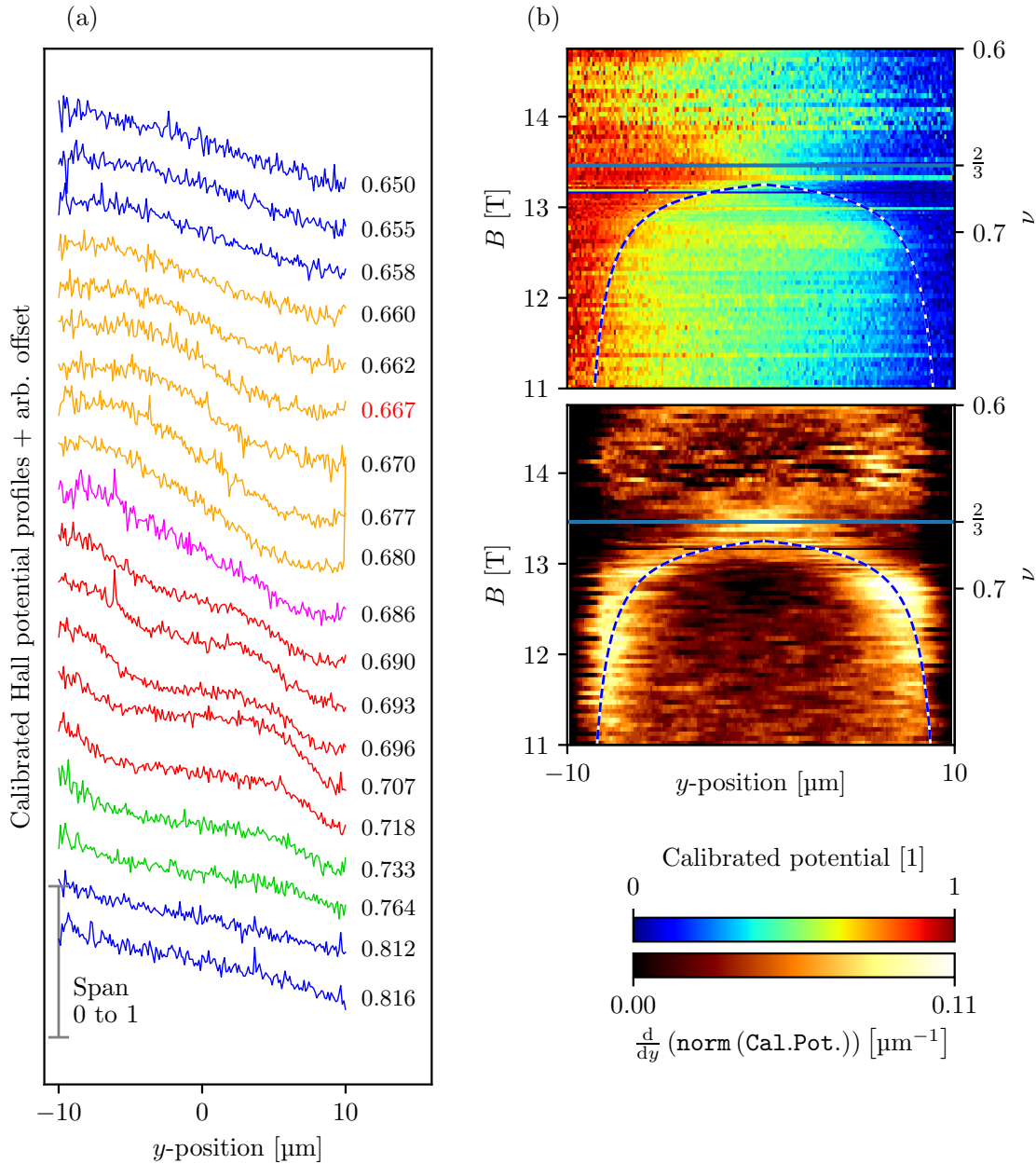


Figure 7.7: Hall potential profiles obtained in the fractional quantum Hall regime around $\nu = 2/3$, plotted versus the SET tip position y and changing magnetic flux densities B , respectively filling factors ν . (a) Selected Hall potential profiles plotted in different colors to emphasize the existence of different types. Each profile is shifted by a constant offset to compare them. (b) (upper) False-color representation of all measured Hall potential profiles $\tilde{V}_{2\text{DES}}^{(\text{norm})}$ (normalized) shows an evolution with B which is comparable to integer filling factors, shown in figure 6.9. In the plateau regime, the Hall voltage drop follows the calculated center position of the $\nu = 2/3$ incompressible stripe, overlaid as dashed line. An overlay of the Hall curve is not possible here, as the probed region has an increased value of $n_{2\text{D}}$, shifting filling factors to higher values of B . (lower) The current density $j_x^*(y, B)$ shows the same evolution. In the plateau region, a high current density is located around the center position of the incompressible stripe. Far from the plateau, at low magnetic fields, the current density is distributed homogeneously over the sample width.

7.4. Evolution of Hall potential profiles and local current density distribution in the $\nu = 2/3$ fractional quantum Hall state

5. An additional decrease of ν leads to wider regions with no voltage drop close to the sample edges. The voltage drop gets subsequently more concentrated in the center region of the sample, depicted from $\nu = 0.680$ to $\nu = 0.662$.
6. By further decreasing ν , the linear Hall voltage drop across the whole Hall bar cross-section is restored.

Figure 7.7 (b) combines in a false-color representation as a function of the magnetic flux density B , respectively filling factor ν , all 85 Hall potential profiles $\tilde{V}_{2\text{DES}}^{(\text{norm})}(y, B)$ that we probed between $11 \text{ T} \leq B \leq 14.75 \text{ T}$. Color changes correspond to positions of a Hall voltage drop and thus, local current densities. Latter one becomes even more visible when the current density $j_x^*(y, B)$ is calculated from $\tilde{V}_{2\text{DES}}^{(\text{norm})}(y, B)$. Here, $j_x^*(y, B)$ is also depicted in figure 7.7 (b) as false-color representation: Bright regions show a high local current density j_x . In both color-coded graphs, a horizontal line indicates the fractional filling factor $\nu = 2/3$, and a dashed line the calculated center position of the $\nu = 2/3$ incompressible stripe. It has to be pointed out, that this time the electron density $n_{2\text{D}}$ we used to calculate both lines differs from the one which was calculated formerly from a Hall measurement. Instead of $n_{2\text{D}} = 2.05 \times 10^{15} \text{ m}^{-2}$, this time a 5.9% higher electron density of $n_{2\text{D}} = 2.17 \times 10^{15} \text{ m}^{-2}$ is assumed. Because of this, the Hall curve is not overlaid to figure 7.7 (b), as an increased value of $n_{2\text{D}}$ shifts filling factors to higher values in B and the experimentally determined (local) Hall curve would no longer fit.

Apart from the correction of $n_{2\text{D}}$, the evolution of the Hall voltage drop, respectively the local current density $j_x^*(y, B)$, is in astonishing agreement with evolutions we already saw in the integer quantum Hall regime, compare figure 3.4 and figure 6.9. The current seems to be concentrated in the lower magnetic field range close to the Hall bar sides, while it moves into the bulk region for higher magnetic flux densities. Even towards $\nu = 3/5$ slight indications of an evolution of the current density may be identified.

7.5 Drop of the dissipation around $\nu = 2/3$

In section 6.2 it is described how the scaling factor γ can be determined with (5.29) from the probed Hall potential profiles. It yields information about dissipation within the sample, more precisely along the path of current flow.

Figure 7.8 depicts the determined values of γ for all shown Hall potential profiles in the fractional quantum Hall regime (magenta dots). Included is also the longitudinal resistance R_{xx} (green) which was determined during a DC transport measurement with a constant applied bias voltage of 2 mV - this data is taken from figure 7.1. Gray data points are excluded as the corresponding Hall potential profiles include large noise.

Compared to the scaling factor γ that was determined at integer filling factor $\nu = 2$, shown in figure 6.6, a similar behavior can be identified. The following is observed here: The curve shape of the scaling factor γ follows the one of R_{xx} . Outside of the $\nu = 2/3$ QH plateau, values above 1.5 are observed which indicate dissipation in the sample. Within both fractional quantum Hall plateaus a reduced dissipation is observed. Looking at $\nu = 2/3$, minimum values of γ are reached in the higher magnetic field region where $R_{xx} = 0$. When R_{xx} starts to rise after the QH plateau, also the dissipation increases.

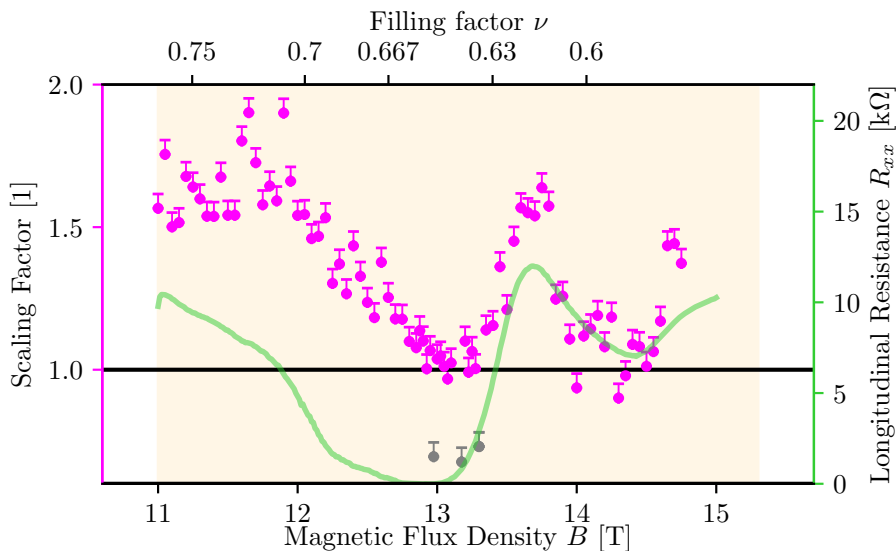


Figure 7.8: Magenta dots indicate the scaling factor γ , necessary to renormalize the Hall potential profiles to span the full range between 0 and 1. Noise within Hall potential profiles can lead to reduced values of γ ; the dots represent the lower limit of the value. Gray dots are excluded from the discussion as they result from large noise in the Hall potential profile. Shown in green is the longitudinal resistance R_{xx} probed with a DC bias of 2 mV.

7.6 Hall potential profiles spatially resolved within an Hall bar area

In the following, the current density landscape $j_x^*(y, B)$ which is shown in figure 7.7 (b) is extended by another spacial axis: Now we spatially resolve $j_x^*(x, y, B)$ in an area scan. This is done at different magnetic flux densities B , respectively filling factors ν .

Figure 7.9 depicts results obtained for three magnetic flux densities (from left to right): $B = 11.00$ T, $B = 12.45$ T, and $B = 13.30$ T, see also figure 7.7. Hereby, figure 7.9 (a) shows probed Hall potential profiles² in a pseudo-3d representation.

²The Hall potential landscape is just shown for completeness. The x and y axis are in the same range as shown for $j_x^*(x, y)$, while the z axis ranges between 0 and 1.

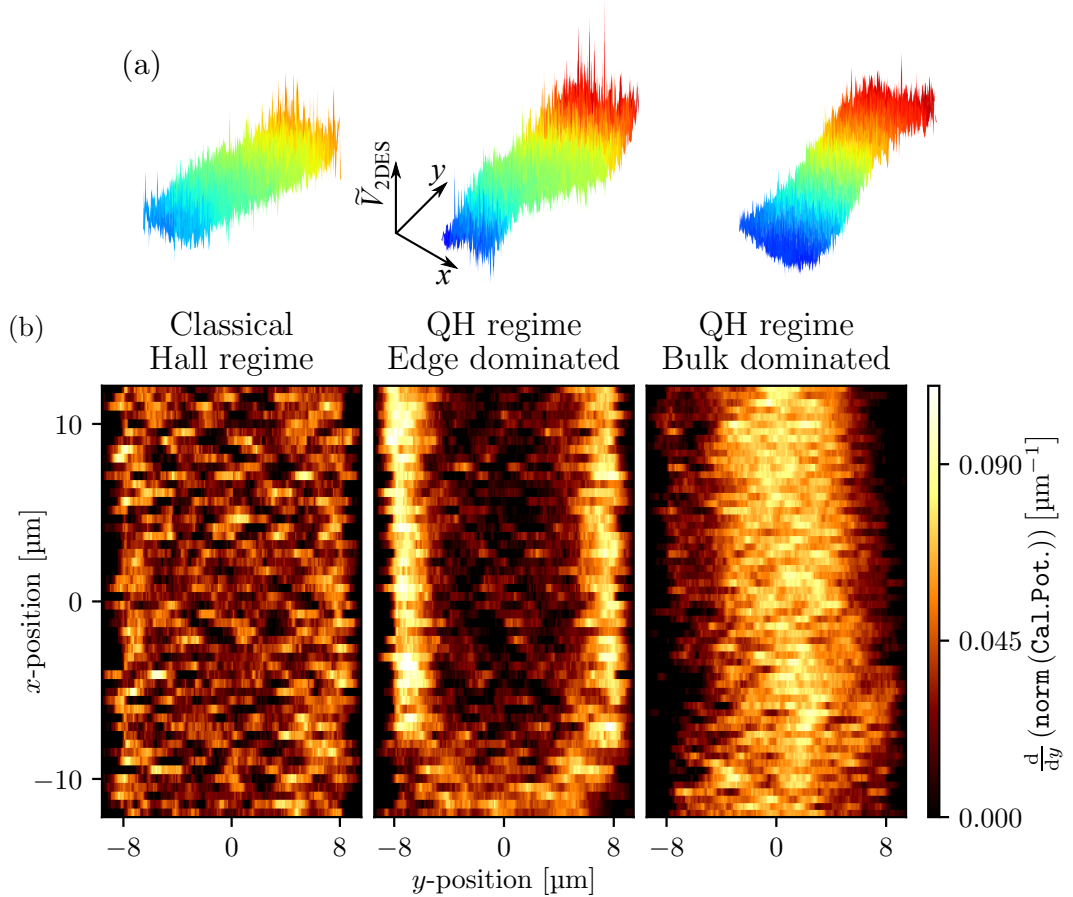


Figure 7.9: Current density $j_x^*(x, y)$ measured in a Hall bar area scan for three different regimes of the $\nu = 2/3$ FQH plateau. (left) Outside of the quantum Hall plateau, a homogeneous current distribution over the sample width is observed. (middle) In the low magnetic field side of the QH plateau the current density is concentrated at the sides of the Hall bar structure. For $x < -7.5 \mu\text{m}$ the current seems to move inside the sample bulk. (right) At the higher magnetic field side of the QH plateau the externally current flows mainly in the center of the sample.

The resulting current density landscape $j_x^*(x, y)$ is color-coded shown in figure 7.9 (b). In the following we concentrate on the discussion of $j_x^*(x, y)$ in (b).

The left panel shows a mainly homogeneous current density in the sample cross-section. Almost no changes along the x nor the y axis are observable within this area. Such a behavior is expected in the classical Hall regime. This situation changes in the centered panel. Here the current density is concentrated at the sample edges, while almost no current density is observable in the bulk region. At the highest magnetic flux density, shown in the right panel, the observed current distribution changes again. An increased current density is present within the bulk region, while towards the edges almost no current density is observed.

But there is more: In the centered panel of figure 7.9 (b) it seems that the lower part of the scan range with $-12\ \mu\text{m} < x < -7.5\ \mu\text{m}$, a different behavior compared to the rest of the graph is observed. It seems the current density is mainly in the bulk of the sample and not close to the edges as it is for other positions. This inhomogeneity is unexpected.

Evolution of the current density landscape $j_x^*(x, y)$ with B

In order to resolve the current density landscape evolution $j_x^*(x, y, B)$ more continuously, Hall potentials are probed for eighteen different applied magnetic flux densities B , respective filling factors ν , within an area. The results are depicted in figure 7.10. The applied magnetic flux density B is overlaid on the top of each plot.

The following can be observed:

1. Coming from low magnetic flux densities ($B = 11.0\ \text{T}$) the current is homogeneously distributed over the sample width. Here the Hall resistance R_{xy} lies between two quantum Hall plateaus.
2. With higher values of B , the current density starts to concentrate close to the sample edges, while the remaining current density in the bulk decreases continuously until $B = 12.7\ \text{T}$ is reached.
3. From there, further increases of B shift the high current density regions away from the edges into the bulk region. At the same time, it seems these regions are getting wider in y direction, up to $B = 13.1\ \text{T}$.
4. Simultaneously, the formerly observed inhomogeneity in the lower part of the graphs shifts towards larger values of x . In section 5.3 it was discussed

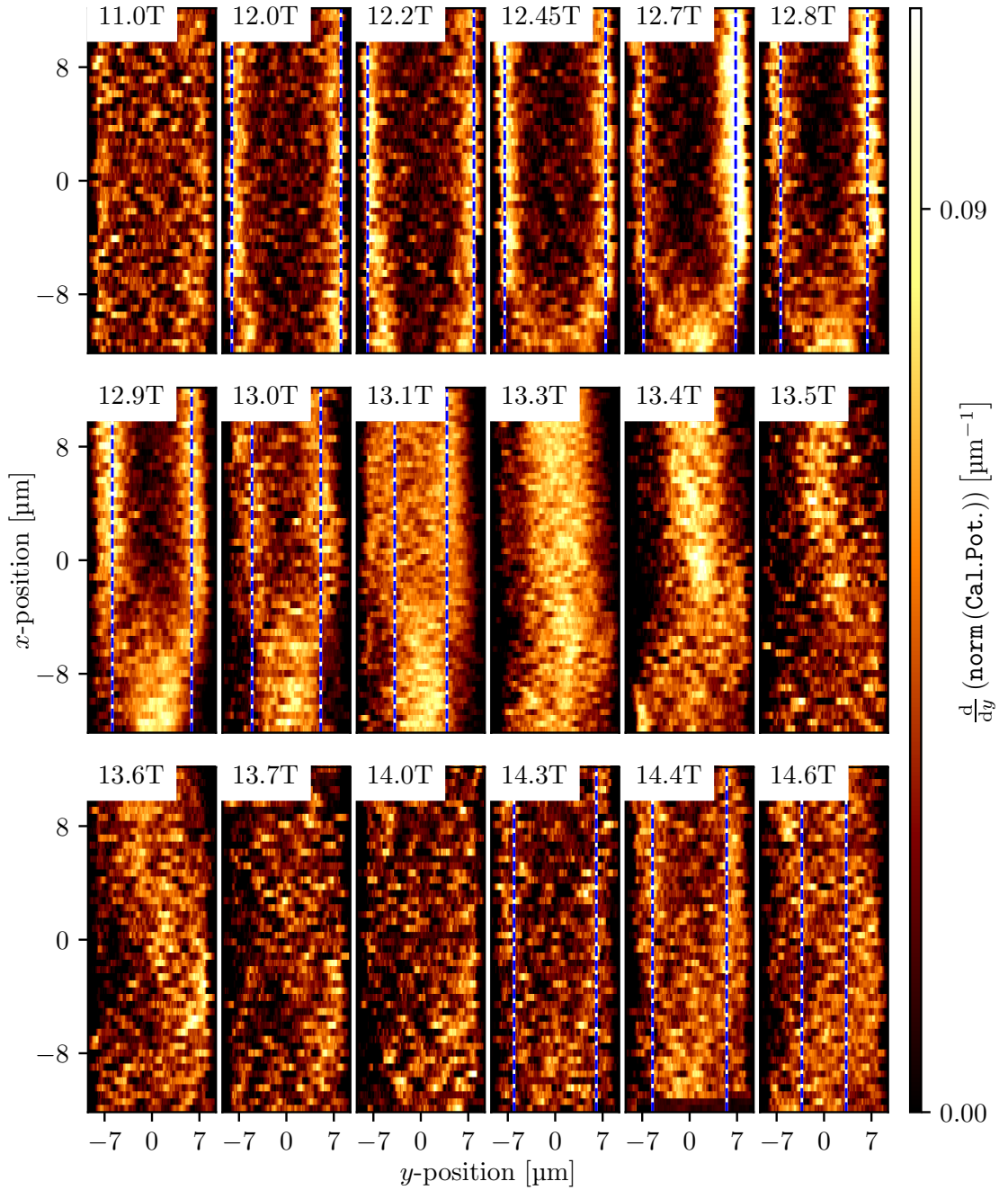


Figure 7.10: Series of eighteen area scans taken at different magnetic flux densities over the fractional quantum Hall plateau $\nu = 2/3$, to probe the local current density $j_x^*(x, y)$. The upper half of each graph is discussed: At 11 T, far from the quantum Hall plateau in the classical Hall regime, the current is homogeneously distributed over the sample width. With increasing B , the current redistributes towards the sample edges until mainly no current density in the bulk remains, see 12 T until 12.9 T. Between 13 T and 13.3 T both current carrying regions move inside the bulk region. Starting at 13.5 T, a linear current distribution is continuously recovered, as the quantum Hall plateau is left. Dashed lines indicate the calculated center position of the $\nu = 2/3$ incompressible stripe.

that an increase of B leads unavoidably to a shift of the SET tip relative to the Hall bar. As almost the full microscope scan range in x direction is used during these area scans, this shift cannot be compensated³ and the inhomogeneity comes continuously from the bottom into the plot.

5. At about $B = 13.3$ T and $B = 13.4$ T the current flow happens exclusively in the bulk region. With higher B it gets more and more concentrated in the center of the sample. The edge region shows mainly no current density. In this magnetic field region the bulk filling factor $\nu = 2/3$ is present⁴.
6. Exceeding $B = 13.5$ T leads to a redistribution of the current density. Until $B = 13.7$ T, the initially homogeneous current distribution of $B = 11.0$ T is mainly restored. The QH plateau is left to the higher magnetic field side.
7. In accordance with the observation of a rudimentary developed $\nu = 3/5$ structure, at $B = 14.4$ T the current distribution seems to show indications of higher current densities at the sample edges compared to the bulk.

In the next section we will clarify the origin of the observed inhomogeneity in x direction, which is unexpected.

7.7 Inhomogeneity of the 2DES is observed

The previous section revealed an inhomogeneity of the current density $j_x^*(x, y)$ within the scanned area. Hence, within this section we concentrate on an experiment to understand the origin of this inhomogeneity. Therefore, the formerly probed Hall bar area is scanned again, but only the DC feedback loop is activated. The resulting feedback signal, which is necessary to keep the current I_{SET} through the SET constant, gives information about the electrostatic potential below the SET island.

Figure 7.11 shows the obtained feedback signal $V_{\text{COM}}(x, y)$ that is applied commonly to both SET lead electrodes. The white dashed line in y direction indicates where Hall potential profiles for $\nu = 2/3$ were taken in section 7.4. It is obvious, that the electrostatic potential drops towards the Hall bar edges, compare section 5.2. But, also along the Hall bar mesa in x direction a change is observed which is unexpected as we expect to have a homogeneous 2DES. For positions $-7\ \mu\text{m} < x < -2\ \mu\text{m}$, the DC feedback loop signal drops. A sudden change could be explained by a jump of the feedback loop, which keeps then a working point

³The scan range is limited and cannot follow the position shift in x direction.

⁴In this region with $n_{2\text{D}} = 2.17 \times 10^{15}\ \text{m}^{-2}$.

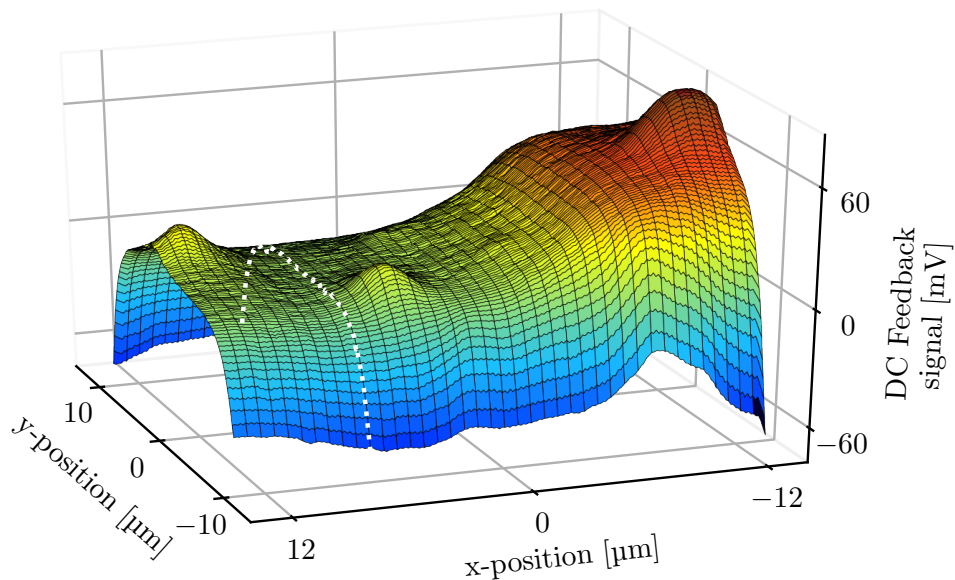


Figure 7.11: DC feedback signal obtained during an area scan over the Hall bar surface. Hall potentials in the fractional quantum Hall regime are probed at an x position that is indicated with a white line; far from the region where the 2DES potential increases, in a homogeneous region in-between dielectric particles.

I_{SET} on another CBO. But the origin of this continuous drop lies somewhere else.

As depicted in equation (5.19), a change of the DC feedback loop signal ΔV_{COM} , which is given by

$$\Delta V_{\text{COM}} = \frac{C_{2\text{DES}}}{C_{2\text{DES}} + C_{\text{Stray}}} \Delta V_{2\text{DES}}, \quad (7.1)$$

can be either the result of (1) a change of the local electrostatic potential $\Delta V_{2\text{DES}}$ of the 2DES, or (2) a change of the capacitive coupling $\Delta C_{2\text{DES}}$ to the 2DES. We assume $C_{2\text{DES}}$ is the strongest capacitive influence during Hall potential measurements, as the distance to the 2DES is reduced as good as possible. The following situations are thinkable: The 2DES is buried 120 nm under the Hall bar surface which is structured on an heterostructure that was grown by molecular-beam epitaxy (MBE). For such heterostructures the layer sequence is normally precise and the surface flat. Thus, a change of the height and subsequently a change of $C_{2\text{DES}}$ is not expected along the Hall bar. Consequently, a change of $V_{2\text{DES}}$ should happen. What could be reasons for that?

Possible in our samples are long-range charge carrier density variations. From the microscopic picture of the IQHE these are known to be present as they stabilize quantum Hall plateaus to the higher magnetic field side, compare chapter 3. Such a change of $n_{2\text{D}}$ along the Hall bar structure would lead to a change of the local electrostatic potential $V_{2\text{DES}}$ and consequently for the SET to a change of V_{COM} . But, their size is expected to be in the several 100 nm range and thus, smaller than

the sample width. Nevertheless, the observed potential drop in ΔV_{COM} along the Hall bar mesa is most probably a local change of the electron density $n_{2\text{D}}$ - maybe induced by the fabrication process or the cool-down of the sample.

More precisely, as the potential change $\Delta V_{2\text{DES}}$ of the 2DES gets more negative and no change in $C_{2\text{DES}}$ is expected, the electron density is locally increased between $-2\text{ }\mu\text{m} < x < 10\text{ }\mu\text{m}$. Consequently, the previous observed inhomogeneity has its origin most probably in a local change of $n_{2\text{D}}$.

In order to verify this assumption, Hall potential profiles around filling factor $\nu = 2/3$ are probed again, but this time at a different position. The new position is chosen closer to the probing contacts. The evolution is depicted in appendix C. There, the center position of the $\nu = 2/3$ incompressible stripes matches nicely the positions of locally increased current densities j_x^* , when the experimentally determined electron density $n_{2\text{D}} = 2.05 \times 10^{15}\text{ m}^{-2}$ is assumed. Consequently, we are pretty sure that $n_{2\text{D}}$ is slightly increased in the region, where the Hall potential profiles presented in figure 7.7 were probed.

To clarify why the first position was chosen in first place, it has to be mentioned that a similar area scan was performed in advance, but only in the scan range of $0\text{ }\mu\text{m} < x < 13.5\text{ }\mu\text{m}$. Thus, the big change of the DC feedback signal was not observed back then. Consequently it was assumed, that the Hall bar region of $0\text{ }\mu\text{m} < x < 10\text{ }\mu\text{m}$ is homogeneous, while a slight inhomogeneity is approached for $x > 12\text{ }\mu\text{m}$. This led to the decision to take the line indicated in white as scan position to probe Hall potential profiles.

7.8 Breakdown of the edge-dominated quantum Hall regime with rising Hall voltage

In figure 7.2 an evolution of the observed breakdown threshold bias voltage V_{DS} was observed. In this section the influence of an increased V_{DS} on the Hall potential profiles is investigated. We want to clarify how V_{DS} affects probed Hall potential profiles. In section 7.1 we have seen that the lower magnetic field side of the $\nu = 2/3$ QH plateau was more fragile against high bias voltages. Hence, we concentrate on this regime here.

Hall potentials are probed in the same cross-section, where already the current density evolution $j_x^*(y, B)$ in section 7.4 was probed. This time different Hall bar bias voltages V_{DS} are applied. Two exemplary magnetic flux densities B are

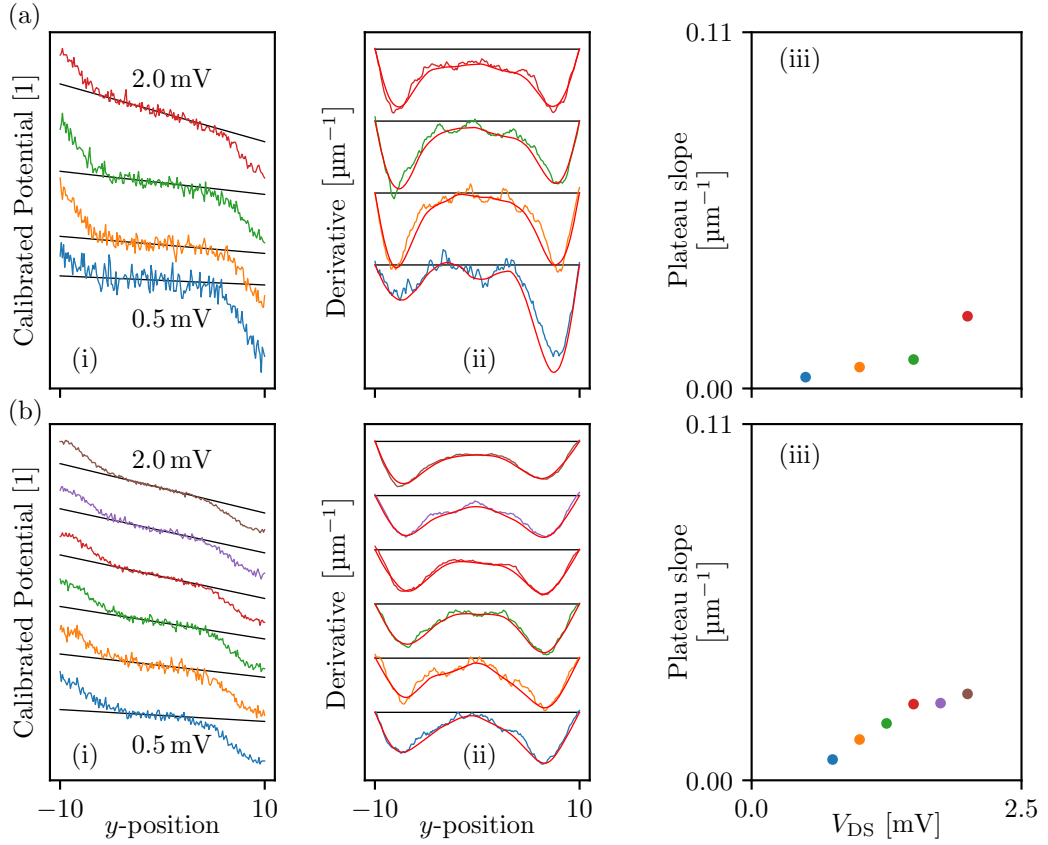


Figure 7.12: Hall potential profiles obtained in the edge-dominated quantum Hall regime of the fractional QH state $\nu = 2/3$ at 12.05 T (upper) and towards $\nu = 3/5$ at 14.25 T (lower) for bias voltages V_{DS} between 0.5 mV and 2.0 mV. In both cases, as a function of the SET tip position y it is shown: the potential profiles (left), the derivative j_x^* (middle) and the slope of the bulk region, determined via a linear regression (right). For higher bias voltages, the bulk region shows finite slopes, while with a decreasing V_{DS} , the slope, respectively the current density j_x^* , approaches zero.

investigated: $B = 12.05$ T, which is in the lower magnetic field regime of the $\nu = 2/3$ quantum Hall plateau, and $B = 14.25$ T, which is in B closer to the fractional filling factor $\nu = 3/5$.

Figure 7.12 depicts the experimental data: The upper graphs in (a) correspond to $B = 12.05$ T, the lower graphs in (b) to $B = 14.25$ T. The graph (i) always depicts the normalized calibrated Hall potential profiles $\tilde{V}_{2DES}^{(norm)}(y)$, shifted by the same constant offset⁵ and averaged over 36 to 96 single scans⁶. The local current density $j_x^*(y)$, calculated as $\partial\tilde{V}_{2DES}^{(norm)}(y)/\partial y$ is shown in (ii). A linear regression is fitted to determine the slope $\Delta\tilde{V}_{2DES}^{(norm)}(y)/\Delta y$ in the bulk region; the slope values are depicted in (iii).

⁵It has to be emphasized that the offset between all curves is the same. Thus, comparisons of slopes in both graphs are valid.

⁶Especially in the more fragile fractional $\nu = 3/5$ QH state, the number of linescans was increased.

In both data series a similar behavior can be observed:

1. For all bias voltages V_{DS} two distinct Hall voltage drops close to the Hall bar edges can be observed. In case of $B = 12.05$ T in (a), these drops seem to be slightly steeper, compared to $B = 14.25$ T in (b).
2. For both magnetic fields, high bias voltages lead to a Hall voltage drop - respectively to a local current density $j_x^*(y)$ - in the bulk region. This decreases with decreasing V_{DS} . This can be seen best in graphs (iii). In case of $B = 14.25$ T the voltage drop in the bulk increases faster with V_{DS} .
3. The signal-to-noise ratio in the Hall potential profiles becomes worse with smaller values of V_{DS} . This happens even as the Hall potential profiles for $V_{\text{DS}} = 0.5$ mV are already averaged over more single lines than for higher V_{DS} .

These measurements explain that some Hall potential profiles in the lower magnetic field side of the $\nu = 2/3$ filling factor show an additional (small) Hall voltage drop inside the bulk region, while the main voltage drop happens close to the sample sides. It is caused by the bias voltage V_{DS} .

On the other hand, they also indicate the following: when smaller bias voltages V_{DS} are used, it could be possible to probe Hall potential profiles in the fractional state $\nu = 3/5$.

7.9 Fractional quantum Hall state $\nu = 3/5$ is probed

In figure 7.7 and figure 7.10 we could already observe slight indications of an evolution in the current density $j_x^*(y, B)$ around filling factor $\nu = 3/5$. This gives reason to investigate $\nu = 3/5$ more in detail. The procedure is similar to previous sections.

From the experimental point of view, two changes are necessary: (1) According to the previous section, Hall potential profiles are probed with bias voltages having 1 mV peak-to-peak oscillation amplitude, compare figure 7.2 and figure 7.12. (2) To achieve comparable signal-to-noise ratios, a smaller bias voltage has to be compensated by an increased measurement time. Mostly the double amount of Hall potentials are probed at a fixed B , and subsequently averaged.

Evolution of the current density $j_x^*(y, B)$ with B

Hall potential profiles are measured in the same cross-section of the Hall bar where already the quantum Hall state $\nu = 2/3$ was probed, compare figures 7.6 and 7.11. The magnetic flux density B is varied between each measurement, while B is chosen to have (1) a small overlap with the $\nu = 2/3$ QH state, and (2) to cover the complete $\nu = 3/5$ QH state.

The resulting current density evolution $j_x^*(y, B)$ is depicted in figure 7.13. Again, bright signals correspond to locally high current densities j_x^* . Horizontal lines indicate bulk filling factor $\nu = 2/3$ and $\nu = 3/5$, respectively. Center positions of incompressible stripes are overlaid for both fractional filling factors as dashed line. They are calculated with an electron density of $n_{2D} = 2.17 \times 10^{15} \text{ m}^{-2}$, which was already used in section 7.4.

Comparing the results for fractional QH state $\nu = 3/5$ with figure 7.4 - where the current density of the fractional quantum Hall state $\nu = 2/3$ is presented - the same behavior is observable. The current density in the lower regime of B -

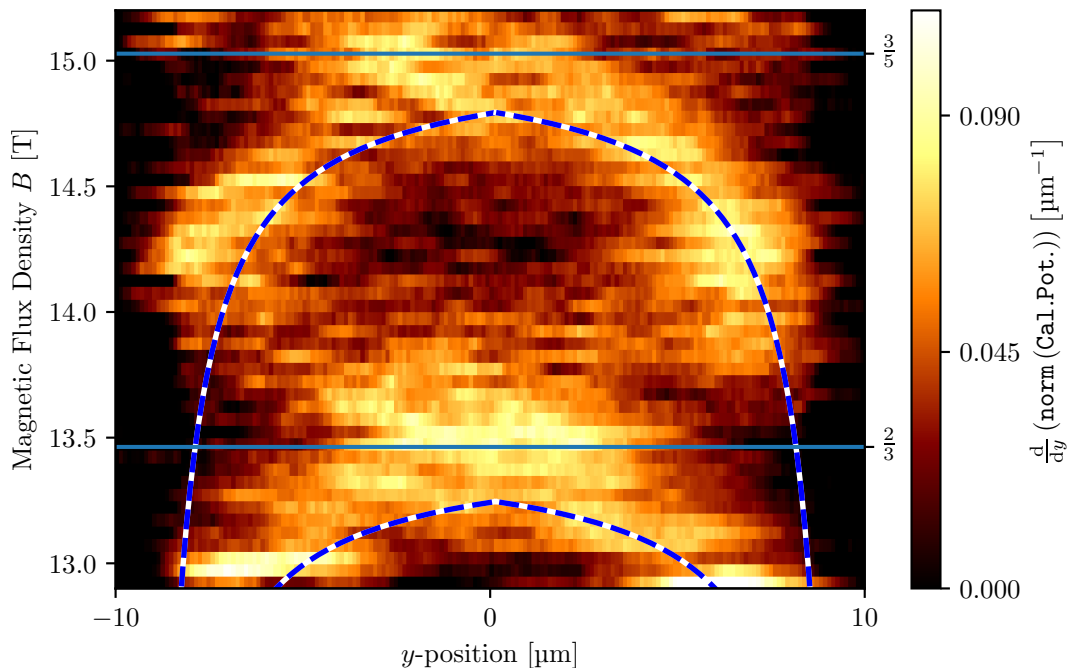


Figure 7.13: Observed current density distribution $j_x^*(y, B)$ across a sample cross-section probed at different magnetic flux densities B around the fractional quantum Hall plateau $\nu = 3/5$. Bright signals correspond to high current densities. Horizontal lines indicate the fractional filling factors $\nu = 2/3$ and $\nu = 3/5$. A dashed line represents the center position of the corresponding incompressible stripe, calculated via equation (3.2). The same evolution as already seen for integer QH states and fractional QH state $\nu = 2/3$ is also observed for the fractional state $\nu = 3/5$. Positions of high local current densities follow exactly the center position of the $\nu = 3/5$ incompressible stripe.

here is the overlap to figure 7.4 - still follows the calculated center position of the $\nu = 2/3$ incompressible stripes. But now, in the upper part of the graph, where the $\nu = 3/5$ QH state is present, the current density evolution is better resolved. It is clearly visible that also for the fractional state $\nu = 3/5$, the current density undergoes an evolution in B . Astonishingly, this evolution is in agreement with the calculated center position of the $\nu = 3/5$ incompressible stripes.

Current density landscape $j_x^*(x, y)$ in different regimes

In the same manner as done for the fractional quantum Hall state $\nu = 2/3$, the spatial current distribution $j_x^*(x, y, B)$ is probed in an area, to get information about the spatial homogeneity. Three different magnetic flux densities, respectively three (quantum) Hall regimes are chosen, compare figure 7.9. Referring to figure 7.13, the magnetic flux densities are chosen as $B \in \{14.25 \text{ T}, 14.95 \text{ T}, 15.50 \text{ T}\}$.

The probed current density landscapes $j_x^*(x, y)$ are shown in figure 7.14, while the magnetic flux density is increased from the left to the right. Compared with figure 7.9, which shows similar measurements around fractional QH state $\nu = 2/3$, the upper half of the graph with $x > 0 \mu\text{m}$ shows the same current distributions within the probed area. From previously investigation we know: The lower part of

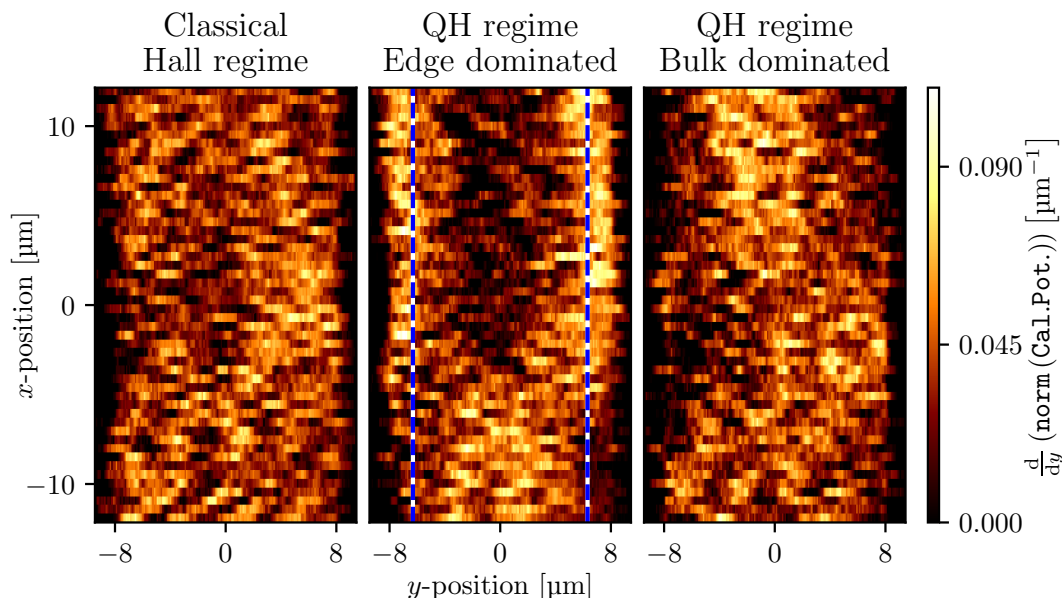


Figure 7.14: Current density $j_x^*(y, x)$ probed in area scans over the Hall bar geometry, for three different magnetic flux densities B , respectively filling factors ν . A comparison with figure 7.9 that shows similar area scans for $\nu = 2/3$ yields that both fractional quantum Hall states behave similar: Outside of the Hall plateau, a homogeneous current density is observed, which changes into a regime of high current densities at the sample edges and afterwards, into a high current density in the bulk region with vanishing current flow at the sample edges.

our scan area has a slightly lower charge carrier density, respectively lower corresponding filling factor $\nu(B)$. Thus, the inhomogeneity is explainable; the observed regimes would be also seen in the lower region of the graphs, simply different magnetic flux densities are necessary to achieve the same filling factors.

We can conclude from these measurements: The fractional quantum Hall states $\nu = 3/5$ and $\nu = 2/3$ show mainly similar regimes of the current density distribution $j_x^*(x, y, B)$.

Dissipation in the sample around $\nu = 3/5$

From Hall potential profiles which were taken around fractional QH state $\nu = 3/5$ the scaling factor γ is determined analogously to sections 6.2 and 7.5. Due to the lower bias voltage V_{DS} which was used to probe these Hall potential profiles, the new values of γ are expected to be more precise. Thus, older values of this magnetic field range in figure 7.8 are replaced in the updated graph 7.15.

Now it becomes more obvious that the dissipation behaves similar between filling factors $\nu = 2/3$ and $\nu = 3/5$. The dissipation along the Hall bar is reduced within the fractional quantum Hall plateaus as R_{xx} decreases.

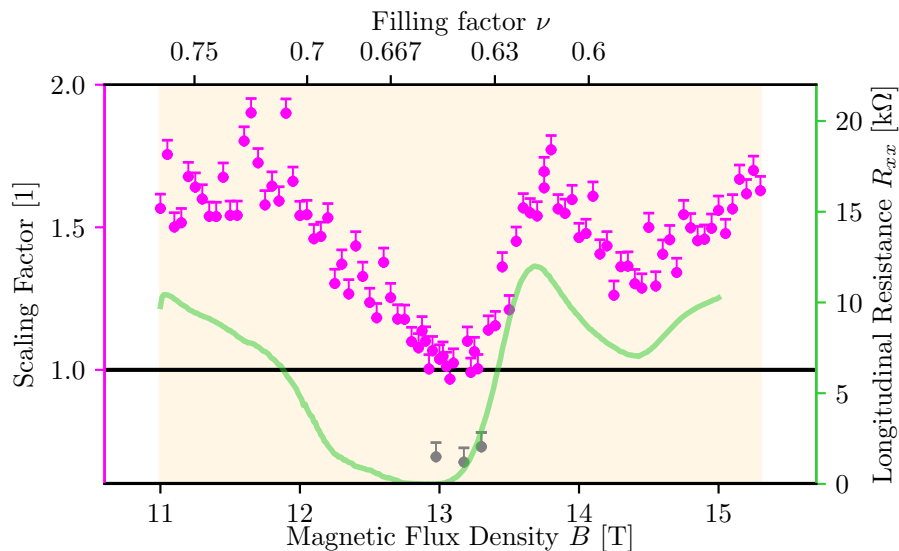


Figure 7.15: Magenta dots indicate the scaling factor γ , necessary to renormalize the Hall potential profiles to span the full range between 0 and 1. Noise within Hall potential profiles can lead to reduced values of γ ; the dots represent the lower limit of the value. Shown in green is the longitudinal resistance R_{xx} probed with a constant DC bias of 2 mV. The highlighted orange region is probed in the fractional quantum Hall regime.

7.10 Summary

Within this chapter the following observations have been made for the fractional QH regime:

1. The breakdown threshold voltage was asymmetric around $\nu = 2/3$.
2. A reversed current direction led to mirrored Hall potential profiles.
3. An evolution of the Hall potential profiles in B could be identified.
4. The evolution followed the expected position of incompressible stripes developing from the edge towards the bulk.
5. Within the QH plateau the overall dissipation dropped.

Similar observations have already been made in the integer QH regime. Thus, both regimes have one thing in common: The formation of an electrically compressible/incompressible landscape that evolves with the magnetic flux density over a quantum Hall plateau, compare figure 7.16 and figure 3.7, and obviously the Hall potential profiles and therefore the current density evolution is determined by this evolution.

The question now is: Why is it the same for the fractional and the integer quantum Hall regime?

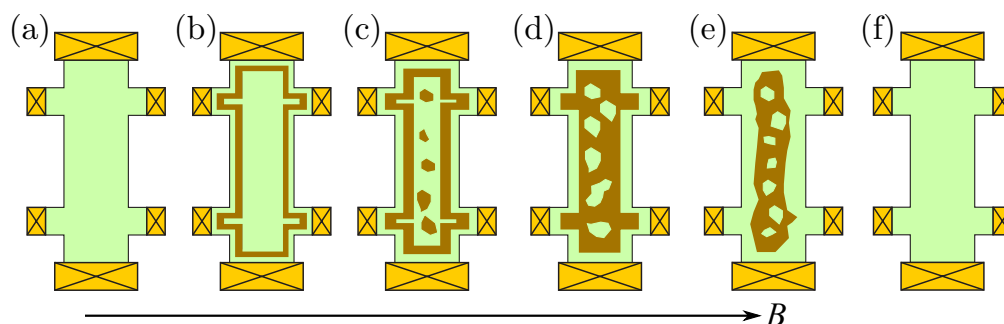


Figure 7.16: Evolution of electrically incompressible (brown) regions within an electrically compressible (green) 2DES, as introduced in section 3.6. In the classical Hall regime between quantum Hall plateaus the sample is compressible. With increasing magnetic flux density B , incompressible stripes form, one at each sample side. They grow in width and move inside the bulk region, where they merge. At this point, the whole bulk is incompressible surrounded by a compressible edge. When the quantum Hall plateau is left to the higher magnetic field side, the 2DES becomes again entirely compressible.

Chapter 8

Why do we see always the same Hall Potential Profile Evolution passing a Quantum Hall Plateau?

It is known that fractional quantum Hall states are an effect of many-body particle correlations. In contrast to that, the integer quantum Hall effect can be described microscopically in a single-particle picture. Now it has to be clarified, why in the fractional quantum Hall regime the same evolution of the current density distribution as for the integer quantum Hall regime can be observed.

During the introduction of the microscopic picture of the IQHE in chapter 3, the intrinsic formation of electrically compressible and incompressible regions - depending on the magnetic flux density B - was discussed.

An exemplary distribution with corresponding Landau level bending for integer filling factor $\nu = 4$ is schematically shown in figure 8.1 (a). The Hall voltage, that results from an external biasing, drops over the innermost incompressible stripes with local filling factor $\nu = 4$; one at each sample edge. Without loss of generality we can concentrate on the right incompressible stripe. The Landau level bending in this region is enlarged in figure 8.1 (b).

A Hall voltage drop in this incompressible region leads to an additional bending of the Landau levels there. Consequently, driven by the Hall field, all occupied single particle states get the same group velocity and they contribute to the local current density, given by

$$j_x = i \frac{e^2}{h} E_y \quad \text{here : } i = 4. \quad (8.1)$$

The direction of this current density is perpendicular to both, the magnetic flux density B and the Hall field E_y .

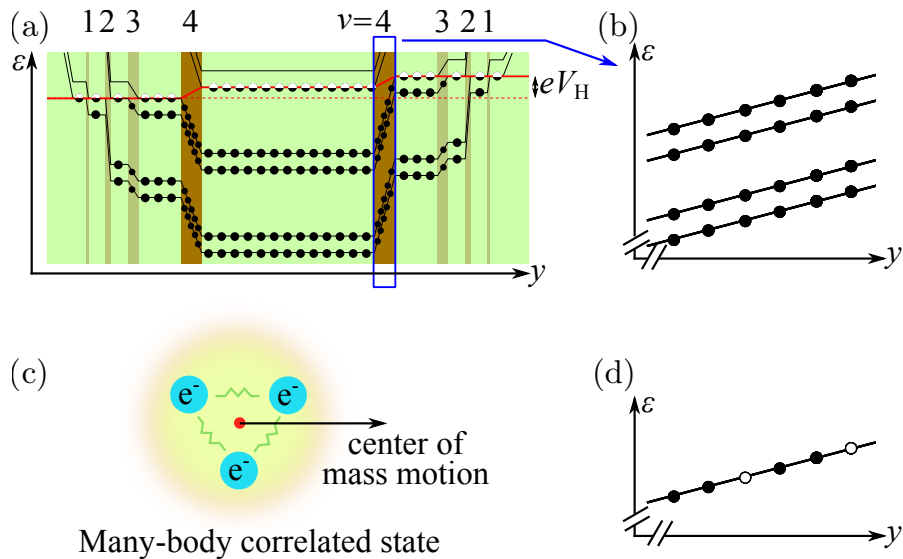


Figure 8.1: Sketches to explain a similar current distribution evolution in integer and fractional quantum Hall states. (a) Landau level bending in electrically incompressible regions. Shown is exemplary filling factor $\nu = 4$ in the innermost incompressible stripes; cyclotron and Zeeman energy gaps lead to the formation of incompressible regions. The Fermi energy lies there between completely empty and completely occupied electronic states. Incompressible regions cannot screen potential gradients. The Hall voltage V_H drops entirely in incompressible regions of filling factor $\nu = 4$. (b) Zoom into the right $\nu = 4$ incompressible stripe. The Hall field additionally bends the Landau levels. (c) In the fractional QH regime, magnetic flux quanta and several electrons form correlated particles; their relative position is determined. With applied Hall field, their center-of-mass moves with a common group velocity. (d) The lowest Landau level is occupied by $2/3$ of all available electronic states. A Hall field results in a tilt and consequently to a drift velocity of all occupied states below the Fermi energy.

The situation changes as the system gets into the fractional quantum Hall regime with filling factors $\nu < 1$ in the following way¹:

1. Only the lowest Landau level remains below the Fermi energy. It is just partly filled, compare figure 8.1 (d) showing exemplary filling factor $\nu = 2/3$. Of all available electronic states only $2/3$ are occupied.
2. Specific ratios between magnetic flux quanta and number of electrons in the same area lead to many-body correlations. They open an energy gap, protecting the 2DES against excitation. For filling factor $\nu = 2/3$, the ratio is three flux quanta per two electrons.
3. The many-body correlations determine the relative positions of electrons to each other, schematically shown in figure 8.1 (c).

¹The situation with filling factors $\nu > 1$ is discussed in chapter 10. For the spatial evolution of the current with B it is not important if incompressibility is formed by a single-particle effect or many-body correlations. This evolution is described by equation (3.2).

-
4. On the other hand, the formed energy gap leads to the formation of electrically incompressible regions within the compressible 2DES. This is comparable to the integer quantum Hall effect, where a cyclotron gap or Zeeman splitting opens an energy gap resulting in incompressible regions.
 5. The Hall voltage drop over these incompressible regions bends the partly filled Landau level with local $\nu = 2/3$ and leads to a center-of-mass motion of all correlated electrons. The relative position of them is irrelevant, as they move all together with a common group velocity.
 6. The common movement of electrons in an incompressible region with well defined (fractional) filling factor leads directly to a well-defined current density

$$j_x = \nu \frac{e^2}{h} E_y \quad \text{here : } \nu = 2/3, \quad (8.2)$$

which is directed perpendicularly to the magnetic flux density B and the Hall field E_y .

The described process repeats for all fractional quantum Hall states.

It can be summarized: The evolution of the compressible/incompressible landscape within the 2DES, underlying the evolution of the current density distribution, is generally common to both quantum Hall regimes - the integer QH regime and the fractional QH regime. But, the reason for this incompressibility is different in both regimes: In the integer QH regime the cyclotron gap or the Zeeman gap is present, while in the fractional QH regime many-body correlations are present. Further, the incompressibility leads to well-defined filling factors ν . If all externally biased current flows within incompressible regions of same ν , R_{xy} is quantized. Hence, via the compressible/incompressible landscape there is a common microscopic picture; it describes the Hall potential evolution in the quantum Hall regime.

Chapter 9

Imaging the Electrically Compressible/Incompressible 2DES Landscape with an SET

In section 3.6 of this thesis we discussed the present microscopic picture of the (integer) quantum Hall effect. There it is mentioned, that in the higher magnetic field range of a quantum Hall plateau the incompressible stripes coming from both 2DES sides merge in the 2DES bulk; a completely incompressible bulk is expected which is only interrupted by compressible droplets that result from long-range electron density fluctuations.

This chapter deals with possible measurement arrangements that make this electrically compressible and incompressible landscape within the 2DES visible. Two different approaches are introduced, where (1) only one SET is used and (2) one SET acts as stimulator, while a second one acts as probe. For the first method also preliminary measurement results are presented and discussed.

9.1 Electrically compressible/incompressible 2DES landscape

Chapter 3 introduced the microscopic picture of the quantum Hall effect. If R_{xy} is quantized with values of $h/\nu e^2$, the externally biased current flows entirely within electrically incompressible regions of the same filling factor ν . An evolution of these electrically incompressible regions within an otherwise electrically compressible landscape is also described there. Figure 9.1 recaps three landscapes which occur when the magnetic flux density is ramped over a quantum Hall plateau. Within a QH plateau, see figure 9.1 (b) and (c), long-range electron density varia-

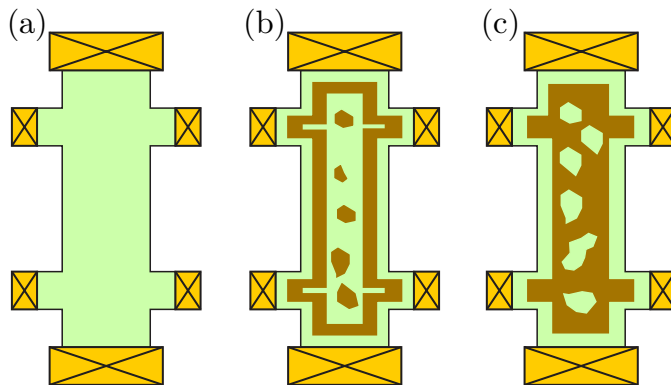


Figure 9.1: Schematic drawing of the expected electrically compressible/incompressible landscape within a 2DES. Outside of a quantum Hall plateau (a), in the lower magnetic field side of a QH plateau (b), and in the high magnetic field side of a QH plateau (c). Compare hereto chapter 3.

tions cause incompressible/compressible droplets within the compressible/incompressible 2DES bulk.

The electrostatic potential of our SET island is affected by (1) changes of the electrostatic potential V_i of close-by electrodes capacitively coupled to the SET island, and (2) a change of this capacitive coupling C_i . The question is now: Can we use the SETs to make this electrically compressible/incompressible landscape visible by measuring C_{2DES} locally within a 2DES area?

9.2 Measurement principle using one SET

In section 5.1 we derived that the Coulomb-blockade oscillations period, induced by a potential change between SET and 2DES, depends on the capacitive coupling C_{2DES} between SET island and 2DES. This effect was also used in section 5.5 to experimentally determine the capacitive coupling C_{2DES} : The slope of the CBOs is probed with a small AC signal applied to the 2DES. In this section we show a new measurement method, which is expected to give spatially more local results.

Figure 9.2 illustrates the circuit diagram schematically. An activated DC feedback loop keeps the current through the SET constant on a predefined working point. Chosen is preferably the point with the highest change $\partial I_{SET}/\partial V_{COM}$. An additional low-pass filter with a (-3 dB)-frequency of about 1 Hz is put between the SET current measurement and the feedback loop input. Thus, we ensure that the feedback loop cannot follow fast changes, but still keeps in average the predefined working point. Then, a small AC voltage modulation V_{COM} is applied commonly to both SET lead electrodes source and drain, to modulate the potential differ-

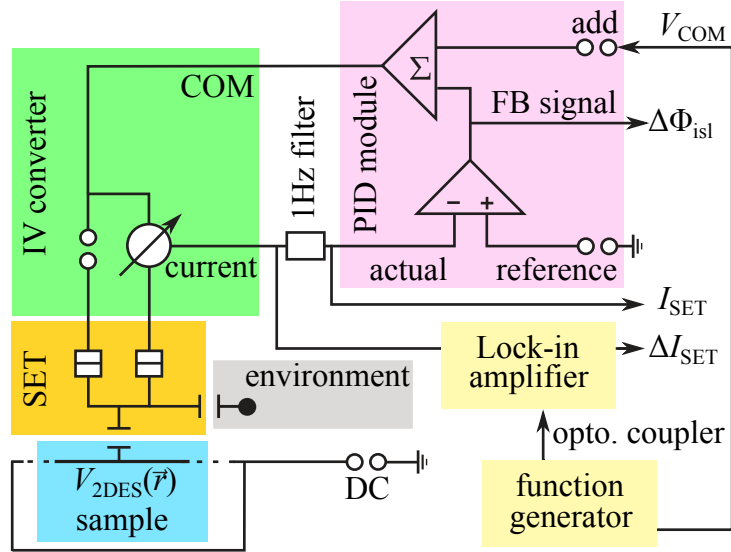


Figure 9.2: Schematic circuit diagram used to measure the capacitive coupling between SET and underlying 2DES more locally. An activated DC feedback loop ensures a constant predefined current I_{SET} . The 2DES is kept on a constant potential, while the potential of the SET is modulated via a frequency generator; an oscillating potential difference between both is introduced. A low-pass filter with a (-3 dB)-frequency of about 1 Hz is responsible that the feedback loop does not follow these oscillations. Hence I_{SET} shows oscillations around the predefined value, while the amplitude ΔI_{SET} depends on the capacitive coupling. Adapted from [21].

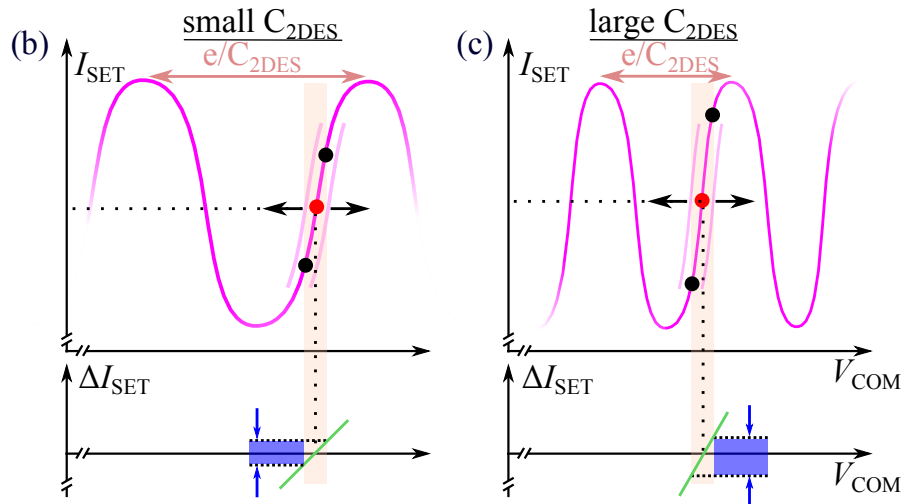


Figure 9.3: An activated DC feedback loop keeps the current I_{SET} through the SET on a predefined working point (red dot). An AC voltage applied commonly to both SET lead electrodes changes the potential difference between underlying 2DES and SET island. A 1 Hz low-pass filter in front of the feedback loop ensures that it will not follow these oscillations. Hence, the current I_{SET} shows small oscillations around its working point. Hereby the amplitude of this change ΔI_{SET} depends on the capacitive coupling between SET and the local 2DES under the SET; large couplings result in large amplitudes.

ence between SET and 2DES. The feedback loop does not see this modulation and consequently, the current I_{SET} oscillates around the working point. Depending on the capacitive coupling $C_{2\text{DES}}$, this oscillation amplitude is smaller or larger, compare figure 9.3. Hence, a demodulation of I_{SET} with a Lock-in amplifier gives information about $C_{2\text{DES}}$.

First experimental results

To verify that this new measurement method can be used to make electrically compressible/incompressible droplets visible, integer filling factor $\nu = 2$ is investigated. The scan is performed at a magnetic flux density of 4.5 T which corresponds to a bulk filling factor of about $\nu = 2$; hence, the bulk of the 2DES should be entirely incompressible, compare also figures 6.1 and 6.2. The chosen Hall bar region is similar to the one in figure 5.6.

Figure 9.4 shows first results we obtained with this method. Compressible/incompressible droplets are expected within the center region of the Hall bar. Hence, the scan area is chosen inside the bulk region of the 2DES, slightly shifted to the left, compare figure 9.4 (d). The edge region far from the bulk is not probed. Figure 9.4 (a) shows the corresponding DC feedback signal in a false-color representation versus both spatial coordinates. The two visible features were already discussed in section 5.4 and do not disturb our measurement.

The demodulated amplitude of the SET current is shown in a false-color representation in figure 9.4 (b). No fine-structure like droplets is visible. But it seems the amplitude has a correlation with the feedback signal as some features are reproduced; regions with a high DC feedback signal can be identified in the demodulated amplitude. In contrast, closer to the edge, where the feedback signal decreases, also an increase of the demodulated amplitude is observed.

With means of figure 9.4 (c) the reason for this correlation becomes clearer. Only the potential of the 2DES is varied while the SET is at a fixed position $(x, y) = (0 \mu\text{m}, 0 \mu\text{m})$; in all graphs this point is indicated by a black dot. The DC feedback loop detects then a deviation between the current I_{SET} through the SET and the predefined nominal value. Consequently, the common potential V_{COM} of both SET lead electrodes is adjusted to keep I_{SET} constant. The slope of the underlying CBO should be unaffected by this adjustment, compare also figure 9.3. Unexpectedly, a measurement of the demodulated current amplitude shows a dependency on the feedback loop signal (blue dots). A polynomial of 2nd order (green), and a polynomial of 4th order (orange) are calculated to fit the data in

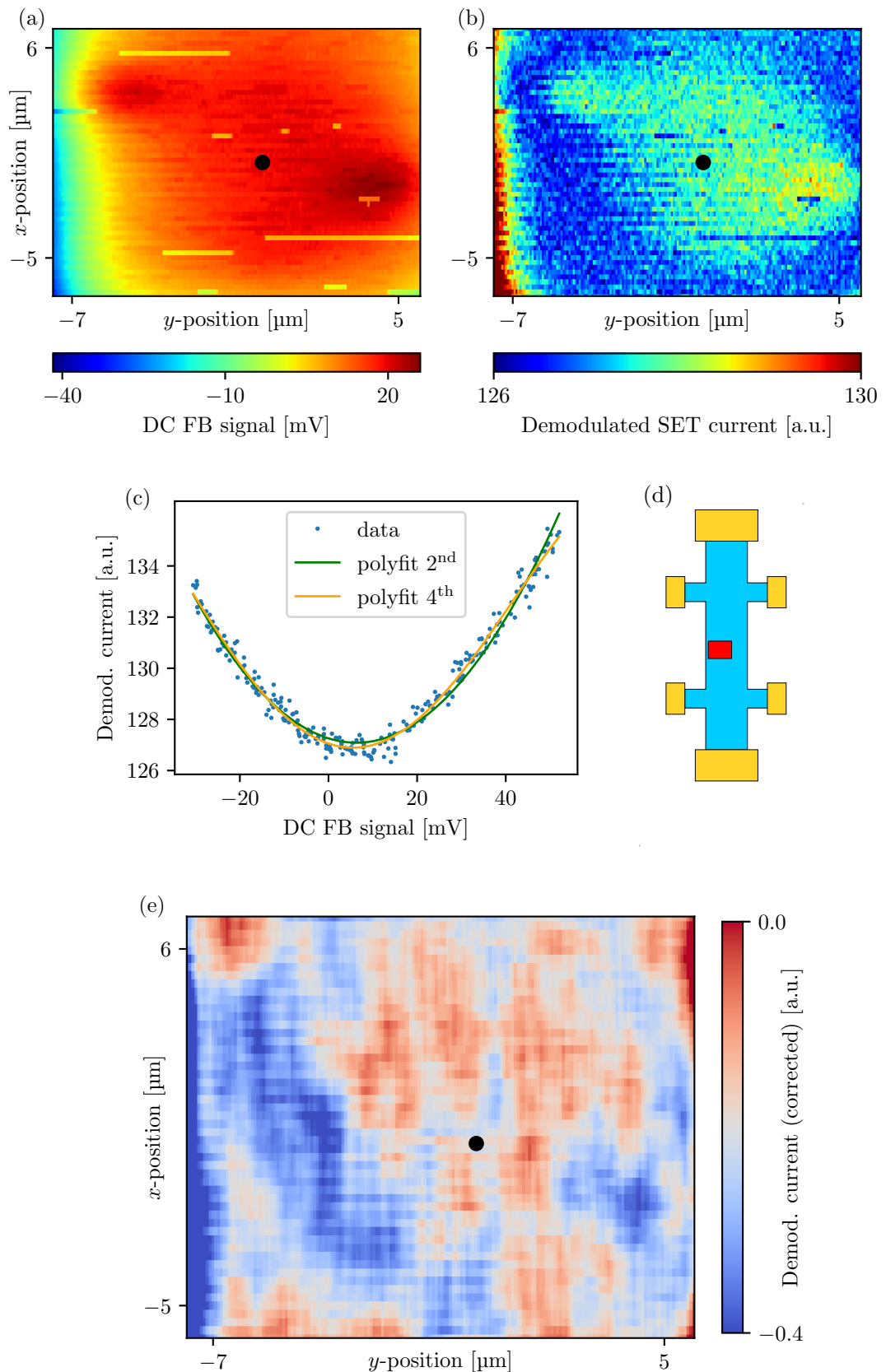


Figure 9.4: Data obtained with one SET during a scan over a Hall bar area. (a) Obtained DC feedback loop signal necessary to keep the current through the SET constant. (b) Demodulated amplitude of SET current. (c) Unexpectedly, the demodulated amplitude depends on the DC feedback signal. (d) Sketch of the scan position above the Hall bar. (e) Corrected demodulated amplitude. To obtain this graph the data in (a) is compared with (c), and the ordinate value is subtracted from (b).

figure 9.4 (c). The polynomial of 2nd order shows deviations around $V_{\text{COM}} \approx 0$ mV, and above 20 mV. But the quartic polynomial of 4th order describes the data well. It is used in the following to correct the demodulated SET current in (b).

At the moment the origin of the quartic-like dependency between demodulated amplitude and DC feedback signal is not clarified. Especially an increase of the amplitude in both directions - the positive and negative feedback signal regime - is not explainable. The following possibilities would lead to a dependence: (1) In case the feedback loop would loose the working point, a potential difference between SET and underlying 2DES becomes present. A shift of the CBO and thus I_{SET} is expected. But, for such a shift the slope of the CBO should decrease¹ or monotonously change in one direction. (2) An influence of our self-built electronics may be considered. Resistor tolerances can result in a dependence $V_{\text{DS}}(V_{\text{COM}})$ of the SET bias voltage V_{DS} on V_{COM} , which is added commonly (e.g. seen in [87]); then the added voltage is not exactly equal for source and drain, changing V_{DS} . Hence, the CBO amplitude changes what leads to a change of the working point on the CBO and thus, to a change of the slope we are probing. But, these tolerances usually lead to a monotonous dependence $V_{\text{DS}}(V_{\text{COM}})$, because one lead electrode gets more/less voltage added, compared to the other one. Quartic-like dependencies were not yet observed in our group.

Furthermore, it is unclear why the polynomial of 2nd order does not fit to the data. The appearance of a parabolic term in the equations derived in section 5.1 may be explainable for some situations. The appearance of a quartic term is not obvious.

In the following we try to correct our data by this dependency observed in figure 9.4 (c). Each data point in figure 9.4 (a) is now mapped with figure 9.4 (c) to a correction value for the demodulated amplitude. These corrections are then subtracted from the data shown in (b). The corrected demodulated current amplitude is shown² in figure 9.4 (e).

After this correction, an entirely homogeneous 2DES would lead to a graph with a homogeneous color. The color would be similar to the one around the region $(x, y) = (0 \mu\text{m}, 0 \mu\text{m})$ and a value around zero is expected. It is obvious that the corrected demodulated signal in the scanned area is not constant.

The following can be seen: (1) Towards the left scan range limit - this is in direction of the left Hall bar edge (see figure 9.4 (d)) - a lower value, indicated

¹Normally the working point is defined as the current I_{SET} , where $\partial I_{\text{SET}}/\partial V_i$ has its highest value. This ensures the highest sensitivity.

²In order to reduce the pixel noise, a Savitsky-Golay- filter is applied.

by a darker blue region is observed. (2) The bulk region shows mainly connected regions that are either blue or red. The geometrical form of the red areas seems to be droplet-like.

In order to obtain more reliable results³ to make statements about capacitive couplings and compressibility, firstly the origin of the dependency between demodulated amplitude and DC feedback signal has to be clarified. Then, a systematic measurement series over a quantum Hall plateau can be performed.

9.3 Proposal for another method - using several SETs

Another way to probe the compressible/incompressible landscape can take advantage of the fact that our SET array hosts eight independent SETs. They have a distance of $4\mu\text{m}$ to each other and they can be used simultaneously. This is indicated in figure 9.5 (a). In the following, one SET⁴ is used to electrostatically stimulate the underlying 2DES locally, while at least one neighboring SET acts as local probe; they will be called stimulator and probe, respectively.

The idea is now the following: A small AC voltage with a frequency ω is applied commonly to both lead electrodes of the stimulator in order to modulate its potential with respect to the 2DES. The probing SET is operated with an activated feedback loop to keep its current constant on a predefined value. This feedback signal is then demodulated with the same frequency ω to determine how much of the stimulator signal is detected by the probe. This demodulated amplitude depends on the underlying electrostatic compressibility of the 2DES below both SETs. The following four cases - that result from the capacitive arrangement shown in figure 9.5 (b) - which are shown in figures 9.5 (c) to (f) can be distinguished:

1. When the 2DES under both SETs is electrically incompressible (c), the 2DES electrons cannot screen the electrostatic potential difference that is locally induced by the stimulator. The incompressible 2DES has an electrically insulating like character. The capacitive coupling between stimulator and probe might be small.
2. When a small compressible region appears between both SETs (d), this region is capacitive coupled to both SETs. More precisely, the capacitive coupling

³Without the necessary correction we would expect the blue regions to be incompressible.

⁴Not necessarily an SET has to be used to stimulate the 2DES. It would be also possible to make use of a completely metal covered tip which electrical potential can be modulated.

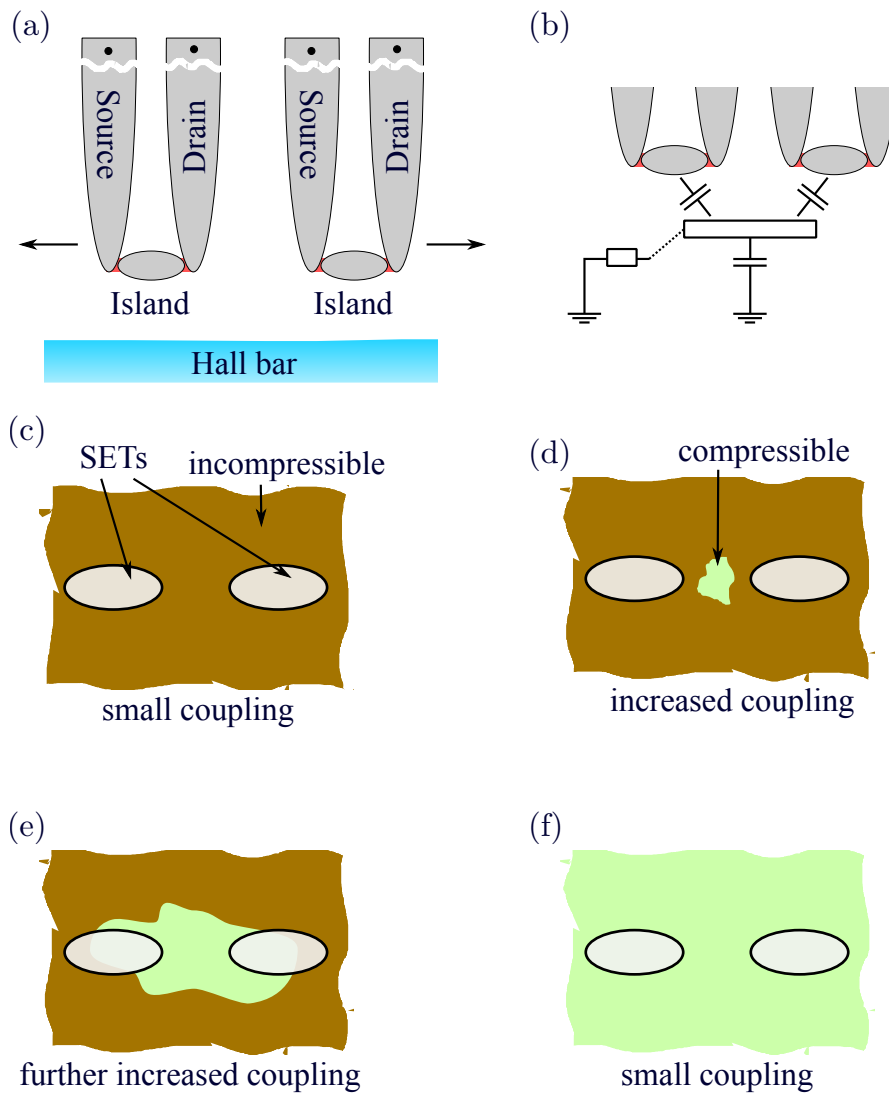


Figure 9.5: (a) Two SETs are used simultaneously to probe the compressible/incompressible landscape. One SET acts as stimulator, its potential is modulated, and one SET acts as probe, its feedback loop signal is demodulated at the same frequency. (b) Circuit schematic that illustrates the given situation, e.g. the capacitive coupling of both SETs to the underlying droplet and couplings of the droplet itself. The following situations can be extracted: (c) In case the 2DES is entirely incompressible the isolating character leads to a small capacitive coupling and a small demodulated signal. (d) This increases as a compressible droplet is present between both SETs. (e) When the region below both SETs is mostly compressible, a large signal is expected. (f) When the 2DES is completely compressible, coupling to the Hall bar electrodes leads to a fixed local potential of the 2DES and this suppresses the capacitive coupling between stimulator and probe.

between both SETs increases. Consequently, the demodulated amplitude increases.

3. When a large compressible droplet lies between and under both SETs, see (e), a strong capacitive coupling between the SETs is present. Thus, the highest oscillation amplitude is expected in this situation.
4. When the whole 2DES is expected to be electrically compressible, the 2DES has a non-zero conductivity σ_{xx} which fixes the potential of these compressible regions. An oscillation induced by the stimulator is expected to be not measurable with the probe.

First prototype measurements to verify the functionality of this measurement technique were performed by the master student Maurizio Bono [87]. A planar SET evaporated on a Hall bar surface is used as probe, while an evaporated gold finger acts as stimulator. His results are not completely understood while writing this thesis. Features could be identified in the measurements, but their origin may be affected for example by the sample design⁵. A first try in the scanning probe microscope indicated that the wiring with a wire length of about 2 m, induces capacitive cross-talk that is overlaid to the measurement signal. Hence, further tests are necessary in both systems to establish this measurement method.

9.4 Summary

In this section we proposed two measurement methods to probe the electrically compressible/incompressible landscape of the 2DES. We could demonstrate that a measurement method using a single SET gives first preliminary results; inhomogeneous regions in the scan range might be visible. Their origin could be a different capacitive coupling between SET island and local 2DES below it. Further measurements are necessary to extend these methods and results.

⁵To have a high outcome of working SETs usable at 1 K a lot of them were fabricated on the Hall bar surface, leading to an inhomogeneous electron density distribution.

Chapter 10

Summary

More than 30 years after the fractional quantum Hall effect was observed for the first time, many questions have been still unanswered. The main goal of this thesis was to use an one-dimensional single-electron transistor (SET) array as sensitive electrometer to locally probe Hall potential profiles in the fractional quantum Hall regime at temperatures below 40 mK to determine where an externally biased current is distributed inside a two-dimensional electron system (2DES). This investigation was done within a 2DES hosted by an (Al,Ga)As heterostructure.

Microscopic picture of the integer quantum Hall effect

This thesis started with an explanation of the microscopic picture of the integer quantum Hall effect. Strong magnetic flux densities lead to the formation of Landau levels that are separated by an energy gap; either by the cyclotron gap or the Zeeman gap. These gaps are responsible for the formation of electrically incompressible regions - with a well defined integer filling factor - within an otherwise compressible 2DES. In the classical Hall regime between two QH plateaus the sample is entirely compressible. A quantum Hall plateau is characterized by two regimes: In the edge-dominated QH regime incompressible stripes start to evolve at both sample edges, and move with increasing magnetic flux density towards the 2DES bulk where they merge and form an incompressible bulk in the bulk-dominated QH regime. Responsible for this evolution is an electron density profile that approaches zero towards the sample edges. A Hall voltage drop across an incompressible region tilts locally the Landau levels, leading to the same change of the electron group velocity for all occupied Landau levels beneath the Fermi energy. The resulting current density is directed perpendicularly to the magnetic field and Hall field directions; the current flow is dissipationless. If the current flow happens exclusively in incompressible regions of same local filling factor ν , a quantized Hall resistance $R_{xy} = h/(\nu e^2)$ is measured.

Scanning single-electron transistor array microscope

In this thesis a single-electron transistor array was used as sensitive local electrometer. A first major task in this thesis included modifications of an already existing fabrication process. It had to be transferred to new heterostructure substrates in order to make the process more reliable and independent of the heterostructure substrate. This was necessary as the original wafer material was no longer available; the wafer replica had variations in the aluminum concentration and showed defects, whereas the outcome of working SETs dropped below 20%. With the introduced improvements the substrate does not necessarily need a two-dimensional electron system anymore. In this way the outcome of working single-electron transistors could be improved from below 20% to 75%.

The single-electron transistor array includes eight independent SETs with an island size of about 155 nm by 220 nm each, separated by 4 μm to each other. Charging energies up to 175 μeV had been reached for these fabricated nano-scale electronic devices which makes them usable at temperatures below 140 mK, where they show well pronounced Coulomb-blockade regions.

Such low temperatures are also necessary to observe fragile fractional quantum Hall states. Measurements were done at temperatures below 40 mK in a $^3\text{He}/^4\text{He}$ dilution refrigerator - built up by M. Mausser - located within a highly vibrational reduced environment.

Measurement principle to probe Hall potential profiles

In order to use the eight single-electron transistors as sensitive local electrometers, three operation modes were introduced, namely a Coulomb-blockade oscillation (CBO) method, a DC feedback loop (DC FBL) method and an AC feedback loop (AC FBL) method.

The fastest way of operation is the CBO method; here the electric current through an SET, which depends on the electrostatic potential of the SET island that is influenced by its electrostatic surrounding, is directly measured. It is a periodic signal with potential variation, which is robust against fast electrostatic potential changes and enables to image electrostatic and capacitive couplings from the underlying sample to the SET island in order to navigate above the sample. By an analogue DC feedback loop circuit which keeps the relative electrostatic potential between SET lead electrodes and SET island constant, a working point on one Coulomb-blockade oscillation can be held and the normally oscillating CBO signal is linearized. Hereby it becomes possible to track whether the mathematical

product of potential change and capacitive coupling is increasing or decreasing. In the AC feedback loop method the DC feedback loop is extended by a small alternating potential change which is applied to the underlying 2DES. In this way, the AC feedback loop signal includes only information about the capacitive coupling between SET island, 2DES and stray capacitances.

To access electrostatic potential changes of the 2DES which result solely from an externally biased current - and not from charged particles nor capacitive coupling changes to the 2DES - a two-step measurement technique was used. The AC FBL method is used, while for a first trace (α -trace), a rectangular shaped AC current is applied to the 2DES, and for a second trace (β -trace), the 2DES potential is periodically varied without any net current flow through the sample. A calibrated Hall potential profile that results only from an externally biased current is obtained by a division of the α -trace by the β -trace for identical tip positions.

A new method to extract the local current density distribution from calibrated Hall potential profiles, by calculating the derivative with respect to the SET tip position, was introduced in order to make a current flow more illustrative in a false-color representation of the data.

Hall potential profiles in the integer quantum Hall regime

During this thesis, systematic measurements of Hall potential profiles in the integer quantum Hall regime were performed with our new scanning single-electron transistor array microscope around integer filling factors $\nu \in \{3, 2, 1\}$. The obtained Hall potential evolution with an applied magnetic field in figure 10.1 shows a good agreement with former experimental results of a scanning electrostatic force microscope depicted in figure 3.4. It was demonstrated that around integer filling factors the Hall voltage drop across a Hall bar cross-section starts to deviate from its linear behavior; the Hall voltage drop is then located at the center position of corresponding electrically incompressible stripes - one at each sample side. An edge-dominated quantum Hall regime with a current flow close to the sample edges and a bulk dominated quantum Hall regime with a current flow exclusively in the sample center were observed; first one in the lower magnetic field side and the latter one in the higher magnetic field side of all investigated quantum Hall plateaus.

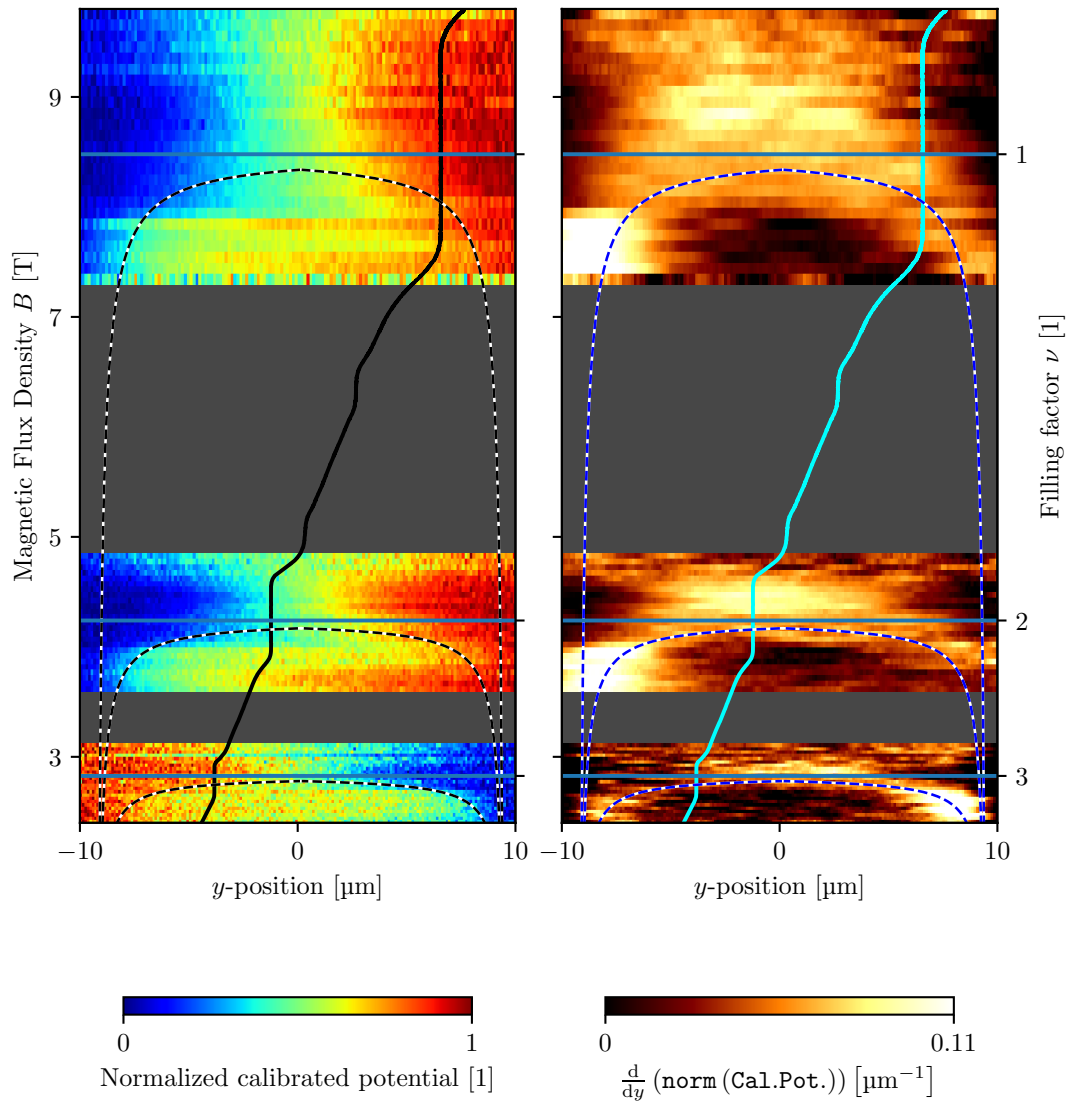


Figure 10.1: Hall potential profile evolution with applied magnetic flux density and corresponding local current density distribution in the integer quantum Hall regime. Hall voltage drop and increased current density follow the center position of incompressible stripe.

Hall potential profiles in the fractional quantum Hall regime

Subsequently, this thesis investigated for the first time the fractional quantum Hall regime with filling factors $\nu = 2/3$ and $\nu = 3/5$ with a scanning probe microscope to probe Hall potential profiles; the main focus was on the fractional state $\nu = 2/3$.

Firstly, the longitudinal resistance R_{xx} , obtained during transport measurements at different magnetic flux densities and varying applied bias voltage, in figure 7.2, revealed the electrical breakdown behavior of the $\nu = 2/3$ state. It has similarities to breakdown behaviors in the integer quantum Hall regime in figure 3.9. At the low magnetic field side of the quantum Hall plateau, the threshold voltage - before R_{xx} deviates from zero - increased with rising magnetic flux densities towards

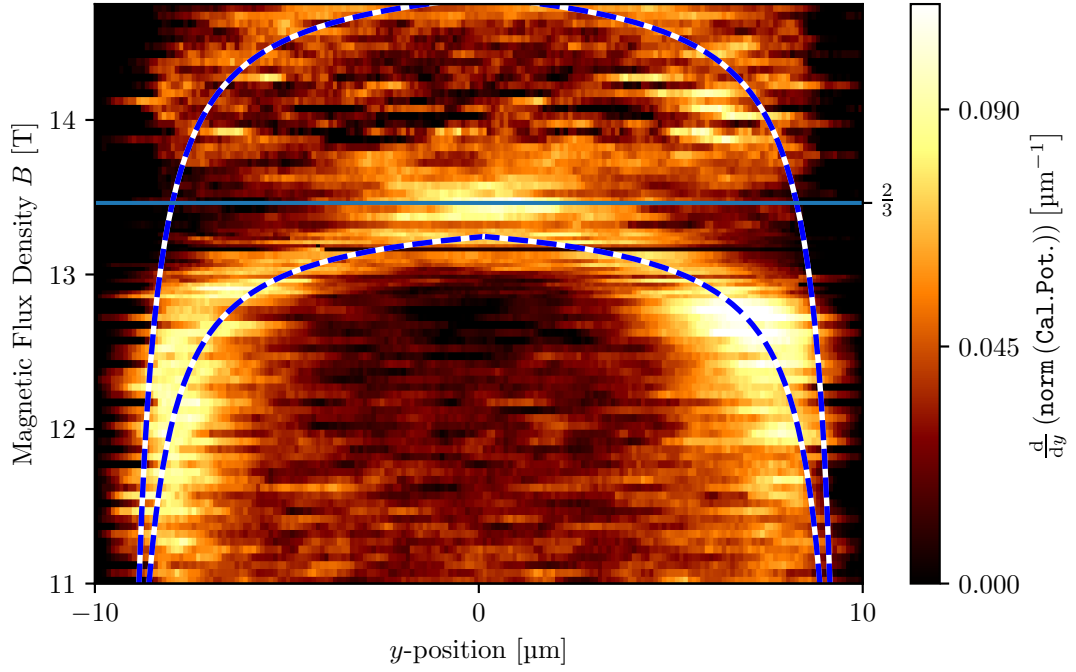


Figure 10.2: Local current density evolution with applied magnetic flux density probed in a Hall bar cross section around fractional filling factor $\nu = 2/3$.

$\nu = 2/3$. Close to $\nu = 2/3$ an abrupt drop of the breakdown threshold voltage was observed.

Locally probing the Hall potential profile evolution across the sample width - with varying magnetic flux density - showed that in the plateau region of $\nu = 2/3$ a high current density appears at the calculated center position of $\nu = 2/3$ incompressible stripes, see figure 10.2. Like in the integer quantum Hall regime, for $\nu = 2/3$, an edge-dominated and a bulk-dominated quantum Hall regime were observed. Between two (fractional) quantum Hall plateaus - in the classical Hall regime - the current flow is homogeneous over the sample width. The homogeneity of these three regimes was demonstrated with area scans of the Hall bar at corresponding magnetic flux densities.

Similar measurements were also shown for the more fragile fractional quantum Hall state $\nu = 3/5$. An evolution was observed that has been seen for $\nu = 2/3$; high local current densities follow the evolution of the center position of the $\nu = 3/5$ incompressible stripes, while mainly no current density is observed in other sample regions.

Is this behavior expected?

At the end of the thesis, a final discussion clarified, that the integer QH regime and the fractional QH regime have generally one thing in common: There is an evolution of the compressible/incompressible landscape within the 2DES which underlies the evolution of the current distribution in the 2DES.

The energy gap responsible for the appearance of this incompressibility is different in both regimes. In the integer quantum Hall regime a cyclotron gap or a Zeeman gap is present. In the fractional quantum Hall regime a specific ratio between magnetic flux quanta and number of electrons in the same area leads to many-body correlations. These correlations define the relative position of electrons. Also an energy gap opens which is protecting the 2DES against excitation. The energy gap leads in both regimes to the formation of these electrically incompressible regions within an electrically compressible 2DES. The current flow in incompressible regions happens dissipationless. Thus, the Hall voltage drop occurs in incompressible regions what leads to a tilt of the Landau levels there. This results in a center-of-mass motion of all occupied electronic states below the Fermi energy, the relative electron position is unimportant. The common electron movement in incompressible regions with well-defined (fractional) filling factor ν leads to a well-defined current density $j_x = \nu (e^2/h) E_y$. If all externally biased current flows within incompressible regions of same ν , the Hall resistance R_{xy} is quantized.

Hence, via the electrically compressible/incompressible landscape in the 2DES, there is a common microscopic picture for both quantum Hall regimes. It describes for all filling factors the distribution of the externally biased current within the 2DES.

Outlook

With the end of this PhD thesis, our scanning single-electron transistor array microscope will be used in further projects. In this last section we want to give a brief guideline about possible projects for coming PhD or master students, to continue with microscopic investigations of the integer and fractional quantum Hall effect (and beyond). The following listing is regardless of the order, as some projects can be realized in parallel.

New Hall sensor on a tip

In appendix E and K, a free-standing Hall sensor tip - compare figure 10.3 - which was developed within this thesis is introduced. With this new sensor a more direct access to the current distribution inside the 2DES - which induces a magnetic flux surrounding them - is possible. Even more, diamagnetic current which are already present in equilibrium are accessible now. This is a further milestone for the functionality of our scanning single-electron array microscope. Hall sensors can be fabricated on the same array with single-electron transistors creating a new hybrid-sensor array. Alternatively, the Hall sensor can be operated by its own; it can detect either electrostatic influences that change its electron concentration or detect magnetic flux densities. A calculation showed that both contributions can be separated when a feedback loop keeps the voltage drop along the Hall sensor constant; magnetic flux density changes are represented in the Hall voltage, while electrostatic influences are projected to the feedback signal.

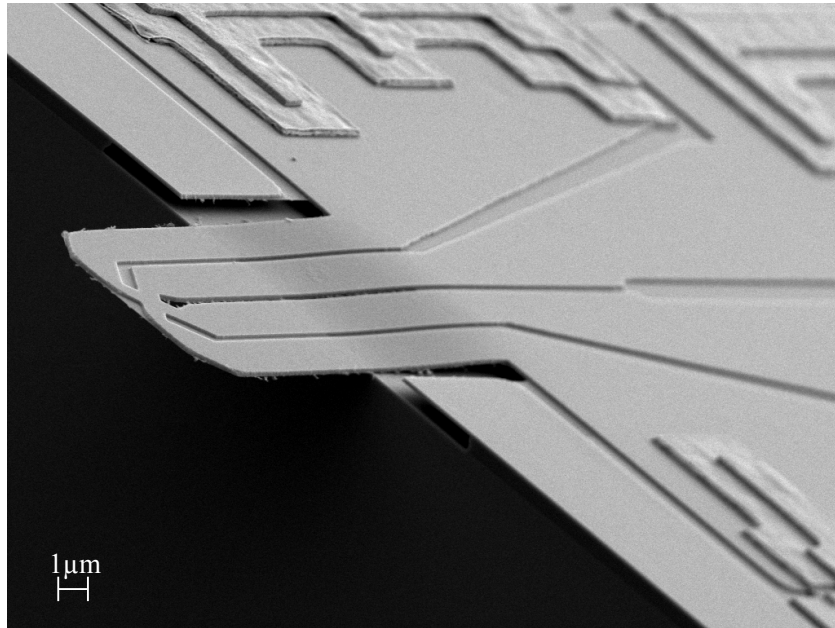


Figure 10.3: Hall sensor on a free-standing tip that was developed within this thesis to probe local magnetic flux densities in order to access also diamagnetic equilibrium currents which are not accessible with an SET. This sensor is designed in a way that it can be fabricated together with SETs on the same array to build a hybrid-sensor array.

Access equilibrium currents with a freestanding Hall sensor

Diamagnetic currents¹, which are present in equilibrium, result directly from a Landau level bending in incompressible regions. They encircle compressible regions, without carrying a net current through the sample. With single-electron

¹Sometimes they are also referred to as persistent currents.

transistors as probes, only changes in the electrostatic potential compared to equilibrium are detectable and thus, diamagnetic currents are not accessible. For this reason, a Hall sensor on a tip had been developed within this thesis, which is capable to detect magnetic fields induced by diamagnetic currents. While this thesis was written, the functionality of the sensor was demonstrated and next steps to scan above a Hall bar around 1.4K are initiated. Further details can be found in appendix E.

Temperature distribution under quantum Hall conditions

The single-electron transistor characteristics can be used to determine its absolute temperature. This can be used to generate a temperature map of a Hall bar which is under quantum Hall conditions. Dependent on the working temperature, two methods can be used: (1) In the low temperature regime where pronounced Coulomb-blockade is observed, the broadening of the CBO peak can be used [21, 88]. (2) In the high temperature regime, thermal activated tunneling is responsible that a Coulomb-blockade is not pronounced; only a deviation from the linear I-V characteristics is observed around $V_{DS} = 0$. This non-linearity depends on the SET temperature [21, 88]. Further details can be found in appendix F.

Probing fractional quantum Hall states with $\nu > 1$

Currently, only fractional quantum Hall states with filling factors ν smaller than 1 have been investigated with our scanning single-electron transistor array microscope. For $\nu < 1$, only the lowest Landau level is partially occupied. On the other hand, also fractional quantum Hall states with fractions $\nu > 1$ have been observed, compare figure 4.11, where more than one Landau level is occupied. Directly after writing this thesis a Hall potential evolution with B will be probed around fractional states $\nu = 4/3$ and $\nu = 5/3$ (in this order). Relating to the microscopic picture of the quantum Hall effect, the same evolution of the Hall potential profiles and the current density is expected.

Probing the anomalous quantum Hall effect

Magnetic topological insulators having a ferromagnetic ordering and strong spin-orbit coupling show an anomalous quantum Hall effect (AQHE) [89]. Locally probing the current distribution within these material systems could clarify the validity of the microscopic picture of the quantum Hall effect within the AQHE. In terms of the microscopic picture of the quantum Hall effect, a similar current evolution as for IQHE and FQHE is expected. A current flow exclusively in in-

compressible regions with the same local filling factor leads to quantized values of R_{xy} .

Probe spatially resolved chemical potential variations

If a 2DES is in thermodynamic equilibrium, then the electrochemical potential $\mu_{\text{elch}}(\mathbf{r}, B) = \mu_{\text{ch}}(\mathbf{r}, B) - e\phi(\mathbf{r})$ is constant over the whole 2DES. Thus, a change of the chemical potential $\mu_{\text{ch}}(\mathbf{r}, B)$ is directly represented in an electrostatic potential change $-e\phi(\mathbf{r})$. This electrostatic potential change can be measured with an SET in order to determine changes in $\mu_{\text{ch}}(\mathbf{r}, B)$, what was already experimentally measured in spatially stationary cases [7, 84, 87, 90]. In a next step, the scanning probe microscope will be used to probe $\mu_{\text{ch}}(\mathbf{r}, B)$ position-dependent. At temperatures below 1 K, hysteretic effects [84] make it necessary to measure the feedback signal during both magnetic field sweeps as $\Delta V_{\text{COM}}^{B\uparrow} + \Delta V_{\text{COM}}^{B\downarrow} = 2\Delta\mu_{\text{ch}}/e$. For fractional states, also an averaging may be necessary. Compare hereto appendix G.

Enhance SET array working temperature to 1.4 Kelvin

In a next step, it is favorable to make our single-electron transistors on a tip working in our second scanning probe microscope, which is operated around 1.4 K. To achieve this, the charging energy E_C has to be increased by a reduction of the overlap between SET island and the lead electrodes source and drain. In appendix H, necessary further steps are explained.

Kapitel 11

Deutsche Zusammenfassung

Mehr als 30 Jahre, nachdem der gebrochenzahlige Quanten-Hall-Effekt zum ersten Mal beobachtet wurde, sind noch viele Fragen offen. Das Ziel dieser Doktorarbeit bestand darin, unter Zuhilfenahme eines eindimensionalen Arrays aus acht Einzel-elektronentransistoren (SETs) als empfindliche Elektrometer, Hall-Potentialprofile im gebrochenzahligen Quanten-Hall-Regime zu messen. Damit sollten Rückschlüsse auf die Stromverteilung des extern angelegten Stromes innerhalb der Probe erhalten werden. Untersucht wurde hierfür ein zweidimensionales Elektronensystem (2DES) innerhalb einer (Al,Ga)As Heterostruktur bei Temperaturen von weniger als 40 mK.

Mikroskopisches Bild des ganzzahligen Quanten-Hall-Effekts

Zu Beginn dieser Arbeit wurde in Kapitel 3 das mikroskopische Bild des ganzzahligen Quanten-Hall-Effekts (QHE) eingeführt. Hohe magnetische Flussdichten führen in einem 2DES zur Ausbildung von Landau-Niveaus, die energetisch durch eine Energielücke zueinander separiert sind. Die Energielücke kann hierbei entweder die Zyklotron-Aufspaltung oder die Zeeman-Aufspaltung sein. Diese Energielücken sind ihrerseits dafür verantwortlich, dass sich elektrisch inkompressible Regionen - mit einem ganzzahligen Füllfaktor - innerhalb eines ansonsten kompressiblen 2DES ausbilden. Zwischen zwei Quanten-Hall-Plateaus, dem klassischen Hall-Regime, ist das 2DES ganzheitlich kompressibel. Ein Quanten-Hall-Plateau wiederum kann in zwei Bereiche eingeteilt werden: Im randdominierten QHE bildet sich jeweils ein inkompressibler Streifen an beiden Probenrändern aus, welche mit zunehmender magnetischer Flussdichte in das Innere des 2DES wandern. Dort vereinen sich beide Streifen und führen somit zu einem vom Probeninneren dominierten QHE, charakterisiert durch ein hauptsächlich inkompressibles Probeninneres. Verantwortlich für diese Evolution ist das inhomogene Elektronendichteprofil des 2DES. In Richtung Probenrand fällt dieses von seinem Wert im Probeninneren auf einen Wert von Null

ab. Weiterhin zeigen metallische Kontakte, die u.a. zur Bestimmung von lokalen Potentialen genutzt werden, eine vergleichbare Verarmung der Elektronendichte an ihrem Übergang zum 2DES. Dadurch entsteht dort ebenfalls ein inkompressibler Streifen, ähnlich zum Probenrand. Ein Hall-Spannungsabfall über inkompressible Bereiche führt lokal zu einer räumlichen Verkipfung der Landau-Niveaus, was wiederum zu einer gemeinsamen Veränderung der Gruppengeschwindigkeit aller Elektronen unter der Fermi-Energie führt. Die resultierende Stromdichte bewegt sich senkrecht zum angelegten Magnetfeld und dem elektrischen Hall-Feld und ist somit dissipationsfrei. Fließt der gesamte extern aufgeprägte Strom ausschließlich über inkompressible Regionen des selben Füllfaktors ν innerhalb eines Querschnittes eines 2DES, wird dort ein quantisierter Hall-Widerstand $R_{xy} = h/(\nu e^2)$ gemessen.

Einzelelektronentransistoren zur Rastersondenmikroskopie

Als erste Aufgabe musste der bereits bestehenden Fabrikationsprozess von Einzelelektronentransistoren (SETs) auf einer Spitzenstruktur, welche später als Sonden verwenden wurden, abgewandelt werden. Die SET-Fabrikation musste auf neue Heterostruktursubstrate angepasst werden, da die ursprüngliche Heterostruktur nicht mehr verfügbar war, und die im Vorfeld angefertigten Replikationen starke Variationen der Aluminiumkonzentration, sowie Kristalldefekte aufwiesen. Mit den replizierten Heterostrukturen fiel die Ausbeute von funktionierenden SETs auf unter 20 %. Durch die hier eingeführten Verbesserungen konnte die Fabrikation zuverlässiger und vor allem unabhängiger vom Ausgangsmaterial gemacht werden. Die verwendete Heterostruktur muss nun nicht mehr zwangsläufig ein zweidimensionales Elektronensystem enthalten. Auf diesem Weg konnte die Ausbeute von funktionierenden Einzelelektronentransistoren von unter 20 % auf 75 % gesteigert werden.

Die acht unabhängigen Einzelelektronentransistoren wurden in Abbildung 4.7 gezeigt. Diese SETs befinden sich zusammen auf einem Array und sind jeweils $4\ \mu\text{m}$ voneinander entfernt. Jede SET-Insel besitzt eine räumliche Ausdehnung von $155\ \text{nm}$ auf $220\ \text{nm}$. Dabei erreichte die Einzelelektronenladeenergie der hier hergestellten SETs Werte von bis zu $175\ \mu\text{eV}$, wodurch diese bei Temperaturen von unter $140\ \text{mK}$ ausgeprägte Coulomb-Blockade-Regionen zeigen und somit funktionsfähig sind.

Solch niedrige Temperaturen sind ebenfalls notwendig, um sehr anfällige gebrochenzahlige Quanten-Hall-Zustände (Abbildung 4.11) zu beobachten. Daher wurden alle Messungen in einem $^3\text{He}/^4\text{He}$ Mischkryostaten, der zusammen mit un-

serem Rastersondenmikroskop (Abbildung 4.1) von M. Mausser aufgebaut wurde und sich in einer sehr vibrationsisolierten Laborumgebung befindet, bei Temperaturen von unter 40 mK durchgeführt.

Messverfahren zur Bestimmung von Hall-Potentialprofilen

Zur Verwendung der Einzelelektronentransistoren auf Spitzen als Elektrometer, wurden in Kapitel 5 drei Messmethoden vorgestellt. Namentlich sind diese die Coulomb-Blockade-Oszillations-(CBO)-Methode, die DC-Rückkopplungsmethode (DC-FBL) und eine AC-Rückkopplungsmethode (AC-FBL).

Hierunter ist die CBO-Methode die schnellste. Der elektrische Strom durch einen SET wird kontinuierlich aufgezeichnet. Dieser hängt dabei vom elektrostatischen Potential der SET-Insel ab, welches von räumlich nahen Elektroden beeinflusst wird. Der Strom ändert sich dabei periodisch mit einer Potentialänderung. Diese Methode ist robust gegen schnelle Potentialänderungen und sie ermöglicht es, elektrostatische und kapazitive Kopplungen zwischen der Probe und der SET-Insel bildlich darzustellen, vergleiche Abbildung 5.3. Dies wird unter anderem zur Navigation über der Probe verwendet. Mittels einer analogen Rückkoppelschaltung, gezeigt in Abschnitt 5.4, kann der oszillierende Strom der CBO-Methode linearisiert werden. Dabei wird das elektrostatische Potential zwischen SET-Insel und SET-Zuleitungen konstant gehalten, um somit einen vordefinierten Arbeitspunkt auf einer einzelnen Coulomb-Blockade-Oszillation zu halten. Auf diese Weise wird ersichtlich, ob sich das mathematische Produkt aus kapazitiver Kopplung und Potentialänderung positiv oder negativ ändert. In der AC-Rückkopplungsmethode, erläutert in Abschnitt 5.5, wird die DC-Rückkopplungsschaltung erweitert: Eine kleine, periodisch oszillierende Potentialänderung wird an das 2DES angelegt und das DC-Rückkopplungssignal auf gleicher Frequenz analysiert. Das somit erhaltene AC-Rückkoppelsignal enthält nur noch Informationen über die kapazitive Kopplung zwischen SET-Insel und 2DES, sowie zu (meist vernachlässigbaren) Streukapazitäten.

Um Potentialänderungen nachweisen zu können, die durch das Anlegen eines externen Stroms verursacht werden, und nicht durch geladene Partikel oder die Änderungen der kapazitiven Kopplung zum 2DES, sind zwei aufeinanderfolgende Messungen unvermeidbar. Diese wurden in Abschnitt 5.7 erläutert. Zuerst wird ein sogenannter " α -trace" gemessen, bei welchem eine periodisch modulierte, rechteckförmige Spannung zu einem Strom durch die Hall-Probe führt. Zur Messung wird die AC-FBL Methode verwendet. In der zweiten Messung, dem sogenann-

ten " β -trace", wird das Potential des 2DES ganzheitlich mit derselben Spannung periodisch variiert, jedoch ohne dass es zu einem Nettostromfluss durch die Hall-Probe kommt. Ein Hall-Potentialprofil, kalibriert auf die angelegte Wechselspannung, wird durch die Division des α -trace durch den β -trace erreicht. Bei dieser Methode ist zu beachten, dass jeweils die selbe Linie entlang der Probe gemessen wird.

Zudem wurde in Abschnitt 5.8 eine neue Methode eingeführt, womit aus den kalibrierten Hall-Potentialprofilen die lokale Stromdichteverteilung extrahiert werden kann. Dies wird über eine Ortsableitung der Hall-Potentialprofile entlang der SET Spitzenposition erreicht. Es ist nun möglich die Stromdichteverteilung anschaulich in einem Falschfarbenbild darzustellen.

Hall-Potentialprofile im ganzzahligen Quanten-Hall-Regime

Während dieser Arbeit wurde unser neues Rastersondenmikroskop zuerst dazu verwendet in Kapitel 6 systematische Messungen von Hall-Potentialprofilen im ganzzahligen Quanten-Hall-Regime, um die Füllfaktoren $\nu \in \{3, 2, 1\}$ herum, durchzuführen. Die beobachtbare Entwicklung der Hall-Potentialprofile mit einem von außen angelegten Magnetfeld, wie in Abbildung 11.1 zu sehen, zeigt eine gute Übereinstimmung zu Ergebnissen aus früheren Experimenten (Abbildung 3.4), die mit einem älteren Rastersondenmikroskop bei höheren Temperaturen und anderen Sonden erhalten wurden.

Es konnte gezeigt werden, dass innerhalb eines Magnetfeldbereichs um den ganzzahligen Füllfaktor herum der Hall-Spannungsabfall über die Probenbreite von seinem linearen Verlauf abweicht (Abbildung 6.2). Die Position des Spannungsabfalls - einer an jeder Probenseite - folgt dabei der berechneten Mittelpunktskoordinate der jeweiligen elektrisch inkompressiblen Streifen. Ein randdominierter Quanten-Hall-Bereich mit einer erhöhten Stromdichteverteilung nahe des Randes und ein vom Probeninneren dominierter Bereich mit einer erhöhten Stromdichteverteilung innerhalb des Probeninneren wurde für alle untersuchten Quanten-Hall-Plateaus beobachtet; ersterer befindet sich im Niedermagnetfeldbereich eines Quanten-Hall-Plateaus, während sich zweiterer auf der Hochmagnetfeldseite des Plateaus befindet.

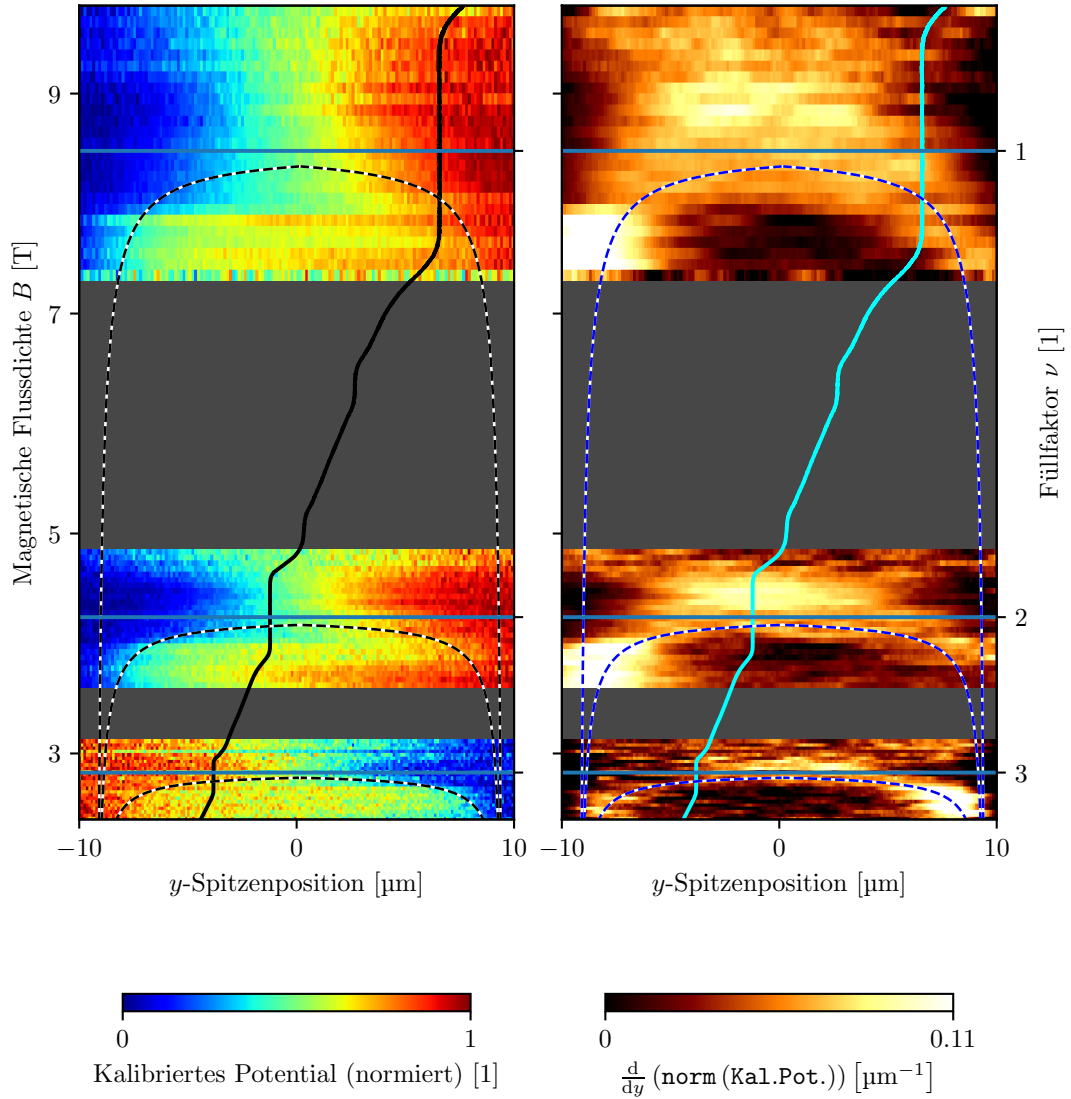


Figure 11.1: Gezeigt ist die Entwicklung der Hall-Potentialprofile mit einer angelegtem magnetischer Flussdichte, und die daraus resultierende Stromdichteverteilung, während sich die Probe im ganzzahligen Quanten-Hall-Bereich befindet. Hall-Spannungsabfall und erhöhte Stromdichten folgen den berechneten Mittelpunktskoordinaten der entsprechenden elektrisch inkompressiblen Streifen, welche sich vom Probenrand in das Innere ausbreiten.

Hall-Potentialprofile im gebrochenzahligen Quanten-Hall-Regime

Danach wurde in Kapitel 7 zum ersten Mal der gebrochenzahlige Quanten-Hall-Effekt mittels unseres Rastersondenmikroskopes untersucht und Hall-Potentialprofile um die Füllfaktoren $\nu = 2/3$ und $\nu = 3/5$ gemessen. Das Hauptaugenmerk lag hierbei auf den besser ausgeprägten, gebrochenzahligen Füllfaktor $\nu = 2/3$ gerichtet.

Zuerst wurde der Längswiderstand R_{xx} (Abbildung 7.2) bei verschiedenen magnetischen Flussdichten und Versorgungsspannungen V_{DS} gemessen. Er gibt Aufschluss über das Zusammenbruchverhalten des Quanten-Hall-Effekts mit Füllfaktor $\nu = 2/3$. Dieses zeigt Übereinstimmungen mit Beobachtungen, die innerhalb des ganzzahligen QHE gewonnen wurden (Abbildung 3.9). Mit ansteigender magnetischer Flussdichte in Richtung $\nu = 2/3$ wurde im Niedermagnetfeldbereich des Quanten-Hall-Plateau ein Anstieg der möglichen Spannung V_{DS} beobachtet, bevor es zu Abweichungen von $R_{xx} = 0$ kam. Nahe an $\nu = 2/3$ konnte ein abrupter Abfall dieser höchstmöglichen Spannung beobachtet werden.

Lokale Messungen von Hall-Potentialprofilen über einen Probenquerschnitt (Abbildung 7.7) zeigten eine Entwicklung der Position des Hall-Spannungsabfalls mit variierender magnetischer Flussdichte. In der Plateauregion um $\nu = 2/3$ wird eine erhöhte Stromdichte an Positionen gefunden, an welchen sich der berechnete, in-

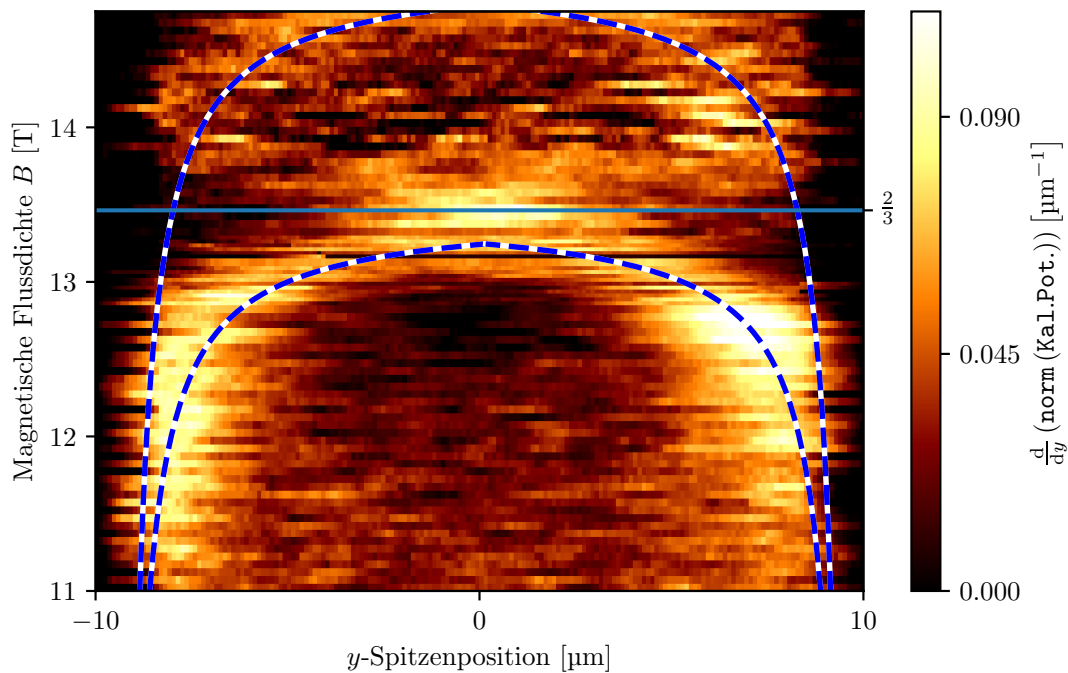


Figure 11.2: Entwicklung der lokalen Stromdichte über einem Querschnitt der Hallbar, gemessen als Funktion der angelegten magnetischen Flussdichte, um den gebrochenzahligen Füllfaktor $\nu = 2/3$ herum.

kompressible Streifen mit Füllfaktor $\nu = 2/3$ befindet, vergleiche Abbildung 11.2. Dabei zeigten andere Bereiche eine verschwindende Stromdichte. Wie bereits zuvor für den ganzzahligen QHE konnte auch für $\nu = 2/3$ ein randdominierter und ein vom Probeninneren dominierter Magnetfeldbereich innerhalb des Quanten-Hall-Plateaus identifiziert werden. Für magnetische Flussdichten zwischen zwei (gebrochenzahligen) Quanten-Hall-Plateaus wurde eine homogene Stromdichteverteilung über die Probenbreite gefunden. Diese drei unterschiedlichen Verhalten wurden durch das Abrastern einer Probenfläche weiter untersucht und ein homogenes Verhalten entlang der Probe konnte demonstriert werden.

Vergleichbare Messungen wurden in Abschnitt 7.9 ebenfalls für den fragileren gebrochenzahligen Quanten-Hall-Zustand $\nu = 3/5$ gezeigt. Dieselbe Entwicklung wie für $\nu = 2/3$ wurde beobachtet: Hohe lokale Stromdichten folgen der Entwicklung der Mittelpunktskoordinate des $\nu = 3/5$ inkompressiblen Streifens, während andere Bereiche des 2DES keine Stromdichte aufweisen.

Ist dieses Verhalten zu erwarten?

Am Ende dieser Arbeit, in Kapitel 8, wurde innerhalb einer abschließenden Diskussion geklärt, dass der ganzzahlige und der gebrochenzahlige Quanten-Hall-Bereich eines gemeinsam haben: Es gibt eine Entwicklung einer elektrisch kompressiblen/inkompressiblen Landschaft innerhalb des 2DES, welcher der Entwicklung der Stromdichteverteilung zugrunde liegt.

Die für das Auftreten von elektrisch inkompressiblen Bereichen verantwortliche Energielücke unterscheidet sich in beiden Quanten-Hall-Bereichen: Im ganzzahligen Quanten-Hall-Bereich sind quantisierte Landau-Niveaus vorhanden, die energetisch durch die Zyklotronenergie oder Zeemanenergie separiert sind. Im Falle des gebrochenzahligen Quanten-Hall-Effekts führt ein spezielles Verhältnis von magnetischen Flussquanten und Anzahl an Elektronen innerhalb der selben Fläche zu Vielteilchenkorrelationen. Dabei definiert diese Korrelation die Relativposition der Elektronen zueinander und es bildet sich eine Energielücke aus, die Anregungen im 2DES verhindert. Die Energielücke führt ihrerseits zur Ausbildung von elektrisch inkompressiblen Streifen in einem ansonsten elektrisch kompressiblen 2DES. Der Stromfluss in inkompressiblen Bereichen ist dissipationsfrei. Deswegen geschieht der Hall-Spannungsabfall in inkompressiblen Bereichen, was dort zu einer räumlichen Verkippung der Landau-Niveaus führt. Das führt zu einer Änderung der Gruppengeschwindigkeit aller besetzten elektronischen Zustände unterhalb der Fermi-Energie und alle Elektronen bewegen sich gemeinsam. Die relative Positi-

on der einzelnen Elektronen wird unwichtig. Diese gesamtheitliche Bewegung der Elektronen innerhalb von inkompressiblen Regionen mit einem wohldefinierten (gebrochenzahligen) Füllfaktor führt dann zu einer wohldefinierten Stromdichte $j_x = \nu (e^2/h) E_y$. Fließt der gesamte extern aufgeprägte Strom in inkompressiblen Bereichen gleichen Füllfaktors ν ist der Hall-Widerstand R_{xy} quantisiert.

Über die elektrisch kompressible/inkompressible Landschaft in einem 2DES gibt es ein gemeinsames mikroskopisches Bild für beide Quanten-Hall-Bereiche. Es beschreibt für alle Füllfaktoren die Verteilung des extern aufgeprägten Stroms innerhalb des 2DES.

Ausblick

Nach Beendigung dieser Arbeit wird unser Rastersondenmikroskop natürlich weiterhin in Folgeprojekten verwendet werden. In diesem letzten Abschnitt möchte ich für kommende Doktoranden bzw. Masterstudenten eine kurze Agenda über mögliche Folgeprojekte geben. Es handelt sich hierbei um weitere Untersuchungen des ganzzahligen und gebrochenzahligen Quanten-Hall-Effekts und um Projekte, die darüber hinaus gehen. Die folgende Liste ist ungeachtet der Reihenfolge, da einige Projekte parallel bearbeitet werden können.

Neuer Sensortyp - Hall-Sensor auf einer Spitze

Im Rahmen dieser Arbeit wurde zusätzlich ein freistehender Hall-Sensor entwickelt, der in einer Aufnahme durch ein Rasterelektronenmikroskop in Abbildung 11.3 zu sehen ist. Dieser erweitert die Funktionalität unseres Rastersondenmikroskops deutlich. Mit diesem Sensortyp ist es möglich, die Stromdichteverteilung innerhalb eines 2DES in einer direkteren Methode zu messen. Detektiert wird hierbei die vom Stromfluss induzierte magnetische Flussdichte und nicht wie bei einem SET ein elektrostatisches Potential. Dadurch werden nun auch diamagnetische Ströme, die bereits im Gleichgewicht innerhalb der Probe fließen, zugänglich. Die Einsetzbarkeit dieses neuen Sensors im Rahmen der Rastersondenmikroskopie konnte bereits in zwei Projekten bestätigt werden. Nähere Informationen sind im Anhang E und im Anhang K dieser Arbeit, sowie in [91] zu finden.

Der Fabrikationsprozess ist so konzipiert, dass die Hall-Sensoren mit Einzelelektronentransistoren gemeinsam auf einem Array prozessiert werden können. Dadurch wird ein neues Hybrid-Sensor-Array möglich. Ist das nicht gewünscht, kann der Hall-Sensor problemlos alleine verwendet werden. Neben magnetischen Flussdichten können auch elektrostatische Effekte mittels des Feld-Effekts detektiert

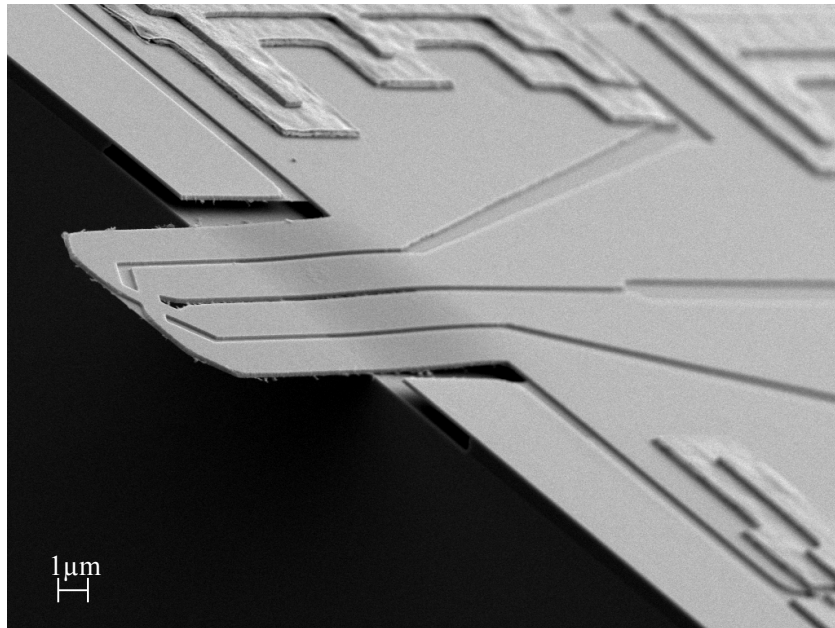


Figure 11.3: Hall-Sensor auf einer freistehenden Spitze, der während dieser Arbeit entwickelt wurde, um lokal magnetische Flussdichten zu detektieren. Somit wird das Messen von diamagnetischen Strömen im Gleichgewicht ermöglicht, welche mit einem SET bisher nicht zugänglich sind. Der Fabrikationsprozess des Sensors ist so konzipiert, dass SETs und Hall-Sensoren gemeinsam auf einem Array hergestellt werden können und somit ein neues Hybrid-Sensor Array möglich wird.

werden, welcher zu einer Elektronendichteveriation innerhalb des Sensors führt. Dabei zeigte eine Berechnung in Anhang E, dass beide Signalanteile getrennt werden können, wenn mittels einer Rückkoppelschaltung der Spannungsabfall über den aktiven Bereich des Hall-Sensor konstant gehalten wird. Änderungen der magnetischen Flussdichte werden dann in der Hall-Spannung abgebildet, während elektrostatische Einflüsse auf die Elektronendichte im Rückkoppelsignal abgebildet werden.

Diamagnetische Ströme mit einem freistehenden Hall-Sensor sichtbar machen

Diamagnetische Ströme¹, welche bereits im Gleichgewicht der Probe vorhanden sind, resultieren von einer lokalen Verkipfung von Landau-Niveaus über elektrisch inkompressiblen Regionen. Diese Ströme umlaufen dabei elektrisch kompressible Bereiche, ohne dass im Querschnitt einer Hall-Probe ein Nettostrom fließt. Werden Einzelelektronentransistoren als Sonden eingesetzt, sind diese Ströme nicht nachweisbar, da nur Änderungen des elektrostatischen Potentials gegenüber der Gleichgewichtssituation gemessen werden können. Aus diesem Grund wurde innerhalb dieser Arbeit ein freistehender Hall-Sensor auf einer Spitze entwickelt.

¹Teilweise auch als Gleichgewichtsströme und persistente Ströme bezeichnet.

Dieser ist fähig die magnetische Flussdichte, welche von diamagnetischen Strömen hervorgerufen wird, zu detektieren. Zum Zeitpunkt als diese Arbeit geschrieben wurde, ist die Funktionalität dieses Sensors bereits demonstriert worden [91]. Der nächste Schritt ist die Messung einer Hall-Probe bei 1.4 K, um diese Ströme sichtbar zu machen. Teile dieses Projekts wurden bereits vorbereitet und weitere Details können im Anhang E gefunden werden.

Temperaturverteilung innerhalb einer Probe im QH-Regime

Ein Einzelelektronentransistor kann dazu verwendet werden, um seine absolute Temperatur zu bestimmen. Diese Eigenschaft kann ausgenutzt werden, um eine Probe unter Quanten-Hall-Bedingungen zu untersuchen. Ziel ist es eine orts aufgelöste Temperaturkarte entlang einer Hall-Probe aufzunehmen. Abhängig von der Arbeitstemperatur sind hierzu zwei Methoden denkbar: (1) im Niedertemperaturbereich, wenn der SET ausgeprägte Coulomb-Blockade-Bereiche zeigt, kann die thermische Verbreiterung des Coulomb-Blockade-Oszillation-Peaks verwendet werden [21, 88]. (2) Im Hochtemperaturbereich wird wegen des thermisch-aktivierten Tunnelns keine ausgeprägte Coulomb-Blockade beobachtet, sondern lediglich eine Nichtlinearität in der Strom-Spannungscharakteristik um $V_{DS} = 0$ herum. Diese Nichtlinearität hängt nur von der SET-Temperatur ab [92–95]. Weitere Details hierzu können in Appendix F gefunden werden.

Untersuchung gebrochenzahliger Quanten-Hall-Zustände mit Füllfaktoren $\nu > 1$

Die bisher mit unserem Rastersondenmikroskop untersuchten, gebrochenzahligen Quanten-Hall-Zustände hatten jeweils Füllfaktoren ν kleiner als 1. Dabei gilt für $\nu < 1$, dass das energetisch tiefste Landau-Niveau nur teilweise besetzt ist. Aus Abbildung 4.11 ist jedoch ersichtlich, dass auch Quanten-Hall-Zustände mit $\nu > 1$ in unseren Proben beobachtbar sind. Bei diesen Zuständen ist mehr als nur ein Landau-Niveau besetzt. Direkt nach Abgabe dieser Arbeit werden wir Hall-Potentialprofile um die Füllfaktoren $\nu = 4/3$ und $\nu = 5/3$ (in dieser Reihenfolge) messen. Interessant ist, ob die Stromdichteverteilung in diesen Zuständen eine vergleichbare Entwicklung wie der untersuchte Quanten-Hall-Zustand $\nu = 2/3$ zeigt. Mit Verweis auf das mikroskopische Bild des Quanten-Hall-Effekts ist eine vergleichbare Entwicklung zu erwarten.

Untersuchung des anomalen Quanten-Hall-Effekts

Magnetische topologische Isolatoren, die eine ferromagnetische Ordnung und eine starke Spin-Bahn-Kopplung besitzen, zeigen einen anomalen Quanten-Hall-Effekt (AQHE) [89]. Eine Untersuchung zur lokalen Stromdichteverteilung in diesen Materialsystemen könnte klarstellen, ob das mikroskopische Bild des Quanten-Hall-Effekts auch auf den AQHE übertragbar ist. Ausgehend vom mikroskopischen Bild des Quanten-Hall-Effekts ist für den AQHE eine vergleichbare Entwicklung der Hall-Potentialprofile wie für den ganzzahligen und gebrochenzahligen Quanten-Hall-Effekt zu erwarten. Ein Stromfluss ausschließlich in elektrisch inkompressiblen Bereichen mit lokal dem gleichen Füllfaktor führen zu quantisierten Werten des Hall-Widerstands R_{xy} .

Arbeitstemperatur des SET Arrays auf 1.4 Kelvin erhöhen

In einem weiteren Schritt ist es erstrebenswert, die Arbeitstemperatur unserer Einzelelektronentransistoren auf Spitzen soweit zu erhöhen, dass diese in unserem zweiten Rastersondenmikroskop, welches eine Temperatur von 1.4 K erreicht, nutzbar sind. Um das zu erreichen, muss die Einzelelektronenladeenergie E_C erhöht werden. Dies kann durch eine Verkleinerung des Überlapps zwischen SET-Insel und SET-Zuleitungen (Source und Drain) erreicht werden. Nähere Informationen und mögliche Vorgehensweisen für dieses Projekt sind in Appendix H beschrieben.

Chapter 12

Appendices

Appendix A

Improved SET Design and Cleanroom Fabrication Process

This appendix is meant to give future members - that are working on scanning single-electron transistor array microscope experiments - the ability to fabricate necessary probes. Eight months of this thesis were spent to make the fabrication process of tips working reliably with a variety of heterostructure materials. Hereby the design and necessary fabrication steps changed a lot; hence, instructions in former theses are not applicable anymore.

In this chapter, firstly some encountered problems are named and their solutions are presented. Afterwards, the new SET array design is introduced, before the chapter ends with a list of necessary cleanroom steps. Under best conditions, the fabrication of one die - including six arrays of SETs - needs approximately two complete weeks in the cleanroom facility.

Encountered issues and how to overcome them

At the beginning of this thesis the original heterostructure material, necessary to fabricate single-electron transistors, was no longer available. Furthermore, the heterostructure replica showed variations in the aluminum concentration and they had crystal defects, whereas the outcome of working SETs dropped below 20%. Thus, the fabrication of working SETs was challenging - some were working but most of them not. As these SETs were urgently needed for the experiments within this thesis, many changes have been made to their fabrication. As a result, the SET output increased from below 20% working SETs to 75%. During this process the following problems were encountered:

Surface Defects in old wafer material: In order to achieve free-standing tip structures an etching step with HF (hydrofluoric acid) is unavoidable. Hereby also randomly distributed spot-like surface defects on the wafer die were

underetched; these defects obviously affected the crystal structure. During the etching, these regions became spatially wider - radius of several tens of micrometers were observed - and they usually tend to break down with time, whereas they destroy gold lines on the die surface, or even tips. New wafer material was grown in the group of Prof. Wegscheider at the ETH Zürich, and the group of Dr. Jetter at the University of Stuttgart in order to solve this problem. The MBE growth parameters were adjusted to prevent gallium splashes coming from the heated cell, which are assumed to be the reason for these defects during the growth.

Post-oxidation of heterostructure: It turned out that heterostructure material that includes a 2DES, which is capped by a 5 nm thick GaAs layer, showed after some years a degradation of the 2DES quality - even non-working heterostructures could be observed. Reason for this time-dependent degradation is most probably an oxidation of the (Al,Ga)As layer below the surface. In the course of growing new wafer material, the originally 5 nm thick GaAs cap layer was increased to 10 nm to prevent such problems in the future.

Droopy SET tip structures: For heterostructures that do not host a 2DES in the tip structure, the free-standing SET tip structure bent down onto the underlying substrate when exposed to an electron beam (for example by an SEM). There, they are probably held by Van-der-Waals forces so that they cannot be broken free properly; sticking to the surface they just break away with the substrate. Even more, the shadow mask assisted SET evaporation is not possible when the tip structure is hanging out of the surface plane. To overcome these drawbacks the free-standing tip structure was modified into the shape of a membrane; now, the free-standing tips are held by two stabilization bridges which keep the tips in-plane. As small drawback these bridges have to be removed after aluminum evaporation in an additional FIB step.

Shortcuts and open leads: Originally, the gold lines - which have a length of several millimeters - going from the SET tip structure to larger bond pads were only 500 nm wide. As they are so fragile they showed in about 20 % of all cases interruptions, making a current flow impossible. These interruptions can be caused by dirt particles on the resist during electron-beam lithography or during gold evaporation. On the other hand, the SET tip structure showed in about 25 % of all cases shortcuts between both lead electrodes. Here the trench (separating them from each other) showed interruptions. Reasons are most probably also dirt particles during electron-beam lithography. As

solution, the gold lines and the trenches were increased in width as close as possible to critical structures.

Interrupted gold lines after Al evaporation: The sample holder that is used in the ultra-high vacuum evaporation system to evaporate aluminum to create SETs led from time to time to interrupted gold lines; the clamp holding the wafer die caused large scratches, which destroyed the work of about 1.5 weeks. Under the clip mechanism covering the upper chip parts, a screw assisted lever was located. By chance this arm got pressed on the chip surface, resulting in these interruptions. Consequently, this lever arm was removed without disadvantages for the process. Contrary, the temperature of the sample holder reaches now temperatures of -60°C compared to former -35°C . This is positive, as the aluminum grain size correlates with the chip temperature; lower temperatures reduce aluminum grain sizes.

Interrupted interface between aluminum and gold: It was figured out that in about 50 % of all fabricated SETs the interface between evaporated gold (going to bond pads) and evaporated aluminum (source and drain) is not working. At the interface between both metals a tearing edge is present which can lead to non-conductive connections. During the second FIB process step, when stabilizing bridge structures are cut, additionally platinum films of rectangular shape are deposited to bridge this gap and to ensuring electrical contact.

Newest SET tip array design

Figure A.1 shows schematically the newest SET tip array design. It exemplarily illustrates a wafer die having one SET tip array on it. The subfigures show the following:

- (a) View on one wafer die. Visible are free-standing SET tips at the bottom of the die and the used shadow evaporation mask, which is already separated from the remaining die material. Yellow colored structure are made of gold. Ohmic contacts at the very top contact the 2DES which is currently unused (but can be used to realize low-temperature amplifiers or Hall sensors).
- (b) Zoom into the region of gold lines where the design was strongly enhanced. Critical gold structures with line widths of 500 nm are reduced to a minimum length. When possible the line width is increased to 5 μm .
- (c) A focused-ion beam is used to deposit platinum rectangles onto the aluminum/gold interface. This ensures electrical contact between SET and gold

lines, respectively bond pads.

- (d) Enlarged view on the free-standing SET array region. Each tip structure has a length of $18\ \mu\text{m}$ and neighboring SETs are separated by $4\ \mu\text{m}$.
- (e) Zoom onto one single-electron transistor structure.
- (f) Two stabilization structures have been introduced to connect SET tips and shadow-mask into a membrane-like structure.
- (g) Complete shadow-mask necessary to evaporate aluminum on all tip structures.

Figure A.2 depicts a wafer die with an SET array which is not yet broken free. The sacrificial layer below the tips is wet-chemically etched and the SET tips are free-standing. The subfigures show:

- (a) A zoom into the SET tip region. Shadow mask and SET tips are still connected via two stabilization bridges which have been introduced within this thesis.
- (b) SET tips free-standing above the underlying heterostructure substrate.
- (c) Stabilizing bridges in a zoom-in.
- (d) SEM picture showing the introduced bridges for stabilization.

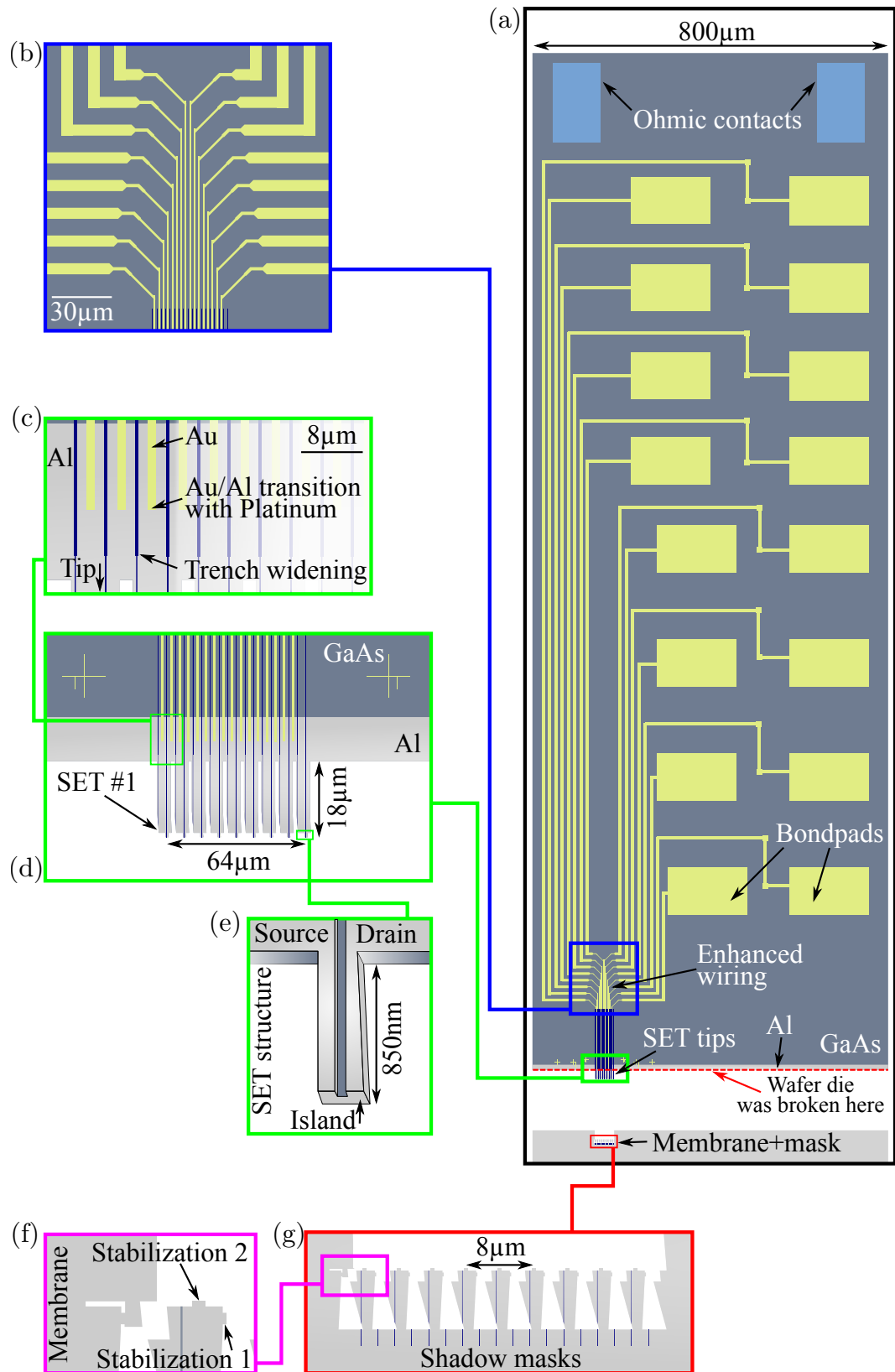


Figure A.1: Modified single-electron transistor array design that was used in this thesis.

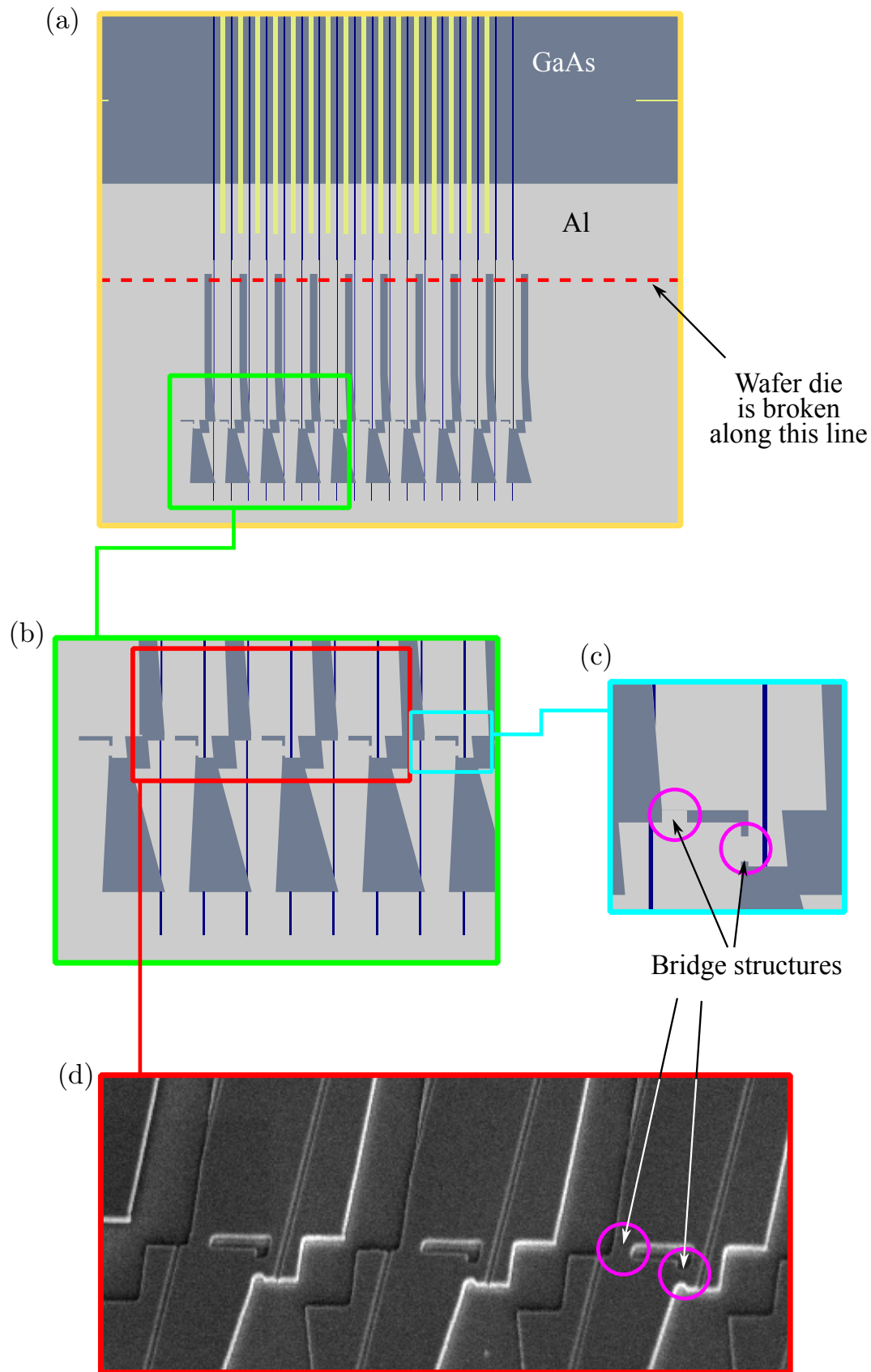


Figure A.2: Modified single-electron transistor array design. The SET tips are still connected via two bridges to their shadow mask.

Cleanroom fabrication steps

This section gives further PhD generations briefly a sketch about necessary cleanroom fabrication steps. Detailed instructions are handed personally to the next PhD student and they are also available digitally. The following instruction is meant for internally usage. We use the following abbreviations:

US		ultra sonic
Ac		acetone
IsoProp		isopropanol
MMS		manual mark scan

The convention for electron-beam lithography is:

eLine (layer; acceleration voltage; aperture; dose; step-size; magnification \times write-field size; position; writefield)

Spatial coordinates are always given as tuple¹ (x/y), both values in millimeters.

1. Break (Al,Ga)As heterostructure die 4 mm by 6 mm (space for 6 arrays)
2. Electron-beam lithography: ohmic contacts
 - (a) 15 min Ac US (70 %) » 5 min Ac » 1 min Ac » 20 s IsoProp
 - (b) Spincoat 200k 7% » 4 min hotplate » spincoat 950k 2.5% » 4 min hotplate
 - (c) eLine (ohmic contacts; 30kV; 60 μ m; 300 μ C; 30nm|60nm; 100x 1000 μ m;
 - i. (26) at 0.8/(0.8+0.9·n); WF=Kontaktpads3)
 - (d) Develop (MIBK; 3:00 min) » 1 min IsoProp » dry
3. High-vacuum deposition: ohmic contacts
 - (a) Prepare Univex 3 (or Univex 1)
 - (b) 30 s O₂ plasmacleaning (old plasmacleaner) (HURRY!!!)
 - (c) 2 min Semicoclean » 5 s Di-water » 5 s HCL (30%) » 1 s Di-water » glue » in Univex and pump (HURRY!!!)
 - (d) Deposition AU (107.2 nm) » Ge (52.8 nm) » Ni (40 nm)
 - (e) 3-4h AR300-70 at 77°C (NMP cup) » 4 min Ac (you can use syringe) » 20 s Ac » 1 min IsoProp » dry
 - (f) Annealing in AZ500 oven
4. Electron-beam lithography: crosses and contacts
 - (a) 4 min Ac US (30-40%) » 20 s Ac » 20 s Ac » 20 s IsoProp
 - (b) Spincoat 200k 7% » 4 min hotplate » Spincoat 950k 2.5% » 4 min hotplate
 - (c) eLine (contacts; 30kV; 30 μ m; 350 μ C; 8nm|8nm; 300x 300 μ m);
 - i. (I=342pA, Ap=8.4|-6.9; Stig=-0.6|-1.2);

¹Sometimes without the bracket.

- ii. Burn points: (0.5/1.1); (2.8/1.1); (2.8/4.7) » activate adaptive focus
 - iii. (2)+(4) 2.45/(0.55+0.9·n) WF=Kontaktpads1
(4) 0.35/(0.75+0.9·n) WF=Kontaktpads1
 - iv. Crosses at positions (0.3/0.3); **(0.6/1.2)**; (0.6/2.1); (0.6/3.0); (0.6/3.9); (0.6/4.8); **(2.7/0.9)**; (2.7/1.8); (2.7/2.7); (2.7/3.6); **(2.7/4.5)**; (2.7/5.4); (3.4/0.45); (3.4/1.45); (3.0/2.25); (3.0/3.25); (3.0/4.25); (3.4/5.15);
 - v. Change aperture!!!
 - (d) eLine (contacts; 30kV; 120 μm; 350 μC; 30nm|60nm; 100x 1000 μm;
 - i. (I=5.57nA, Ap=9.8|-2.7; Stig=-1.2|-0.2);
 - ii. Burn points: (0.5/1.15); (2.8/1.25); (2.8/4.75) » activate adaptive focus
 - iii. (1) 2.1/(0.85+0.9·n) WF=Kontaktpads2
(1) 1.11/(0.85+0.9·n) WF=Kontaktpads3;
 - (e) Develop (MIBK; 3:00 min) » 1 min IsoProp » Dry
5. High-vacuum deposition: crosses and contacts
- (a) Prepare Univex 3 (or Univex 1 or Univex 2)
 - (b) 20 s O₂ plasma cleaning (old plasma cleaner) or 5 s O₂ plasma cleaning (new Plasmacleaner)
 - (c) In Univex and pump
 - (d) Deposition Cr (7 nm) » Au (50 nm)
 - (e) 3-4h AR300-70 77°C (NMP cup) » 4 min Ac (you can use syringe) » 20 s Ac » 1 min IsoProp » dry
6. Electron-beam lithography: trenches
- (a) 4 minAc (no US) » 20 s Ac » 20 s Ac » 20 s IsoProp
 - (b) Spincoat 950k 5% » 4 min hotplate
 - (c) eLine (Trenches; 30kV; 10 μm; 360 μC; 2nm|8nm; 500x 200 μm);
 - i. (I=32pA, Ap=4.1|-4.9; Stig=-1.2|1.4);
 - ii. MMS (63) 0.4/(0.75+0.9·n) WF=Spitzen;
MMS (63) 2.5/(0.55+0.9·n) WF=Spitzen;
(21) at 2.5/(0.55+0.9·n) WF=Spitzen
 - (d) Develop (MIBK; 2:36 min) » 1 min IsoProp » dry
7. Etch trenches
- (a) 20 s O₂ plasma cleaning (old plasma cleaner) or 5 s O₂ plasma cleaning (new Plasmacleaner)
 - (b) RIE with "Lochwaver" 40 s
 - (c) Measure reference sample (≈ 138 nm)
8. HF dip to remove SiO₂ etch residues
- (a) 12 min Ac US (30-40%) » 20 s Ac » 20 s Ac » 20 s IsoProp
 - (b) HF 50% 1s
9. Electron-beam lithography: tip structure

-
- (a) 4 min Ac (no US) » 20 s Ac » 20 s Ac » 20 s IsoProp
 - (b) Spincoat 950k 5% » 4 min hotplate
 - (c) eLine (Tips; 30kV; 20 μ m; 330 μ C; 2nm|4nm; 500x 200 μ m;
 - i. (I=132pA);
 - ii. MMS (63) at 0.4/(0.75+0.9·n) WF=Spitzen;
 - MMS (63) 2.5/(0.55+0.9·n) WF=Spitzen;
 - Tips (22) 2.5/(0.55+0.9·n) WF=Spitzen;
 - (d) Develop (MIBK; 2:36 min) » 1min IsoProp » dry
10. Underetching of the tip membrane structure
 - (a) 20 s O₂ plasma cleaning (old plasma cleaner) or 5 s O₂ plasma cleaning (new Plasmacleaner)
 - (b) RIE without "Lochwaver" 40 s
 - (c) 12 min liftoff in AC300-70 » 4 min Ac » IsoProp » dry » HF etching 25% 6 s (Jetter wafer) / 11 s (Jochen wafer) / 9 s (replica) » critical point drying (HURRY!!!)
 - (d) Measure reference (\approx 400 nm)
 11. Focused-ion beam FIB: make SET tip structure thinner (\approx 200 nm) and smoother; 2pA and 30kV FIB; 20kV SEM; 850 nm SET length, 2° left angle and 5° right angle (lowest part thickest)
 12. Break chip into 3 pieces (2 arrays each); close to Au contact lines
 13. Scratch every array (close to transition from wafer to free-standing tip)
 14. Ultra-high-vacuum deposition: Aluminum SET structure (two arrays)
 - (a) SET lead contacts: 1250C°, 0.13 nm s⁻¹, 45 nm, 60° tilted to sample norm, 1°-2° downwards
 - (b) Oxidation: 20 min in total, pure oxygen, 0 mbar to 1.95 \times 10⁻¹ mbar
 - (c) SET island: 1250C°, 0.13 nm s⁻¹, 30 nm, 88° tilted to sample norm, 5° to the left
 15. Deposit platinum rectangles using FIB; 2pA and 30kV FIB; 20kV SEM
 16. Separate each SET from the membrane using focused-ion beam; 2pA and 30kV FIB; 20kV SEM
 17. Break away wafer substrate below free-standing tips
 18. Glue centered on tip array holder
 19. Bond

Appendix B

Electrical Characterization of Further SETs

In section 4.4 we showed the experimentally determined charge stability diagram of the SET which was mostly used in the fractional quantum Hall regime. Figure B.1 depicts charge stability diagrams of three additional SETs.

The left graph shows always the current $I_{\text{SET}}(V_{\text{DS}}, V_{\text{COM}})$ through the respective SET as function of (1) the voltage V_{COM} commonly applied to lead electrodes and (2) as function of the bias voltage V_{DS} . The working point in V_{DS} that shows highest CBOs amplitudes along V_{COM} is indicated for each SET by a white line. In the right graphs the differential conductance $\partial I_{\text{SET}}/\partial V_{\text{DS}}$ that is calculated from the data shown on the left, is shown. All presented SETs show well defined Coulomb-blockade regions (black), single-electron tunneling (gray) and multi-electron tunneling (bright). Jumps in the characteristics are most probably the result of charge redistribution in close proximity to the SET island. Table B.1 summarizes the total capacitance C_{Σ} , the charging energy E_C and the capacitive coupling to the environment C_{Env} for all four SETs presented in this thesis. The SET written in red font was used for most measurements in the fractional quantum Hall regime.

SET #	1 (a,b)	2	3 (c,d)	4 (e,f)
C_{Σ} [10^{-16}F]	4.6	6.7	4.6	4.7
$E_C = \frac{e^2}{2C_{\Sigma}}$ [μeV]	175	120	175	170
C_{Env} [10^{-18}F]	2.6	2.6	2.7	1.7

Table B.1: Experimentally determined capacitive couplings and charging energies. The SET number two - in red font - is used for most measurements in the fractional quantum Hall regime.

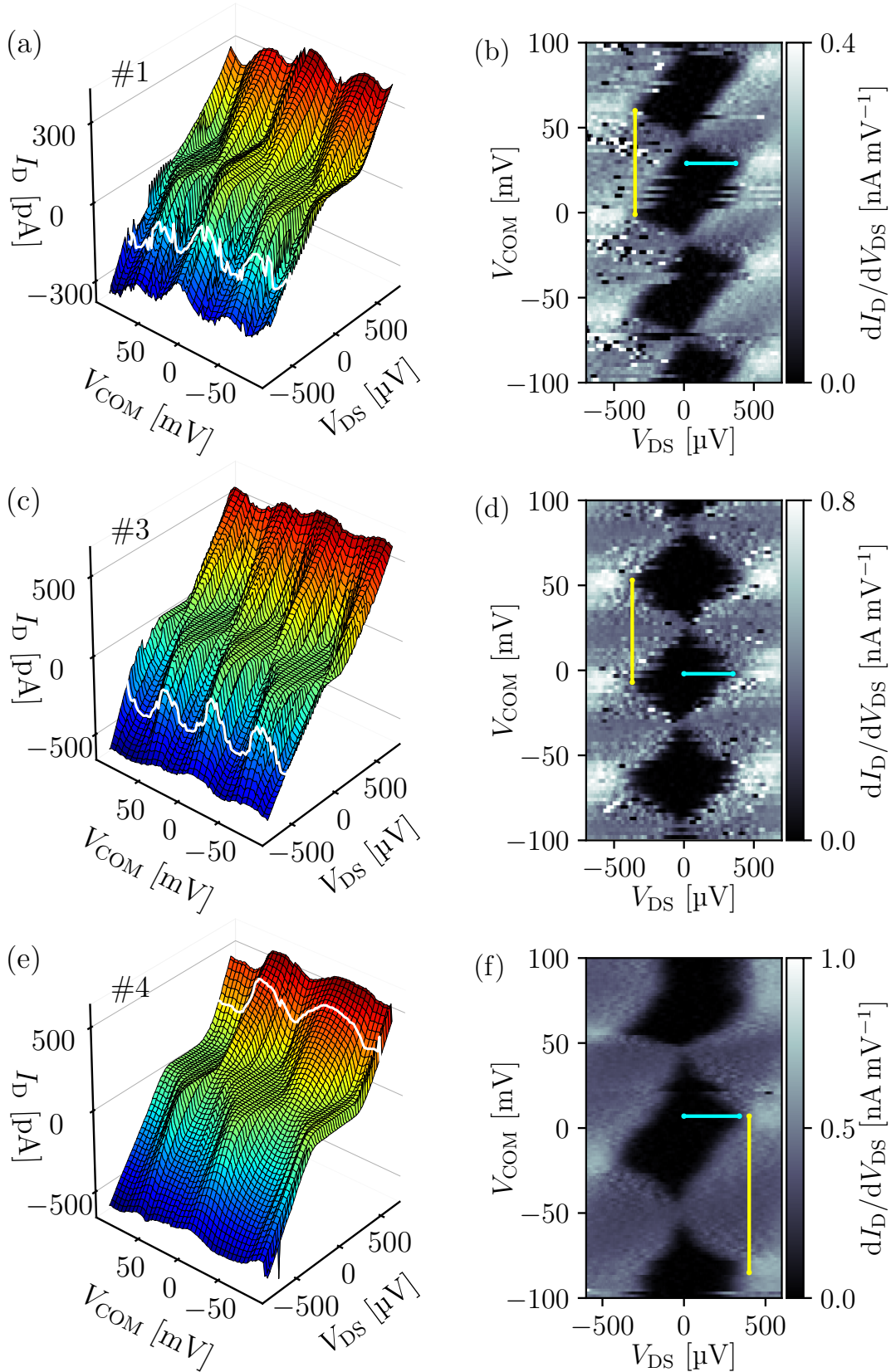


Figure B.1: Electrical characterization of three further SETs obtained around 20 mK. (a,c,e) Pseudo-3d representation of the SET current I_{SET} ($V_{\text{DS}}, V_{\text{COM}}$) versus bias voltage V_{DS} and voltage V_{COM} commonly applied to both lead electrodes. Working points in V_{DS} with the largest CBO amplitude along V_{COM} are indicated as white traces. (b,d,f) False-color representation of the differential conductance $\partial I_{\text{SET}}/\partial V_{\text{DS}}$, calculated from the data shown in the left. Well defined black regions correspond to the Coulomb-blockade regime.

Appendix C

Hall Potential Profiles around $\nu = 2/3$ close to Potential Probing Contact

The Hall potential evolution, that we have observed around fractional filling factor $\nu = 2/3$ in section 7.4 is in agreement with the microscopic picture of the quantum Hall regime. On the other hand, the experimentally determined electron density n_{2D} had to be increased by 5.9% to $n_{2D} = 2.17 \times 10^{15} \text{ m}^{-2}$; otherwise, the center position of the $\nu = 2/3$ incompressible stripe would be shifted to lower magnetic flux densities B , compared to the experimentally determined positions of high current densities. In section 7.4 it was pointed out, that this n_{2D} change is reasonable; an area scan with the DC FBL method showed an electrostatic potential drop within the region, where Hall potential profiles have been determined.

In order to show, that a changed charge carrier density can be the reason for the observed shift in B , the Hall potential evolution around $\nu = 2/3$ is probed again. This time it is probed in a region which is closer to the lower probing contacts that were used to determine n_{2D} , compare the sketch in figure C.1.

It has to be pointed out, that the resolution of the scans presented in this appendix is intentionally lower than shown in figure 7.7, simply because such measurement series are highly time-consuming. Furthermore, the current direction is reversed. But, in section 7.5 we demonstrated that a reversed current direction only changes the high and low potential at the sample sides, while leaving the potential profile¹ and current density distribution mainly unaffected.

Figure C.2 shows obtained Hall voltage drops $\tilde{V}_{2DES}(y, B)$. Figure C.2 (a) shows

¹It is just mirrored around $y = 0$.

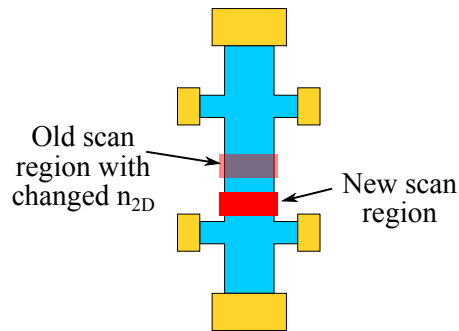


Figure C.1: Schematic of the investigated Hall bar to illustrate the position of a new scan region, to probe Hall potential profiles again in the $\nu = 2/3$ fractional quantum Hall states. In case the electron density n_{2D} is just increased locally within the old (upper) scan region, a similar evolution of the current density is expected, but shifted to lower magnetic flux densities B .

selected Hall potential profiles as a function of the SET tip position y , while they are shifted by a constant offset in order to make a comparison of them easier. In figure C.2 (b) all Hall potential profiles from this measurement set are illustrated in a false-color representation. Also the determined current density $j_x^*(y, B)$ is depicted there. For latter one, bright signals correspond to high current densities. Both graphs have overlaid the center position of the $\nu = 2/3$ incompressible stripes, calculated with equation (3.2); the experimentally determined electron density $n_{2D} = 2.05 \times 10^{15} \text{ m}^{-2}$ is used.

A comparison of Hall potential profiles taken in this new region - in figure C.2 - and ones obtained in the old scan region - figure 7.7 - reveals a similar evolution with the magnetic flux density B . Classical Hall regime, edge-dominated Hall regime and bulk-dominated Hall regime are present. In both cases, at bulk filling factor $\nu = 2/3$ the current flows exclusively in the sample bulk, no current density at the sample edges is observed.

Even more important is the fact that in this scan region the largest current density within the 2DES is observed at the calculated center position of the $\nu = 2/3$ incompressible stripe; no adaption in n_{2D} is necessary. Thus, it is reasonable, that a long-range electron density change in the former scan position led there to an increased value of n_{2D} , and consequently, to a relative shift of the filling factors ν to higher magnetic flux densities B . This can be seen as they are correlated via

$$\nu = \frac{n_{2D}h}{Be}. \quad (\text{C.1})$$

Moreover, statements that the fractional quantum Hall state $\nu = 2/3$ shows a similar Hall potential evolution as the integer QH states is once more verified with

this measurement series.

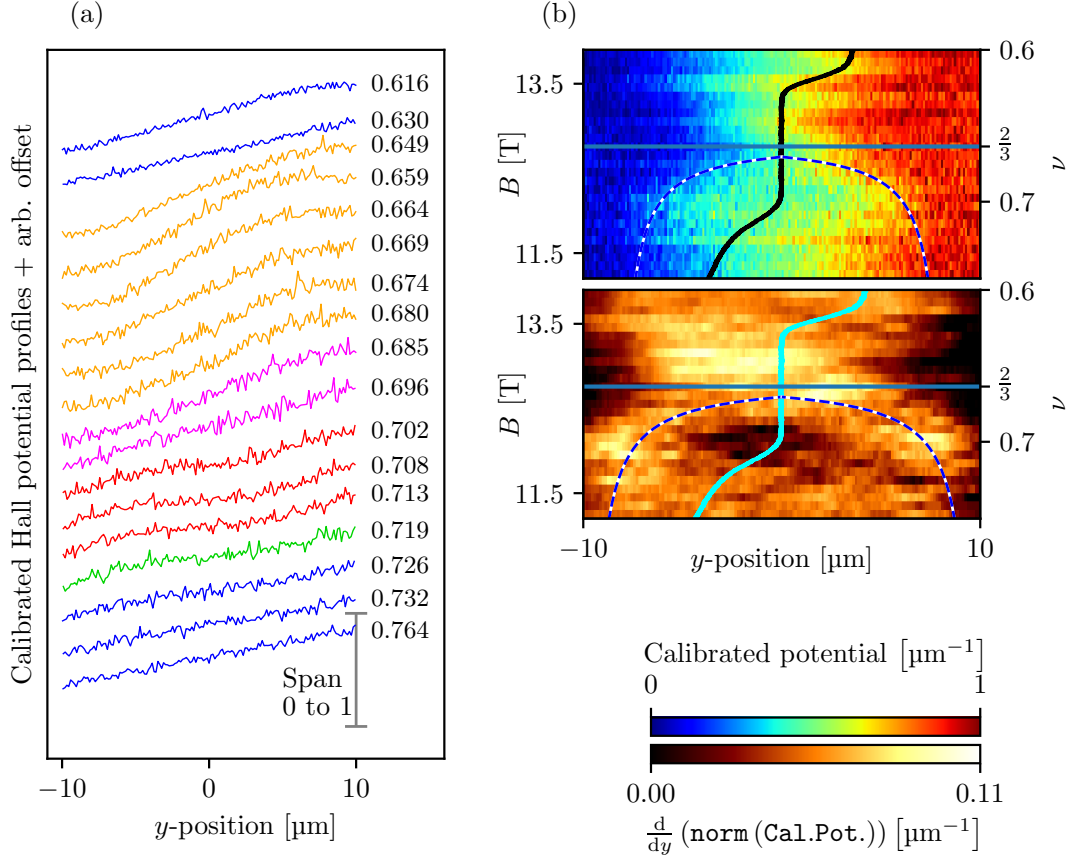


Figure C.2: Hall potential profiles $\tilde{V}_{2DES}(y)$ probed around fractional quantum Hall state $\nu = 2/3$. (a) Selected potential profiles, colored by their potential type. Classical Hall regime (blue), edge-dominated QH regime (red) and bulk-dominated QH regime (orange) are observed. (b, upper) All probed profiles of this measurement set in a false-color representation. (b, lower) Current density $j_x^*(y, B)$ determined as $\partial \tilde{V}_{2DES}^{(\text{norm})}(y) / \partial y$. Bright signals indicate high local current densities. Overlaid in (b) are the filling factor $\nu = 2/3$ (horizontal line) and the center position of the $\nu = 2/3$ incompressible stripe. The calculation of the center position of the incompressible stripe included the experimentally determined electron density $n_{2D} = 2.05 \times 10^{15} \text{ m}^{-2}$. Also shown - in black and cyan - is the Hall curve, which was already shown in figure 7.3.

Appendix D

Supplementary Measurement Data Showing the 2DES Inhomogeneity along the Hall Bar

In section 7.4, the evolution of Hall potential profiles around fractional filling factor $\nu = 2/3$ were presented. Then, in section 7.7 a pseudo-3d representation of the DC feedback signal in the same scan area was shown to explain why a change of the experimentally determined electron density became necessary.

For completeness we show here the same DC feedback signal, now in a false-color representation. The SET current $I_{\text{SET}}(x, y)$ which is taken with the CBO method during a first scan over this sample region is depicted in figure D.1 (a). Figure D.1 (b) shows the DC feedback signal that is obtained with an activated feedback loop to keep I_{SET} constant.

In both graphs the axes correspond to the spatial position of the SET tip. The abrupt change of the CBO signal between $-5 \mu\text{m} < x < -2 \mu\text{m}$ is a measurement artifact; the SET characteristic shifted due to electrostatic changes in proximity to the SET island. A white dashed line around $x \approx 8 \mu\text{m}$ indicates where Hall potential profiles in chapter 7 were probed.

The graphs illustrate a strong change of the electrostatic potential along the Hall bar towards $x = -13.5 \mu\text{m}$, while the upper half of the scan range looks mainly homogeneous. On a first view the data could be misleading: The region with $x \geq -2 \mu\text{m}$ looks homogeneous, what implies that the experimentally determined electron density $n_{2\text{D}}$ can be expected there, while the lower part of the scan range is inhomogeneous. With this consideration we have chosen the line $x \approx 8 \mu\text{m}$

to probe Hall potential profiles. But, in section 7.7 we figured out that n_{2D} is increased in the region $0\ \mu\text{m} < x < 10\ \mu\text{m}$. Thus, Hall potential profiles around $\nu = 2/3$ are measured again at a different position along the Hall bar, see appendix C. There, the electron density seems to have the experimentally determined value. This supports our assumption that the probed area in section 7.4 has an increased n_{2D} .

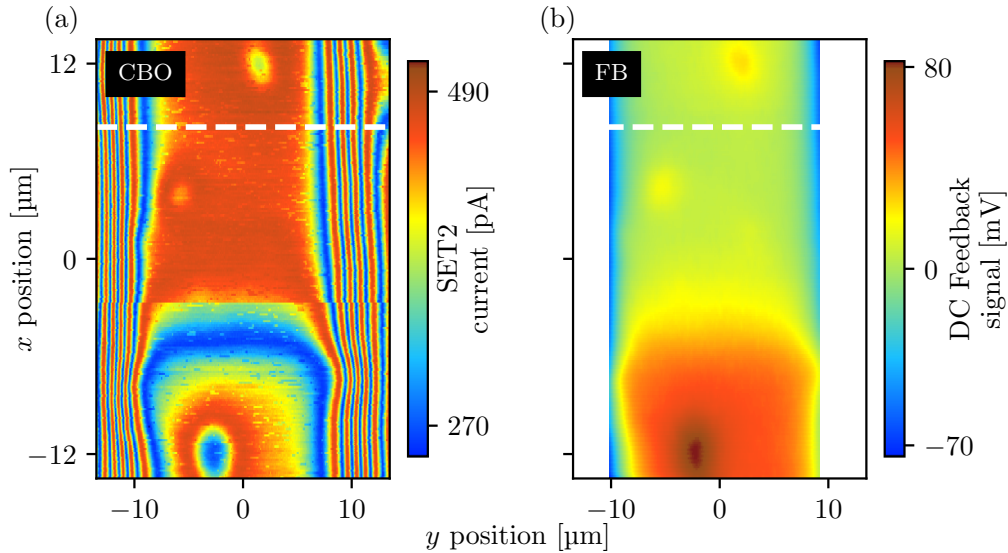


Figure D.1: Two area scans that show the region where Hall potential profiles around fractional quantum Hall state $\nu = 2/3$ were probed, compare section 7.4. (a) The area is scanned in the CBO method; the current $I_{\text{SET}}(x, y)$ is tracked as a function of the SET tip position. Electrostatic changes of the SET island lead to a shift of CBOs. Towards the sample edges a strong change is observed. In addition, an unexpected change along the Hall bar, towards $x = -13.5\ \mu\text{m}$ is present. (b) Same area scanned with the FBL method. The electrostatic potential increases in the lower part of the graph. Most probably the electron density there equals the experimentally determined one of $n_{2D} = 2.05 \times 10^{15}\ \text{m}^{-2}$.

Appendix E

Accessing Equilibrium Currents with a Free-standing Hall Sensor

Up to now, the scanning single-electron transistor array is limited to the detection of electrostatic changes. To get access to the Hall potential distribution, which is the change in the electrostatic potential of the 2DES, two traces have to be measured as described in chapter 5. The gradient of the Hall potential distribution along the y direction is correlated with the current density distribution. But, already in equilibrium there are intrinsic diamagnetic currents present, which are not accessible when an SET array is used as probe.

Diamagnetic currents¹ result directly from a Landau level bending in incompressible regions. These currents encircle compressible regions without carrying a net current through the sample. The current density in an incompressible stripe is given as $j_x = \nu(e^2/h)E_y$. The intrinsic² potential drop $V = \hbar\omega_c e^{-1}$ across this incompressible stripe, together with the relation³ $B = nh(\nu e)^{-1}$ between filling factor ν and magnetic flux density B , results in a diamagnetic current in this stripe of

$$I_{\text{Dia}} = \frac{\hbar e}{m^*} n_{2\text{D}}. \quad (\text{E.1})$$

For the (Al,Ga)As sample investigated in this thesis, the electron density is in the range of $n_{2\text{D}} = 2 \times 10^{15} \text{ m}^{-2}$, while the effective electron mass in GaAs is $0.067m_e$ [31,32]. That means, diamagnetic currents of about 550 nA are expected. For samples with higher charge carrier densities, e.g. the one of Ahlswede *et al.* [12], I_{Dia} increases to almost 1.6 μA . In a distance of 50 nm to the stripe with an assumed width of 200 nm this is equal to magnetic flux densities of about 1.2 μT and 3.5 μT , see [43]. These values are meant to get a rough guess about the magnetic

¹Sometimes they are also referred to as persistent currents.

²Here, the Landau level splitting without Zeeman splitting is discussed.

³The cyclotron gap is given by $\omega_c = eB(m^*)^{-1}$

flux density; we are aware that in our sample the 2DES is buried 120 nm below the sample surface making an approach down to 50 nm not possible.

This current in incompressible regions leads to magnetic fields. Hence, a magnetic field sensor is able to measure current distributions within a 2DES also in equilibrium. In this case, several boundary conditions for the sensor have to be fulfilled: (1) In order to reach the QH regime, high magnetic fields of several Tesla will be applied. (2) The temperature will be 1.4 K or below. (3) A high spatial resolution across the sample width is necessary to resolve incompressible stripes. (4) Optical readout of the sensor is not possible as this leads to electron excitation and persistent changes in the electron density distribution. We evaluated that a Hall sensor fulfills all conditions [43].

Free-standing Hall sensor that is developed during this thesis

During this thesis such an Hall sensor was developed. It can be incorporated into the existing fabrication process of an SET array; an hybrid sensor array can be achieved. Two of the master students, namely Bamidele Onipede [96] and Konstantin Riegel [91], contributed to this development. A first version of this sensor is schematically shown in figure E.1 and an SEM picture is shown in figure E.2. A complete overview about the development and cleanroom steps can be found in appendix K.

A 2DES inside an (Al,Ga)As heterostructure is formed by reactive-ion etching into a Hall cross - see figure E.1 (d) - with an active area of $1\ \mu\text{m}$ by $1\ \mu\text{m}$ (red). This cross is located at the end of an $18\ \mu\text{m}$ long, free-standing membrane shaped as tip. Four alloyed AuGeNi contacts electrically connect the 2DES of the Hall cross. Wide gold leads end in larger gold pads, where a wire can be bonded. Before the heterostructure die surrounding the sensor tip is broken away, a pre-characterization of the Hall sensor can be done with an additional gold line that is located in close proximity to the Hall sensor cross. A current through that line induces a well-defined magnetic field that can be detected by the sensor.

Different heterostructures with varying GaAs quantum well widths - containing the 2DES - have been systematically investigated in regard to their intrinsic $1/f$ noise behavior when the applied bias voltage is varied. It turned out, that the noise level is reduced for heterostructures with smaller quantum wells; here, the energy separation between subbands is large. Above a threshold bias voltage, the

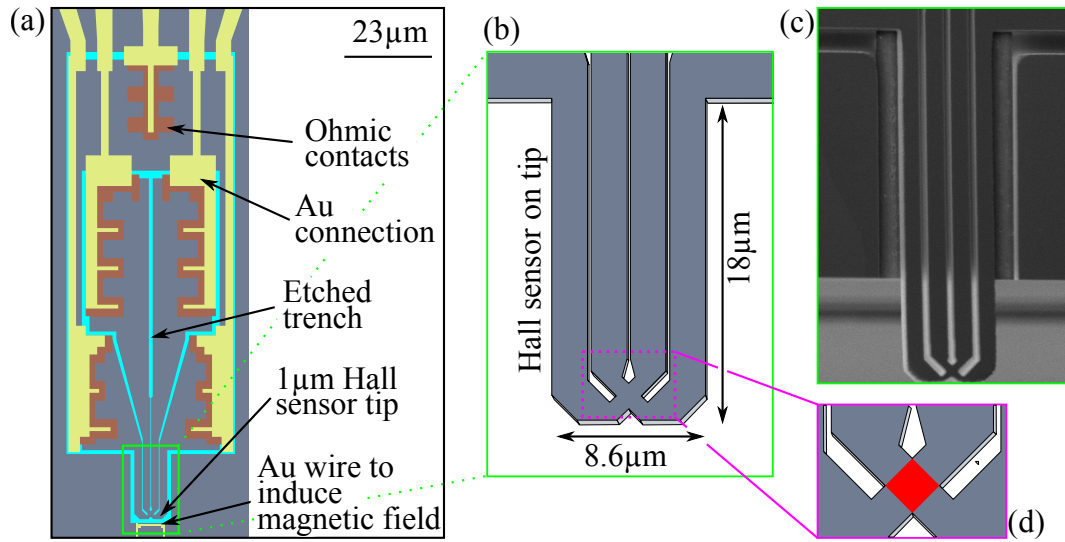


Figure E.1: Sketch of the first Hall sensor tip design realized in a $(\text{Al,Ga})\text{As}$ heterostructure (internal notation #D180508A). (a) By dry-etching (light blue) a 2DES is shaped in four regions that form a Hall cross in a tip structure. Annealed AuGeNi contacts (brown) electrically connect the 2DES, while gold lines (yellow) lead to large bond pads. (b) Free-standing tip region enlarged. The $(\text{Al,Ga})\text{As}$ membrane hosts a 2DES that forms a Hall cross. Tip dimensions are included. (c) SEM picture of one sensor. (d) The spatial length of the active sensor region (red) is varied between 500 nm and 2 μm .

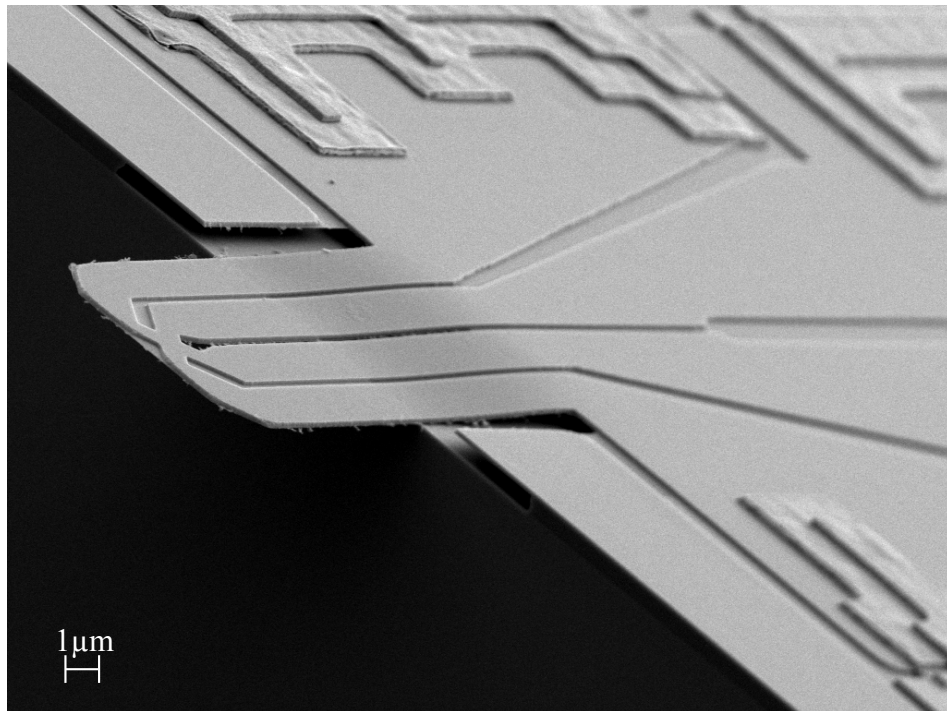


Figure E.2: SEM picture of one $(\text{Al,Ga})\text{As}$ 2DES based Hall sensor on a free-standing tip structure. A sensor of the very first charge of working tips is shown. The free-standing membrane, hosting the 2DES of the sensor, has a thickness of just 175 nm. Dry-etched trenches define the Hall cross with an active area of 1 μm by 1 μm . The tip itself has a length and width of 18 μm and 8.6 μm , respectively. Annealed AuGeNi contacts electrically connect the 2DES, while additional gold lines enable wedge bonding. Picture was recorded in collaboration with T. Reindl and the master student K. Riegel.

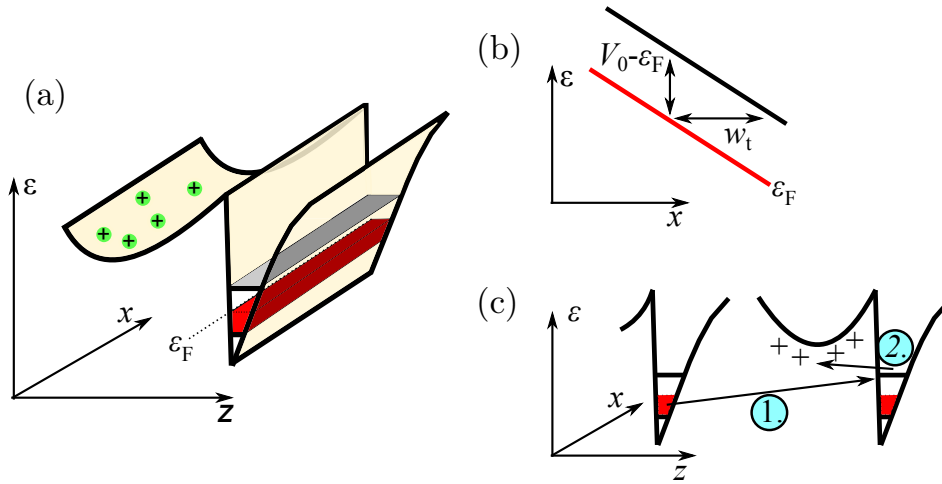


Figure E.3: Sketch to illustrate possible tunneling events. (a) Pseudo-3D representation showing the band bending of the conduction band minimum in the region around the 2DES. (b) Large electric fields along the active sensor region lead to a strong tilt of the band bending. Reduction of the triangular potential barrier leads to an increased tunneling between the lowest and the next higher 2DES subband. (c) A subsequent tunneling of electrons from the lowest subband into the next higher one, and from there into the donor layer is thinkable. Trap states - as DX centers - inside the donor layer prevent electrons from relaxing back into the 2DES. Adapted from [43].

current density in the 2DES started to decrease; sometimes even non-reversible. A model including a two-step tunneling process has been developed [43], compare figure E.3: (1) Strong electric fields across the sensor region - due to the current flow - lead to a tilt of the subband levels along the current flow in x direction, see figure E.3 (b). (2) The triangular potential barrier between the lowest occupied and next unoccupied subband decreases in width w_t . Thus, (3) with an increasing voltage drop across the sensor, the probability for electron tunneling between both subbands increases. (4) This leads to two parallel electron systems with different electron densities and mobilities. As a result, non-linear $V_H(I_{DS})$ characteristics are observed. (5) Even higher bias voltages favor a second tunneling process, see figure E.3 (c), into the spatially separated donor layer. This second tunneling is not reversible at low temperatures as DX centers may hinder electrons from relaxing back into the 2DES. Consequently, small quantum wells (which have a high subband energy separation) together with low charge carrier densities (to increase the Hall voltage) are favorable for sensitive Hall sensors.

Pre-characterization

At 4.2K one sensor which is not yet underetched - and thus, not free-standing - was characterized [91]. It shows quantum Hall plateaus of R_{xy} when a perpendicular B is applied. A well-defined current flow through a close-by gold wire leads

to a magnetic flux density that is then detected by the Hall sensor. Experimental data for this experiment demonstrated the functionality of the sensor. In a further experiment, performed around 1.4 K, a free-standing sensor which is mounted inside a scanning probe microscope was positioned above a gold wire. Hereby, the Hall sensor is used as a field-effect transistor, tracking electrostatic effects on the electron density n_{2D} of the sensor. The data can be found in [91].

Extract externally induced magnetic flux density

In the currently used Hall sensor configuration⁴, when the Hall voltage is used as measurement signal it is sensitive to both: (1) Electrostatic influences and (2) magnetic fields. Hence, the sensor also acts as field-effect transistor. The first contribution changes the electron density n_{2D} and the current I through the sensor, while the second contribution is the one of interest. A change of the Hall voltage $V_H = IB(n_{2D}e)^{-1}$ can be described as

$$\Delta V_H = \frac{B}{n_{2D}e} \Delta I + \frac{I}{n_{2D}e} \Delta B - \frac{IB}{n_{2D}^2 e} \Delta n_{2D}, \quad (\text{E.2})$$

for a current change ΔI , a magnetic flux density change ΔB or a electron density change Δn_{2D} . A contribution of ΔI can be excluded when a feedback loop is used, in order to keep I constant. But, is it enough to keep I constant to access ΔB ?

We assume a Hall sensor with a spacial width \tilde{w} and a length \tilde{l} of the active sensor area that is biased by a constant voltage V_{DS} . In case of no series resistances to this sensor, I and n_{2D} are directly correlated. The Hall voltage is then given by $V_H = V_{DS} B \tilde{w} \mu \tilde{l}^{-1}$ and does not depend on n_{2D} . Here, μ denotes the 2DES mobility. But - in a real experiment - series resistances R_{series} to the active sensor area, for example due to the wiring, are expected; hence, the Hall voltage V_H has to be described as⁵

$$V_H = \frac{B(V_{DS} - I(n_{2D}) \cdot R_{\text{series}}) \tilde{w} \mu}{\tilde{l}} = \frac{BV_{\text{sensor}} \tilde{w} \mu}{\tilde{l}}. \quad (\text{E.3})$$

A change of the Hall voltage can be written⁶ as

$$\Delta V_H = \frac{V_{\text{sensor}} \tilde{w} \mu}{\tilde{l}} \Delta B + \frac{B \tilde{w} \mu}{\tilde{l}} \Delta V_{\text{sensor}}. \quad (\text{E.4})$$

⁴Coating the free-standing tip with a thin metal layer that can be fixed in potential could decrease an electrostatic influence. On the other hand, this could decrease the maximum current that can be biased, as self-depletion effects may occur.

⁵For $R_{\text{series}} = 0$ the initial equation $V_H = IB(n_{2D}e)^{-1}$ is restored.

⁶Here, the dimensions ω and l , as well as the mobility μ are assumed to be constant.

In principle, the voltage drop

$$V_{\text{sensor}} = V_{\text{DS}} \cdot \left(1 + \frac{R_{\text{series}}}{R_{\text{sensor}} (n_{2\text{D}})} \right)^{-1} \stackrel{!}{=} \text{const}, \quad (\text{E.5})$$

over the sensor has to be kept constant. This can be realized by (1) keeping R_{series} constant while changing V_{DS} , or (2) by keeping a constant bias voltage V_{DS} and adjusting R_{series} . In an experiment the first method seems easier applicable; two voltage probes at the sensor lead electrodes source and drain - the closer to the active area the better - could determine V_{sensor} . This is then compared in a feedback loop to a predefined target value and V_{DS} is adjusted to keep V_{sensor} constant.

In this way, without the feedback loop, navigation is easily possible by the electrostatic field-effect, while this contribution can be switched off by activating the feedback loop by which the sensor becomes sensitive only to the magnetic flux density.

Summary

We reached a project status, so that in the near future a Hall sensor can be used to probe magnetic field distributions, caused by the current distribution inside a 2DES, while it is in the quantum Hall regime. Equilibrium and non-equilibrium currents are now accessible with this new sensor type. It can be used in an array together with SETs, or just by its own. Firstly, a scan over a gold wire should be performed as a proof-of-concept measurement. Secondly, diamagnetic and externally biased currents in a Hall bar should be probed. While writing this thesis first experiments are ongoing to achieve these goals.

Appendix F

Probing the Temperature Distribution above a Hall Bar under Quantum Hall Conditions

A single-electron transistor can be used to determine its absolute temperature. Thus, if a good thermal coupling between sample and SET array can be assumed, it is possible to create a spatial map of the temperature distribution of the underlying sample. Two methods are discussed in the following.

Thermal broadening of the CBO peak

A low frequency AC signal with an energy eV_{DS} that is smaller than the thermal energy $k_{\text{B}}T$ is applied to an SET. When the 2DES potential is swept, conductance peaks $G(V_{\text{2DES}})$ occur, compare figures F.1 (a) and (b). The electron temperature in our SET can be determined via $G(V_{\text{2DES}})$ as [21, 88]

$$G(V_{\text{2DES}}) \approx G_{\text{max}} \cdot \cosh^{-2} \left(\frac{C_{\text{2DES}}}{C_{\Sigma}} (V_{\text{2DES}} - V_{\text{max}}) e \cdot \frac{1}{2.5k_{\text{B}}T} \right). \quad (\text{F.1})$$

Here, V_{max} describes, where the conductance peak appears along V_{2DES} , and C_{Σ} and C_{2DES} are the total SET island capacitance and the capacitive coupling of the SET island to the 2DES, respectively. Fit parameters are G_{max} , V_{max} and T . Determining the temperature as a function of the spatial position above the Hall bar surface gives a temperature map. In the quantum Hall regime, an externally biased current flows dissipationless within incompressible regions. Expected points of increased thermal heat are located at the hot spots, close to the sample's source and drain, compare section 3.5. Hence, this method can be used to visualize these hot spots. On the other hand, our SET array - as well as the sample - is operated within a $^3\text{He}/^4\text{He}$ mixture. Firstly it has to be verified that there is a measurable

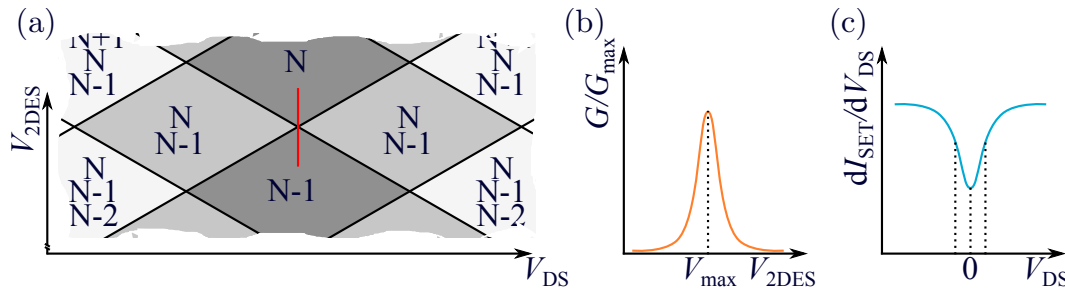


Figure F.1: Two measurement methods to determine the absolute temperature with a single-electron transistor. (a) Charge stability diagram of an SET showing the current $I_{\text{SET}}(V_{\text{DS}}, V_{2\text{DES}})$ as function of the bias current V_{DS} and 2DES potential $V_{2\text{DES}}$. In the low-temperature regime, a trace (red line) is measured. (b) Shows the resulting Coulomb-blockade peak. A broadening in $V_{2\text{DES}}$ is correlated with the absolute temperature T . (c) In the high-temperature regime, $I_{\text{SET}}(V_{\text{DS}})$ does not reach zero anymore. The full width half minimum is correlated with T .

thermal influence of the Hall bar on the SET. It could be possible that the cooling power of the mixture suppresses such temperature differences.

Non-linearity of the $I_{\text{SET}}(V_{\text{DS}})$ characteristic around $V_{\text{DS}} = 0$

When the thermal energy $k_{\text{B}}T$ is higher than the SET charging energy E_{C} the Coulomb-blockade region is only weakly pronounced. The current $I_{\text{SET}}(V_{\text{DS}})$ will be decreased around $V_{\text{DS}} = 0$, but non-zero as thermal activated tunneling is possible, compare figure F.1 (c). In this regime, the conductance dip $\partial I_{\text{SET}}/\partial V_{\text{DS}}$ around $V_{\text{DS}} = 0$ becomes independent of E_{C} . The absolute temperature can be approximated for two tunneling barriers [92–95] by

$$\frac{eV_{\text{DS}}^{(1/2)}}{2k_{\text{B}}T} \approx 5.439. \quad (\text{F.2})$$

$V_{\text{DS}}^{(1/2)}$ denotes the full width at half minimum (FWHM) of the conductance drop. For 1.4 K and 4.2 K the thermal energy $k_{\text{B}}T$ calculates approximately to 95 μeV and 360 μeV , respectively. Usual SETs have a charging energy E_{C} around 150 μeV , compare appendix B. Consequently, at 1.4 K and above, our SETs are in this high-temperature regime. The temperature can be determined via equation (F.2); this has been experimentally shown by the master student Maximilian Kühn at temperatures around 1.4 K [95].

While writing this thesis, a collaboration with Dr. Andreas Rost from the University of St. Andrews is ongoing, where this method will be used to locally probe temperatures in close proximity to a sample which undergoes a phase transition.

Appendix G

Eddy Currents with Changing Magnetic Field

An increase of B leads to an increased degeneracy of Landau levels and a subsequent depopulation of them. Once a Landau level is completely empty, the chemical potential jumps to the next lower Landau level. Consequently, a saw-tooth like chemical potential variation $\mu_{\text{ch}}(\vec{r}, B)$ is expected around the Fermi-energy $\varepsilon_{\text{F}}(B = 0)$. Hereby, $\mu_{\text{ch}}(\vec{r}, B)$ increases until the next lower Landau level is depopulated whereas a jump occurs.

In case a 2DES is in thermodynamic equilibrium, then the electrochemical potential $\mu_{\text{elch}}(\vec{r}, B)$ across the 2DES is constant. It is the sum of the chemical potential $\mu_{\text{ch}}(\vec{r}, B)$ and the electrostatic energy $e\phi(\vec{r})$. Hence, a change of $\mu_{\text{ch}}(\vec{r}, B)$ is represented in a change of $\phi(\vec{r})$. This could be already seen in experiments with stationary SETs above a 2DES [84, 87, 90, 97, 98].

A single-electron transistor is a very sensitive and local electrometer to detect changes in the electrostatic potential $\phi(\vec{r})$. Within this appendix this characteristic is used to determine $\mu_{\text{ch}}(\vec{r}, B)$ spatially resolved in an unbiased¹ 2DES.

¹The potential is fixed to $V_{\text{2DES}} = 0 \text{ V}$.

G.1 Hysteretic potential changes of the 2DES during magnetic flux variations

Firstly, the SET is positioned stationary² above the 2DES bulk for the measurement. There, the SET is operated with an activated DC feedback loop, which keeps the current through it on a predefined working point $I_{\text{SET}}^{(\text{nom})}$. Instead of changing the magnetic flux density B in a step-wise manner to determine $\phi(\vec{r})$, it is ramped with a constant rate $\dot{B} = \partial B / \partial t$ between 0.05 T min^{-1} and 0.20 T min^{-1} . Hereby, B is changed above integer quantum Hall plateaus $\nu = 2$ and $\nu = 1$.

The upper graphs of both panels in figure G.1 depict the obtained voltage ΔV_{COM} , commonly applied to the SET lead electrodes to keep I_{SET} on its working point. A change in ΔV_{COM} indicates a local electrostatic potential change in the underlying 2DES. For both filling factors a variation of ΔV_{COM} in B is observed. But unexpectedly, no saw-tooth like behavior is measured. Instead, the change of ΔV_{COM} depends on the ramp-direction of the magnetic flux density, while large changes of ΔV_{COM} are observed around integer filling factor ν (indicated by a blue line). Moreover, the recorded traces seem to be independent of the ramp-speeds $|\dot{B}|$.

If these magnetic field sweeps are repeated, but the field ramping is stopped for a time $t = 60 \text{ s}$ after certain changes ΔB , the results are different, compare the lower graphs in both panels of figure G.1. During the times when $\dot{B} = 0$, the DC feedback signal ΔV_{COM} tends to go back to its initial value, but without reaching it. This means the sample does not reach thermodynamic equilibrium. Further, it seems that for faster ramp rates \dot{B} , values of ΔV_{COM} come closer to the initial value.

Similar hysteretic behaviors were also observed on wider Hall bar samples by Hüls *et al.* [84] and Weber *et al.* [76], wherein they are additionally investigated detailed as a function of time. It turns out that the assumption of a thermodynamic equilibrium during the magnetic field sweep is not valid.

A magnetic flux density change in an area A , which is induced by \dot{B} , leads to an electric field \vec{E}_{ind} around the boundary ∂A . Together with a non-zero conductivity σ_{xy} this leads to a current flow perpendicular to \vec{B} and \vec{E}_{ind} . That means: Compared to the 2DES edge, the bulk region of the 2DES gets electrically charged, which leads to a non-equilibrium situation. Depending on the longitudinal conductivity σ_{xx} this charging can be compensated or not. For an entirely compressible

²Slight relative shifts between B and the SET tip cannot be compensated during these measurements.

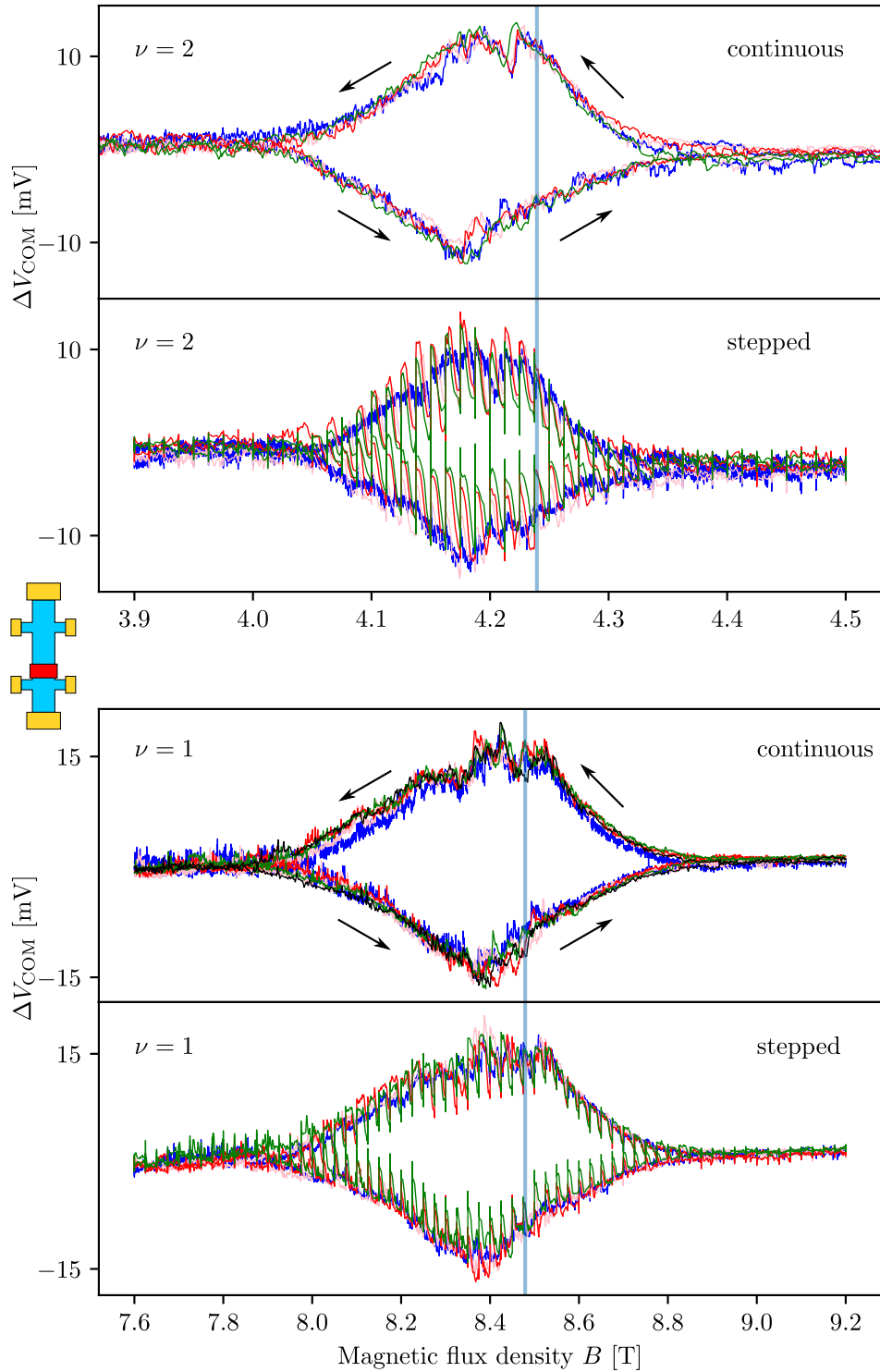


Figure G.1: Change of the DC feedback loop signal $\Delta V_{\text{COM}}(B)$ at a fixed SET position y during magnetic field ramps over $\nu = 2$ and $\nu = 1$, respectively. Different colors correspond to different sweep rates \dot{B} . The upper graph in each panel shows a continuous sweep, while in the lower panel, the ramping was stopped in predefined intervals.

2DES σ_{xx} is finite and local differences in the electrochemical potential can be compensated, no charging is expected. In the QH regime an incompressible ring with $\sigma_{xx} \approx 0$ isolates the 2DES bulk from the 2DES edge. With an increasingly wider incompressible ring towards integer filling factor this effect becomes more pronounced; this can be seen in our experiments. The electrochemical potential difference itself causes persistent currents within incompressible stripes. For further information see [76, 84, 99].

In a next step the spatial dependence of this hysteretic behavior is investigated for the first time.

G.2 Hysteretic potential changes spatially resolved

In former experiments the single-electron transistors were limited to a fixed location on the Hall bar [76, 84, 99]. In this section the first spatially resolved measurements are presented.

Figure G.2 depicts the DC feedback signal $\Delta V_{\text{COM}}(B, y)$ in a false-color representation as a function of the changing magnetic flux density B and the tip position y . During the experiment, the magnetic flux density is ramped as fast parameter with $\dot{B} = -0.1 \text{ T min}^{-1}$, while y is changed step-wise as slow parameter when a trace along B is completed. The center position of the $\nu = 2$ incompressible stripe and integer filling factor $\nu = 2$ are plotted as dashed line. The following can be

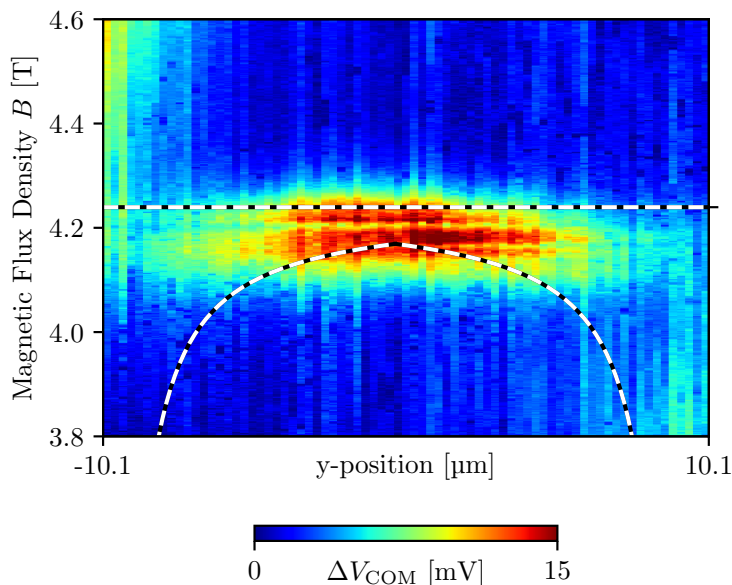


Figure G.2: Position dependent measurement of $\Delta V_{\text{COM}}(B, y)$ for magnetic flux densities including $\nu = 2$. An increased change is observed when $\nu = 2$ incompressible stripes, one from each sample side, merge in the sample bulk.

observed:

1. In direction of y , the highest change ΔV_{COM} is observed within the center region³ of the 2DES.
2. In direction of B , it is obvious that the highest change ΔV_{COM} is observed, when both incompressible stripes - one from each sample edge - have merged in the 2DES bulk. Here the incompressible ring around the sample has its widest spatial extension and the compensation of electrochemical potential differences between 2DES bulk and 2DES edge is most effectively suppressed. For bulk filling factor $\nu < 2$ the feedback signal ΔV_{COM} drops as the incompressible bulk is expected to shrink in width.

G.3 Chemical potential variation

In former measurements it turned out that the 2DES is not in thermodynamic equilibrium while the magnetic flux density is varied. Consequently, extracting the chemical potential variation by simply measuring the electrostatic potential change $\Delta\phi$ is not suitable.

Hüls *et al.* [84] indicated that the chemical potential variation $\Delta\mu_{\text{ch}}(B)$ may be hidden within both hysteretic curves; it is superposed to the electrochemical potential difference $e\Delta V_{\text{b}\rightarrow\text{e}}$ between 2DES bulk and edge. From section G.1 we know that latter one depends on the direction of \dot{B} . The suggestion to extract $\Delta\mu_{\text{ch}}(B)$ is the following: For a rising magnetic flux density $B \uparrow$ and a falling one $B \downarrow$ both traces of ΔV_{COM} are summed up, as

$$\Delta V_{\text{COM}}^{B\uparrow} + \Delta V_{\text{COM}}^{B\downarrow} = \left(\frac{\Delta\mu_{\text{ch}}}{e} - \Delta V_{\text{b}\rightarrow\text{e}} \right) + \left(\frac{\Delta\mu_{\text{ch}}}{e} + \Delta V_{\text{b}\rightarrow\text{e}} \right) \quad (\text{G.1})$$

$$= \frac{2\Delta\mu_{\text{ch}}}{e}. \quad (\text{G.2})$$

The left panel of figure G.3 depicts $2\Delta\mu_{\text{ch}}/e$ in a false-color representation versus the SET position y and the magnetic flux density B . It seems the chemical potential is almost homogeneous with a deviation around integer filling factor $\nu = 2$. There, an increase which is followed by a drop is observed. This can be seen more pronounced in a line-cut at fixed SET position $y = 0$, which is shown in the right panel of figure G.3.

³It has to be mentioned that towards the sample sides the DC feedback signal drops as the Hall bar mesa is left, compare section 5.2 and section 5.4. This effect is included in the data.

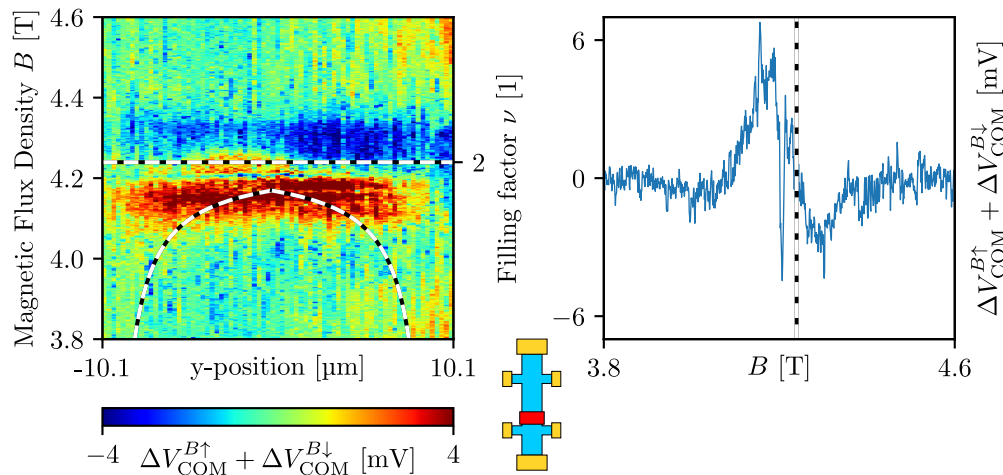


Figure G.3: A summation of ΔV_{COM} for both directions of the magnetic field ramp yields $2\Delta\mu_{\text{ch}}/e$. (left panel) $\Delta V_{\text{COM}}^{B\uparrow} + \Delta V_{\text{COM}}^{B\downarrow}$ spatially resolved in y direction over a Hall bar cross section. Around $\nu = 2$, a change of $\Delta\mu_{\text{ch}}$ can be observed, while it stays mainly homogeneous in other regions. (right panel) Line-cut at fixed SET position $y = 0$ to illustrate mentioned changes.

As introduced in the beginning of this chapter, the expected behavior of the chemical potential $\mu_{\text{ch}}(B)$ would be a saw-tooth like variation around the value $\varepsilon_{\text{F}}(B = 0)$. This is not observed in figure G.3. Contrary, an increase and a decrease of $\mu_{\text{ch}}(B)$ around $\nu = 2$ can be seen.

A comparable behavior was already seen by Hüls *et al.* [84] at integer filling factor $\nu = 5$. It seems that the simple assumption in equation (G.1) is not sufficient to describe the dynamic process in the 2DES. More precisely, it indicates that the electrochemical potential change $\Delta V_{\text{b}\rightarrow\text{e}}$ is not independent of the ramping direction \dot{B} .

G.4 Summary

The influence of a continuous magnetic flux change \dot{B} on the chemical potential $\mu_{\text{ch}}(\vec{r}, B)$ was investigated with one single-electron transistor.

We recognized that the DC feedback loop signal ΔV_{COM} does not show the expected saw-tooth behavior, but an hysteretic-like trace which has different direction dependently on the ramp direction of B . This was explained by an electron rearrangement between 2DES bulk and 2DES edge. The 2DES is not in thermodynamic equilibrium during a magnetic flux density change. This effect became more pronounced as the width and thus, isolating properties of the incompressible stripe increased with B .

At the end we tried to extract the chemical potential change $\Delta\mu_{\text{ch}}(B)$ by summing up both hysteretic feedback loop traces $\Delta V_{\text{COM}}^{B\uparrow} + \Delta V_{\text{COM}}^{B\downarrow}$. A change around $\nu = 2$ could be observed, but it was not the expected saw-tooth behavior. Consequently, this method seems not sufficient to extract $\Delta\mu_{\text{ch}}(B)$ in the milli-Kelvin regime.

Appendix H

Design Proposal to Enhance the Working Temperature of the SET Array to 1.4 Kelvin

Currently, our single-electron transistors on tips have charging energies E_C in the range of 25 μeV to 265 μeV [19–21]. In chapter 4 we introduced that it is necessary to fulfill $E_C \gg k_B T$ in order to observe well-defined Coulomb-blockade regions. Assuming a ratio of $E_C = 10k_B T$ to fulfill this condition, this means the working temperature has to be below 140 mK. Consequently, to use them as a probe inside a scanning probe microscope, which is operated inside a pumped ^4He cryostat at 1.4 K, it is unavoidable to increase the working temperature into this regime.

In chapter 4 the single-electron transistor charging energy E_C was introduced as

$$E_C = \frac{e^2}{2C_\Sigma}, \quad (\text{H.1})$$

with $C_\Sigma = \sum_i C_i$ as sum of all partial capacitances between SET island and close-by electrodes. To enhance E_C , the total capacitance C_Σ has to decrease - more precisely for our case, decrease by a factor of about four. The partial capacitances increase with their area A and decreases with the distance d to the island. Normally, tunnel barriers between SET island and the lead electrodes source and drain have a thickness d_{tunnel} of roughly 13 \AA . Hence, these partial capacitances to the lead electrodes will dominate C_Σ . A reduction of C_S and C_D can be achieved either by (1) increasing the tunneling barrier thickness or (2) reducing the overlap area A between SET island and lead electrodes. An increase of the tunnel barrier thickness would lead to exponentially smaller currents through the SET. As currents are already in the order of only 100 pA, the first possibility is not favorable. Instead, the overlap area A has to be reduced.

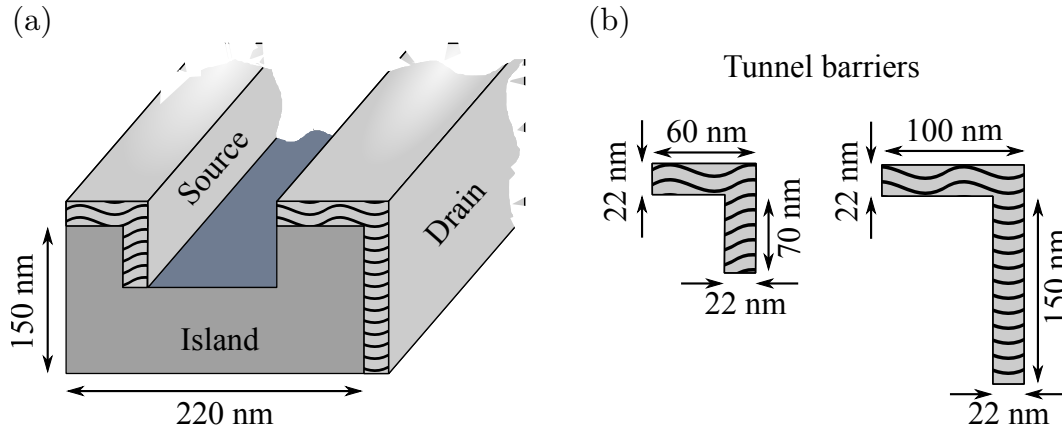


Figure H.1: (a) Schematic representation of the SET tip structure. The height of 150 nm (old wafer) to 155 nm (new wafer) is defined by the wafer heterostructure, while the width of 220 nm is a usual value achieved by focused-ion beam milling. The SET is formed by aluminum evaporation under a 60° angle to the wafer norm, in combination with controlled oxidation to form tunneling barriers. The final aluminum thickness is about 22 nm. (b) The total capacitance of an SET is mainly determined by the overlap areas of the tunneling barriers between lead electrodes and SET island. In the usual situation, the overlap area is about 8400 nm^2 . A reduction of these overlaps results in an increasing charging energy E_C and higher working temperatures for the SET.

Figure H.1 (a) shows schematically an SET tip structure. A usual width that we achieve for the SET island size is about 220 nm. A 60 nm wide and 70 nm deep reactive-ion etched trench separates the lead electrodes source and drain. They are formed by evaporating 45 nm aluminum under an angle of 60° to the normal vector of the heterostructure surface; the final layer has a thickness of about $d = \cos(60^\circ) \cdot 45 \text{ nm} \approx 22 \text{ nm}$. The total overlap area calculates to $A = 8360 \text{ nm}^2$. In case of two symmetrical and squarish areas, each side would have a length of about $x = 65 \text{ nm}$. To reduce A by a factor of 4, the side length x of the squarish overlap has to be approximately 32 nm.

Within the collaboration with the master student Maurizio Bono [87] two questions have to be clarified: Firstly, if smaller overlaps can be fabricated reliably and secondly, if post-evaporation oxidation at ambient pressure makes these SETs unusable as they may become non-conductive. As a first step on the way to achieve this overlap reduction we investigate a simpler SET structure; we fabricate during this thesis a planar SET structure on a GaAs substrate - realized by a shadow evaporation technique which is explained in [83,84]. A sketch of this structure is shown in figure H.2 (a) and (b). The resulting overlap - sketched in (c) - consists of two parts: (1) One overlap area defined by the electron-beam lithography and (2) perpendicular to it, an area defined by the evaporated aluminum height.

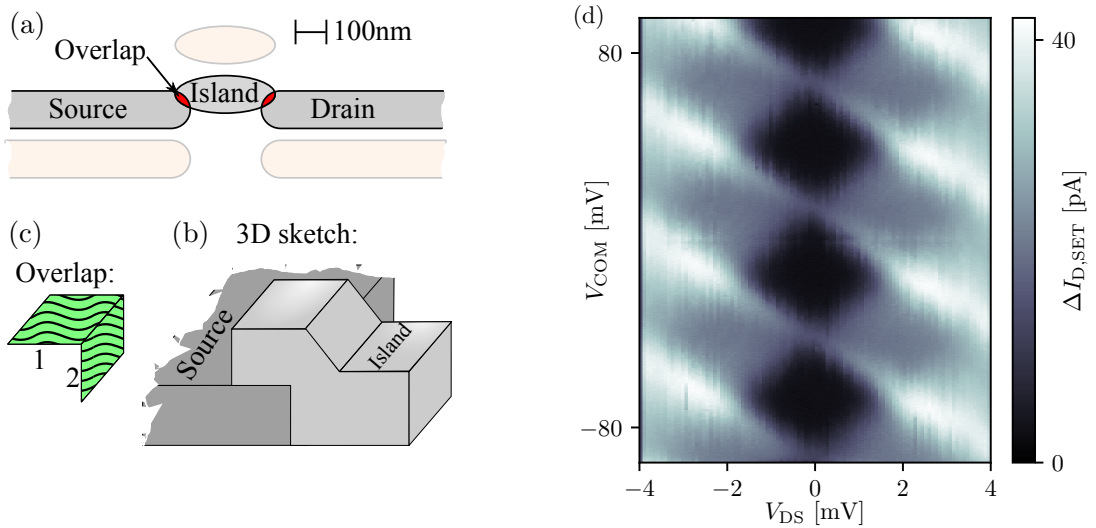


Figure H.2: Planar SET structure to investigate fabrication and stability of SETs with reduced overlap areas. (a) Schematic sketch of a planar SET fabricated by a two-angle evaporation; shadow lines are colored in light orange. (b) Sketch to illustrate SET overlap between lead electrode source and island. (c) Resulting overlap that defines the charging energy E_C consists of two contributions; one at the top defined by electron-beam lithography, and one from the aluminum flank defined by the height of the evaporated aluminum. (d) Charge stability diagram of one planar SET taken at $T = 1.4$ K; replot of data from [87]. Well pronounced Coulomb-blockade regions (black) and single-electron tunneling regions (gray) can be observed. The charging energy was determined as 0.75 meV. Thereby, it could be proven that the working temperature of such SET structures can be increased (even up to 4.2 K) without problems of post-oxidation.

To reduce the overlap as far as possible the following ways are thinkable: (1) A reduction of the width of the lead electrodes and the island, (2) enhancing the electron-beam lithography step to realize smaller overlaps, (3) reducing the aluminum layer thickness and (4) changing the evaporation angle so that the island covers only a part of the lead electrodes¹ width.

Within his master thesis, M. Bono was able to fabricate tunnel barriers with an overlap side length as low as 15 nm, while the experimentally determined charging energy increased to 0.75 meV. Figure H.2 (d) depicts a charge stability diagram of one of his SETs. The estimated overlap in this case is roughly [87] 30 nm by 20 nm for each tunnel barrier. These data are taken at 1.4 K using Lock-in technique. Well defined Coulomb-blockade regions, single- and multi-electron tunneling regimes are observed, compare section 4.6. Moreover, the SETs show already at liquid helium temperatures of 4.2 K a non-linear current-voltage characteristics².

¹A change of the evaporation angle results in a shift of the SET island out of the lead electrode line.

²At these temperatures, $E_C = 10k_B T$ is not fulfilled anymore. This leads to a broadening of energetic states and thermal activated tunneling becomes possible; non-zero and smeared-out

In summary, it was shown that a reduction of the overlap area between SET island and lead electrodes does not necessarily lead to non-working SETs. In contrast, single-electron transistors with well defined Coulomb-blockade regions at 1.4 K have been achieved. In future works, this knowledge has to be transferred to the SET tip structure. The following steps may help to reduce the overlap area A and increase the charging energy E_C for SETs on a tip:

1. As part of this thesis, the fabrication process of the SET arrays became more reliable, see appendix A. Now, SETs can be fabricated also from heterostructure wafers which host no 2DES. The free-standing GaAs membrane thickness - and thus the SET tip thickness - can be reduced with a simpler heterostructure sequence below 155 nm. One overlap area can be reduced in this way, compare figure H.3 (1,i) and (1,ii).
2. One step that is necessary to fabricate an SET tip structure is a milling by a gallium focused-ion beam to further sharpen the tips, before the aluminum is evaporated. This step can also be used to reduce the membrane thickness. Controlled milling of the tip area reduces the heterostructure thickness from the top; the trench becomes shallower. This also reduces the overlap area of both tunnel barriers, compare H.3 (2,i) and (2,ii). In case the reduced trench depth leads to shortcuts between source and drain, the etching time for the trenches has to be increased.
3. In the same gallium focused-ion beam step both walls of the tips are shaped that they are not parallel anymore, but come together under an angle as indicated in figure H.3 (3,i). This is necessary for the aluminum shadow evaporation afterwards. A drawback of these non-parallel SET walls is a larger tunneling barrier on the right side. This can be overcome by (1) changing the angle, for example by bringing it closer to 90° , see figure H.3 (3,i) and (3,ii). Or (2) by shaping the right SET wall staircase-like. Instead of milling the whole SET wall with one angle, subsequent smaller parts can be milled to get a saw-blade-like structure on the right, compare figure H.3 (3,iii) and (3,iv).

Coulomb-blockade regions result.

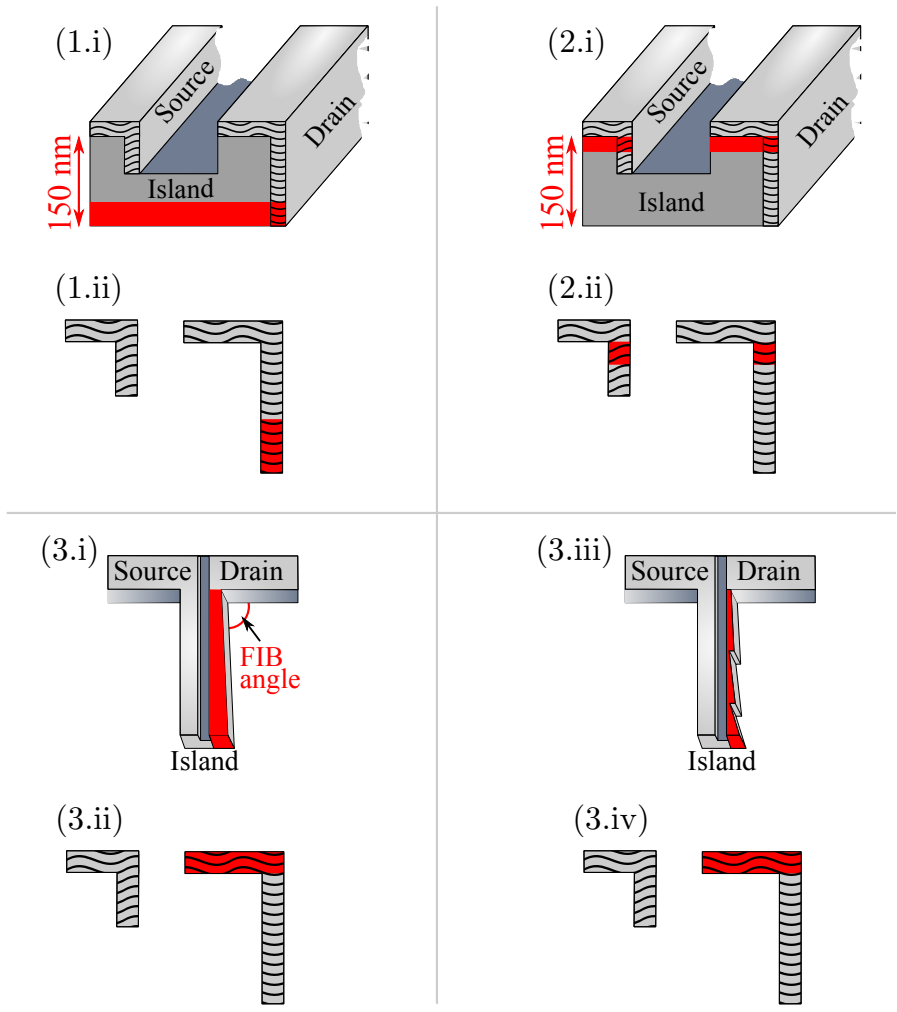


Figure H.3: Sketches to illustrate possible changes (red) which lead to smaller overlap areas. Numbering corresponds to enumeration in text.

Appendix I

Decoupling of the 2DES-Bulk from the Edge in the Quantum Hall Regime

Within this chapter one SET is used to probe the evolution of the underlying compressible/incompressible 2DES landscape which was shown in section 3.6. The following discussion is done with means of figure I.1. We assume that the SET is spatially stationary above the 2DES.

For a 2DES potential change ΔV_{2DES} , which is applied commonly via the Hall bar lead electrodes, the SET island potential is shifted by $(C_{2DES}/C_{\Sigma}) \Delta V_{2DES}$. When the 2DES is entirely compressible and thus metallic (figure I.1 ①) the total SET island capacitance¹ C_{Σ} calculates to $C_{\Sigma} = C_S + C_D + C_{2DES}$. For a strong capacitive coupling C_{2DES} between the 2DES and the SET island the potential change $\Delta\Phi_{isl}$ of the SET island is equal to ΔV_{2DES} , the one of the 2DES. The ratio

$$\xi(\vec{r}, t) = \frac{\Delta\Phi_{isl}(\vec{r})}{\Delta V_{2DES}(t)} \quad (\text{I.1})$$

has a value of 1. The situation changes when an incompressible stripe evolves at each 2DES edge, compare figure I.1 ②. The isolator-like incompressible stripes decouple the 2DES bulk from the 2DES edge. They remain only coupled via an almost vanishing longitudinal conductivity σ_{xx} and a capacitance. For the circuit diagram of this arrangement (orange box in figure I.1) that means, that an additional capacity C_{Network} is introduced. Consequently, the potential change $\Delta\Phi_{isl}$ decreases and the ratio $\xi(\vec{r}, t)$ becomes smaller than 1. For an incompressible 2DES interrupted by compressible droplets, compare figure I.1 ③, a further drop

¹Other electrodes are neglected as they are assumed to be small.

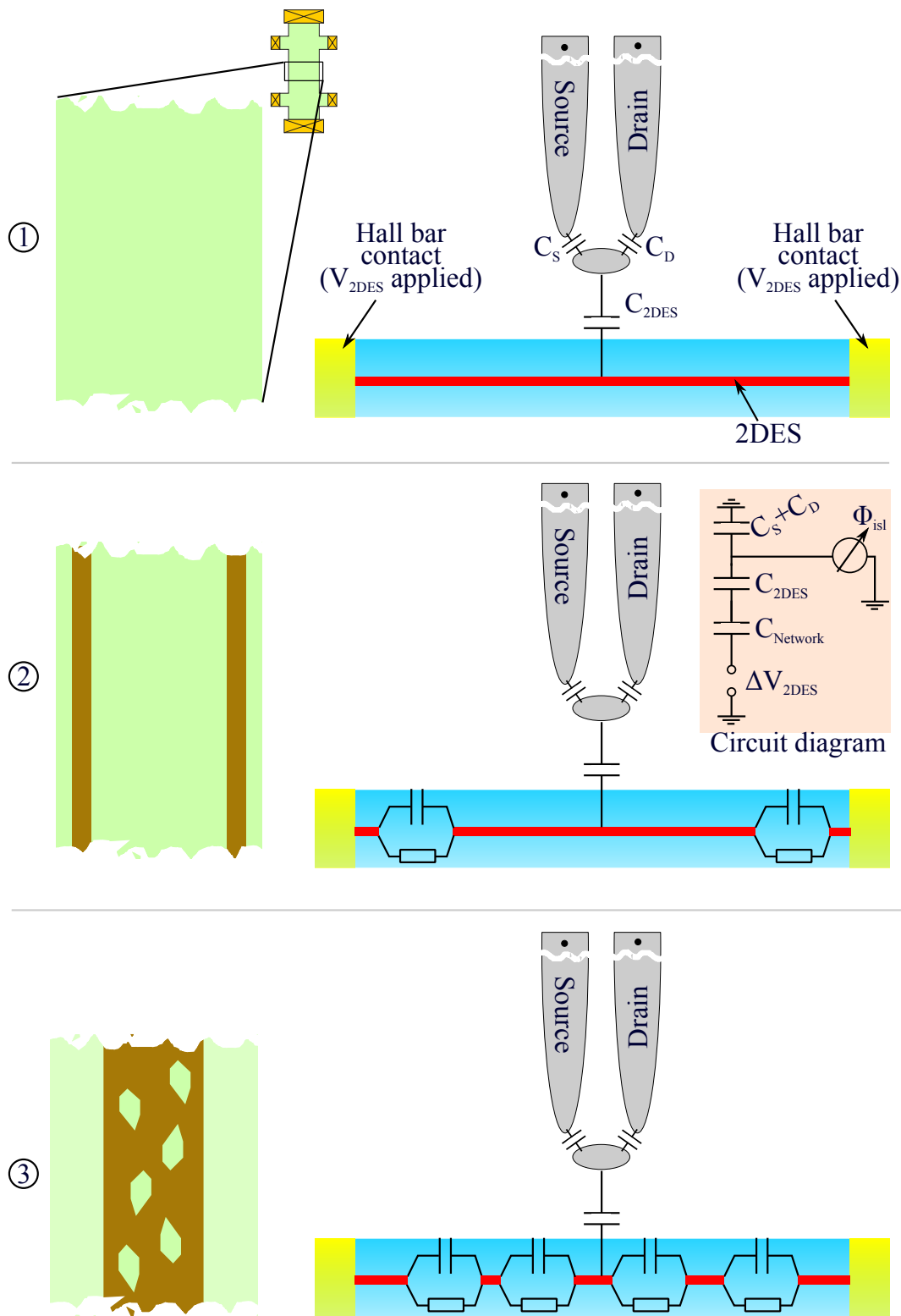


Figure I.1: An SET is used to probe the compressible/incompressible landscape inside a 2DES by a common voltage modulation at both Hall bar contacts source and drain. Depending on local capacitive couplings and conductivities inside the 2DES the overall capacitive situation changes, locally the change of the SET island potential $\Delta\Phi_{isl}$ varies. Three regimes can be distinguished: (1) An entirely compressible 2DES, (2) an compressible 2DES with one incompressible stripe at each side of the 2DES, and (3) an incompressible bulk with compressible droplets.

of $\xi(\vec{r}, t)$ is expected as C_{Network} is expected to further decrease. The minimum value $\xi(\vec{r}, t)$ can take is 0. Two measurements methods to probe $\xi(\vec{r}, t)$ are discussed in the following.

I.1 DC method

In the DC method the SET is operated in the CBO method, only the current I_{SET} through the SET is recorded. The 2DES potential is changed by a predefined value of $\Delta V_{2\text{DES}} = 200 \text{ mV}$ with a rate of about 5 mV s^{-1} . The potential change $\Delta\Phi_{\text{isl}}(\vec{r})$ of the SET island can be determined by counting the numbers of Coulomb-blockade oscillations within $\Delta V_{2\text{DES}}$. Practically, the counting of CBOs is realized by fitting a sinusoidal curve

$$f(x) = a \cdot \sin(b \cdot \Delta V_{2\text{DES}} + c) + d \quad (\text{I.2})$$

to the measured data I_{SET} . Here, a denotes an amplitude, c a phase shift and d a current offset. The factor b describes the periodicity of the signal and is the one we are interested in. The highest value of b (which is obtained outside of the QH plateau) is normalized to 1 in the following.

Figure I.2 depicts results of four independent SETs. Probed is a Hall bar cross-

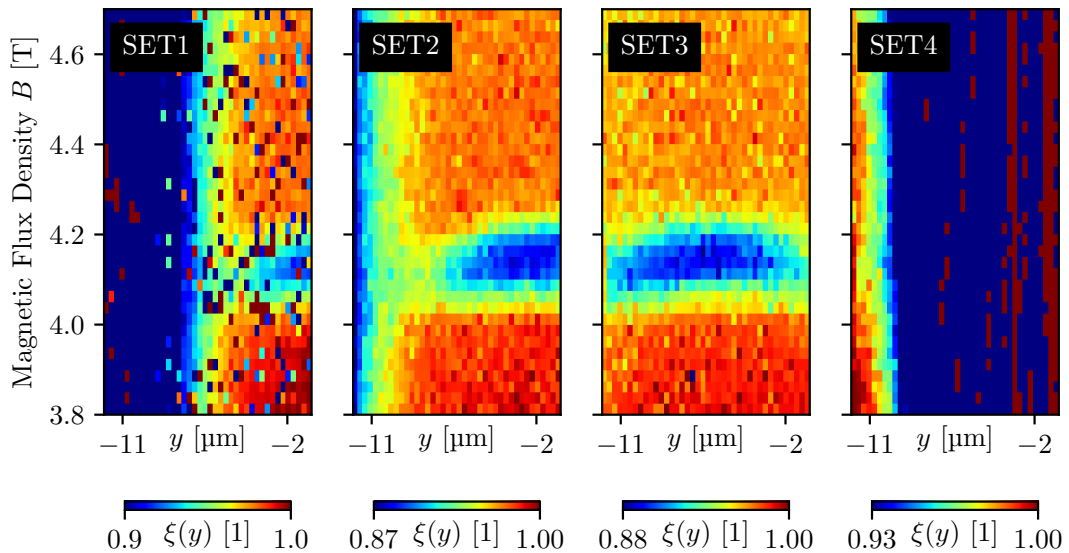


Figure I.2: Spatially resolved capacitive coupling to outer compressible regions carrying μ_{elch} . Information is obtained with the DC method. A line along y in a cross-section of the Hall bar is scanned repeatedly, while the magnetic flux density B is changed stepwise. The color-coded fit parameter b includes information about $\xi(y)$. A blue region appears in the center of the sample for about $4 \text{ T} < B < 4.3 \text{ T}$. Here, the bulk couples less to the outer compressible region.

section² at different magnetic flux densities B around integer filling factor $\nu = 2$. On a first view it is obvious that b - respectively $\xi(y)$ - changes with B . In blue regions within otherwise reddish areas, less CBOs are measured. There, the capacitive coupling of the locally probed 2DES region towards the outer compressible region, conducting μ_{elch} , is reduced. The blue regions can be found in B within the quantum Hall plateau $\nu = 2$, as expected from the former discussion. In the next section a more sensitive method to determine $\xi(y)$ is introduced.

I.2 AC method

A more sensitive and faster method is an AC measurement. This time one SET is used which is operated in the DC FBL method. The SET current is fixed on a defined working point $I_{\text{SET}}^{(\text{nom})}$, compare section 5.4. A favorable working point is at the steepest slope $\partial I_{\text{SET}}/\partial V_{2\text{DES}}$. The measurement principle is mainly the same as described for the DC method; the 2DES potential $V_{2\text{DES}}$ is varied, while the change $\Delta\Phi_{\text{isl}}$ is measured.

In the AC method the 2DES potential $\Delta V_{2\text{DES}}(t) = \hat{V}_{2\text{DES}} \cdot \sin(\omega t)$ is modulated by a frequency generator. The peak-to-peak amplitude is chosen to be 2 mV with a frequency of either $f = \omega(2\pi)^{-1} = 1.283$ Hz or $f = 3.771$ Hz. The AC method is faster compared to the DC method, as only a small change of $\Delta V_{2\text{DES}}$ is required. The sensitivity of this method is increased due to the Lock-In technique. Furthermore, correlations with the modulation frequency f can be investigated.

Results are presented in figures I.3 to I.5. The left plot always includes the ratio³ $\xi(y)$ we are interested in, while the right plot depicts the DC feedback signal which is necessary to keep a fixed SET current $I_{\text{SET}}^{(\text{nom})}$. Latter one is shown to demonstrate that a spatial change between SET island and sample is neglectable during the measurement; a homogeneous DC feedback signal along B indicates that all lateral shifts induced by B are compensated.

In the left panel, the center position y_ν for the incompressible stripes with filling factor ν is overlaid as dashed line. It is calculated with equation (3.2) and an electron density of $n_{2\text{D}} = 2.17 \times 10^{15} \text{ m}^{-2}$. This value for $n_{2\text{D}}$ was derived in section 7.4 during measurements of the Hall potential evolution in the $\nu = 2/3$ fractional state. It is chosen here, as decoupling experiments are performed in the same region as already used in section 7.4.

²Over the Hall bar width along the y direction.

³For comparison the highest measured value of $\xi(y)$ in each measurement is normalized to 1.

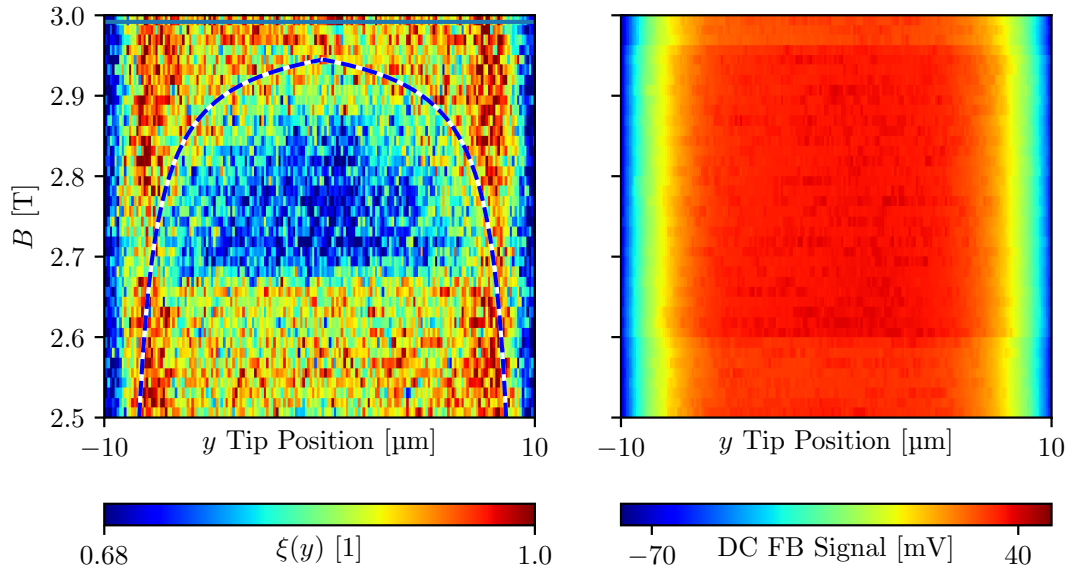


Figure I.3: AC measurement to spatially resolve the capacitive coupling between outer compressible region and the 2DES bulk around integer filling factor $\nu = 3$. (left) AC feedback signal $\hat{V}_{\text{COM}}^{(\text{AC})}(\vec{r}) = \xi(\vec{r}) \cdot \Delta V_{2\text{DES}}$. Blue regions in the 2DES bulk indicate a weak capacitive coupling. The $\nu = 3$ incompressible stripe center position is overlaid as dashed line. The blue region seems to follow this dashed line. (right) DC feedback signal. A homogeneous color along B illustrates that spatial changes between SET island and 2DES, caused by relative shifts with B , can be ruled out.

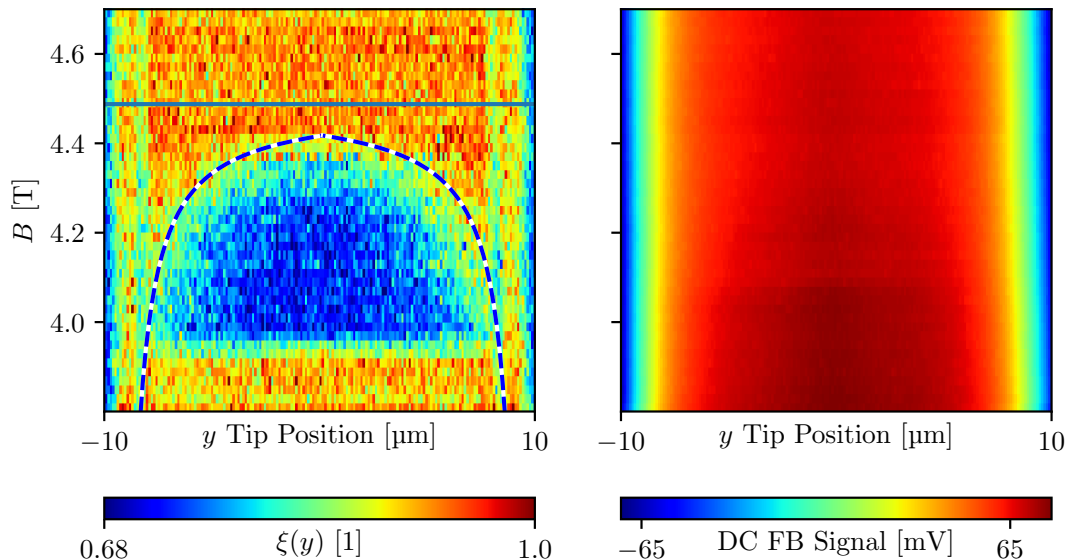


Figure I.4: AC measurement to spatially resolve the capacitive coupling between outer compressible region and the 2DES bulk around integer filling factor $\nu = 2$. Further description follows figure I.3.

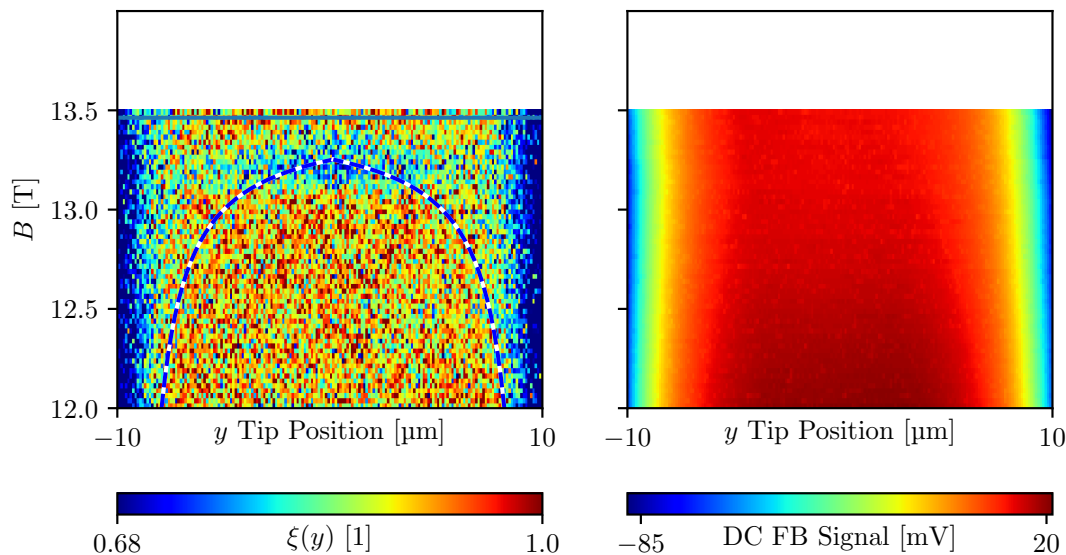


Figure I.5: Spatially resolved capacitive coupling between outer compressible region and the 2DES bulk around fractional filling factor $\nu = 2/3$. For more detailed description read caption in figure I.3.

Firstly we have a look on filling factors $\nu = 3$ and $\nu = 2$ in figure I.3 and figure I.4, respectively. In both graphs it is obvious that:

- $\xi(y)$ shows a change along B . Depending on the position y , the bulk region shows a reduced value of $\xi(y)$ between $2.65 \text{ T} < B < 2.9 \text{ T}$ (for $\nu = 3$) and $3.9 \text{ T} < B < 4.4 \text{ T}$ (for $\nu = 2$).
- The spatial width Δy of the region with a reduced $\xi(y)$ changes along B . In the lower magnetic field range, $\xi(y)$ drops within a small change of B , while for higher magnetic flux densities the drop is concentrated in the 2DES center. Furthermore, the behavior is symmetric around the 2DES center at $y = 0$.
- There is an agreement between the region with a reduced $\xi(y)$ and the calculated center positions y_ν of the ν incompressible stripe. It seems, y_ν describes more or less the outer boundary for the blue region, where $\xi(y)$ is reduced.
- Reduced values of $\xi(y)$ are not observable after the incompressible stripe from both 2DES edges have merged in the 2DES bulk.

This behavior can be understood with means of figure I.1. Starting from small magnetic flux densities B the following happens when B is increased:

1. Before the quantum Hall plateau is entered, $\xi(y)$ has values around 1 as the 2DES is entirely compressible, compare figure I.1 (1).

2. In the low magnetic field side of the QH plateau one incompressible stripe evolves at each 2DES edge which decouples the 2DES bulk from the 2DES edge and thus, the Hall bar contacts. A series capacitance C_{Network} between SET island and $\Delta V_{2\text{DES}}$ appears, compare figure I.1 (2). Consequently $\xi(y)$ drops suddenly along B and has its widest extension in y .
3. By increasing B , the incompressible stripe moves into the bulk region and the outer compressible region increases in width. Hence, the outer boundary of the blue region moves with the center position y_ν of the incompressible stripe.

Unexpected is an increase of $\xi(y)$ along B when the incompressible stripe from both 2DES edges have merged in the 2DES center. Here, the widest incompressible region is expected to be present, interrupted only by some compressible droplets, compare figure I.1 (3). A small capacitive coupling between SET island and $\Delta V_{2\text{DES}}$ in the outer compressible 2DES region is expected. The experimental observation indicates that there are many compressible droplets present that couple capacitively to each other - and more important, via each other to the outer compressible region.

It is also possible that the used $n_{2\text{D}}$ to calculate the center position of the incompressible stripe has a small error. This would shift the incompressible stripe position along B . But we expect the first explanation to be more reasonable, as the electron density $n_{2\text{D}}$ has fitted in a variety of experiments, see chapter 7.

Figure I.5 depicts measurement data obtained in vicinity of fractional quantum Hall state $\nu = 2/3$. In the range of $13.1 \text{ T} < B < 13.4 \text{ T}$ a region with a decreased $\xi(y)$ appears. Its shape in B is comparable to the one formerly seen for integer filling factors, but the decoupling seems strongest when the $\nu = 2/3$ incompressible stripes have already merged. Towards small magnetic fields this region is not widely extended. This indicates that the incompressible stripe has to be wider to have effective decoupling properties. This seems reasonable as the fractional quantum Hall regime is more fragile against excitation inside the 2DES, compared to the integer quantum Hall states.

To summarize this measurement set: Our new method can be used to probe the capacitive coupling between outer compressible edge and inner compressible bulk region with an SET. All measurements showed a decoupled bulk region that was restricted in width by the position of the ν incompressible stripes. This evolution can be understood directly with the microscopic picture of the quantum Hall effect.

I.3 Comparison with results obtained in previous works

Erik Ahlswede [12] modulated a back-gate electrode below the 2DES to spatially probe the transparency of different 2DES positions y . This was done for varying magnetic flux densities B in vicinity of integer filling factor $\nu = 2$. His data is presented in figure I.6; white and black regions correlate with a high transparency, while gray regions indicate a low transparency. The calculated center position - in accordance to equation (3.2) - of the $\nu = 2$ incompressible is also included [12].

The transparency is correlated with electrical screening properties of electrons at the Fermi-level. Only electrically compressible regions with a metallic behavior that are connected to an electron reservoir, as source and drain electrodes, can screen modulations of the back-gate electrode [12]. Consequently, bright regions in figure I.6 indicate 2DES regions with an insulator-like behavior; the incompressible stripes/regions. They follow directly the calculated center position of the $\nu = 2$ incompressible stripes. When they merge in the center of the sample, the entire 2DES bulk region becomes incompressible around 9 T (black).

This measurement is complementary to our measurement; by determining the transparency, incompressible regions become visible. They follow the calculated center positions of the incompressible stripe. A comment for completeness: It is not possible to extract positions of a current density from such transparency measurements. The current flow happens counter-intuitively in incompressible regions.

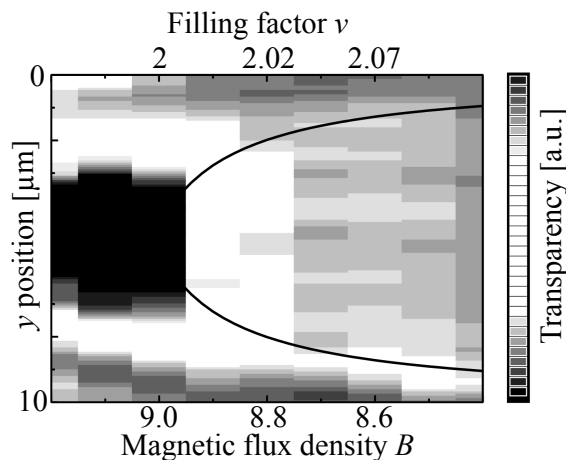


Figure I.6: Transparency of a 2DES towards a back-gate electrode modulation. Bright and black regions indicate a high transparency, while gray regions indicate a low transparency. Adapted from [12].

I.4 Summary

In this chapter we introduced a DC and an AC method to use a single-electron transistor in order to locally probe the capacitive coupling of the 2DES towards the Hall bar lead electrodes. Under quantum Hall conditions a decoupling of the bulk is observed. The spatial boundary for the decoupled region matches the calculated center position of incompressible stripes. This is reasonable, as incompressible regions have an insulator-like behavior, separating the bulk region from the lead electrodes. This observation was made in both, the integer and the fractional quantum Hall effect.

Appendix J

Hall Potential Profiles in more Complex Situations

During one of the very first approaches to the six-terminal Hall bar structure, the SET array was located close to the upper potential probing contacts, see small inset in figure J.1. An area scan performed with the DC FBL method is depicted in figure J.1 (a). Visible round shaped features are also observed at other Hall bar positions, but with a lower area density. Towards the sample sides at about $\pm 10 \mu\text{m}$ the FBL signal drops; the electron density goes to zero and additionally the capacitive coupling changes in this region, compare section 5.4. In the upper part of the graph, first signs of a widened Hall bar structure can be seen; here, the mesa structure is shaped to form potential probing arms, compare also figure 2.2.

The $20 \mu\text{m}$ wide Hall bar structure is mainly centered around $y = 0$. Nevertheless, figure J.1 (a) shows something unusual; on the left side the feedback signal ΔV_{COM} drops smoother than on the right side. Also towards $x = 12 \mu\text{m}$ an asymmetry between left side and right side is observed. In figure J.1 (b) a line-cut through the depicted FB signal along y is shown; the mentioned asymmetry is obvious, see red arrows. In figure 7.11 we already discussed, that a more negative DC feedback signal can be an indication for an increased electron density¹.

We shortly recap the working principle of the DC FBL method: In section 5.4 it was introduced that the commonly applied potential ΔV_{COM} to both lead electrodes keeps a fixed SET working point $I_{\text{SET}}^{(\text{nom})}$. The necessary voltage ΔV_{COM} depends on both: The capacitive coupling between SET island and 2DES, and the potential of the 2DES, compare also equation (5.19). From this measurement it cannot be stated where this asymmetry comes from. Possibilities are:

1. An asymmetric doping and consequently an asymmetric electron density

¹Back then, this statement was valid, as the capacitive coupling above the 2DES center region can be assumed to be mainly constant.

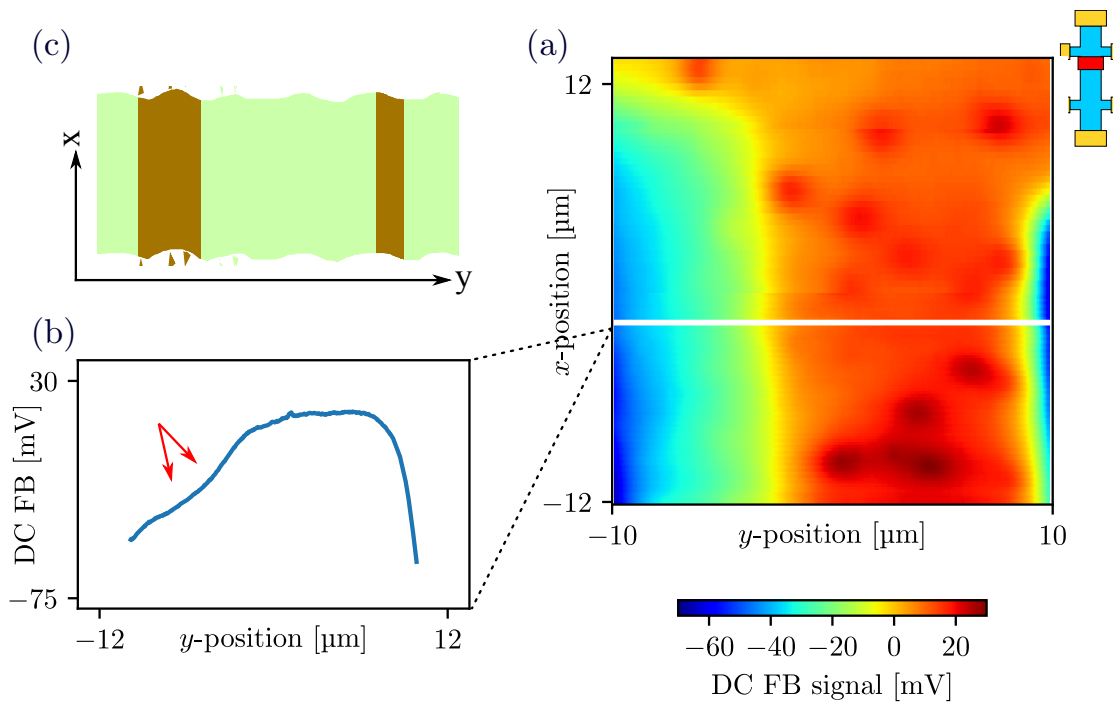


Figure J.1: Area scan reveals an inhomogeneous Hall bar region close to the upper potential probing arms. (a) Area scan with the DC feedback loop method. Round features are most probably resist remains with changing the capacitive couplings with their ϵ_r . The left Hall bar side shows a smoother and more negative probed potential ΔV_{COM} . (b) Line-cut at position of the white line. The asymmetry between right and left sample side is obvious. (c) In case of a smoother electron density profile on the left, incompressible stripes (brown) would be wider compared to the right side.

profile $n_{2\text{D}}(y)$ is present. But, as the heterostructure is MBE grown, we think this effect is less probable.

2. Charge accumulation on the left side of the sample, or on top of the left sample side. These additional charges would result in a smoother or steeper electron density profile, dependent on the polarity.
3. Resist residuals on the left side, more precisely next to the Hall bar in the 90° corner between longitudinal Hall bar path and potential probe. They affect ϵ_r and consequently change the capacitive couplings to the SET island.
4. A part of the Hall bar layer structure may be slivered. Without changing the 2DES electron density too much, one can think about the GaAs cap layer.

It is also feasible that a superposition of different influences is present; more measurements could help to clarify this observation; e.g. by revealing the capacitive coupling to the 2DES via an AC feedback method. Here, the focus lies on the effect of this asymmetric potential profile on the Hall potential profile evolution with B , respectively the local current density evolution. Probed is a cross-section

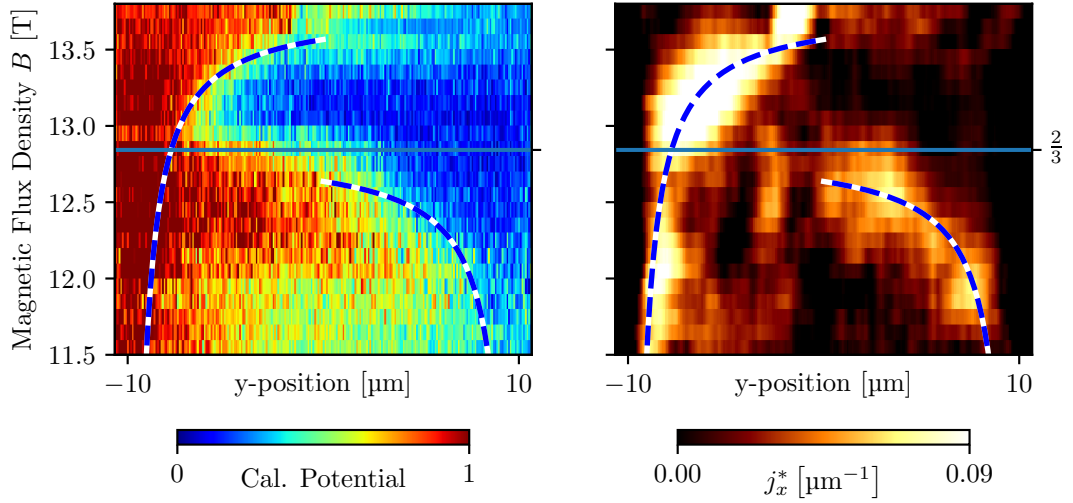


Figure J.2: Obtained Hall potential profiles in an inhomogeneous Hall bar region. (left panel) Evolution of Hall potential $\tilde{V}_{2DES}(y, B)$ with the magnetic flux density B , in a false-color representation. An asymmetric behavior is observed. (right panel) Derived local current density $j_x^*(y, B)$ in a false-color representation. (Common) In dashed lines, the $\nu = 2/3$ incompressible stripe center position is calculated for an experimentally determined electron concentration $n_{2D} = 2.05 \times 10^{15} \text{ m}^{-2}$ (right) and a higher $n_{2D} = 2.22 \times 10^{15} \text{ m}^{-2}$ for the left side. In this configuration, Hall voltage drop and current density on both sides follow the incompressible stripe position.

as indicated by the white line in figure J.1 (a) at varying magnetic flux densities B .

Hall potentials are probed in usual configurations, with a 2 mV peak-to-peak amplitude. For more details see former chapters, as e.g. chapter 5. Obtained Hall potential profiles $\tilde{V}_{2DES}(y, B)$ are depicted in the left panel of figure J.2 in a false-color representation. Resulting current densities $j_x^*(y, B)$ are shown in the same graph, in the right panel². A comparison with Hall potential profiles at other sample positions, for example for $\nu = 2/3$ in figure 7.7, shows that here the high-potential side (left) is shifted in B , compared to the low-potential side (right). In the right panel, the current density $j_x^*(y, B)$ also shows an asymmetric evolution. The left sample side has mostly an increased current density. On the right sample side, the current density shows an evolution like already seen in figure 7.7.

For the discussion of these data we concentrate first on the right Hall bar side, where the low potential is carried. Here, the $\nu = 2/3$ incompressible stripe center position $y_\nu(B)$ is calculated with the experimentally determined electron density $n_{2D} = 2.05 \times 10^{15} \text{ m}^{-2}$, see section 4.6. In both graphs, the center position is in agreement with the Hall potential drop on the right side; $j_x^*(y, B)$ follows also the calculated evolution. This is the behavior expected for a homogeneous Hall bar

²In order to reduce the noise level of $j_x^*(y, B)$, the data is smoothed minimally with a two-dimensional Savitzky-Golay filter. The window size is set to three neighbouring points.

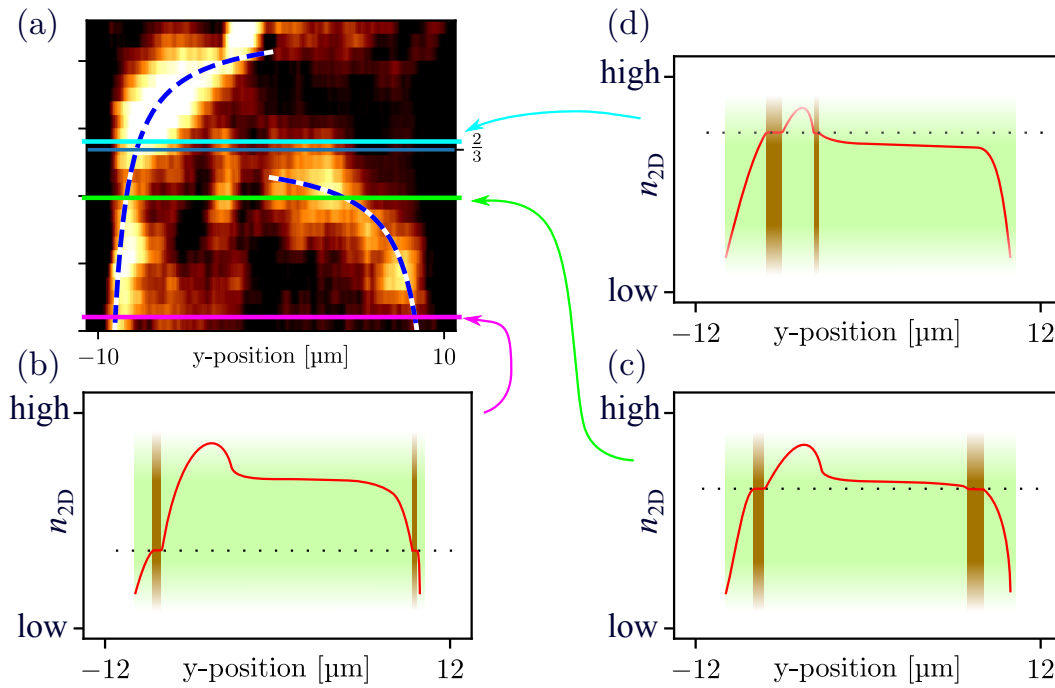


Figure J.3: A first guess of the electron density profile along the Hall bar cross-section y . (a) Local current density $j_x^*(y, B)$ evolution. For discussion, three magnetic flux densities are marked. (b,c,d) An increased electron density concentration on the left sample side leads to $\nu = 2/3$ incompressible regions, even when bulk filling factor $\nu = 2/3$ is exceeded. Electrically compressible (green) and incompressible (brown) regions are overlaid.

region. On the left sample side, the behavior is different; here, above the calculated bulk filling factor $\nu = 2/3$, the current flow is still concentrated on the left side. The FB signal in figure J.1 (b) indicates a possibly higher electron density in this region. The filling factor ν is correlated with the magnetic flux density B by $\nu = n_{2D}h(Be)^{-1}$. Hence, this leads to a shift of incompressible stripes to higher magnetic flux densities. In both graphs the $\nu = 2/3$ incompressible stripe center position in the left Hall bar side is calculated with an increased electron density of $n_{2D} = 2.22 \times 10^{15} \text{ m}^{-2}$. The current density $j_x^*(y, B)$ follows this evolution.

At the same time, the electron density profile in the left may increase smoother, compared to the right side. Consequently, the incompressible stripe that forms on the left sample side would always be spatially wider. This is indicated by a sketch in figure J.1 (c). This would explain, why also for low magnetic flux densities, respectively high filling factors ν , a higher current density is already observed in the left region; the critical electric field $E_C = V_H/w$ responsible for a breakdown of the QHE is inversely proportional to the width w of the incompressible region. Hence, over a wider incompressible region a larger Hall voltage drop is possible, and thus, more current can flow in this region.

In figure J.3 a rough guess about the charge carrier density in this region is sketched. The electron density n_{2D} increases slower on the left side, but reaches a higher "bulk"-value. Three situations are described: (1) Far from $\nu = 2/3$, two incompressible stripes form at the sample edges, see figure J.3 (b). (2) With increasing B , the right incompressible region moves towards the 2DES bulk. At a given value B , the left incompressible region is still in the edge-dominated QH regime, while the right one moves already into the bulk, see (c). (3) Once, bulk filling factor $\nu = 2/3$ is exceeded in all regions of the right Hall bar side, only the electron density dome on the left side remains. Here, still incompressible stripes are present, see (d). With higher values of B these regions move closer into the sample.

As mentioned, this assumption is vague; it is just a first guess of the situation. More measurements are necessary to really state the exact electron density profile and capacitive couplings in such complex situations.

Summary

In this chapter we discussed Hall potential profiles in an inhomogeneous 2DES region. The symmetrical current density $j_x^*(y, B)$ we are used to have in homogeneous 2DES regions is not observed, compare chapter 6 and chapter 7. Instead, it seems that an increased charge carrier density in the left sample region leads to a shift in B of the incompressible $\nu = 2/3$ stripe (in the left sample part). An imagined electron density profile was presented that would mainly explain the observed behavior. However, further measurements in this region would be necessary to make more statements about n_{2D} and the capacitive arrangements.

Appendix K

Development Steps necessary to Realize a Hall Sensor Cross on a Free-Standing Tip

In course of this thesis, a free-standing Hall sensor cross was developed, which uses a 2DES hosted by an (Al,Ga)As heterostructure. This free-standing sensor can be incorporated into the existing fabrication process of single-electron transistor tips, whereas a hybrid sensor array becomes possible which is sensitive to electrostatic changes as well as magnetic fields. This appendix gives an overview of encountered problems and their solutions. Maybe this knowledge can be transferred to similar problems encountered with other samples. Afterwards, the current design of the Hall sensors is introduced, before necessary cleanroom fabrication steps are sketched.

Encountered problems and how to overcome them

These problems were solved in cooperation with the master student Konstantin Riegel [91]. Handing him my developed Hall sensor tip array design, together with planned cleanroom fabrication parameters and steps, he fabricated first working and free-standing Hall sensors under our supervision. During fabrication the following problems had to be solved:

No electric conductivity at AuGeNi contacts: Annealed ohmic AuGeNi contacts to conduct the 2DES are small in these Hall sensors, compared to samples we usually process with ohmic contacts. Consequently, bonding cannot be done directly on the ohmic contacts, but gold lines have to go from there to larger bond pads. This method is normally not used. The usual way is to bond directly the gold which is evaporated onto the ohmic contact. It was al-

ready reported in [43], that in case bonding and ohmic contacts are spatially separated, electrical contact to the 2DES is not always given. Furthermore, conductivity of non-conductive contacts is restored, when mechanical force is temporarily applied onto the contact. The reason is the following: A time-of-flight secondary ion mass spectrometer (TOF-SIMS) revealed that aluminum from the (Al,Ga)As heterostructure moves to the surface of the AuGeNi ohmic contact [82]. An exposure with air, which will happen during our fabrication process, leads to an oxidation of this aluminum layer, forming an electrical non-conductive Al_2O_3 layer¹. Mechanical pressure destroys this layer, mixing the gold with the alloyed ohmic contact materials. As our sensor is too small to apply mechanical pressure exclusively on the ohmic contacts, a work-around is necessary. We figured out that a pre-cleaning², including hydrochloric acid, before evaporating the gold lines removes this oxide layer and solves the problem.

Hydrofluoric acid attacks AuGeNi: It turned out that annealed ohmic contacts made of AuGeNi are not working after they are exposed to hydrofluoric acid (HF). Our assumption is that nickel gets partly dissolved by the HF; only gold and platinum are resistant against HF [100,101]. Nevertheless, HF is necessary as fabrication step to underetch the sensor tips in order to make them free-standing; a work-around had to be found. To protect ohmic contacts from HF, a rectangular region of Al_2O_3 that covers all ohmic contacts - but not the free-standing tip structure - is grown by atomic layer deposition. It was shown that annealed contacts protected by this layer are working after an HF dip.

Underetching destroys 2DES: At the beginning, fabricated Hall sensors were pre-characterized before underetching the tips. During this characterization they showed the formation of Hall plateaus of R_{xy} in the magnetic flux density B . After an underetching of the sensors with hydrofluoric acid, the 2DES was not conducted anymore. We figured out, that the second surface on the Hall sensor, generated after the sacrificial layer under the sensor is removed, leads to an electrostatic depletion of the 2DES. The reasons are: (1) Electrons from the donor layer occupy appearing surface states and n_{2D} in the 2DES becomes too low; and (2) electrons on the sensor surfaces lead to an electrostatic gating effect on the 2DES, additionally lowering n_{2D} . To

¹In course of the SET fabrication process, a controlled oxidation process of the evaporated aluminum is used to form tunneling barriers with a well-defined thickness.

²It is the same cleaning process with Semicoclean and HCL, as performed before ohmic contacts are evaporated.

overcome this influence, the doping of the donor layer had to be increased³. It could be verified that a newly grown heterostructure with a higher doping concentration solved this problem.

Current Hall sensor tip design

Figure K.1 (a) shows a sketch of one Hall sensor tip array. The spatial dimension of such a die is usually around 0.8 mm by 3.7 mm. In this first design version, each array has three tips with one four-terminal Hall sensor on each tip.

In figure K.1 (e) an active Hall sensor area is highlighted in red. The active sensor size varies between (1) 0.5 μm by 0.5 μm , (2) 1.0 μm by 1.0 μm and (3) 1.5 μm by 1.5 μm , compare also figure K.1 (b). Small sensors are favorable as the design allows the sensor cross to come closer to the sample surface, and at the same time, guarantees a higher spatial resolution. On the other hand, sensors with 0.5 μm by 0.5 μm active area seem to be too small, as they have not yet shown a 2DES in the tip.

Figure K.1 (d) sketches the tip structure with a length and width of 18 μm and 8.6 μm , respectively, that hosts the 1.0 μm by 1.0 μm Hall sensor. After the sensor is broken free, tips are at the very end of the heterostructure die.

Ohmic contacts (brown) and gold lines (yellow) allow electrical connection to the 2DES, compare figure K.1 (c). An additional gold line going in front of each Hall sensor allows a pre-characterization; a current I_{Au} induces a well-known magnetic flux density B at the active sensor area that can be detected. Furthermore, each sensor array has two gold lines as "guidelines" in height of the free-standing sensors. It makes scratching and breaking of the wafer die easier and more precise. Due to this enhancement no array has been lost by inaccurate scratches.

³Here, the group around Prof. W. Wegscheider in the ETH Zürich - especially Dr. Stefan Falk and Prof. W. Dietsche - helped us with discussions and the supply of new wafer material.

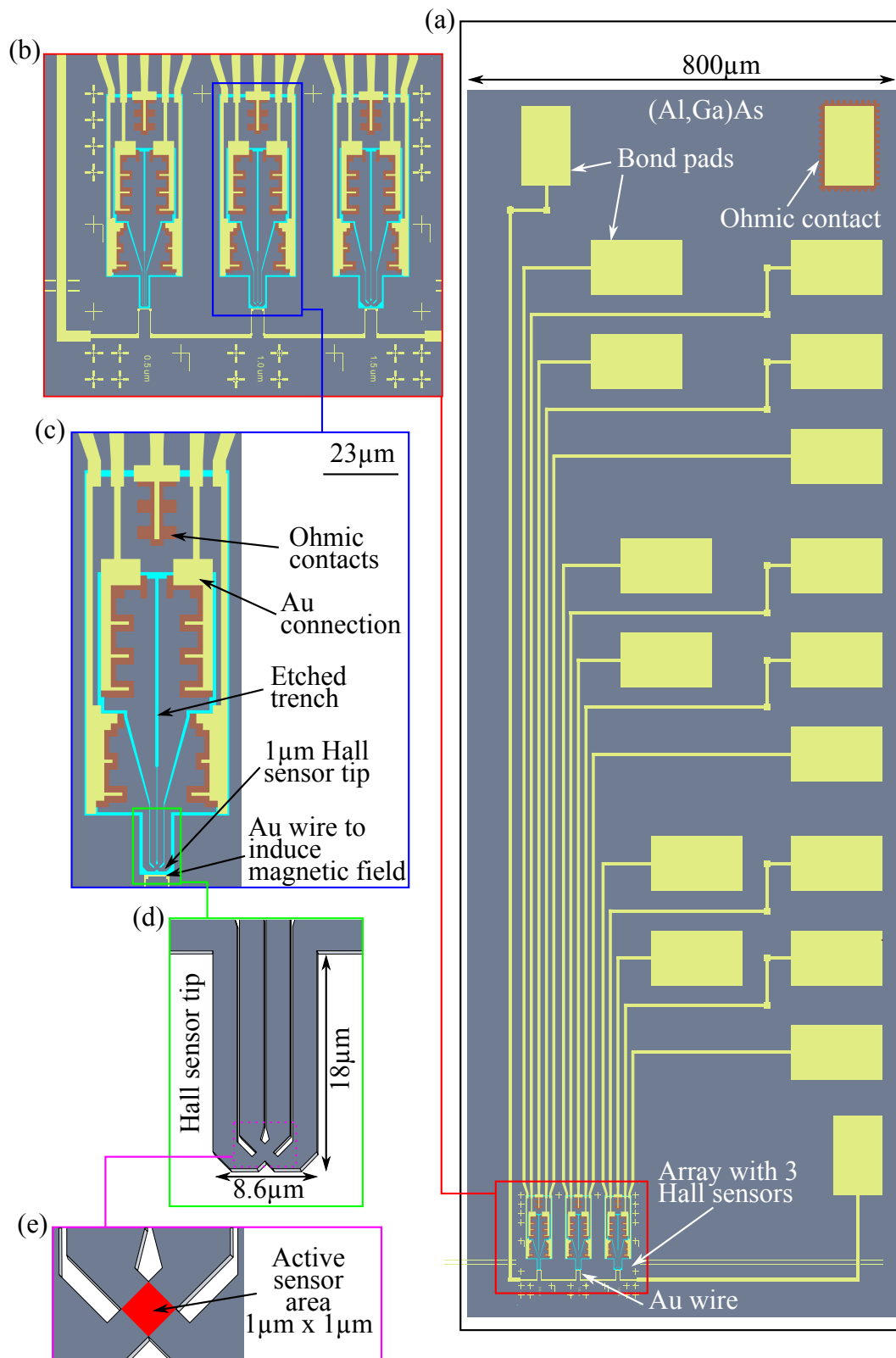


Figure K.1: First design version of an array of three Hall sensors free-standing tips, to probe the magnetic flux density distribution above a Hall bar structure in the quantum Hall regime. The cross shaped Hall sensor is realized with a 2DES. Active areas differ between (1) $0.5\mu\text{m}$ by $0.5\mu\text{m}$, (2) $1.0\mu\text{m}$ by $1.0\mu\text{m}$ and (3) $1.5\mu\text{m}$ by $1.5\mu\text{m}$. (a) Overview of the Hall sensor array. (b) Zoom into the region, where the sensor 2DES is defined and electrically conducted. (c) Zoom into one sensor area. (d) Zoom on one sensor tip structure. (e) Active area of the sensor is highlighted in red.

Cleanroom fabrication steps

This section is meant to give further PhD generations a brief sketch about necessary cleanroom fabrication steps to achieve free-standing Hall sensor tip arrays. Detailed instructions are handed to the next PhD and they are available digitally. We use the following abbreviations:

US		ultra sonic
Ac		acetone
IsoProp		isopropanol
MMS		manual mark scan

The convention for electron-beam lithography is:

eLine (layer; acceleration voltage; aperture; dose; step-size; magnification \times write-field size; position; writefield)

Spatial coordinates are always given as tuple (x/y) , both values in millimeters.

1. Break (Al,Ga)As heterostructure chip 3.7 mm by 5.9 mm (space for 7 arrays)
2. Electron-beam lithography: marker system
 - (a) 15 min Ac US (70%) \gg 5 min Ac \gg 1 min Ac \gg 20 s IsoProp
 - (b) Spincoat 200k 3.5% \gg 4 min hotplate \gg Spincoat 950k 2.5% \gg 4 min hotplate
 - (c) eLine (contacts; 20kV; 7.5 μ m; 290 μ C; 5nm|5nm; 500x 200 μ m);
 - i. Positions: **(0.2/0.2)**; **(0.5/1.1)**; **(2.0/0.3)**; (3.0/0.4); (0.5/3.0); **(2.0/3.0)**; (2.8/3.0)
 - (d) Develop (MIBK; 1:00 min) \gg 60 s IsoProp \gg Dry
3. High-vacuum deposition: gold contacts
 - (a) Prepare Univex 3 (or Univex 1 or Univex 2)
 - (b) 5 sO₂ plasma cleaning (new plasma cleaner)
 - (c) In Univex and pump
 - (d) Deposition Cr (10 nm) \gg Au (30 nm)
 - (e) 30 min AR300-70 77°C (NMP cup) \gg 4 min Ac (you can use syringe) \gg 20 s Ac \gg 1 min IsoProp \gg dry
4. Electron-beam lithography: mesa
 - (a) 4 min Ac US (30-40%) \gg 20 s Ac \gg 20 s Ac \gg 20 s IsoProp
 - (b) Spincoat 950k 2.5% \gg 4 min hotplate
 - (c) eLine (mesa; 20kV; 20 μ m; 270 μ C; 10nm|10nm; 500x 200 μ m);
 - (d) Develop (MIBK; 1:00 min) \gg 1 min IsoProp \gg dry
5. Etch mesa

Appendix K. Development Steps necessary to Realize a Hall Sensor Cross on a Free-Standing Tip

- (a) 5 s O₂ plasma cleaning (new plasma cleaner)
 - (b) RIE with "Lochwaver" 40 s
 - (c) Measure reference sample (≈ 130 nm)
6. HF dip to remove SiO₂ etch residues
- (a) 12 min Ac US (30-40%) » 20 s Ac » 20 s Ac » 20 s IsoProp
 - (b) HF 50% 1 s
7. Electron-beam lithography: ohmic contacts
- (a) 4 min Ac US (30-40%) » 20 s Ac » 20 s Ac » 20 s IsoProp
 - (b) Spincoat 200k 7% » 4 min hotplate » spincoat 950k 2.5% » 4 min hotplate
 - (c) eLine (ohmic contacts; 20kV; 20 μ m; 270 μ C; 10nm|10nm; 500x 200 μ m)
 - (d) Develop (MIBK; 1:00 min) » 1 min IsoProp » dry
8. High-vacuum deposition: ohmic contacts
- (a) Prepare Univex 3 (or Univex 1)
 - (b) 5 s O₂ plasma cleaning (new plasma cleaner) (HURRY!!!)
 - (c) 2 min Semicoclean » 5 s Di-water » 5 s HCL (30%) » 1 s Di-water » glue » in Univex and pump (HURRY!!!)
 - (d) Deposition AU (126.7 nm) » Ge (62.4 nm) » Ni (47.3 nm)
 - (e) 30 min AR300-70 at 77°C (NMP cup) » 4 min Ac (you can use syringe) » 20 s Ac » 1 min IsoProp » dry
 - (f) Annealing in AZ500 oven
9. Electron-beam lithography: gold contacts
- (a) 4 min Ac US (30-40%) » 20 s Ac » 20 s Ac » 20 s IsoProp
 - (b) Spincoat 200k 7% » 4 min hotplate » Spincoat 950k 2.5% » 4 min hotplate
 - (c) eLine (contacts; 20kV; 20 μ m; 270 μ C; 10nm|10nm; 500x 200 μ m)
 - (d) eLine (contacts; 20kV; 60 μ m; 270 μ C; 80nm|80nm; 100x 1000 μ m)
 - (e) Develop (MIBK; 1:00 min) » 1 min IsoProp » dry
10. High-vacuum deposition: gold contacts
- (a) Prepare Univex 3 (or Univex 1 or Univex 2)
 - (b) 5 s O₂ plasma cleaning (new plasma cleaner)
 - (c) In Univex and pump
 - (d) Deposition Cr (30 nm) » Au (200 nm)
 - (e) 30 min AR300-70 at 77°C (NMP cup) » 4 min Ac (you can use syringe) » 20 s Ac » 1 min IsoProp » dry
11. Electron-beam lithography: rectangles to protect ohmic contacts
- (a) 4 min Ac US (30-40%) » 20 s Ac » 20 s Ac » 20 s IsoProp
 - (b) Spincoat 200k 7% » 4 min hotplate » Spincoat 950k 2.5% » 4 min hotplate

-
- (c) eLine (contacts; 20kV; 20 μm ; 270 μm ; 10nm|10nm; 500x 200 μm)
 - (d) Develop (MIBK; 1:00 min » 1 min IsoProp » Dry
12. Atomic layer deposition: rectangles to protect ohmic contacts
- (a) 5 s O₂ plasma cleaning (new plasma cleaner)
 - (b) Deposit: AL₂O₃ (10 nm)
 - (c) 30 min AR300-70 at 77°C (NMP cup) (sometimes shortly US necessary) » 4 min Ac (you can use syringe) » 20 s Ac » 1 min IsoProp » dry
13. Electron-beam lithography: tip structure
- (a) 4 min Ac without US » 20 s Ac » 20 s Ac » 20 s IsoProp
 - (b) Spincoat 950k 5% » 4 min hotplate
 - (c) eLine (Tips; 20kV; 20 μm ; 270 μC ; 10nm|10nm; 500x 200 μm ;
 - (d) Develop (MIBK; 1:00 min) » 1 min IsoProp » dry
14. Underetching of tip structure
- (a) 5 s O₂ plasma cleaning (new plasma cleaner)
 - (b) RIE without "Lochwaver" 40 s
 - (c) 12 min liftoff in AC300-70 » 4 min Ac » IsoProp » dry » HF etching 25% (buffered) 20 s to 25 s » critical point drying
 - (d) Measure reference (\approx 400 nm)
15. Break chip into 7 pieces (1 arrays each); close to Au contact lines
16. Scratch every array (close to transition from wafer to free-standing tip; use golden guideline)
17. Break away wafer substrate below free-standing tips
18. Glue centered on tip array holder
19. Bond

Appendix L

View on the Microscopic Setup

Figure L.1 shows a photograph of the scanning single-electron transistor array microscope setup in the vibrationally isolated Precision Laboratory at the Max Planck Institute. This setup was used to obtain the experimental results described within this thesis.

We can see from the right to the left:

- Desk with a measurement computer to record data, and a computer to control the piezo positioners.
- Two oscilloscopes showing as real-time signal the SET currents and the DC feedback loop signals.
- Voltmeters and Lock-In amplifiers together with an SPM controller to move the piezo tube inside the microscope.
- The very top of the sample rod containing the scanning probe microscope. It is inside the dilution refrigerator which itself is sunk into the 180 t concrete block.
- Above the dilution refrigerator is our self-built measurement electronics as current-voltage converters, PID controllers and differential amplifiers.
- A magnet controller necessary to ramp the superconducting magnet.
- A gas-handling system which is in the meantime mostly self-built.



Figure L.1: View on the scanning single-electron array microscope setup located in the Precision Laboratory of the Max Planck Institute, Stuttgart.

Bibliography

- [1] von Klitzing, K. The quantized Hall effect. *Rev. Mod. Phys.* **58**, 519–531 (1986). URL <https://link.aps.org/doi/10.1103/RevModPhys.58.519>.
- [2] Outcomes of recent CIPM meetings; Decision CIPM/105-13 (2016). URL <https://www.bipm.org/utis/en/pdf/CIPM/CIPM2016-EN.pdf>.
- [3] Gibney, E. New definitions of scientific units are on the horizon. *Nature* **550**, 312–312 (2017).
- [4] Road to the Revised SI (2019). URL <https://www.nist.gov/si-redefinition/road-revised-si>.
- [5] Tsui, D. C., Stormer, H. L. & Gossard, A. C. Two-Dimensional Magnetotransport in the Extreme Quantum Limit. *Phys. Rev. Lett.* **48**, 1559–1562 (1982). URL <http://link.aps.org/doi/10.1103/PhysRevLett.48.1559>.
- [6] Laughlin, R. B. Anomalous Quantum Hall Effect: An Incompressible Quantum Fluid with Fractionally Charged Excitations. *Phys. Rev. Lett.* **50**, 1395–1398 (1983). URL <https://link.aps.org/doi/10.1103/PhysRevLett.50.1395>.
- [7] Weitz, K. P. Untersuchungen zum Verlauf der Hall-Spannung in einem zweidimensionalen Elektronensystem unter den Bedingungen des Quanten-Hall-Effekts mittels eines Raster-Kraft-Mikroskops (1999).
- [8] Weitz, P., Ahlswede, E., Weis, J., Klitzing, K. & Eberl, K. A low-temperature scanning force microscope for investigating buried two-dimensional electron systems under quantum Hall conditions. *Applied Surface Science* **157**, 349–354 (2000). URL <http://www.sciencedirect.com/science/article/pii/S0169433299005504>.
- [9] Weitz, P., Ahlswede, E., Weis, J., Klitzing, K. V. & Eberl, K. Hall-potential investigations under quantum Hall conditions using scanning force microscopy. *Physica E: Low-dimensional Systems and Nanostructures* **6**, 247–250 (2000). URL <http://www.sciencedirect.com/science/article/pii/S1386947799001368>.
- [10] Ahlswede, E., Weitz, P., Weis, J., von Klitzing, K. & Eberl, K. Hall potential profiles in the quantum Hall regime measured by a scanning force microscope. *International Conference on High Magnetic Fields in Semiconductors* **298**,

- 562–566 (2001). URL <http://www.sciencedirect.com/science/article/pii/S0921452601003830>.
- [11] Ahlswede, E., Weis, J., v. Klitzing, K. & Eberl, K. Hall potential distribution in the quantum Hall regime in the vicinity of a potential probe contact. *Proceedings of the Fourteenth International Conference on the Electronic Properties of Two-Dimensional Systems* **12**, 165–168 (2002). URL <http://www.sciencedirect.com/science/article/pii/S1386947701002673>.
- [12] Ahlswede, E. Potential- und Stromverteilung beim Quanten-Hall-Effekt bestimmt mittels Rasterkraftmikroskopie (2002).
- [13] Dahlem, F., Ahlswede, E., Weis, J. & v. Klitzing, K. Adiabatic transport and Hall potential measurements in the integer quantum Hall effect. *AIP Conference Proceedings* **893**, 675–676 (2007). URL <http://scitation.aip.org/content/aip/proceeding/aipcp/10.1063/1.2730071>.
- [14] Dahlem, F. Adiabatic transport in the quantum Hall regime : comparison between transport and scanning force microscopy investigations (2008).
- [15] Dahlem, F., Ahlswede, E., Weis, J. & v. Klitzing, K. Cryogenic scanning force microscopy of quantum Hall samples: Adiabatic transport originating in anisotropic depletion at contact interfaces. *Phys. Rev. B* **82**, 121305 (2010). URL <https://link.aps.org/doi/10.1103/PhysRevB.82.121305>.
- [16] Panos, K. *Current distribution and Hall potential landscape within the quantum Hall effect in graphene and towards the breakdown in a (Al,Ga)As heterostructure*. Ph.D. thesis, Universität Stuttgart, Holzgartenstr. 16, 70174 Stuttgart (2014). URL <http://elib.uni-stuttgart.de/opus/volltexte/2014/9360>.
- [17] Panos, K., Gerhardts, R. R., Weis, J. & von Klitzing, K. Current distribution and Hall potential landscape towards breakdown of the quantum Hall effect: a scanning force microscopy investigation. *New Journal of Physics* **16**, 113071 (2014). URL <http://stacks.iop.org/1367-2630/16/i=11/a=113071>.
- [18] Lier, K. & Gerhardts, R. R. Self-consistent calculations of edge channels in laterally confined two-dimensional electron systems. *Phys. Rev. B* **50**, 7757–7767 (1994). URL <https://link.aps.org/doi/10.1103/PhysRevB.50.7757>.
- [19] Mausser, M. D. *Aufbau eines Milli-Kelvin-Rastersondenmikroskops mit Einzelelektronentransistoren als Sonden*. Master’s thesis (2012).
- [20] Weber, J., Weis, J., Hauser, M. & v Klitzing, K. Fabrication of an array of single-electron transistors for a scanning probe microscope sensor. *Nanotechnology* **19**, 375301 (2008). URL <http://stacks.iop.org/0957-4484/19/i=37/a=375301>.

- [21] Mausser, M. D. *Scanning single-electron transistor array microscope to probe a two-dimensional electron system under quantum Hall conditions below 40 milli-Kelvin*. Ph.D. thesis (2017).
- [22] Klitzing, K. v., Dorda, G. & Pepper, M. New Method for High-Accuracy Determination of the Fine-Structure Constant Based on Quantized Hall Resistance. *Phys. Rev. Lett.* **45**, 494–497 (1980). URL <http://link.aps.org/doi/10.1103/PhysRevLett.45.494>.
- [23] Ando, T., Fowler, A. B. & Stern, F. Electronic properties of two-dimensional systems. *Rev. Mod. Phys.* **54**, 437–672 (1982). URL <http://link.aps.org/doi/10.1103/RevModPhys.54.437>.
- [24] Novoselov, K. S. *et al.* Electric Field Effect in Atomically Thin Carbon Films. *Science* **306**, 666 (2004). URL <http://science.sciencemag.org/content/306/5696/666.abstract>.
- [25] Ohtomo, A. & Hwang, H. Y. A high-mobility electron gas at the LaAlO₃/SrTiO₃ heterointerface. *Nature* **427**, 423 (2004). URL <https://doi.org/10.1038/nature02308>.
- [26] Hwang, H. Y. *et al.* Emergent phenomena at oxide interfaces. *Nature Materials* **11**, 103 (2012). URL <https://doi.org/10.1038/nmat3223>.
- [27] Kane, C. L. & Mele, E. J. Z₂ Topological Order and the Quantum Spin Hall Effect. *Phys. Rev. Lett.* **95**, 146802 (2005). URL <https://link.aps.org/doi/10.1103/PhysRevLett.95.146802>.
- [28] Hsieh, D. *et al.* A topological Dirac insulator in a quantum spin Hall phase. *Nature* **452**, 970 (2008). URL <https://doi.org/10.1038/nature06843>.
- [29] Umansky, V. *et al.* MBE growth of ultra-low disorder 2DEG with mobility exceeding 35*10⁶cm²/Vs. *International Conference on Molecular Beam Epitaxy (MBE-XV)* **311**, 1658–1661 (2009).
- [30] Cho, A. Y. & Arthur, J. R. Molecular beam epitaxy. *Progress in Solid State Chemistry* **10**, 157–191 (1975). URL <http://www.sciencedirect.com/science/article/pii/0079678675900059>.
- [31] Davies, J. H. *The Physics of Low-dimensional Semiconductors: An Introduction* (Cambridge University Press, 1998). URL http://books.google.de/books?id=_YXoT2Tyq6oC.
- [32] Hunklinger, S. *Festkörperphysik* (De Gruyter, 2012). URL https://books.google.de/books?id=oN_oBQAAQBAJ.
- [33] 1D Poisson from Greg Snider (2012). URL <http://www.nd.edu/~gsnider/>.

- [34] Abramowitz, M. & Stegun, I. Jacobian elliptic functions and theta functions. Chapter 16 in Handbook of mathematical functions with formulas, graphs, and mathematical tables. *Dover, New York* 567–581 (1972).
- [35] Olver, F. W. J. *NIST Handbook of Mathematical Functions* (2010).
- [36] Drude, P. Zur Elektronentheorie der Metalle. *Ann. Phys.* **306**, 566–613 (1900). URL <https://doi.org/10.1002/andp.19003060312>.
- [37] Drude, P. Zur Elektronentheorie der Metalle; II. Teil. Galvanomagnetische und thermomagnetische Effecte. *Ann. Phys.* **308**, 369–402 (1900). URL <https://doi.org/10.1002/andp.19003081102>.
- [38] Kittel, C. *Einführung in die Festkörperphysik* (Oldenbourg, 2006). URL <https://books.google.de/books?id=b3L3flBBavQC>.
- [39] MacDonald, A. H., Rice, T. M. & Brinkman, W. F. Hall voltage and current distributions in an ideal two-dimensional system. *Phys. Rev. B* **28**, 3648–3650 (1983). URL <https://link.aps.org/doi/10.1103/PhysRevB.28.3648>.
- [40] Schulz, L. *Parallel arrangements of quantum dots and quantum point contacts in high magnetic fields: periodic conductance modulations with magnetic flux change*. Ph.D. thesis (2014).
- [41] Tong, D. Lectures on the quantum Hall effect. *arXiv preprint arXiv:1606.06687* (2016).
- [42] Weis, J. & von Klitzing K. Metrology and microscopic picture of the integer quantum Hall effect. *Philosophical Transactions of the Royal Society A: Mathematical, Physical and Engineering Sciences* **369**, 3954–3974 (2011). URL <https://doi.org/10.1098/rsta.2011.0198>.
- [43] Gauß, A. W. *Fabrication and Evaluation of Small Magnetic Field Sensors for Cryogenic Applications*. Master’s thesis (2014).
- [44] Isihara, A. & Smrcka, L. Density and magnetic field dependences of the conductivity of two-dimensional electron systems. *Journal of Physics C: Solid State Physics* **19**, 6777 (1986). URL <http://stacks.iop.org/0022-3719/19/i=34/a=015>.
- [45] SCHUBNIKOW, L. & DE HAAS, W. J. A New Phenomenon in the Change of Resistance in a Magnetic Field of Single Crystals of Bismuth. *Nature* **126**, 500 (1930). URL <https://doi.org/10.1038/126500a0>.
- [46] Taylor, B. N. & Witt, T. J. New International Electrical Reference Standards Based on the Josephson and Quantum Hall Effects. *Metrologia* **26**, 47 (1989). URL <http://stacks.iop.org/0026-1394/26/i=1/a=004>.

-
- [47] Hartland, A. The Quantum Hall Effect and Resistance Standards. *Metrologia* **29**, 175 (1992). URL <http://stacks.iop.org/0026-1394/29/i=2/a=006>.
- [48] Jeckelmann, B. & Jeanneret, B. The quantum Hall effect as an electrical resistance standard. *Reports on Progress in Physics* **64**, 1603 (2001). URL <http://stacks.iop.org/0034-4885/64/i=12/a=201>.
- [49] Jeckelmann, B. & Jeanneret, B. The quantum Hall effect as an electrical resistance standard. *Measurement Science and Technology* **14**, 1229 (2003). URL <http://stacks.iop.org/0957-0233/14/i=8/a=306>.
- [50] Willett, R. *et al.* Observation of an even-denominator quantum number in the fractional quantum Hall effect. *Phys. Rev. Lett.* **59**, 1776–1779 (1987). URL <https://link.aps.org/doi/10.1103/PhysRevLett.59.1776>.
- [51] Stormer, H. L., Tsui, D. C. & Gossard, A. C. The fractional quantum Hall effect. *Rev. Mod. Phys.* **71**, S298–S305 (1999). URL <http://link.aps.org/doi/10.1103/RevModPhys.71.S298>.
- [52] Frieß, B. *Spin and Charge Ordering in the Quantum Hall Regime*. Dissertation, Munich (2014).
- [53] Jain, J. K. Composite-fermion approach for the fractional quantum Hall effect. *Phys. Rev. Lett.* **63**, 199–202 (1989). URL <https://link.aps.org/doi/10.1103/PhysRevLett.63.199>.
- [54] Weis, J. & von Klitzing, K. Metrology and microscopic picture of the integer quantum Hall effect. *Philos Transact A Math Phys Eng Sci* **369**, 3954 (2011). URL <http://rsta.royalsocietypublishing.org/content/369/1953/3954.abstract>.
- [55] Halperin, B. I. Quantized Hall conductance, current-carrying edge states, and the existence of extended states in a two-dimensional disordered potential. *Phys. Rev. B* **25**, 2185–2190 (1982). URL <https://link.aps.org/doi/10.1103/PhysRevB.25.2185>.
- [56] Büttiker, M. Absence of backscattering in the quantum Hall effect in multiprobe conductors. *Phys. Rev. B* **38**, 9375–9389 (1988). URL <http://link.aps.org/doi/10.1103/PhysRevB.38.9375>.
- [57] Beenakker, C. W. J. Edge channels for the fractional quantum Hall effect. *Phys. Rev. Lett.* **64**, 216–219 (1990). URL <https://link.aps.org/doi/10.1103/PhysRevLett.64.216>.
- [58] Chklovskii, D. B., Shklovskii, B. I. & Glazman, L. I. Electrostatics of edge channels. *Phys. Rev. B* **46**, 4026–4034 (1992). URL <http://link.aps.org/doi/10.1103/PhysRevB.46.4026>.

- [59] Svensson, S. P., Kanski, J., Andersson, T. G. & Nilsson, P.-O. Photoemission studies of the band bending on MBE-grown GaAs(001). *Journal of Vacuum Science & Technology B: Microelectronics Processing and Phenomena* **2**, 235–239 (1984). URL <https://avs.scitation.org/doi/abs/10.1116/1.582792>.
- [60] Chen, W., Dumas, M., Mao, D. & Kahn, A. Work function, electron affinity, and band bending at decapped GaAs(100) surfaces. *Journal of Vacuum Science & Technology B: Microelectronics and Nanometer Structures Processing, Measurement, and Phenomena* **10**, 1886–1890 (1992). URL <https://avs.scitation.org/doi/abs/10.1116/1.586217>.
- [61] NSM Archive - Aluminium Gallium Arsenide (AlGaAs) (2001). URL <http://www.ioffe.ru/SVA/NSM/Semicond/AlGaAs/basic.html>.
- [62] Issa Diakite, Y. *et al.* Accurate Electronic, Transport, and Bulk Properties of Gallium Arsenide (GaAs) (2016). URL <https://ui.adsabs.harvard.edu/#abs/2016arXiv160105300I>.
- [63] Klauß, U., Dietsche, W. & von Klitzing K. et al. Imaging of the dissipation in quantum-Hall-effect experiments. *Z. Physik B - Condensed Matter (1991)* **82**, 351–354.
- [64] Klaus von Klitzing, R. G. u. J. W. 25 Jahre Quanten-Hall-Effekt. *Physik Journal* **6**, 37–44 (2005). URL http://www.pro-physik.de/details/physikjournalIssue/1089761/Issue_6_2005.html#1096515.
- [65] Klass, U., Dietsche, W., von Klitzing, K. & Ploog, K. Image of the dissipation in gated quantum Hall effect samples. *Surface Science* **263**, 97–99 (1992). URL <http://www.sciencedirect.com/science/article/pii/003960289290314V>.
- [66] Haremski, P. *Electrical Breakdown of the Quantum Hall Effect: Influence of Hall bar Width and Potential probing Contacts on the Edge- and the Bulk-dominated regime*. Master’s thesis (2015).
- [67] Eber, G., von Klitzing, K., Ploog, K. & Weinmann, G. Two-dimensional magneto-quantum transport on GaAs – Al_xGa_{1-x}As heterostructures under non-ohmic conditions. *Journal of Physics C: Solid State Physics* **16**, 5441 (1983). URL <http://stacks.iop.org/0022-3719/16/i=28/a=012>.
- [68] Savytsky, R. Quantum Hall samples: Tuning the edge-dominated regime by gate electrodes (2017).
- [69] attocube systems AG (2018). URL <http://www.attocube.com/>.
- [70] Molex Electronic Solutions (2018). URL <https://www.molex.com/molex/home>.

- [71] Gömmel, A. *et al.* Entwicklung von hochgradig erschütterungsarmen Fundamenten für elf Versuchsumgebungen in einem neugebauten Präzisionslabor. *Bauingenieur* **89**, 4–12 (2014).
- [72] Precision Laboratory (2018). URL https://www.fkf.mpg.de/2489208/001Precision_Laboratory.
- [73] Averin, D. & K. Likharev, K. *Coulomb Blockade of Single-Electron Tunneling, and Coherent Oscillations in Small Tunnel Junctions*, vol. 62 (1986).
- [74] Meirav, U. & Foxman, E. B. Single-electron phenomena in semiconductors. *Semiconductor Science and Technology* **11**, 255–284 (1996). URL <https://doi.org/10.1088%2F0268-1242%2F11%2F3%2F003>.
- [75] Weis, J. *Electrical Transport Through Quantum Dot Systems* (Habilitation, University of Stuttgart, 2002).
- [76] Weber, J. *Einzelelektronen-Transistoren auf Spitzen zur Verwendung in der Rastersondenmikroskopie bei tiefen Temperaturen*. Ph.D. thesis, Max-Planck-Institut für Festkörperforschung, Stuttgart (2009).
- [77] Zwirger, W. & Scharpf, M. Crossover from Coulomb-blockade to ohmic conduction in small tunnel junctions. *Zeitschrift für Physik B Condensed Matter* **85**, 421–426 (1991). URL <https://doi.org/10.1007/BF01307639>.
- [78] Finkler, A. *et al.* Self-Aligned Nanoscale SQUID on a Tip. *Nano Letters* **10**, 1046–1049 (2010). URL <https://doi.org/10.1021/nl100009r>. PMID: 20131810, <https://doi.org/10.1021/nl100009r>.
- [79] Finkler, A. *et al.* Nano-sized SQUID-on-tip for scanning probe microscopy. *Journal of Physics: Conference Series* **400**, 052004 (2012). URL <http://stacks.iop.org/1742-6596/400/i=5/a=052004>.
- [80] Yoo, M. J. *et al.* Scanning Single-Electron Transistor Microscopy: Imaging Individual Charges. *Science* **276**, 579–582 (1997). URL <http://science.sciencemag.org/content/276/5312/579>. <http://science.sciencemag.org/content/276/5312/579.full.pdf>.
- [81] Lina, S., Xinxing, L., Hua, Q. & Xiaofeng, G. A sensitive charge scanning probe based on silicon single electron transistor. *Journal of Semiconductors* **37**, 044008 (2016). URL <http://stacks.iop.org/1674-4926/37/i=4/a=044008>.
- [82] Oktay, G. *Small alloyed ohmic contacts to 2DES and submicron scale corbino devices in strong magnetic fields : observation of a zero bias anomaly and single electron charging*. Ph.D. thesis (2009).
- [83] Wei, Y. *Two-Dimensional Electron System in Quantum Hall Regime Probed by Metal Single-Electron Transistor*. Ph.D. thesis (1998).

- [84] Hüls, J. Experimente zur Potentialverteilung zweidimensionaler Elektronensysteme im ganz- und gebrochenzahligen Quanten-Hall-Bereich mit Hilfe eines Einzelelektron-Transistors als Elektrometer (2001). URL <http://lib.ugent.be/catalog/rug01:000723655>.
- [85] Rompelman, O. & Ros, H. Coherent averaging technique: A tutorial review Part 1: Noise reduction and the equivalent filter. *Journal of Biomedical Engineering* **8**, 24 – 29 (1986). URL <http://www.sciencedirect.com/science/article/pii/S0141542586900269>.
- [86] Hassan, U. & Anwar, M. S. Reducing noise by repetition: introduction to signal averaging. *European Journal of Physics* **31**, 453 (2010). URL <http://stacks.iop.org/0143-0807/31/i=3/a=003>.
- [87] Bono, M. P. Single-Electron Transistors for Operation Temperature beyond 1K and setting up a Simulation Program for calculating the Current density Distribution within the Quantum Hall Regime (2018).
- [88] Beenakker, C. W. J. Theory of Coulomb-blockade oscillations in the conductance of a quantum dot. *Phys. Rev. B* **44**, 1646–1656 (1991). URL <https://link.aps.org/doi/10.1103/PhysRevB.44.1646>.
- [89] Bestwick, A. J. *et al.* Precise Quantization of the Anomalous Hall Effect near Zero Magnetic Field. *Phys. Rev. Lett.* **114**, 187201 (2015). URL <https://link.aps.org/doi/10.1103/PhysRevLett.114.187201>.
- [90] Weis, J., Wei, Y. & v. Klitzing, K. Probing the depletion region of a two-dimensional electron system in high magnetic fields. *Physica B: Condensed Matter* **256-258**, 1–7 (1998). URL <http://www.sciencedirect.com/science/article/pii/S0921452698005742>.
- [91] Riegel, K. *Hall sensor for scanning probe microscope to investigate quantum Hall samples below 1 Kelvin*. Master’s thesis (2018).
- [92] Pekola, J. P., Hirvi, K. P., Kauppinen, J. P. & Paalanen, M. A. Thermometry by Arrays of Tunnel Junctions. *Phys. Rev. Lett.* **73**, 2903–2906 (1994). URL <https://link.aps.org/doi/10.1103/PhysRevLett.73.2903>.
- [93] Weis, J. Single-Electron Devices. In *CFN Lectures on Functional Nanostructures Vol. 1: Vol. 1*, 87–121 (Springer Berlin Heidelberg, Berlin, Heidelberg, 2005). URL https://doi.org/10.1007/978-3-540-31533-9_5.
- [94] Meschke, M., Engert, J., Heyer, D. & Pekola, J. P. Comparison of Coulomb Blockade Thermometers with the International Temperature Scale PLTS-2000. *International Journal of Thermophysics* **32**, 1378 (2011). URL <https://doi.org/10.1007/s10765-011-1033-8>.

- [95] Kühn, M. *Renewing a scanning probe microscope set up for operation below 1 K and simulating the Hall potential distributions of inhomogeneous quantum Hall samples*. Master's thesis (2018).
- [96] Onipede, B. O. *Fabrication and Characterization of (AlGa)As Heterostructures for Hall Sensor Application*. Master's thesis (2016).
- [97] Wei, Y. Y., Weis, J., v. Klitzing, K. & Eberl, K. Single-electron transistor as an electrometer measuring chemical potential variations. *Applied Physics Letters* **71**, 2514–2516 (1997). URL <https://doi.org/10.1063/1.120104>. <https://doi.org/10.1063/1.120104>.
- [98] Wei, Y. Y., Weis, J., Klitzing, K. v. & Eberl, K. Edge Strips in the Quantum Hall Regime Imaged by a Single-Electron Transistor. *Phys. Rev. Lett.* **81**, 1674–1677 (1998). URL <http://link.aps.org/doi/10.1103/PhysRevLett.81.1674>.
- [99] Klaffs, T., Krupenin, V. A., Weis, J. & Ahlers, F. J. Eddy currents in the integer quantum Hall regime spatially resolved by multiple single-electron transistor electrometers. *15th International Conference on Electronic Properties of Two-Dimensional Systems (EP2DS-15)* **22**, 737–740 (2004). URL <http://www.sciencedirect.com/science/article/pii/S1386947703009366>.
- [100] Hauffe, K. Gegen Flusssäure korrosionsbeständige Werkstoffe. *Materialwissenschaft und Werkstofftechnik* **16**, 259–270 (1985). URL <http://dx.doi.org/10.1002/mawe.19850160805>.
- [101] Williams, K. R., Gupta, K. & Wasilik, M. Etch rates for micromachining processing-Part II. *Journal of Microelectromechanical Systems* **12**, 761–778 (Dec.).

Statement of Originality

This thesis has been performed independently with support by my supervisor/s. It contains no material that has been accepted for the award of a degree in this or any other university. To the best of the candidate's knowledge and belief, this thesis contains no material previously published or written by another person except where due reference is made in the text.

Stuttgart, February 11th 2019

.....

(signature of candidate)

Acknowledgments

My project would have been even more difficult without support of other persons from both, inside and outside of the institute, either by supporting me personally during hard times, by helping me with technical problems, by offering me a highly developed laboratory, by allowing discussions about relevant topics and by trusting me and giving me an enormous freedom in planning and conducting my projects.

Regardless of the order I want to thank the following persons:

- my supervisor Prof. Dr. Jürgen Weis for all his support during all my ups and downs during the last years, his constructive suggestions concerning measurements, the cryogenic setup or the lab in general and during the correction of this thesis. I appreciate that he trusted me to successfully end this project and the large amount of freedom I had during all my projects.
- Prof. Dr. Klaus von Klitzing for giving me the privilege to become one of his PhD students in his group, his financial support concerning measurement equipment or the cryogenic setup, constructive discussions about achieved measurement data and a lot of freedom for both, planing and realizing my project.
- Prof. Dr. Peter Michler for taking his time to read and make the external report of this thesis.
- Prof. Dr. Werner Wegscheider, Dr. Christian Reichel from the ETH Zurich and Prof. Dr. Peter Michler, Dr. Michael Jetter and Dr. Matthias Paul from the University of Stuttgart and Maik Hauser from the MPI Stuttgart, for supplying me with wafer material necessary to fabricate either Hall bar samples or single-electron transistors. Without this support, the development of the new single-electron transistor array design and fabrication of working tips would have not been possible.
- our technicians Manfred Schmid, Ingo Hagel, Steffen Wahl and Gunther Euchner who never hesitated to support me when a sample rod had to be changed or developed, answering my questions concerning the cryogenic setup and helping me to exchange pumps in my system what would have been impossible alone.

- the mechanical workshop and low temperature service for always being helpful in constructing and manufacturing of special parts, either for the UHV system, the cryogenic setup, or the microscope, and for the reliable supply with liquid Helium even during Christmas times.
- the cleanroom team, Achim Güth, Marion Hagel, Ulrike Weizmann, Maik Hauser, Thomas Reindl and Bernhard Fenk for the great support and introduction into the cleanroom facility. Special thank to Bernhard Fenk who always entrusted me his focused-ion beam setup for many night shifts when SETs had to be fabricated and his helpful tips and Thomas Reindl who became a good friend, never hesitating to answer my questions and supporting me in maintaining the UHV system and sometimes filling our cryogenic systems.
- the whole IT group for their support with computer related issues. They never hesitated to give quick advices or to exchange hardware parts despite their stressful day-to-day work.
- my six master students I have supervised during my PhD time. I appreciate the time with you a lot, learning about different cultures, different personalities, planning your projects and discussing your results (even during our late night hours)...
 - M.Sc. Patricia Haremski for performing transport measurements towards breakdown in the integer quantum Hall regime nicely showing edge-dominated and bulk-dominated regimes, which supports the microscopic picture of the quantum Hall effect.
 - M.Sc. Bamidele Oluwagbenga Onipede for investigating dependencies of intrinsic wafer specific Hall sensor noise, an important step on the way to our new free-standing Hall sensor.
 - M.Sc. Rostyslav Savytsky for your transport measurement on gated Hall bar structures in order to enrich the variety of measurements supporting the microscopic picture of the quantum Hall effect. All the best for you and your wife with your PhD in Sydney.
 - M.Sc. Maurizio Pietro Bono for fabricating and characterizing so many planar SET structures in order to show that an overlap reduction is possible and makes them working even at 4.2K. You have laid the base for the next generation of SET tips.
 - M.Sc. Maximilian Kühn for setting up a second version of my scanning probe microscope, improving existing simulations to calculate Hall potential distributions in the quantum Hall regime and being my successor, taking over my working microscope and my SETs for your PhD; take good care of them.

- M.Sc. Konstantin Riegel for bringing my Hall sensor to life in the cleanroom facility and performing first characterization and scanning measurements with it. This sensor makes new physics accessible in our microscopes, and hopefully other microscopes around the world.
- my previous colleagues Dr. Konstantinos Panos, Dr. Stefan Falk, Dr. Maximilian Köpke, Dr. Leonhard Schulz, Dr. Marcel Mausser and Dr. Marcus Rommel for creating a happy and generous working atmosphere in the institute. Special thanks to Dr. Konstantinos Panos, who introduced me in the first place into the group, back then as a HiWi student.
- my predecessor, reliable colleague during my first PhD years and dear friend Marcel Mausser for building such an astonishing and reliable microscope setup, introducing me into the world of scanning probe microscopy, encouraging me during this time and being a friend of mine. Together we figured out that absolutely everything is possible when you are eager to work for it. I also very enjoyed our holidays together with you and Johanna.
- my whole family for their enduring support during this thesis, especially Nicole Gauß who always listened to my problems in the lab and my solutions and cheering me up when I was down. I wish you all the best for you PhD thesis.
- my beloved girlfriend Lisa Ullrich for always supporting and encouraging me, cheering me up when things in the lab did not work as planned and for being such a lovely person. Without you my life would be less beautiful and I do my best to give you the same support during your PhD thesis. Also, I will never forget our adventure holiday in beautiful Iceland where I practically learned that cars are able to cross rivers even without bridges.

